Université de Lille

Faculté des Sciences et Technologies

Ecole Doctorale 104 - Sciences de la Matière, du Rayonnement, et de l'Environnement

Thèse de Doctorat

par

Artem Shagurin

pour l'obtention du titre de

Docteur de l'Université de Lille

Discipline: Chimie théorique, physique, analytique

Structure et dynamique de l'interface entre la curcumine et le dioxyde de carbone supercritique: Analyse par dynamique moléculaire

Thèse présentée et soutenue à Lille, le 23/05/2025 devant le jury:

Alexander	**LYUBARTSEV** *Professeur, Stockholm University*	**Rapporteur**
Milan	**PŘEDOTA** *Professeur, University of South Bohemia*	**Rapporteur**
Abdenacer	**IDRISSI** *Professeur, Université de Lille*	**Directeur de thèse**
Frederic	**AFFOUARD** *Professeur, Université de Lille*	**Co-directeur de thèse**
Michael	**KISELEV** *Professeur, Russian Academy of Sciences*	**Co-directeur de thèse**
Pál	**JEDLOVSZKY** *Professeur, Eszterházy Károly Catholic University*	**Président**
Alessandro	**TRIOLO** *Professeur, ISM-CNR*	**Examinateur**
Sameer	**DALVI** *Professeur, Indian Institute of Technology Gandhinaga*	**Examinateur**
Natalia	**Correia** *Maîtresse de conférences, Université de Lille*	**Invitée**
Bertrand	**Chazallon** *Professeur, Université de Lille*	**Invité**

University of Lille

Faculty of Sciences and Technologies

Doctoral School 104 – Science of the Matter, of the Radiation, and of the Environment

Doctoral Thesis

by

Artem Shagurin

to obtain the degree of

Doctor of the University of Lille

Discipline: Theoretical, physical, analytical chemistry

Structure and Dynamics of the Curcumin-Vacuum and Curcumin-supercritical CO_2 interfaces: a molecular dynamics analysis

Thesis presented and defended in Lille, on 23/05/2025 before the jury:

Alexander	**LYUBARTSEV** *Professor, Stockholm University*	**Referee**
Milan	**PŘEDOTA** *Professor, University of South Bohemia*	**Referee**
Abdenacer	**IDRISSI** *Professor, University of Lille*	**Supervisor**
Frederic	**AFFOUARD** *Professor, University of Lille*	**Co-supervisor**
Michael	**KISELEV** *Professor, Russian Academy of Sciences*	**Co-supervisor**
Pál	**JEDLOVSZKY** *Professor, Eszterházy Károly Catholic University*	**President**
Alessandro	**TRIOLO** *Professor, ISM-CNR*	**Examiner**
Sameer	**DALVI** *Professor, Indian Institute of Technology Gandhinaga*	**Examiner**
Natalia	**Correia** *Assistant professor, University of Lille*	**Invited**
Bertrand	**Chazallon** *Professor, University of Lille*	**Invited**

Acknowledgements

The work done so far would not have been possible without support and dedication of my supervisors. I would like to express my sincere gratitude to Prof. Abdenacer Idrissi, Prof. Frederic Affouard and Prof. Mikhail Kiselev for their support and guidance.

Beside my advisors, I also would like to thank to Prof. Francois-Alexandre Miannay, who has helped out with my work on many occasions.

I am very grateful to the University of Lille and Hauts-de-France region for hosting me and providing the financial support.

I would like to thank all of my colleagues in France and in Russia who helped with this research. I express my utmost gratitude to all my friends for their continued support. I would like to personally thank Olena Moskaieva and Ana Licia Mouria Gomez for keeping me company in Lille, Artem Sherudillo, Alexandra Popkova, Dmitro Dudaev and Evhenii Vaksler for getting me accustomed to France. I am grateful to my previous colleagues – Sergey Usoltsev, Alexander Bobrov, Evgeniy Molchanov, Maxim Lebedev, Ksenia Ksenofontova and Yurii Marfin. Finally, I would like to thank my dear friends – Pavel Bocharov, Anastasiya Kerner, Dmitriy Khalabudin, as well as Evgeniy Krestyaninov, Alexander Novosyolov, Alexey Volgutskov, Anton Cimbal and Valentina Dunaeva for always encouraging me to keep going even in the worst times.

Most importantly, I would like to thank my family: my mother, Elena, and my late father, Yurii, as well as my grandparents, my aunts and my cousin for their love, support and help during all my life.

Résumé

Le contrôle des formes polymorphes des ingrédients pharmaceutiques actifs (API) constitue un enjeu majeur tant pour la recherche fondamentale que pour l'industrie pharmaceutique. Des avancées récentes ont mis en évidence le rôle crucial joué par les propriétés de surface des différentes structures cristallines, et en particulier par la distribution conformationnelle des molécules d'API à l'interface solide, dans la promotion du polymorphisme.

Dans ce contexte, cette thèse présente une étude approfondie de l'interface entre la curcumine (CUR) et le dioxyde de carbone supercritique ($scCO_2$) à l'aide de simulations de dynamique moléculaire (MD). La curcumine, une molécule d'intérêt croissant en médecine, a fait l'objet d'un reparamétrage spécifique de son champ de force, basé sur des calculs de chimie quantique (QC), afin de reproduire avec précision les différences thermodynamiques entre polymorphes ainsi que leurs distributions conformationnelles.

Nous avons développé de nouveaux algorithmes pour l'échantillonnage des conformations de la CUR, ainsi que pour le calcul de diverses propriétés structurales et dynamiques à son interface. Afin d'étudier de manière fiable le système CUR–$scCO_2$, nous avons évalué plusieurs champs de force pour le CO_2 et identifié celui qui reproduit le plus fidèlement les propriétés du point critique. Nous avons démontré comment certaines observables locales peuvent être utilisées pour caractériser l'organisation et la dynamique du fluide supercritique à proximité du point critique. Ce protocole a ensuite été appliqué pour comparer les comportements structuraux et dynamiques du $scCO_2$ avec ceux de l'eau et de l'ammoniac dans leurs régimes supercritiques respectifs.

Enfin, nous avons caractérisé les changements de structure locale à l'interface CUR–vide et CUR–$scCO_2$ dans différentes conditions thermodynamiques. Un algorithme spécifique a été utilisé pour identifier les molécules de CUR appartenant à chaque couche interfaciale, permettant une analyse fine des propriétés structurelles, dynamiques et énergétiques au sein de ces régions critiques pour la stabilité et l'évolution des formes polymorphes.

Mots-clés : Polymorphisme, Principes actifs, curcumine, fluides supercritiques, dynamique moléculaire, analyse conformationnelle.

Abstract

Controlling the polymorphic forms of active pharmaceutical ingredients (APIs) is a major challenge for both fundamental research and the pharmaceutical industry. Recent advances in this field have highlighted the crucial role played by the surface properties of different crystalline structures, and in particular by the conformational distribution of API molecules at the solid interface.

In this context, this thesis presents an in-depth study of the interface between curcumin (CUR) and supercritical carbon dioxide ($scCO_2$) using molecular dynamics (MD) simulations. Curcumin, a molecule subject to growing interest in medicine, has been parametrized, based on quantum chemical (QC) calculations, in order to accurately reproduce thermodynamic differences between polymorphs as well as their conformational distributions.

We have developed new algorithms for sampling CUR conformations, as well as for calculating various structural and dynamic properties at its interface. In order to reliably study the CUR-$scCO_2$ system, we have evaluated several force fields for the CO_2 and identified the one that most faithfully reproduces the critical point properties. We demonstrated how certain local observables can be used to characterize the organization and dynamics of the supercritical fluid near the critical point. This protocol was then applied to compare the structural and dynamic behaviors of $scCO_2$ with those of water and ammonia in their respective supercritical regimes.

Finally, we characterized local structural changes at the CUR-vacuum and CUR-$scCO_2$ interface under different thermodynamic conditions. A specific algorithm was used to identify CUR molecules belonging to each interfacial layer, allowing analysis of the structural, dynamic and energetic properties within these critical regions.

Keywords: polymorphism, active pharmaceutical ingredients, curcumin, supercritical fluids, molecular dynamics, conformational analysis.

Table of Contents

List of Figures

List of Tables

List of Equations

List of Algorithms

List of Abbreviations

API	Active Pharmaceutical Ingredient
SCF	Supercritical Fluid
CUR	Curcumin
COM	Center of mass
DBSCAN	Density-Based Spatial Clustering of Applications with Noise
$scCO_2$	Supercritical Carbon Dioxide
MD	Molecular Dynamics
MC	Monte Carlo
RDF	Radial Distribution Function
NRDF	Nearest-Neighbor Radial Distribution Function
ADF	Angle Distribution Function
NADF	Nearest-Neighbor Angle Distribution Function
ES	Electrostatic
LJ	Lennard-Jones (potential)
TOT	Total (referring to energy)
OPLS	Optimized Potential for Liquid Simulations
GAFF	General Amber Force Field
CHARMM	Chemistry at Harvard Macromolecular Mechanics (hereafter only force field, not the program with the same name)
GROMOS	GROningen MOlecular Simulation (hereafter only force field, not the program with the same name)
VP	Voronoi Polehydra
ITIM	Identification of Truly Interfacial Molecules
VdW	Van Der Waals (radius)

CHAPTER 1
INTRODUCTION

This chapter gives a brief overview of the current state of research of polymorphic transformations of active pharmaceutical ingredients, methods of control of said transformations and their most notable causes. Particular attention is paid to the surface properties of different crystals of pharmaceutical compounds. We also introduce supercritical fluids and their relevant properties.

1.1. APIs and Polymorphism

The polymorphic form of an active pharmaceutical ingredient (API) is a critical aspect in pharmaceutical development because it directly affects the drug's physicochemical properties, including solubility, stability, bioavailability, and manufacturability. One can recall that polymorphism refers to the ability of a substance to exist in more than one crystalline form. This can manifest in the same API having different molecular arrangements in the solid state or having different molecular conformations inside the crystal. Controlling the transformation between polymorphs of an API is a critical challenge in pharmaceutical development. Polymorphic transformations can occur during manufacturing, storage, or even after administration, potentially altering the drug's performance.

Polymorphism by itself is a very complicated subject that involves a variety of factors. One of the more obvious factors is the nature of the substance under study. Indeed, even within one family of compounds, chemical substitution of functional groups can significantly affect the ability to form different polymorphs e.g., introduction of long carbon chains can lead to the appearance[1] of conformational polymorphism. Thermodynamic conditions or, even more broadly, thermochemical properties of the system i.e., pressure, temperature, purity of solvent, choice of solvent, pH, choice of the atmosphere, etc., have a profound influence on the formation[2] of different polymorphs. Relatedly, kinetic factors, and their interplay[3] with the thermodynamic parameters, also have a markedly big effect. Since crystallization involves multiple stages, from small cluster formation, to nucleation, to growth, some polymorphs, disadvantaged energetically, can still be found due to their faster rates of precipitation.

Recent research has revealed the **significant role of the solid surface in polymorphic formation.** The molecules at the solid interface differ from those in the bulk, exhibiting higher mobility, special packing and particular conformations due to fewer molecular neighbors. Indeed, flexible APIs quite often possess large number of different conformations, and the proximity to the interface modifies which conformations are accessible to the API.

In the following, we will summarize the literature data on the critical role of the properties of the interface in the crystallization process of APIs. At interfaces, atoms or molecules experience reduced coordination and higher mobility, which lowers the energy barrier for nucleation and promotes crystal growth. This leads to faster crystallization at surfaces compared to the bulk material. Additionally, interfaces can induce structural ordering and reduce surface

energy, further driving the crystallization process. The importance of phenomena occurring at the interface was pointed out[4] by the seminal paper of Sun et al. The authors investigate the accelerated crystallization behavior observed at the free surfaces of organic glasses. The researchers focused on indomethacin (IMC), an organic glass capable of forming two polymorphs, α and γ. They discovered that, unlike in the bulk, where crystal growth is relatively slow, crystallization at the free surface is significantly faster. Notably, as these surface crystals grow laterally, they also extend upward, protruding hundreds of nanometers above the glass surface without penetrating deeply into the bulk material. This upward-lateral growth mode suggests that surface molecular mobility plays a crucial role in facilitating rapid crystallization, effectively bypassing the slower dynamics of the bulk. These findings provide valuable insights into the mechanisms of surface-enhanced crystallization in amorphous materials.

Recently, a paper[5] by Xinlu et al. emphasized the importance of functionalized interfaces as versatile platforms for a broad spectrum of applications. Regarding the role of surfaces in the transformation of solids, the authors of this paper point out that the dynamic behaviors at liquid-based interfaces, influenced by factors such as wettability and molecular interactions, can significantly impact processes like crystallization and phase transitions in adjacent solid materials. By tailoring these interfacial properties, it is possible to control and direct the transformation of solids, which is crucial in applications like material synthesis and pharmaceutical development.

In another paper[6] by Yang et al., the authors investigate how different surface materials influence the nucleation and polymorphic forms of carbamazepine (CBZ) crystals in ethanol solutions. The researchers examined three surfaces: glass, polytetrafluoroethylene (PTFE), and tin. They found that the introduction of these foreign surfaces, each with distinct surface chemistries and areas, significantly impacted both the crystal morphology and the specific polymorphic form of CBZ that crystallized. Specifically, increasing the number of surface inserts led to a direct increase in the available surface area for heterogeneous nucleation, which, in turn, affected the likelihood of forming either the metastable Form II or the stable Form III of CBZ. The study highlights the critical role that surface properties play in directing the selective crystallization of different CBZ polymorphs, offering valuable insights for controlling crystallization processes in pharmaceutical applications.

Furthermore, Zhang et al.[7] examine how different surface properties influence the nucleation and growth of clotrimazole polymorphs. The researchers utilized various substrates to assess their impact on the crystallization process of clotrimazole, a common antifungal medication known for its polymorphic forms. The study found that the nature of the substrate

significantly affects both the nucleation rate and the specific polymorphic form that crystallizes. Certain surfaces promoted the formation of specific polymorphs by providing favorable nucleation sites, thereby influencing the overall crystallization pathway. These findings underscore the critical role of surface properties in directing the nucleation and growth of pharmaceutical compounds, which has important implications for drug formulation and manufacturing processes.

To go further, Sun et al.[8] examined how surface properties influence the crystallization behavior of molnupiravir, an antiviral medication. Researchers measured crystal nucleation rates both at the surface and within the bulk of amorphous molnupiravir. They found that surface nucleation rates were significantly higher – by approximately six orders of magnitude – compared to bulk nucleation rates. This substantial enhancement suggests that the molecular packing at the surface closely resembles the structure of the nucleating crystal, facilitating faster nucleation. Notably, this acceleration occurred without any change in the polymorphic form of the crystallized molnupiravir. These findings highlight the critical role of surface properties in accelerating crystal nucleation and could have significant implications for understanding the stability and manufacturing processes of amorphous pharmaceutical drugs.

In another paper[9] by Xao et al., the authors investigated how surface properties influence the crystallization behavior of amorphous posaconazole, a rod-like pharmaceutical compound. The researchers measured crystal nucleation rates both at the surface and within the bulk of amorphous posaconazole. They discovered that surface nucleation is significantly faster than bulk nucleation, by approximately nine orders of magnitude. Moreover, surface nucleation favors the formation of polymorph II, whereas bulk nucleation predominantly leads to polymorph I. This indicates that the surface environment not only accelerates nucleation but also influences the specific crystalline form that emerges. The study attributes these effects to the preferred orientation and layering of posaconazole molecules at the surface, which resemble the structure of polymorph II, thereby facilitating its nucleation. These findings underscore the critical role of surface properties in determining both the rate of nucleation and the selection of polymorphic forms during the solid-state transformation of amorphous materials.

Shi et al.[10] also bring new insight by showing that, in fact, the crystallization process can occur below the surface. Indeed, this study investigates the nucleation behavior of supercooled acetaminophen (a common pharmaceutical compound) and reveals that nucleation often occurs below the surface rather than at the surface or in the bulk. Using advanced imaging and analytical techniques, the researchers observed that subsurface regions provide favorable

conditions for nucleation due to localized variations in temperature, density, or molecular arrangement. These findings challenge the conventional assumption that nucleation primarily occurs at surfaces or in the bulk and highlight the importance of considering subsurface phenomena in understanding and controlling crystallization processes.

Furthermore, the interfacial conformation plays a significant role in determining the thermodynamic and kinetic stability of a polymorph. A more stable conformation at the interface can resist phase transitions under stress, such as changes in temperature or humidity. Metastable polymorphs, on the other hand, may persist due to kinetic barriers, even if they are less thermodynamically stable. This stability is crucial for ensuring the shelf life and performance of the drug product.[11,12] Of note is that that the crystal's mechanical properties, such as hardness, brittleness, and plasticity, are also affected by the conformation of the API at the interface. These mechanical properties influence the ease of processing, such as milling or tableting, and the final product's performance. More importantly, the conformation at the interface influences crystal growth and morphology. For example, specific conformations may promote the formation of needle-like or plate-like crystals, which can affect processes like filtration, drying, and flow properties.

Due to the large implications of polymorphic control in pharmaceutical industry, significant amount of effort has been directed toward development and modification of industrially viable methods of crystallization of specific polymorphs. Rapid Solvent Evaporation techniques are subsections of solvent crystallization – large, heavily investigated class of preparation methods. Solvent Evaporation processed can control polymorph formation by modulating temperature-pressure balance (for the same rate of evaporation), use seed crystals[13] to promote specific polymorph formation or use additives, such as certain polymers or inorganic ions,[14] to suppress nucleation and growth of undesirable polymorphic forms.

Mechanical activation[15–17] methods, e.g., grinding, share some similarities with solvent techniques, such as use of polymers[18] to selectively obtain desired polymorphs, but are fundamentally different in the way the molecules are arranged and their freedom of movement prior to the phase transition, leading to favoritism towards different polymorphic forms.

Somewhere between solvent and mechanical methods sits the Microfluidic Platform[19] class of crystallization methods. This relatively recent approach creates unique conditions by using tiny, droplet sized amounts of fluid. This significantly improves solute mobility compared to the grinding methods, but also keeps working volume of fluid small enough to rapidly control thermodynamic conditions. It has been reported that microfluidic crystallization can inhibit

spontaneous conversion from meta-stable to stable polymorphic form. However, due to its very nature, scaling and industrial application of microfluidics are rather difficult.

Melt crystallization[20–22] techniques are a great tool for crystallization of compounds that are stable at high temperatures. Melt crystallization is often used for purification and separation, where it can be considered a rather "green" procedure. But advent of techniques like layer-melt crystallization adds another set of variables that make polymorphic control possible.

Solvent-Mediated Phase[23] crystallization, often applied to synthesis of metal-containing frameworks, is another viable solvent-based method for controlling polymorphic selectivity. It can be combined with often utilized templating techniques or seed crystallization.

Supercritical Fluid (SCF) Techniques[24] constitute a big class of crystallization methods. Using unique properties of supercritical fluids, one can quickly obtain oversaturated medium via rapid expansion (de-pressurization) or with additives, such as another solvent. The fact that many of SCFs are highly tunable, i.e., responsive to small changes in temperature and pressure, makes them quite appealing to the study of polymorphic control.

1.2. Supercritical Fluids

The SCFs are in a prominent position in the development of new crystallization processes.[25] Although known for quite some time, at least from the times of French Baron Charles Cagniard de la Tour, who discovered them in 1822, SCFs are now gaining renewed interest. This innovative technology is helpful in meeting the more and more stringent requirements of regulatory authorities in terms of solid-state characterization and purity, as well as environmental acceptability. But SCFs are used not only due to their "green" nature, they have unique, valuable traits of their own. SCFs, generally speaking, have properties that are between those of liquid and gas (see Fig. 1.1.). This manifests in their diffusion coefficients, which are couple of magnitudes bigger than those in corresponding liquids, all while having slightly lower, but comparable densities. Analogously, viscosities of SCFs are also lower than liquid-state ones.

Density fluctuations in SCFs underlie many of their unique properties. These fluctuations influence their solvation, solubility behavior, and their transport properties that are at the heart of their applications.[26–31] The density fluctuations can be analyzed using neutron and X-Ray scattering,[32,33] vibration spectroscopy[34–36] (measuring the shape of a vibration mode and correlating them with the density fluctuations[37–40]), NMR,[41] and molecular dynamic simulations that complement the experimental approaches.[42,43] Several investigations point out that the density fluctuations are the result of variations in local molecular arrangements where densely packed molecules (liquid-like domains) coexist with sparsely distributed molecules (vapor-like domains).[44,45] For some molecules, e.g. supercritical water,[46] specific intermolecular interactions, such as hydrogen bonding,[47–49] have been identified as key contributors. For others, like CO_2, the direct connection between the above-mentioned local arrangement of molecules and the interplay of their attractive and repulsive interactions remains an outstanding issue. To the best of our knowledge, this interplay was often discussed based on the shift of a given vibration mode. Indeed, as the thermodynamic conditions are varied, the average forces along a given a vibrational coordinate exerted by the surrounding molecules cause the shift of the vibration frequency. This shift is described in terms of competing contribution from the repulsive and the attractive force components.[50–52] The results show that the shift is mainly due to the attractive component that shows a considerable non-linear density and temperature dependence. This non-linearity increases with a maximum near the critical conditions.

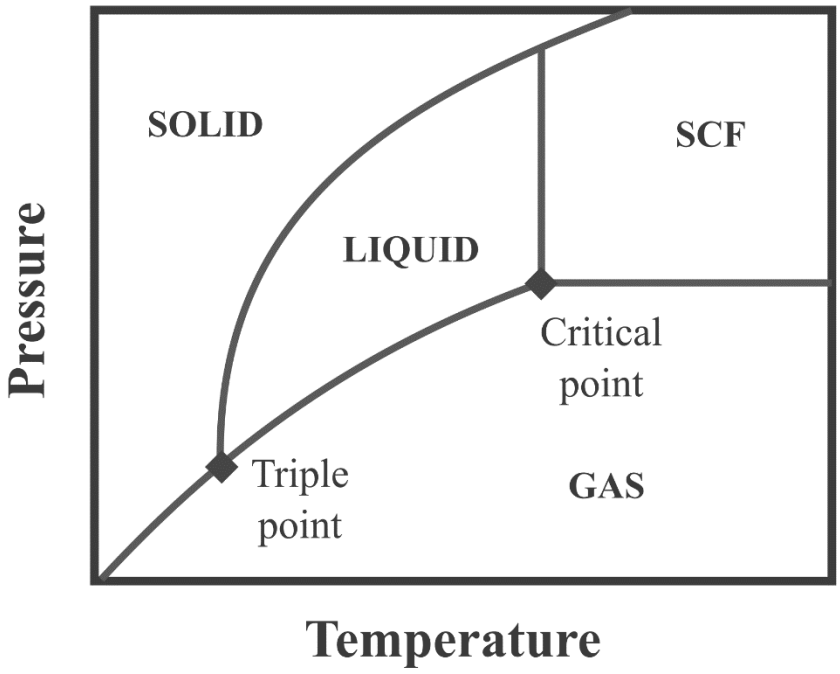

Figure 1.1. Schematic representation of a typical Temperature – Pressure phase diagram of low-weight molecular substances.

Significant number of chemical compounds upon application of sufficient heat and pressure will enter the supercritical state. However, each SCF has unique critical point temperature, pressure and density, which largely dictate their applicability and usefulness. Properties of some of the more common SCFs are summarized in Table 1.1. Among those, $scCO_2$ and scH_2O stand out as clear favorites for many industrial applications. This comes from their relatively lax operational requirements, environmentally friendly nature and ease of procurement. Supercritical H_2O faces some additional challenges, however, as it can be quite corrosive in the fluid state. This is why $scCO_2$ has become the de-facto standard, most researched[27] and most utilized SCF.

Table 1.1. Critical point thermodynamic properties of several common supercritical fluids.

	Critical temperature, K	Critical Pressure, atm	Critical density, g/cm^3
CO_2	304.1	72.8	0.469
H_2O	647.1	217.8	0.322
CH_4	190.4	45.4	0.162
NH_3	405.0	112.0	0.244
C_2H_5OH	513.9	60.68	0.276
N_2O	306.6	72.5	0.452

SCFs have the advantage of having an adjustable solvent power by proper variation of the operating conditions (pressure and temperature).[53] The processes using SCFs are generally classified into two distinct groups according to the role played by the SCF. It can act as a crystallization solvent in the RESS (rapid expansion of a supercritical solution) scheme. In contrast, in SAS (Supercritical Anti Solvent) the SCF is used as an anti-solvent. Several SAS variants exist, based on how the contact between the solution and the anti-solvent is achieved, namely GAS (gaseous anti solvent), ASES (aerosol solvent extraction system) and SEDS (solution enhanced dispersion by supercritical fluids).

Up to now, several polymorph-forming compounds have been discovered using SCF-based technologies. For example, powders of high polymorphic purity of carbamazepine, sulfathiazole, and salmeterol xinafoate[24,25] have been produced by selecting appropriate mixture of supercritical CO_2 ($scCO_2$) with an organic solvent, as well as controlling temperature and pressure. However, these processes require many steps. Between each step, time and energy are spent to separate, to isolate and to purify the processed samples. Limitations of these processes are the poor predictive control of particle size, and more importantly, the lack of the fundamental understanding of the factors determining the control of the polymorphic forms.[54]

In our recent work we combined melt crystallization and $scCO_2$ as a solvent to investigate the operating conditions (temperature, pressure, rate of cooling) that affect the transformation between the various polymorph of paracetamol,[55] mefenamic acid[56] and ibuprofen.[57] In particular, we investigated the populations of ibuprofen conformers in supercritical CO_2 across a temperature range of 35–90 °C using IR spectroscopy, quantum chemical calculations, and molecular dynamics simulations. Among the ibuprofen molecules dissolved in $scCO_2$, two conformers were identified, with the first conformer (Conf. I) being dominant, reaching its peak population at 60 °C for both isochors. We showed that there is a correlation between the distribution conformations of paracetamol molecules which are dissolved in $scCO_2$ and their polymorph state.[58] This finding was supported by the analysis of micronized ibuprofen obtained

via RESS using DSC and XRPD, which confirmed that polymorph populations align with the conformer populations under corresponding conditions. These results suggest that the conformation at the interface of a polymorph of an API is a key factor that determines its physicochemical and mechanical properties,[59] which ultimately influence its performance, stability, and manufacturability. The molecular arrangement at a crystal's surface significantly influences the packing density within the lattice. Polymorphs with tightly packed structures exhibit strong intermolecular interactions, leading to lower solubility, whereas those with looser packing dissolve more readily.[60,61] This can be attributed to the exposure of functional groups on crystal planes that facilitate hydrogen bonding, thereby enhancing dissolution. For instance, a hydrophilic surface conformation can improve solubility, which is critical for bioavailability. Additionally, the surface conformation affects the crystal's wettability and surface energy, factors that can either enhance or impede the dissolution rate. In addition, the arrangement of molecules at the surface can expose or shield reactive groups, affecting the API's chemical stability. For instance, certain conformations may make the compound more susceptible to degradation through oxidation or hydrolysis, which can compromise its efficacy and safety.

Our hypothesis is that the conformation distribution of API molecules at the interface with supercritical fluid (in this work $scCO_2$) determines the polymorphic form after the melting-cooling cycles of the melt crystallization process. Indeed, conformational changes are bound to occur for any flexible organic molecule during the melt crystallization process. Large organic molecules with several rotational bonds adjust at the supramolecular level by slightly twisting their molecular conformations leading to minimization of lattice energy by negotiating a small conformational energy penalty.[62]

1.3. Choice of the API and Curcumin

A variety of polymorph-forming APIs could be a good fit for this study. Ultimately, we have settled on Curcumin (CUR for short). CUR has attracted a considerable attention in the recent years for its wide variety of medicinal benefits, such as anti-inflammatory, anti-carcinogenic, antimalarial and antioxidant activity. However, its extremely low solubility in polar media and, hence, extremely low bioavailability, represents a very significant technological barrier in its use in food and pharmaceutical industry. As it shown in Fig 1.2, CUR consists of three key structural regions, the β-Diketone Bridge (Central Core) – flexible and involved in intramolecular hydrogen bonding and the Aromatic Rings (Terminal Groups) – two phenolic rings with -OH (hydroxyl) and -OCH_3 (methoxy) groups at positions 4 and 5 of each ring. Those hydroxyl and methoxy groups affect hydrogen bonding and polarity

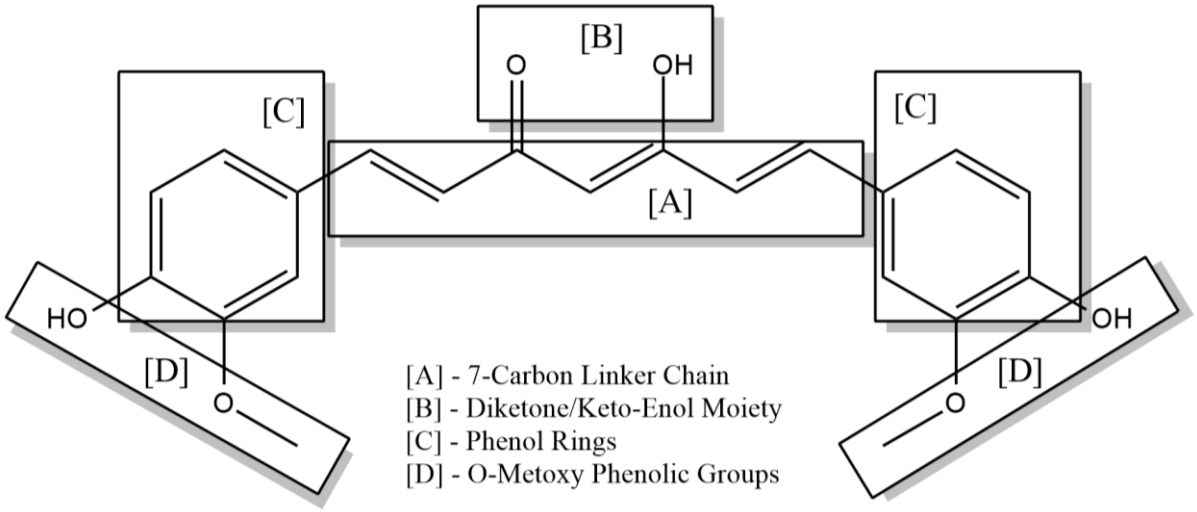

Figure 1.2. Schematic representation of different parts of CUR.

CUR is a hydrophobic phenol having a chemical name (1E,4Z,6E)-5-hydroxy-1,7-bis(4-hydroxy-3-methoxyphenyl)-hepta-1,4,6-trien-3-one, commonly used as a spice from the plant *Tumeric*. It exists in multiple **polymorphic forms**, meaning it can crystallize in different structural arrangements while maintaining the same molecular composition. These polymorphs can exhibit variations in **solubility, stability, and bioavailability**, which are crucial for pharmaceutical and nutraceutical applications. Curcumin has been reported to exist in at least **three distinct polymorphic forms**.[61,63]

Form I (monoclinic space group **$P2_12_12_1$**) is less stable and loosely packed (1.39 $g.cm^{-3}$) with weaker H-bonds (mainly C-H···O), allowing more interaction with solvents and with moderate stability. The molecule has a curved, slightly twisted conformation (see Fig. 1.3).

Form II (orthorhombic space group $Pca2_1$) is meta stable and the least ordered (see Fig. 1.4) among the three, but still denser than Form I, with low stability and the highest solubility. The molecules within this form are less twisted, adopting a planar cis-enol form with weakened hydrogen bonding.

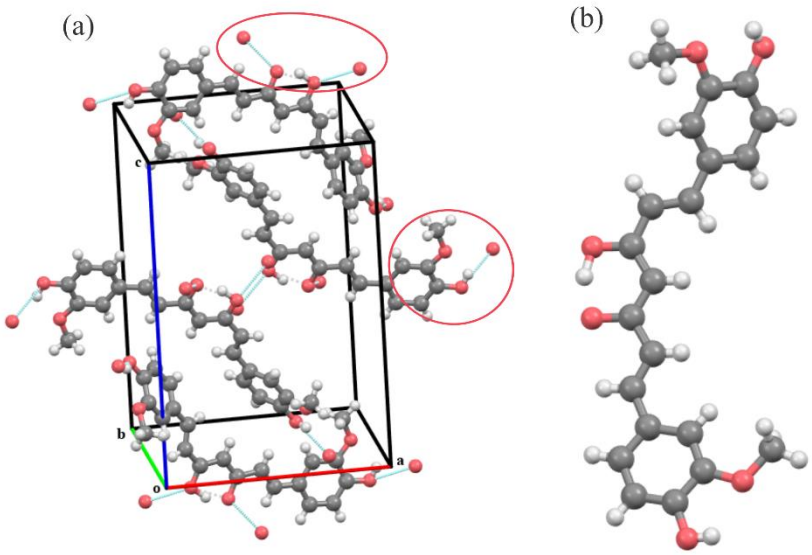

Figure 1.3. (a) Unit cell of CUR in POLY I with highlighted hydrogen bonding. (b) Molecular conformations of CUR in POLY I.

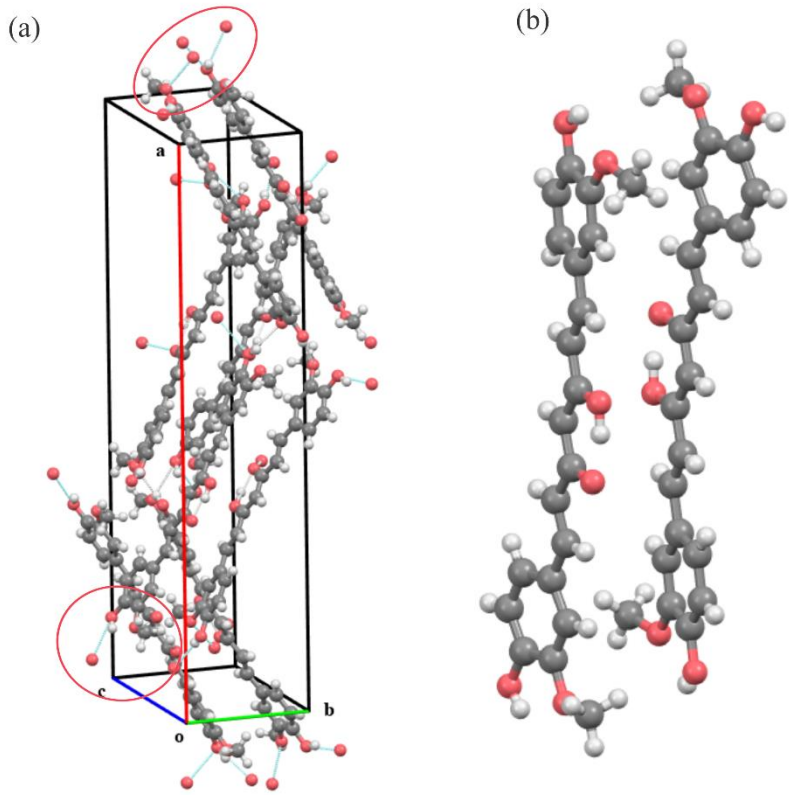

Figure 1.4. (a) Unit cell of CUR in POLY II with highlighted hydrogen bonding. (b) Molecular conformations of CUR in POLY II.

Form III (P_{bca} space group) is the most tightly packed (see Fig. 1.5) form, with low melting point and high solubility at room temperature. The constituent molecules adopt a nearly flat configuration. This planarity allows **efficient molecular packing**, increasing **crystal stability** but reducing solubility. Compared to **Form II**, greater number of CUR molecules in **Form III** have possibility to form intermolecular hydrogen bonds.

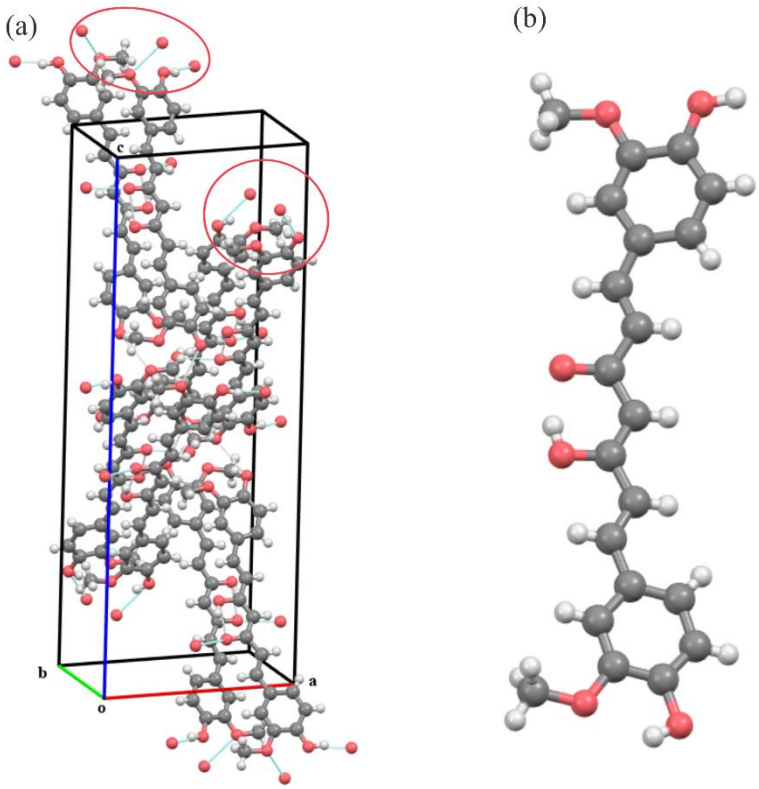

Figure 1.5. (a) Unit cell of CUR in POLY III with highlighted hydrogen bonding. (b) Molecular conformations of CUR in POLY III.

1.4. Aim and Objectives

The goal of the thesis is to use molecular dynamics simulation to elucidate the mechanisms and phenomena occurring at the interface of CUR and $scCO_2$ that determine the transformation between its three known polymorphic forms. Specifically, we will investigate melt-crystallization and solvent (here $scCO_2$) crystallization methods and focus on the structure and dynamics changes at the interface between the solid API and $scCO_2$.

Molecular dynamics (MD) simulations are used to study the dynamics and structure of the CUR-$scCO_2$ interface. In the third chapter of this investigation, we will characterize the local structure and conformational changes of different polymorphs of CUR in the bulk during the increase of the temperature beyond the model melting temperature. We have examined available force fields of CUR in terms of their capacity to replicate the conformational distribution and the experimental melting temperature. Next, using quantum chemical calculations, we have suggested new parameters for the force field, specifically those that describe the rotation around the key flexible dihedral angles. Significant attention is paid to the conformational changes of CUR in the simulation. After much testing of many literature and novel algorithms, we adopted a new approach that permits semi-automatic, accurate and representative sampling of the conformation of CUR molecules in the simulation. To correlate conformational behavior of CUR with crystal structure, we used statistical local distributions of observables such as the nearest neighbor radial distributions, the interactions energies (electrostatic – ES, Lennard-Jones – LJ) and Voronoi Polyhedra.

In the fourth chapter, we characterize the change in the local structure at the interface of CUR during heating beyond the melting temperature. Of note is that, during the increase of the temperature, analyzing a CUR interface in computer simulation, i.e., when the interfacial region is seen at atomistic resolution, is not a trivial task. We overcome this problem by using tested algorithms to identify the truly interfacial molecules.[64] The mass density profile of CUR molecules along the macroscopic surface normal axis and the contribution of the first couple of layers were investigated to give information about the spatial extent of the interface. Furthermore, MD simulations have allowed us to investigate dynamical properties, such as diffusion coefficient or residence time of CUR at the interface.

In a fifth chapter, we optimized the choice of the force field of CO_2, in particular with respect to its ability to reproduce the critical temperature, pressure and density. We investigate structural features of CO_2 in liquid and supercritical phases at different isobars. Density

fluctuations, which mark the liquid-to-gas-like crossover, were quantified using advanced statistical tools such as nearest-neighbor distance distributions, interaction energies, and local density profiles derived from Voronoi analysis and density-based spatial clustering of applications with noise (DBSCAN). Our findings reveal that these fluctuations arise from the temperature-dependent difference in the spatial extent of attractive contributions from electrostatic (ES) and Lennard-Jones (LJ) potentials, leading to a maximum in the contrast between the packed and loose density domains. Specifically, we demonstrate that neighbors experiencing maximal LJ and minimal ES attractive contributions characterize the first and second solvation shells. Within these shells, the orientation of CO_2 molecules is governed by the maximal attractive contribution of ES interactions. We took advantage of the developed methodology to investigate supercritical water and ammonia Our results point to similar behavior of the statistical distributions of the chosen observables, namely a large variation in the associated average values when crossing the critical temperature, and the occurrence of a maximum in their fluctuations.

In the sixth chapter, that constitutes the ultimate goal of the thesis work, we investigate the CUR-scCO_2 interface. The simulations were carried out under isochoric conditions along the $1.1\rho_c$ isochore (ρ_c is the critical density of CO_2). We focus on the effect of the thermodynamic conditions on the melting temperature of the three polymorphs of CUR. At the same time, attention is paid to the local structure of both scCO_2 and CUR. We have also investigated, during the melt-cooling cycles of CUR in the presence of scCO_2 as a solvent, the temperature and pressure dependencies of the interface's structure, surface tension, lateral pressure, conformation and orientation distributions of CUR molecules, hydrogen bonding, diffusion, and the time CUR molecules spend at the interface. Furthermore, we used the fluctuation of the interfacial layer to compute the interfacial free energy that control the nucleation of CUR during the cooling phase.[65,66]

1.5. Bibliography

(1) Kitamura, M. Controlling Factor of Polymorphism in Crystallization Process. J. Cryst. Growth 2002, 237–239, 2205–2214. https://doi.org/10.1016/S0022-0248(01)02277-1.

(2) Liendo, F.; Arduino, M.; Deorsola, F. A.; Bensaid, S. Factors Controlling and Influencing Polymorphism, Morphology and Size of Calcium Carbonate Synthesized through the Carbonation Route: A Review. Powder Technol. 2022, 398, 117050. https://doi.org/10.1016/j.powtec.2021.117050.

(3) Zhu, L.; Wang, L.; Sha, Z.; Wang, Y.; Yang, L.; Zhao, X.; Du, W. Interplay between Thermodynamics and Kinetics on Polymorphic Appearance in the Solution Crystallization of an Enantiotropic System, Gestodene. Cryst. Growth Des. 2017, 17 (9), 4582–4595. https://doi.org/10.1021/acs.cgd.7b00335.

(4) Sun, Y.; Zhu, L.; Kearns, K. L.; Ediger, M. D.; Yu, L. Glasses Crystallize Rapidly at Free Surfaces by Growing Crystals Upward. Proc. Natl. Acad. Sci. 2011, 108 (15), 5990–5995. https://doi.org/10.1073/pnas.1017995108.

(5) Fan, Y.; Huang, X.; Ji, J.; Zhang, W.; Zhang, J.; Hou, X. Building Functional Liquid-Based Interfaces: From Mechanism to Application. Angew. Chem. Int. Ed. 2024, 63 (32), e202403919. https://doi.org/10.1002/anie.202403919.

(6) Yang, H.; Song, C. L.; Lim, Y. X. S.; Chen, W.; Heng, J. Y. Y. Selective Crystallisation of Carbamazepine Polymorphs on Surfaces with Differing Properties. CrystEngComm 2017, 19 (44), 6573–6578. https://doi.org/10.1039/C7CE01317E.

(7) Zhang, J.; Xu, M.; Wu, S.; Chen, Z.; Luo, L.; Zi, T.; Peng, X.; Yang, Q.; Liu, M.; Zeng, Z. Investigation into Surface Effects on the Crystal Nucleation and Growth of Clotrimazole Polymorphs. Cryst. Growth Des. 2023, 23 (5), 3535–3543. https://doi.org/10.1021/acs.cgd.3c00043.

(8) Sun, K.; Han, P.; Yao, C.; Zhao, Y.; Zhang, C.; Zhang, Y.; Jiang, J.; Wang, L. Surface Accelerates Crystal Nucleation: The Case of Molnupiravir. Cryst. Growth Des. 2024, 24 (15), 6413–6420. https://doi.org/10.1021/acs.cgd.4c00650.

(9) Yao, X.; Borchardt, K. A.; Gui, Y.; Guzei, I. A.; Zhang, G. G. Z.; Yu, L. Surface-Enhanced Crystal Nucleation and Polymorph Selection in Amorphous Posaconazole. J. Chem. Phys. 2022, 157 (19), 194502. https://doi.org/10.1063/5.0117668.

(10) Shi, L.; Sun, C. C. Subsurface Nucleation of Supercooled Acetaminophen. CrystEngComm 2018, 20 (43), 6867–6870. https://doi.org/10.1039/C8CE01148F.

(11) Firaha, D.; Liu, Y. M.; Van De Streek, J.; Sasikumar, K.; Dietrich, H.; Helfferich, J.; Aerts, L.; Braun, D. E.; Broo, A.; DiPasquale, A. G.; Lee, A. Y.; Le Meur, S.; Nilsson Lill, S. O.; Lunsmann, W. J.; Mattei, A.; Muglia, P.; Putra, O. D.; Raoui, M.; Reutzel-Edens, S. M.; Rome, S.; Sheikh, A. Y.; Tkatchenko, A.; Woollam, G. R.; Neumann, M. A. Predicting Crystal Form Stability under Real-World Conditions. Nature 2023, 623 (7986), 324–328. https://doi.org/10.1038/s41586-023-06587-3.

(12) Censi, R.; Di Martino, P. Polymorph Impact on the Bioavailability and Stability of Poorly Soluble Drugs. Molecules 2015, 20 (10), 18759–18776. https://doi.org/10.3390/molecules201018759.

(13) He, Y.; Gao, Z.; Zhang, T.; Sun, J.; Ma, Y.; Tian, N.; Gong, J. Seeding Techniques and Optimization of Solution Crystallization Processes. Org. Process Res. Dev. 2020, 24 (10), 1839–1849. https://doi.org/10.1021/acs.oprd.0c00151.

(14) Han, G.; Chow, P. S.; Tan, R. B. H. Salt-Dependent Growth Kinetics in Glycine Polymorphic Crystallization. CrystEngComm 2016, 18 (3), 462–470. https://doi.org/10.1039/C5CE01974E.

(15) Lee, E. H. A Practical Guide to Pharmaceutical Polymorph Screening & Selection. Asian J. Pharm. Sci. 2014, 9 (4), 163–175. https://doi.org/10.1016/j.ajps.2014.05.002.

(16) Yao, C.; Zhang, S.; Wang, L.; Tao, X. Recent Advances in Polymorph Discovery Methods of Organic Crystals. Cryst. Growth Des. 2023, 23 (1), 637–654. https://doi.org/10.1021/acs.cgd.2c00960.

(17) Zhou, Y.; Lv, C.; Liu, X.; Gao, J.; Gao, Y.; Wang, T.; Huang, X. An Overview on Polymorph Preparation Methods of Active Pharmaceutical Ingredients. Cryst. Growth Des. 2024, 24 (1), 584–600. https://doi.org/10.1021/acs.cgd.3c00199.

(18) Hasa, D.; Carlino, E.; Jones, W. Polymer-Assisted Grinding, a Versatile Method for Polymorph Control of Cocrystallization. Cryst. Growth Des. 2016, 16 (3), 1772–1779. https://doi.org/10.1021/acs.cgd.6b00084.

(19) Thorson, M. R.; Goyal, S.; Gong, Y.; Zhang, G. G. Z.; Kenis, P. J. A. Microfluidic Approach to Polymorph Screening through Antisolvent Crystallization. CrystEngComm 2012, 14 (7), 2404. https://doi.org/10.1039/c2ce06167h.

(20) Li, X.; Ou, X.; Wang, B.; Rong, H.; Wang, B.; Chang, C.; Shi, B.; Yu, L.; Lu, M. Rich Polymorphism in Nicotinamide Revealed by Melt Crystallization and Crystal Structure Prediction. Commun. Chem. 2020, 3 (1), 152. https://doi.org/10.1038/s42004-020-00401-1.

(21) Yao, C.; Guzei, I. A.; Jin, Y.; Ruan, S.; Sun, G.; Gui, Y.; Wang, L.; Yu, L. Polymorphism of Piroxicam: New Polymorphs by Melt Crystallization and Crystal Structure Prediction. Cryst. Growth Des. 2020, 20 (12), 7874–7881. https://doi.org/10.1021/acs.cgd.0c01165.

(22) Zhu, X.; Kelly, A. W.; Cao, T.; Iuzzolino, L.; Gozzo, F.; Reinle-Schmitt, M.; Robison, L.; Patel, A.; Lee, A. Y. Interrogating the Solid–Solid Phase Transition Behavior of a Molecular Crystal with a Diverse Range of Solid-State Analytical Techniques and Computational Predictions. Cryst. Growth Des. 2024, acs.cgd.4c01078. https://doi.org/10.1021/acs.cgd.4c01078.

(23) Raza, K.; Kumar, P.; Ratan, S.; Malik, R.; Arora, S. Polymorphism: The Phenomenon Affecting the Performance of Drugs. 2014.

(24) Kordikowski, A.; Shekunov, T.; York, P. Polymorph Control of Sulfathiazole in Supercritical CO_2.

(25) Moribe, K.; Tozuka, Y.; Yamamoto, K. Supercritical Carbon Dioxide Processing of Active Pharmaceutical Ingredients for Polymorphic Control and for Complex Formation. Adv. Drug Deliv. Rev. 2008, 60 (3), 328–338. https://doi.org/10.1016/j.addr.2007.03.023.

(26) Knez, Ž.; Markočič, E.; Leitgeb, M.; Primožič, M.; Knez Hrnčič, M.; Škerget, M. Industrial Applications of Supercritical Fluids: A Review. Energy 2014, 77, 235–243. https://doi.org/10.1016/j.energy.2014.07.044.

(27) Okolie, J. A.; Nanda, S.; Dalai, A. K.; Kozinski, J. A. Chapter 9 - Advances in the Industrial Applications of Supercritical Carbon Dioxide. In Carbon Dioxide Capture and Conversion; Nanda, S., Vo, D.-V. N., Nguyen, V.-H., Eds.; Elsevier, 2022; pp 237–256. https://doi.org/10.1016/B978-0-323-85585-3.00008-0.

(28) Prasad, S. K.; Sangwai, J. S.; Byun, H.-S. A Review of the Supercritical CO_2 Fluid Applications for Improved Oil and Gas Production and Associated Carbon Storage. J. CO_2 Util. 2023, 72, 102479. https://doi.org/10.1016/j.jcou.2023.102479.

(29) Zhang, X.; Heinonen, S.; Levänen, E. Applications of Supercritical Carbon Dioxide in Materials Processing and Synthesis. RSC Adv. 2014, 4 (105), 61137–61152. https://doi.org/10.1039/C4RA10662H.

(30) Subramaniam, B.; Rajewski, R. A.; Snavely, K. Pharmaceutical Processing with Supercritical Carbon Dioxide. J. Pharm. Sci. 1997, 86 (8), 885–890. https://doi.org/10.1021/js9700661.

(31) Nishikawa, K.; Kusano, K.; Ayusawa Arai, A.; Morita, T. Density Fluctuation of a van Der Waals Fluid in Supercritical State. J. Chem. Phys. 2003, 118 (3), 1341–1346. https://doi.org/10.1063/1.1526469.

(32) Morita, T.; Kusano, K.; Ochiai, H.; Saitow, K.; Nishikawa, K. Study of Inhomogeneity of Supercritical Water by Small-Angle x-Ray Scattering. J. Chem. Phys. 2000, 112 (9), 4203–4211. https://doi.org/10.1063/1.480965.

(33) Ranieri, U.; Formisano, F.; Gorelli, F. A.; Santoro, M.; Koza, M. M.; De Francesco, A.; Bove, L. E. Crossover from Gas-like to Liquid-like Molecular Diffusion in a Simple Supercritical Fluid. Nat. Commun. 2024, 15 (1), 4142. https://doi.org/10.1038/s41467-024-47961-7.

(34) Samanta, T.; Dutta, R.; Biswas, R.; Bagchi, B. Infrared Spectroscopic Study of Super-Critical Water across the Widom Line. Chem. Phys. Lett. 2018, 702, 96–101. https://doi.org/10.1016/j.cplett.2018.05.005.

(35) Walrafen, G. E.; Yang, W.-H.; Chu, Y. C. Raman Spectra from Saturated Water Vapor to the Supercritical Fluid. J. Phys. Chem. B 1999, 103 (8), 1332–1338. https://doi.org/10.1021/jp9831233.

(36) Ikushima, Y.; Hatakeda, K.; Saito, N.; Arai, M. An in Situ Raman Spectroscopy Study of Subcritical and Supercritical Water: The Peculiarity of Hydrogen Bonding near the Critical Point. J. Chem. Phys. 1998, 108 (14), 5855–5860. https://doi.org/10.1063/1.475996.

(37) Musso, M.; Matthai, F.; Keutel, D.; Oehme, K.-L. Isotropic Raman Line Shapes near Gas–Liquid Critical Points: The Shift, Width, and Asymmetry of Coupled and Uncoupled States of Fluid Nitrogen. J. Chem. Phys. 2002, 116 (18), 8015–8027. https://doi.org/10.1063/1.1468885.

(38) Saitow, K.; Otake, K.; Nakayama, H.; Ishii, K.; Nishikawa, K. Local Density Enhancement in Neat Supercritical Fluid Due to Attractive Intermolecular Interactions. Chem. Phys. Lett. 2003, 368 (1–2), 209–214. https://doi.org/10.1016/S0009-2614(02)01851-1.

(39) Idrissi, A.; Ruckebusch, C.; Debus, B.; Boussekey, L.; Damay, P. Probing Local Structure of Sub and Supercritical CO_2 by Using Two-Dimensional Raman Correlation Spectroscopy. J. Mol. Liq. 2011, 164 (1–2), 11–16. https://doi.org/10.1016/j.molliq.2011.07.015.

(40) Fan, J.; Ly, N.; Ihme, M. Heterogeneous Cluster Energetics and Nonlinear Thermodynamic Response in Supercritical Fluids. Phys. Rev. Lett. 2024, 133 (24), 248001. https://doi.org/10.1103/PhysRevLett.133.248001.

(41) Matubayasi, N.; Wakai, C.; Nakahara, M. Structural Study of Supercritical Water. I. Nuclear Magnetic Resonance Spectroscopy. J. Chem. Phys. 1997, 107 (21), 9133–9140. https://doi.org/10.1063/1.475205.

(42) Shagurin, A.; Miannay, F. A.; Kiselev, M. G.; Jedlovszky, P.; Affouard, F.; Idrissi, A. Widom Line in Supercritical Water in Terms of Changes in Local Structure: Theoretical Perspective. J. Phys. Chem. Lett. 2024, 15 (22), 5831–5837. https://doi.org/10.1021/acs.jpclett.4c01142.

(43) Idrissi, A.; Vyalov, I.; Georgi, N.; Kiselev, M. On the Characterization of Inhomogeneity of the Density Distribution in Supercritical Fluids via Molecular Dynamics Simulation and Data Mining Analysis. J. Phys. Chem. B 2013, 117 (40), 12184–12188. https://doi.org/10.1021/jp404873a.

(44) Simeoni, G. G.; Bryk, T.; Gorelli, F. A.; Krisch, M.; Ruocco, G.; Santoro, M.; Scopigno, T. The Widom Line as the Crossover between Liquid-like and Gas-like Behaviour in Supercritical Fluids. Nat. Phys. 2010, 6 (7), 503–507. https://doi.org/10.1038/nphys1683.

(45) Jones, G. O.; Walker, P. A. Specific Heats of Fluid Argon near the Critical Point. Proc. Phys. Soc. Sect. B 1956, 69 (12), 1348. https://doi.org/10.1088/0370-1301/69/12/125.

(46) Simeski, F.; Ihme, M. Supercritical Fluids Behave as Complex Networks. Nat. Commun. 2023, 14 (1), 1996. https://doi.org/10.1038/s41467-023-37645-z.

(47) Skarmoutsos, I.; Guardia, E.; Samios, J. Local Structural Fluctuations, Hydrogen Bonding and Structural Transitions in Supercritical Water. J. Supercrit. Fluids 2017, 130, 156–164. https://doi.org/10.1016/j.supflu.2017.08.004.

(48) Skarmoutsos, I. Substantial Breakdown of the Hydrogen-Bonding Network, Local Density Inhomogeneities and Fluid-Liquid Structural Transitions in Supercritical Octanol-1: A Molecular Dynamics Investigation. J. Chem. Phys. 2024, 161 (4), 044506. https://doi.org/10.1063/5.0219417.

(49) Kalinichev, A. G. Universality of Hydrogen Bond Distributions in Liquid and Supercritical Water. J. Mol. Liq. 2017, 241, 1038–1043. https://doi.org/10.1016/j.molliq.2017.06.114.

(50) Pan, X.; Cooper McDonald, J.; MacPhail, R. A. Solvent–Solute Interactions and the Raman CH Stretching Spectrum of Cyclohexane-D11. II. Density Dependence in Supercritical Carbon Dioxide. J. Chem. Phys. 1999, 110 (3), 1677–1686. https://doi.org/10.1063/1.477809.

(51) Kajiya, D.; Saitow, K. Solvation Structures of Cis - and Trans -1,2-Dichloroethylene in Supercritical CO_2 Investigated by Raman Spectroscopy and Attractive Energy Calculations. J. Phys. Chem. B 2009, 113 (40), 13291–13299. https://doi.org/10.1021/jp903240v.

(52) Saitow, K.; Nakayama, H.; Ishii, K.; Nishikawa, K. Attractive and Repulsive Intermolecular Interactions of a Polar Molecule: Short-Range Structure of Neat Supercritical CHF3 Investigated by Raman Spectroscopy. J. Phys. Chem. A 2004, 108 (27), 5770–5784. https://doi.org/10.1021/jp049225c.

(53) Pasquali, I.; Bettini, R.; Giordano, F. Solid-State Chemistry and Particle Engineering with Supercritical Fluids in Pharmaceutics. Eur. J. Pharm. Sci. 2006, 27 (4), 299–310. https://doi.org/10.1016/j.ejps.2005.11.007.

(54) Llinàs, A.; Goodman, J. M. Polymorph Control: Past, Present and Future. Drug Discov. Today 2008, 13 (5–6), 198–210. https://doi.org/10.1016/j.drudis.2007.11.006.

(55) Oparin, R. D.; Idrissi, A.; Fedorov, M. V.; Kiselev, M. G. Dynamic and Static Characteristics of Drug Dissolution in Supercritical CO_2 by Infrared Spectroscopy: Measurements of Acetaminophen Solubility in a Wide Range of State Parameters. J. Chem. Eng. Data 2014, 59 (11), 3517–3523. https://doi.org/10.1021/je500456s.

(56) Oparin, R. D.; Vaksler, Y. A.; Krestyaninov, M. A.; Idrissi, A.; Shishkina, S. V.; Kiselev, M. G. Polymorphism and Conformations of Mefenamic Acid in Supercritical Carbon

Dioxide. J. Supercrit. Fluids 2019, 152, 104547. https://doi.org/10.1016/j.supflu.2019.104547.

(57) Oparin, R. D.; Ivlev, D. V.; Vorobei, A. M.; Idrissi, A.; Kiselev, M. G. Screening of Conformational Polymorphism of Ibuprofen in Supercritical CO 2. J. Mol. Liq. 2017, 239, 49–60. https://doi.org/10.1016/j.molliq.2016.10.132.

(58) Oparin, R. D.; Moreau, M.; De Walle, I.; Paolantoni, M.; Idrissi, A.; Kiselev, M. G. The Interplay between the Paracetamol Polymorphism and Its Molecular Structures Dissolved in Supercritical CO_2 in Contact with the Solid Phase Eur. J. Pharm. Sci. 2015, 77, 48–59. https://doi.org/10.1016/j.ejps.2015.05.016.

(59) Zhoujin, Y.; Li, Y.; Liang, P.-Y.; Zhou, P.-P.; Parkin, S.; Li, T.; Yu, F.; Long, S. Anti / Gauche Conformations Lead to Polymorphism in Homologous Phenylalkylamino-Nicotinic Acids. Cryst. Growth Des. 2023, 23 (5), 3154–3163. https://doi.org/10.1021/acs.cgd.2c01319.

(60) Xing, W.; Yu, H.; Zhang, B.; Liu, M.; Zhang, L.; Wang, F.; Gong, N.; Lu, Y. Quantitative Analysis the Weak Non-Covalent Interactions of the Polymorphs of Donepezil. ACS Omega 2022, 7 (41), 36434–36440. https://doi.org/10.1021/acsomega.2c04201.

(61) Sanphui, P.; Goud, N. R.; Khandavilli, U. B. R.; Bhanoth, S.; Nangia, A. New Polymorphs of Curcumin. Chem. Commun. 2011, 47 (17), 5013. https://doi.org/10.1039/c1cc10204d.

(62) Nangia, A. Conformational Polymorphism in Organic Crystals. Acc. Chem. Res. 2008, 41 (5), 595–604. https://doi.org/10.1021/ar700203k.

(63) Tønnesen, H. H.; Karlsen, J.; Mostad, A.; Samuelsson, B.; Enzell, C. R.; Berg, J.-E. Structural Studies of Curcuminoids. I. The Crystal Structure of Curcumin. Acta Chem. Scand. 1982, 36b, 475–479. https://doi.org/10.3891/acta.chem.scand.36b-0475.

(64) Lbadaoui-Darvas, M.; Idrissi, A.; Jedlovszky, P. Computer Simulation of the Surface of Aqueous Ionic and Surfactant Solutions. J. Phys. Chem. B 2022, 126 (4), 751–765. https://doi.org/10.1021/acs.jpcb.1c08553.

(65) Gerges, J.; Affouard, F. Insight From Molecular Dynamics Simulations on the Crystallization Tendency of Indomethacin Polymorphs in the Undercooled Liquid State. J. Pharm. Sci. 2020, 109 (2), 1086–1095. https://doi.org/10.1016/j.xphs.2019.10.054.

(66) Gerges, J.; Affouard, F. Predictive Calculation of the Crystallization Tendency of Model Pharmaceuticals in the Supercooled State from Molecular Dynamics Simulations. J. Phys. Chem. B 2015, 119 (33), 10768–10783. https://doi.org/ 10.1021/acs.jpcb.5b05557.

CHAPTER 2
METHODOLOGY

The purpose of this chapter is to give a brief overview of the algorithms and methods most often utilized throughout the subsequent chapters. First few sections cover the basics of computer simulation in general and molecular dynamics in particular. After, attention is given to common methods of structural and dynamical analysis. Later sections of the present chapter detail method specific to the present work, including those developed or improved by us.

2.1. Basics of Molecular Dynamics

Computer simulations, sometimes referred to as *in silico*[1] experiments, have nowadays become large, standalone parts of biochemistry[2], materials science[3], physics[4,5], engineering[6] and countless other disciplines. Computer experiments can be similar to the laboratory ones – both require preparation, execution and analysis stages, make use of specialized tools, require considerable training, etc. At the same time, computer simulations offer[7,8] several advantages, such as cost-effectiveness, rapidness and an ability to *directly* measure atomistic and molecular properties. Indeed, computational and laboratory chemical experiments often obtain same quantities – absorption wavelength, diffusion constants, conductivities, polarizabilities, all manner of things – but most experimental setups give indirect results, results which require comparison with a known etalon or heavy statistical processing. That is not to say, of course, that computations always give exact or direct results.

Another similarity between laboratory and computer experiments lies in the variety[9,10] of available tools and techniques. Physical processes studied by chemistry occupy large range of timescales[11,12], from femtosecond excitations to seconds or minutes of aggregation and precipitation. It would not be possible to study all of those processes with the same analytical technique. So, experimental chemists pick an appropriate method – infrared[13] or visible-light[14] spectroscopy, nuclear magnetic resonance[15], electrochemical[16] and calorimetric methods[17], the list goes on and on. Accordingly, computational chemistry can also be divided into subsections, each one appropriate for its own timescale. A schematic representation of some of those methods is given in Fig. 2.1.

The main topic of the present thesis is molecular dynamics[18–20], or MD for short. MD simulations can encompass large swaths of the abovementioned timescales, since, technically speaking, MD simulations can utilize different potential energy functionals, making them *ab initio*[21–23] (accurate and expensive), classical[24,25], i.e., force field based, (fast, but approximate) and everything in between.

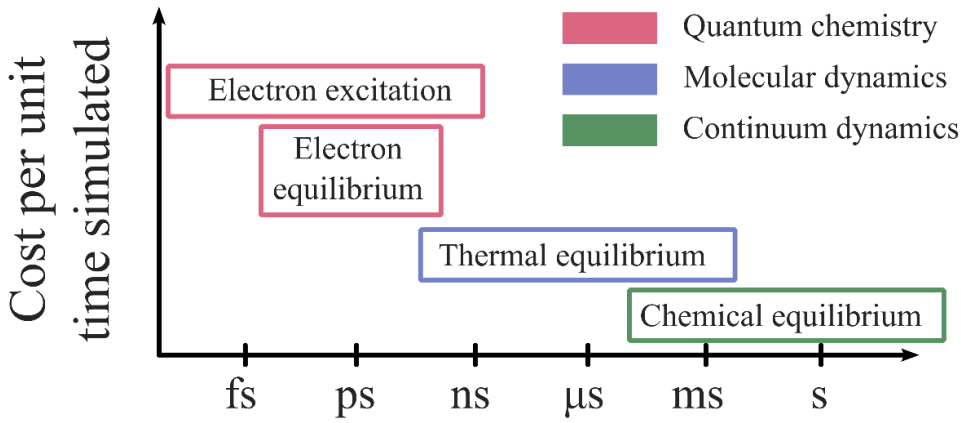

Figure 2.1. Schematic representation of different processes' timescales and computational methods appropriate for them. List is non-exhaustive.

The main point of any MD simulation, distinguishing it from methods like Monte Carlo[26], is to evolve the system under study in time. This is accomplished by solving classical Newtonian equations of motion. Those equations can be written in Lagrangian or, indeed, Hamiltonian form:

$$\dot{q}_i = \frac{\partial H}{\partial p_i} \tag{2.1}$$

$$\dot{p}_i = -\frac{\partial H}{\partial q_i} \tag{2.2}$$

Here, the Hamiltonian is a sum of the kinetic and potential energies (Eq. 2.3.) of the system. In classical MD, the kinetic energy is represented by the atomic-velocity dependent term (Eq. 2.4.), while the potential energy is decomposed (Eq. 2.5.) into contributions from intramolecular interactions (Eqs. 2.6.-2.9.) – bonds, angles, proper and improper torsions – and intermolecular interactions – electrostatic and non-electrostatic (Eqs. 2.10-2.11.). There is a significant number of possible functional forms for each of the terms in the Hamiltonian.

$$H = K + V \tag{2.3}$$

$$K = \frac{mv^2}{2} \tag{2.4}$$

$$V = V_b + V_a + V_d + V_i + V_{ES} + V_{NES} \tag{2.5}$$

In the first-generation classical force fields, like the ones utilized in the subsequent chapters, the intramolecular parts are often represented by harmonic forms, while electrostatic and non-electrostatic parts are often given by the Coulomb and Lennard-Jones functionals.

$$V_b = \sum_{i=1}^{N_b} \frac{k_i^r}{2}(r_i - r_i^0)^2 \tag{2.6}$$

$$V_a = \sum_{i=1}^{N_a} \frac{k_i^\theta}{2}(\theta_i - \theta_i^0)^2 \tag{2.7}$$

$$V_d = \sum_{i=1}^{N_d} \sum_{j=1}^{n_{max}} k_{i,j}^\varphi (1 + cos(n_j \varphi_i - \varphi_i^0)) \tag{2.8}$$

$$V_i = \sum_{i=1}^{N_i} \frac{k_i^\zeta}{2}(\zeta_i - \zeta_i^0)^2 \tag{2.9}$$

$$V_{ES} = \sum_{i=1}^{N} \sum_{j<i}^{N} \frac{q_\mathrm{i} q_\mathrm{j}}{4\pi\varepsilon_0 r_{ij}} \tag{2.10}$$

$$V_{NES} = \sum_{i=1}^{N} \sum_{j<i}^{N} 4\varepsilon_{ij} \left(\left(\frac{\sigma_{ij}}{r_{ij}} \right)^{12} - \left(\frac{\sigma_{ij}}{r_{ij}} \right)^{6} \right) \tag{2.11}$$

The numerical solution of the atomic equations of motion with different methods[27] leads to sampling of configurations (atomic positions, velocities and forces) from the *microcanonical ensemble*. A thermodynamic ensemble is a representation of the degree of separation of the system from the surrounding environment. They are defined by the combination of state variables that are kept constant, often abbreviated by the letters representing the constant variables. Overview of different ensembles is given in Table 2.1. In order to sample the desired ensemble, the Hamiltonian of the system must be modified by the addition of thermostats (constant temperature), barostats (constant pressure) or chemostats (constant chemical potential). Many different algorithms[28–30] are possible, and many more are being developed every year. Each subsequent chapter will contain a small summary of ensembles, integrators, thermostats, barostats and their related parameters used in that particular chapter.

Thermodynamic ensembles provide closed formulas for the calculation of ensemble average values. In MD, the ergodic hypothesis[31,32] provides the ability to calculate an ensemble average by averaging the quantity of interest over the whole system over time.

Table 2.1. Common thermodynamic ensembles, their names, which properties are kept constant and whether or not the system under each ensemble is isolated.

Ensemble	Name	Constant?	Isolated?
NVE	Microcanonical	Number of particles, volume, total energy	Isolated
NVT	Canonical	Number of particles, volume, temperature	Closed
NPT	Isobaric	Number of particles, pressure, temperature	Closed
μPT	Grand canonical	Chemical potential, pressure, temperature	Open

Due to the difference in scales between laboratory experiments with a few mols of substance and computational experiments with a few thousand atoms, a problem of edge effects and inefficient sampling occurs. Indeed, as a system grows in size, the ratio between its surface area and volume decreases. Because systems studied by MD are small in comparison with experimental ones, this ratio is highly overestimated. Surfaces, as will be discussed in subsequent sections, are special in chemistry and have properties different from those of the bulk. To somewhat circumvent this problem, MD simulations almost always employ periodic boundary conditions[33,34] – a set of boundary conditions that imply a wrap-around of the coordinates along each axis. A schematic representation is given in Fig. 2.2. Periodic boundary conditions simulate an infinite system with full set of translational invariances around the center of mass of the whole simulation box. The primary simulation box is termed “unit cell”, and offset simulation boxes are called its periodic images.

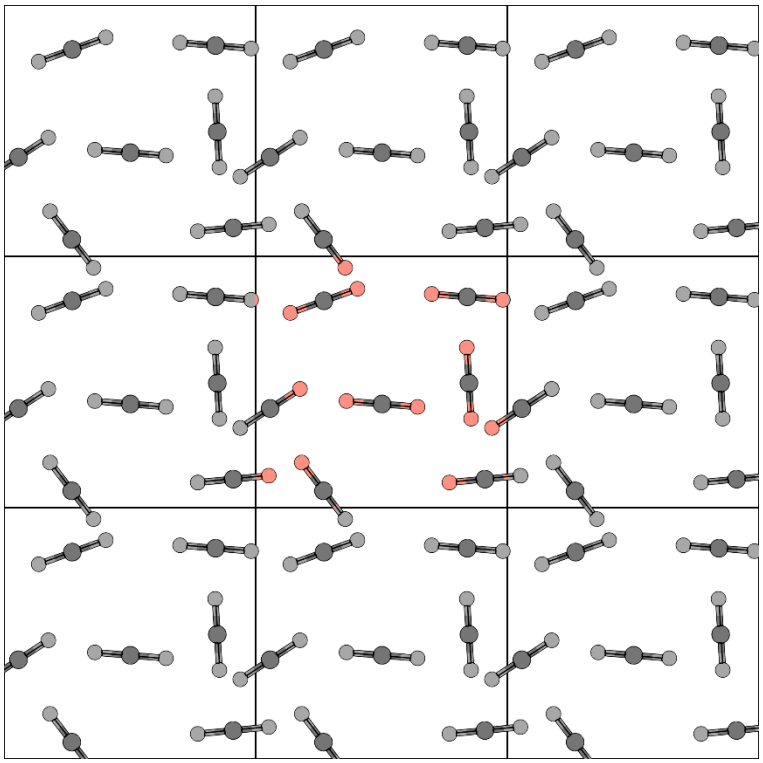

Figure 2.2. Schematic representation (does not correspond to a real system) of periodic boundary conditions. Colorful molecules denote the primary unit cell.

MD simulations by themselves only provide the evolution of the particle positions, velocities and forces in time – a trajectory. Computation of relevant quantities, such as density or diffusivity, constitutes analysis of MD trajectories. Some of the more common trajectory analysis techniques are summarized below.

2.2. Distribution Functions

In the study of condensed matter, pair distribution functions[35] play a special role, both as a method of analysis and as a component of integral equation theories. General pair-distribution function, $g_{ab}(\vec{r})$ gives the probability of finding a particle at a given position relative to the reference particle. If given as a 3D map over cartesian coordinates, it is referred to as Spatial Distribution Function[36] (SDF). Usually, simplified assumptions are made. For example, integrating over all the angular components in the polar coordinates one obtains Radial Distribution Function[37] (RDF):

$$g_{ab}(r) = \frac{1}{N_a N_b} \sum_{i=1}^{N_a} \sum_{j=1}^{N_b} \langle \delta(|r_{ij}| - r) \rangle \tag{2.12}$$

RDFs are extremely important because they can, in principle, for a subset of chemical systems, be obtained from the experimental[38,39] quantities, such as structure factor, which is itself obtained from the X-ray experiments. However, such determination involves challenging experimental setups and statistical processing techniques. On the other hand, MD offers almost instantaneous access to the RDFs for all manner of systems under different thermodynamic conditions.

An important distinction between distribution functions and simple histograms is the normalization. RDFs, for example, are normalized such that they provide probability density over the uniform density of substance, which is achieved as r→∞. In this form, RDFs are connected to the Kirkwood-Buff integrals[40,41] and the related theory of liquids:

$$G_{ab}(r) = \int_0^\infty 4\pi r^2 [g_{ab}(r) - 1] dr \tag{2.13}$$

Higher order correlation functions also exist. They can be used[42] to distinguish processes that give the same RDFs or their evolution. However, they are notably less popular and it's inherently more difficult to obtain them experimentally.

Distribution functions are usually averaged over the whole system. If one instead computes RDFs of the first "neighbor" – a particle that has lowest distance to the reference one – one

obtains what is termed Nearest-Neighbor RDF, or NRDF for short, denoted afterwards by $g_{ab}^{(n)}(r)$ for the nth closest particle. The total RDF is then a sum over N-1 possible NRDFs:

$$g_{ab}(r) = \sum_{n=1}^{N-1} g_{ab}^{(n)}(r) \tag{2.14}$$

Unlike the total RDF, NRDFs are often, though care must still be taken, normal distributions centered around average distance between the reference molecule and its nth neighbor. A typical decomposition of the RDFs unto the constituent NRDFs is given in Fig. 2.3.

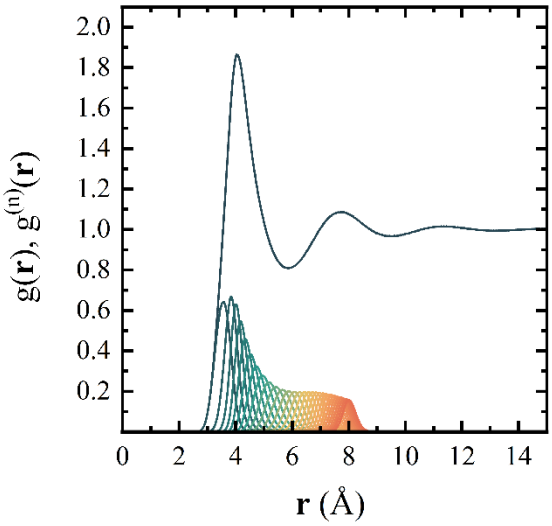

Figure 2.3. Total RDF and its decomposition onto the first 30 NRDFs.

Such NRDFs, treated as un-normalized probability distribution functions (PDF), can give estimates of not only the average distance between molecules, but of its fluctuation, asymmetry, and so on. Thus, some pair distribution functions like NRDFs can provide significant amount of information about the local arrangement of only a few particles, allowing effective access to information about system inhomogeneity, non-equilibrium processes, and more.

2.3. Voronoi Tessellation

Besides distributions functions, space tessellation algorithms can be used to give highly localized information about closest neighbors. Though many partitioning algorithms[43] are possible, one of the most interesting ones, applied to MD trajectories, QC electronic densities, city maps, and so on, is the Voronoi tessellation.[44] A Voronoi cell is defined as a set of points of the space that are closer, often meaning they have lower L_2-norm, though other metrics can be utilized, to the reference point than to the any other point.

What is generally termed "Voronoi analysis" can be subdivided into two parts – the construction of the Voronoi cells, represented by convex Voronoi polyhedra (VP) in 3D, and the computation of the volumes, surface areas and other properties of said cells. Several[45,46] high-throughput algorithms of Voronoi cell construction for 2D and 3D spaces have been developed throughout the years. Recent interest[47,48] towards Voronoi analysis of AI parameter spaces has also seen the rise of the approximate methods. Many such methods rely on first getting the dual of the Voronoi graphs – Delaunay Triangulation[49] – and performing edge-flipping afterwards. Despite the ability of performant procedures like the Fortune's algorithm[50] to construct VP for all points in one sweep they all have one drawback – they are really difficult to implement, which is not helped by the complex geometry of the 3D periodic triclinic MD box. In our work, we construct each cell separately, using the algorithm[51] of Ruocco et al. Typical cell, here for the center of mass of CO_2 molecule, is shown in Fig. 2.4.

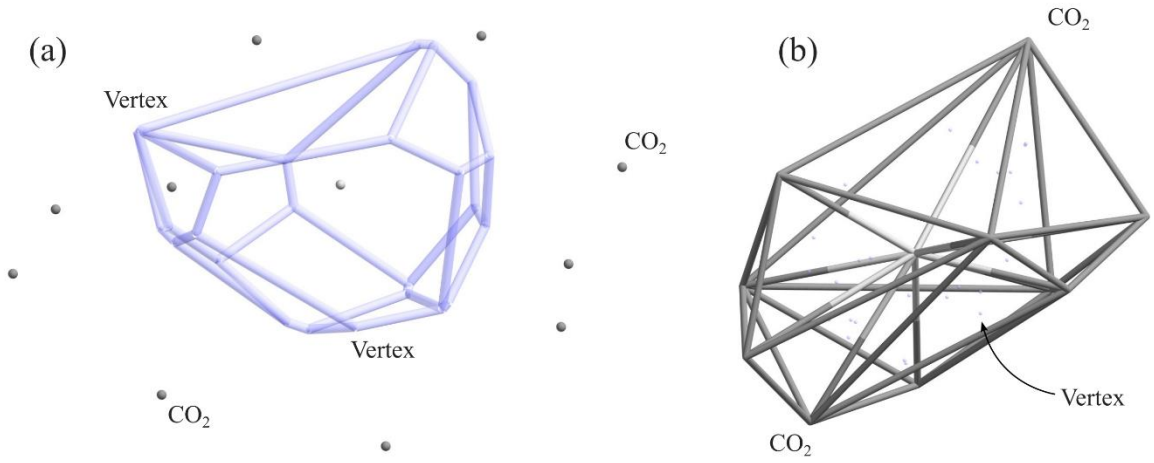

Figure 2.4. (a) Visualization of the Voronoi cell around a center of mass of a CO_2 molecule (white), surrounded by other CO_2 molecules (dark gray), defined by the vertices and edges (blue). (b) Dual of the Voronoi graph – Delaunay triangulation.

The resulting VP is then analyzed by computing its volume, density (as a reciprocal volume), surface area, sum of edge-lengths, and a number of different qualitative metrics. Those metrics readily provide information about the distribution of the neighbors. For example, surface polygons with bigger areas correspond to closer neighbors. Another property, available directly as a result of the dual relationship between VP and Delaunay triangulation, is the radii of the vertices, referred in MD literature sometimes as “VP voids”, as they measure spacing between the datapoints.

2.4. Clustering and DBSCAN

An important class of chemical processes are those of aggregation – protein aggregation[52,53] in biology/biochemistry, dye aggregation[54,55] in optoelectronics, substance precipitation[56,57] from the mixture, etc. Even when one is not directly interested in studying aggregation, it is on occasion quite useful to check if the force field parametrization causes systems containing multiple molecular types to unexpectedly split[58,59] or be incompatible in other ways. In order to study equilibrium aggregation using MD simulations, one often treats the positions of atoms/molecules as distinct points in 3D space and applies data clustering algorithms. Data clustering, in this context, means performing a particular statistical analysis[60] that separates the dataset into distinct groups, such that members of the group are more similar to each other than to the members of other groups.

General clustering algorithms[61] include k-means, mixture of gaussians, mean shift, and, perhaps relatively recently, DBSCAN[62] – Density-Based Spatial Clustering of Applications with Noise. Each method has its strengths and weaknesses, and no clustering method is truly free of parameter or hyper-parameters. We focus on DBSCAN specifically because it can discover arbitrary-shaped density domains, with any number of molecules in each domain and no constraints on the number of such domains. A schematic representation of the DBSCAN algorithm is given in Fig. 2.5.

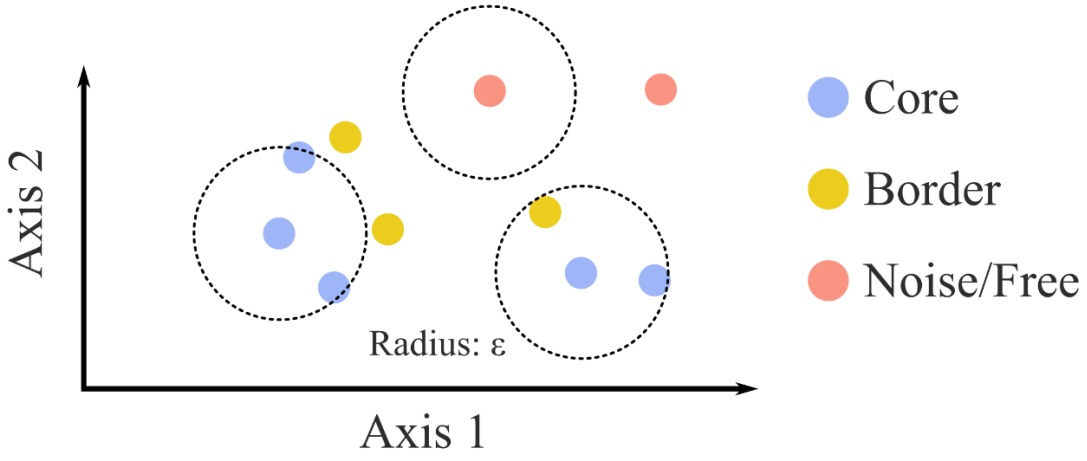

Figure 2.5. Schematic representation of the DBSCAN algorithms key steps for arbitrary 2D data. Extension to 3D atomic coordinates is straightforward.

At first, one of the datapoints is picked as a seed. From that seed, the cluster grows by selecting all datapoints with a certain radius – ε – from the current one, and adding them to the list of core members if they themselves have more than N neighbors within their radius, designating them as border members otherwise. After a cluster is established with its core and border points, next seed is picked from a list of unassigned datapoints until there are no more. Simplest DBSCAN procedure is summarized in Alg. 2.1.

ALGORITHM 2.1. **DBSCAN**(D, ε, N) → $\{C_i\}$, $\{B_i\}$, F

```
1   id = 0
2   foreach x ∈ D do
3     | Compute s1 = {y ∈ D : ‖x-y‖ < ε}
4     if |s1| > N
5       | id = id + 1
6       | Cid = Cid ∪ {x}
7       foreach y ∈ s1 do
8         | Compute s2 = {z ∈ D : ‖y-z‖ < ε}
9         if |s2| > N
10          | Cid = Cid ∪ {y}
11          | s1 = s1 ∪ s2
12        else
13          | Bid = Bid ∪ {y}
14  F = {x ∈ D : x ∉ Ci & x ∉ Bi foreach I < id}
```

In the context of MD simulations, after establishing core and border molecules, one could, of course, apply any of the typical MD analysis methods, such as distribution functions, to the members of a specific domain. Otherwise, statistical analysis of distributions of the sizes of density domains can be used to predict phase transitions, aggregation scenarios or spontaneous splitting of a given mixture.

Disadvantages associated with DBSCAN typically include the inability to separate domains with significantly different densities (addressed in more complex methods of hierarchical DBSCAN[63] and OPTICS[64]) and reliance on the empirical parameters. The former problem is mitigated by not relying solely on DBSCAN, as we supplement its density calculations with the abovementioned Voronoi tessellation. By its very nature, DBSCAN represents a mix between strict and fuzzy space partitioning schemes, provided that clusters can share border datapoints, which contrasts against explicitly strict Voronoi partitioning. The latter challenge has been[65] previously addressed, and it was shown that analysis of the RDFs of homogeneous bulk systems can provide good, physically motivated values for the radius and the number of neighbors, needed by the DBSCAN algorithm.

2.5. Conformational Analysis

The problem of distinguishing between different molecular conformers in the context of the MD simulations, especially at high temperatures, does not have one unique solution. Conformers, are, according to IUPAC[66], "One of a set of stereoisomers, each of which is characterized by a conformation corresponding to a distinct potential energy minimum". This means that vibrations of atomic bond or atomic angles, movement of molecules and their rotation as a whole, do not change the conformation – only dihedral angles do. Since in MD simulations molecules end up with all matter of bond lengths and angles, it is best to know conformations to be assigned in advance, perhaps from crystallographic data or quantum chemical simulations.

One intuitive idea is to compute the distance between a molecule in the simulation and a reference molecule. Defining a distance function between two molecules is surprisingly complex, but one straightforward way, at least for MD simulations, is to use the sum of distances (or their squares) between pairs of atoms. After normalizing to the number of molecules, this results in the following set of equations for the residual mean square difference (RMSD):

$$RMSD = \sqrt{\frac{1}{N}\sum_{i=1}^{N}\sum_{\alpha=x,y,z}(x_i^{\alpha} - x_0^{\alpha})^2} \tag{2.15}$$

In practice, such distance metrics would perform exceedingly poorly, even if the sample and reference molecule were to be rotated to best match each other. Since Eq. 2.15 deals with Cartesian coordinates, it would be sensitive to the bond and angle vibrations, which should not have an impact on the conformational assignment. A better option, sometimes used as collective variable in metadynamics, relies on computing RMSD with internal coordinates:

$$RMSD = \sqrt{\frac{1}{N_{int}}\sum_{i=1}^{N_{int}}(s_i - s_0)^2} \tag{2.16}$$

The advantage of internal coordinates lies in the ability to remove bonds, angles and other extraneous degrees of freedom, leaving explicitly dihedral angles, and even those can be

screened. The disadvantage comes from the need to constantly make molecules whole, as computing dihedral angles in periodic space can be rather tricky, though this problem is not unique to this particular method. Afterwards, all obtained distances (RMSDs) can be transformed to similarity measures via a number of different ways, but most of them would fall into the inverse (Eq. 2.17) or difference (Eq 2.18) categories.

$$P_i = \frac{d_i}{\sum_{j=1}^{N} d_j} \tag{2.17}$$

$$P_i = \sum_{j=1}^{N} d_j \; - \; d_i \tag{2.18}$$

This method of computation of conformational distributions can be summarized via the following Alg. 2.2, where $\mathbf{D_{mol}}$ is the set of atomic positions, $\{R_i\}$ is the set of sets of atomic positions for each reference conformation and $\mathbf{\{P_{each}\}}$ is the probability of a given molecule to be in each of the reference conformations.

ALGORITHM 2.2. **CONFORMATION**(D_{mol}, $\{R_i\}$) → P_{each}

```
n = |{Rᵢ}|
s₁ = internals(D_mol)
N₁ = |s₁|
d = {}
for i = 1,2...n do
    s₂ = internals(Rᵢ)
    d = d ∪ {||s₁-s₂||}
P_each = {}
for i = 1,2...n do
    P_each = P_each ∪ {d_i / Σ_{j=1}^{n} d_j}
```

A potential problem with Alg. 2.2 can be demonstrated by examining force field potentials associated with dihedral angles. If the potential function in question has evenly spaced energy minima, like that of Fig. 2.6 (a), then Eq. 2.16 would be appropriate. However, under uneven spacing of minima, akin to Fig. 2.6 (b), Eq. 2.16 would give results that are intuitively incorrect.

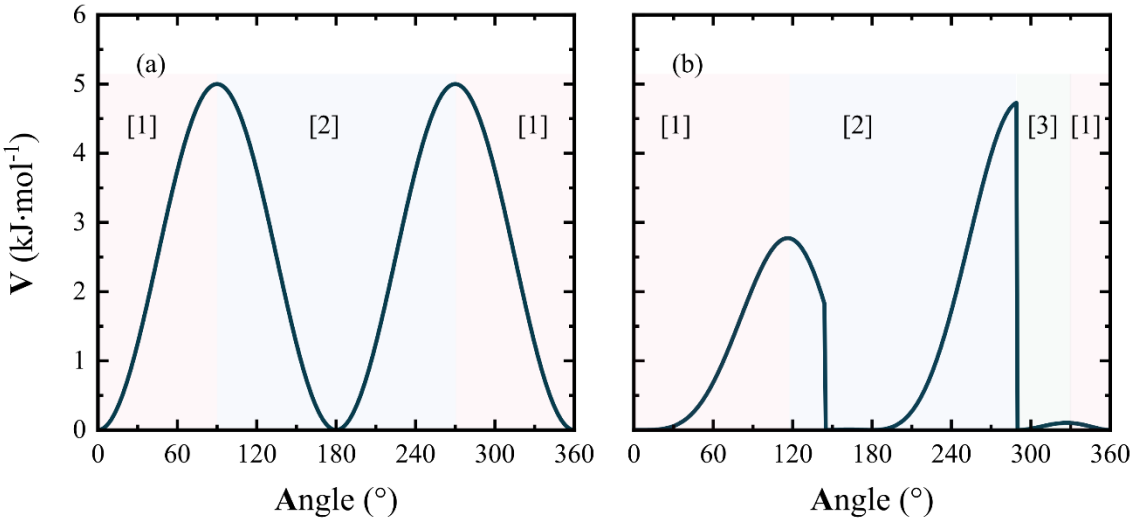

Figure 2.6. An example of (a) "smooth" and (b) "unsmooth" potential energy surfaces for a dihedral angle.

An alternative is to strictly adhere to the IUPAC definitions and consider energy minima directly. Since the potential functions in classical force fields are often cosines or sums of cosines, it is not difficult, given the current value of a dihedral angle, to determine which minimum it "belongs to". In this context, we say that the dihedral angle "belongs to" a particular minimum, or its basin, when it has not crossed the potential energy barrier to move to another minimum. Similarity score can then be obtained directly by counting how many basins of a sample molecule correspond to basins of a reference molecule, simply numbering them as in Fig 2.6. As long as local maxima of a potential function can be determined, differentiable or not, this algorithm would perform well, and gives similar results to the Alg. 2.2 for most of the examined force fields.

Alg. 2.3 is still not without its problems however. In practice, it is impossible (and most of the time even undesirable) to take into account all of the conformations of highly flexible molecules. Since Alg. 2.3 only considers how many minima are equal, and not which of those minima, it does not consider the importance of each minimum or how difficult it is to move from on minimum to another. Possible extensions of this method could lie in the fields of probability theory and statistical mechanics, though they would be beyond the scope and needs of this work.

ALGORITHM 2.3. **CONFORMATION**(D_{mol}, $\{R_i\}$) → P_{each}

```
n = |{Rᵢ}|
s₁ = internals(D_mol)
B^R = {BASIN(s₁)}
N₁ = |s₁|
B = {}
for i = 1,2...n do
    s₂ = internals(Rᵢ)
    B = B ∪ BASIN(s₂)
P_each = {}
for i = 1,2,...n do
    P_each = P_each ∪ {∏_{j=1}^{N₁} δ(B_j, B_j^{R_i})}
```

Although all of the abovementioned algorithms were employed at one stage or another, subsequent chapters only contain results from the basin-matching Alg. 2.3. While not without its flaws, it is the best-performing non-parametric estimator that we were able to develop.

2.6. Simulation of Interfaces

Although not as prevalent as bulk calculations, interfacial simulations constitute a large, important class of computational problems in field like biochemistry,[67] biology[68] and material science.[69]

A particular care must be taken when attempting to compute non-radially symmetric properties of simulation boxes with interfaces. Properties that require absolute positions along the normal of the interface, like mass-density profiles, would give erroneous results due to the movement of the center of mass of the system. This is commonly referred[70] to as "flying ice cube effect". This effect is present, in one way or another, in most MD simulations of vacuum interfaces. To combat it, one has to remove the translational motion of the center of mass (COM) of the whole system, either during the simulation itself or as a trajectory post-processing step. The latter option means aligning COMs of different steps in the MD trajectory to one common point, usually center of the box. The tricky part, as it turns out, is to accurately compute the COM in the periodic system. It is tempting to use the following simple formula:

$$\overrightarrow{COM} = \sum_{i=1}^{N} m_i \vec{r}_i \tag{2.19}$$

where m is atomic mass. This is, in fact, the formula internally used by many MD simulation packages. The biggest problem with Eq. 2.19 can be demonstrated by Fig. 2.7.

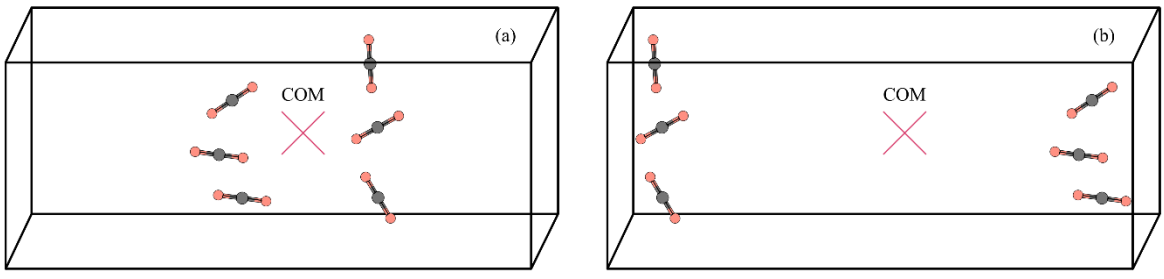

Figure 2.7. Schematic representation of (a) correct and (b) incorrect determination of the COM using Eq. 2.19.

In a periodic system, given some arrangements of masses, it is possible for the computed COM to be, nominally, in the center, while the true COM lies on the periodic boundary. In order to get an accurate estimation of the COM, the following formula[71], which explicitly includes periodicity, can be used, where *i* is an imaginary number:

$$R_\alpha = \sum_{j=1}^{N} m_j e^{2\pi i \frac{x_j^\alpha}{L_\alpha}} \tag{2.20}$$

$$\overrightarrow{COM} = \frac{L_\alpha}{2\pi} ang(R_\alpha) \tag{2.21}$$

Afterwards, COM vector is given by the angles the complex numbers make with the positive direction of each of the axes. Care still must still be taken when dealing with completely uniformly distributed masses, as Eq. 2.20. can give *0+0i*. In this case, one is free to pick any arbitrary angle. Fig 2.8 demonstrates pathological case of the mass-density profiles computed on the trajectories centered with each of the abovementioned COM formulas.

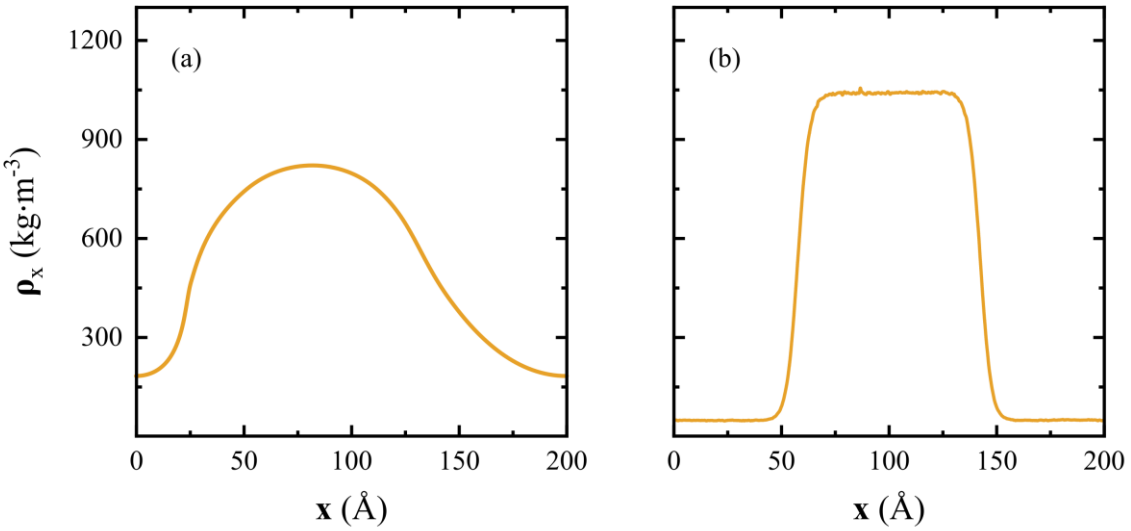

Figure 2.8. Schematic representation of mass-density profiles of CO_2 with trajectory centering performed using (a) Eq. 2.19 and (b) Eq. 2.20.

2.7. Interfacial Molecules

Along with other challenges of interfacial simulations come the challenge of analysis. Specifically, if the goal of the atomistic simulation is to obtain some kind of a property of the interface, the total amount of atoms in the system has to be separated into those that are "at the interface" and those that are not. This comes by necessity, as atomistic simulations give information about atoms, pairs of atoms and molecules comprised of atoms, not abstract surfaces in the system. This then raises a question of what it even means for a molecule to be "at the interface".

Intuitively, interfacial molecules are those close to the surface, close to the invisible boundary between the thermodynamic phases, almost opposite to those of the "bulk". This intuition can be stated more rigorously[72] via the Gibbs dividing surface. Normally, systems containing flat interfaces can be divided into three subsystems – two phases and a "transition region", which contains the mix of the phases and has unknown size and properties. Gibbs introduced an alternative division, one where the transition region is replaced by a sharp boundary that has zero volume, but preserves the extensive properties. Those two treatments are illustrated in Fig. 2.9. Although definition of the transition/boundary regions can use volume density of any extensive property, mass-density profiles are commonly preferred.

We will not explore thermodynamical implications of the Gibbs model (see other[73] references), because it is unsuitable for our purposes. Indeed, one disadvantage of this model lies in the implicit need to average the extensive property used to get the position of the surface over the entire ensemble i.e., MD trajectory. This introduces problems for fast-varying systems, equilibrium or not.

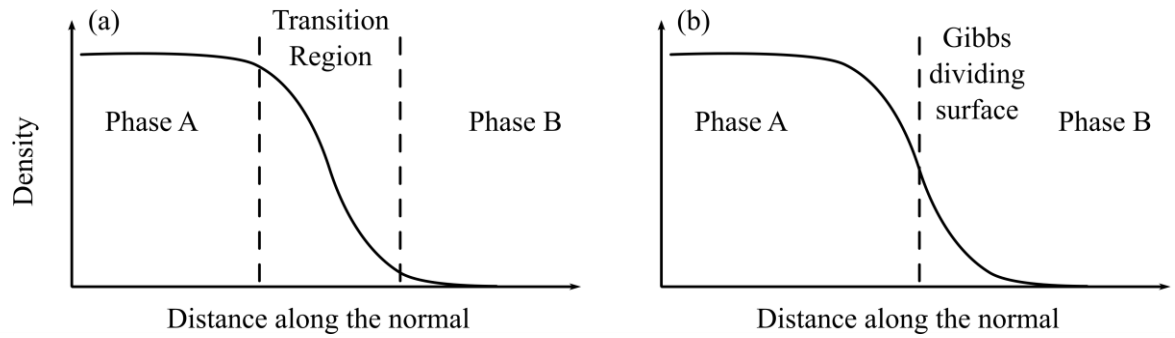

Figure 2.9. Definition of the three regions in the two-phase system with a flat interface according to (a) "Realistic" and (b) Gibbs dividing surface descriptions.

Several other methods are possible, such as using order parameters, i.e., tetrahedral order parameter, in order to find molecules with less than the average number of neighbors, as those molecules would likely be at the interfacial boundary, though most have the same drawback as the Gibbs definition. Instead, subsequent chapters utilize what is termed by Partay et al. "Identification of truly Interfacial Molecules" method, or ITIM[74,75] for short. This method proceeds by defining a grid of spheres outside of the simulation box, on both sides, and moving them along the normal of the interface toward the center of the box. When the distance between a sphere and an atom of any molecule is less than the sum of their radii, the collision is detected, the sphere movement stops, and the corresponding atom or a molecule the atom belongs to is flagged as interfacial. After all the spheres have stopped, identification of the subsequent layer can begin by ignoring already identified molecule and/or atoms. In this manner, any number of layers can be found on each side of the system. The visualization of the described steps is given in Fig. 2.10.

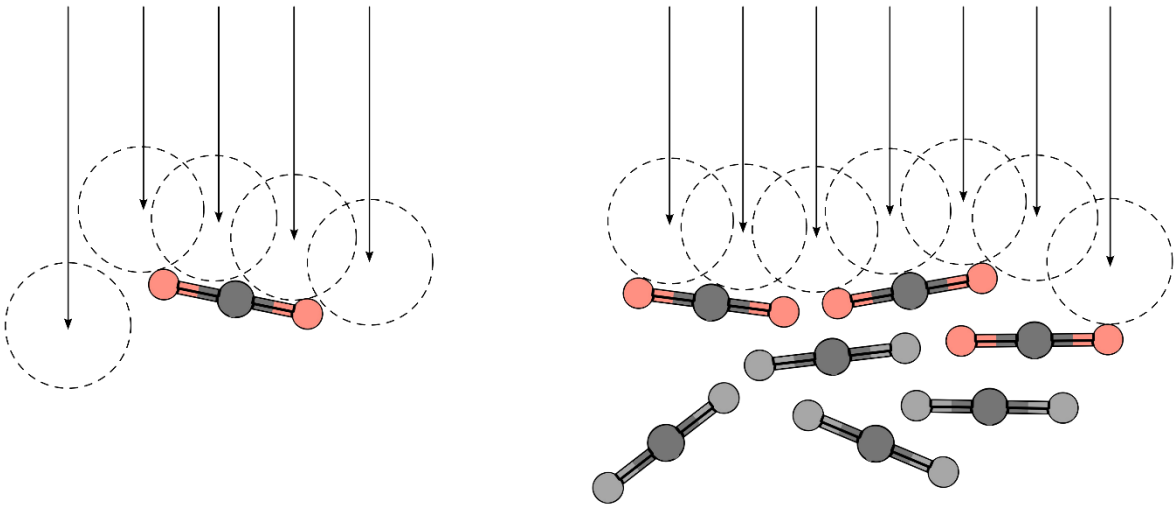

Figure 2.10. Schematic representation of the ITIM algorithm.

The main advantage of ITIM is the ability to identify different sets of interfacial atoms/molecules at each configuration. The disadvantage lies in the parametric nature of the method. Indeed, three main sets constants need to be defined – mesh spacing, radius of probe spheres and radii of elements. Fortunately, mesh spacing only affects the tradeoff between accuracy and computational time – any sufficiently fine spacing, around 35% of the radius of probe spheres, is enough. Element-dependent radii can be defined on the basis of the corresponding Lennard-Jones parameters. Similarly, good performance can be achieved by

selecting probe radius as a Van der Waals radius of some common elements, for example oxygen, to simulate water probe. Such definitions often give results similar to the concept[76] of the Solvent Accessible Surface, but for the interfacial atoms/molecules. We specifically make heavy use of the PYTIM[77] python library implementing the IITM method and defining sensible default parameters.

2.8. Interfacial Energy

One of the key concepts to the discussion of the morphology and thermodynamics of interfaces is that of interfacial (or surface) energy. Surface (free) energy[78] quantifies the reduction in the number and strength of intermolecular interactions that occur upon the creation of the surface. Interfacial energy of solids and liquids is non-negative, as negative surface energy would result in spontaneous creation of new surfaces as the system tends toward lower and lower energy state. Surface energy is extremely important for crystal growth research. Experimentally, it is often measured[79,80] with contact angle experiments. Mathematically, interfacial energy (γ), given by Eq. 2.22 in its most general form, is equal to the work (W) needed to crease one unit area (A) of the given substance:

$$dW = \gamma dA \tag{2.22}$$

For MD simulations of liquid-vapor interfaces, one could use the total pressure tensor[81] to define surface tension (σ) according to the following Eq. 2.23. for the interface along the z-axis (other interfaces are accessible with permutation of the indices):

$$\sigma = \frac{L_z}{n}\left\{P_{zz}(t) - \frac{P_{xx}(t) + P_{yy}(t)}{2}\right\} \tag{2.23}$$

where L_z is the size of the box along the z-axis, n is the number of interfaces and P_{xx} are the corresponding components of the total pressure tensor.

For MD simulations of solid-liquid interfaces, two main protocols have achieved significant popularity – Adiabatic Cleaving Method[82] (ACM) and Capillary Fluctuation Method[83] (CFM). ACM uses thermodynamic integration in order to connect several distinct systems and simulations, created as a result of "cleaving" and rearranging the system. In contrast, CFM uses the fluctuation of the position of the interface as a measure of its roughness, which is then connected to the work needed to create it. CFM simulations require almost 1D interfaces, so the systems have to be very thin. Additionally, extracting interface fluctuation from the simulation requires application of Fourier transform and ensemble averages over the resulting power spectrum.

Although both models, ACM and CFM, are significantly more complicated than Eq. 2.23, and require specific system geometry, they underline a key concept – interfacial energy is proportional to an intensive property of the system. In subsequent chapters, instead of directly

obtaining the interfacial energy, we focus on the effective surface area per molecule and its dependence on the temperature. Since surface area enters Eq. 2.22, it can be used to understand how the interfacial energy would behave. Due to the fixed box vectors of the NVT simulation, all gains or losses of the surface area would come from the movement of molecules along the normal of the interface, including interchange in the number of molecules per layer, and all the work being done on the system would be thermal. The problem then changes to determining the effective surface area of the interfacial layer.

ALGORITHM 2.4. **SURFACE**(D, m) → S_{mol}

$s_1 = \{D : ITIM(D) = m\}$
$N_1 = |s_1|$
$S = 0$
$s_2 = \{\}$
foreach $x \in s_1$ **do**
  $s_2 = s_2 \cup \{\forall P : P \in Fibonacci(x,n)\}$
$s_3 = \{s_2 : ITIM(s_2) = 1\}$
foreach $x \in s_1$ do
  $S_t = 4\pi R_{VdW}^2$
  $N_2 = |\{P : P \in Fibonacci(x,n)\}|$
  $N_3 = |\{P : P \in Fibonacci(x,n) \ \& \ P \in s_3\}|$
  $S = S + S_t \cdot \frac{N_2}{N_3}$
$S_{mol} = \frac{S}{N_1}$

To tackle this problem, we propose the following algorithm, summarized in Alg. 2.4. Here, *m* is the cardinal number of the layer to be studied (1st, 2nd , etc), while *n* is the number of points for each Fibonacci sphere. We first perform the ITIM analysis and find out which molecules occupy the interfacial layer. Next, we construct a Fibonacci sphere around every atom in the interfacial layer according to said atoms radius. A Fibonacci sphere makes it very easy to calculate the surface area of a slice due to it effectively being a uniform[84] quadrature. We then perform second ITIM interaction on the points of the spheres in order to prune any points not accessible from the surface. Lastly, surface area can be calculated as sum of atomic surface areas, which, in turn, are given as a proportion of the total sphere surface area based on the proportion of points not pruned by the second ITIM pass. Performance of this algorithm will be discussed in the subsequent chapters.

2.9. Dynamical Properties and Diffusion

Although this work is primarily concerned with static, i.e., time-independent, equilibrium structural characteristics of various substances, it would be remiss not to mention the dynamical part[85,86] of molecular dynamics.

Typical dynamical properties, constituting a large class, are those derived from autocorrelation functions of atomic or molecular characteristics. Autocorrelation function[87] is a statistical tool, calculated by taking an expectation value E of the product of original signal X_t and its complex conjugate $\bar{X}_\mathrm{t}$ at every pair of times, represented by the following equation:

$$R_{XX}(t_1, t_2) = E\left[X_{t_1}\bar{X}_{t_2}\right] \tag{2.24}$$

For example, if one considers velocity to be a distinct property of a given atom, it is possible to compute velocity autocorrelation function,[88] which gives insight into fast molecular processes and the forces behind them. Equally valid is the autocorrelation of something like VP density of a given molecule. Autocorrelation functions provide information about the relationship between the state of the system at different times, allowing identification of timescales of different processes, as well as hints about the driving forces of those processes.

Besides autocorrelation functions, a very descriptive dynamical quantity is the diffusion coefficient. Diffusion coefficient, given between two substances, or self-diffusion coefficient, given for an individual substance, describes how quickly two sub-regions of a system would mix unto uniformity. Experimentally,[89] it can be solved for on the basis of Fick's laws and various laboratory setups. Computationally, diffusion constant can be obtained from the mean squared displacement (MSD) of atoms on the basis of Einstein[90] relation:

$$MSD = \langle |x(t) - x(0)|^2 \rangle \tag{2.25}$$

Usually, one would fit[91] the MSD in the linear part of its graph, and use the slope to compute the diffusion coefficient. MSD, like the name suggests, measures how much a given atom has deviated from the reference position between two given times. In equilibrium MD, it is given by the following[92] equation:

$$D = \frac{MSD(t)}{2t} \tag{2.26}$$

Several other techniques, not discussed here, are used throughout this work. Discussion of the methodological basis of those methods will be given in the appropriate chapters.

2.10. Bibliography

(1) Danchin, A.; Médigue, C.; Gascuel, O.; Soldano, H.; Hénaut, A. From Data Banks to Data Bases. *Res. Microbiol.* **1991**, *142* (7), 913–916. https://doi.org/10.1016/0923-2508(91)90073-J.

(2) Becker, O. M.; MacKerell, A. D.; Roux, B.; Watanabe, M. *Computational Biochemistry and Biophysics*; Crc Press Boca Raton, FL, USA:, 2001; Vol. 10.

(3) Steinhauser, M. O.; Hiermaier, S. A Review of Computational Methods in Materials Science: Examples from Shock-Wave and Polymer Physics. *Int. J. Mol. Sci.* **2009**, *10* (12), 5135–5216. https://doi.org/10.3390/ijms10125135.

(4) Jardin, S. *Computational Methods in Plasma Physics*; CRC Press, 2010.

(5) Thijssen, J. *Computational Physics*; Cambridge University Press, 2007.

(6) Na, T. Y. *Computational Methods in Engineering Boundary Value Problems*; Academic Press, 1980.

(7) Alcamí, M.; Mó, O.; Yáñez, M. Computational Chemistry: A Useful (Sometimes Mandatory) Tool in Mass Spectrometry Studies. *Mass Spectrom. Rev.* **2001**, *20* (4), 195–245. https://doi.org/10.1002/mas.10005.

(8) Lewars, E. G. *Computational Chemistry*; Springer International Publishing: Cham, 2016. https://doi.org/10.1007/978-3-319-30916-3.

(9) Jensen, F. *Introduction to Computational Chemistry*; John Wiley & Sons, 2017.

(10) Young, D. *Computational Chemistry: A Practical Guide for Applying Techniques to Real World Problems*; John Wiley & Sons, 2004.

(11) Zewail, A. H. Femtochemistry: Atomic-Scale Dynamics of the Chemical Bond Using Ultrafast Lasers (Nobel Lecture). *Angew. Chem. Int. Ed.* **2000**, *39* (15), 2586–2631. https://doi.org/10.1002/1521-3773(20000804)39:15<2586::AID-ANIE2586>3.0.CO;2-O.

(12) Prather, M. J. Lifetimes and Time Scales in Atmospheric Chemistry. *Philos. Trans. R. Soc. Math. Phys. Eng. Sci.* **2007**, *365* (1856), 1705–1726. https://doi.org/10.1098/rsta.2007.2040.

(13) Barth, A. Infrared Spectroscopy of Proteins. *Biochim. Biophys. Acta BBA - Bioenerg.* **2007**, *1767* (9), 1073–1101. https://doi.org/10.1016/j.bbabio.2007.06.004.

(14) Picollo, M.; Aceto, M.; Vitorino, T. UV-Vis Spectroscopy. *Phys. Sci. Rev.* **2019**, *4* (4). https://doi.org/10.1515/psr-2018-0008.

(15) Hall, L. D. Nuclear Magnetic Resonance. In *Advances in Carbohydrate Chemistry*; Wolfrom, M. L., Ed.; Academic Press, 1964; Vol. 19, pp 51–93. https://doi.org/10.1016/S0096-5332(08)60279-9.

(16) Labib, M.; Sargent, E. H.; Kelley, S. O. Electrochemical Methods for the Analysis of Clinically Relevant Biomolecules. *Chem. Rev.* **2016**, *116* (16), 9001–9090. https://doi.org/10.1021/acs.chemrev.6b00220.

(17) Ferrannini, E. The Theoretical Bases of Indirect Calorimetry: A Review. *Metabolism* **1988**, *37* (3), 287–301. https://doi.org/10.1016/0026-0495(88)90110-2.

(18) Hansson, T.; Oostenbrink, C.; van Gunsteren, W. F. Molecular Dynamics Simulations.

(19) Hospital, A.; Goñi ,Josep Ramon; Orozco ,Modesto; and Gelpí, J. L. Molecular Dynamics Simulations: Advances and Applications. *Adv. Appl. Bioinforma. Chem.* **2015**, *8*, 37–47. https://doi.org/10.2147/AABC.S70333.

(20) Karplus, M.; Petsko, G. A. Molecular Dynamics Simulations in Biology. *Nature* **1990**, *347* (6294), 631–639. https://doi.org/10.1038/347631a0.

(21) Car, R.; Parrinello, M. Unified Approach for Molecular Dynamics and Density-Functional Theory. *Phys. Rev. Lett.* **1985**, *55* (22), 2471–2474. https://doi.org/10.1103/PhysRevLett.55.2471.

(22) Hutter, J. Car–Parrinello Molecular Dynamics. *WIREs Comput. Mol. Sci.* **2012**, *2* (4), 604–612. https://doi.org/10.1002/wcms.90.

(23) Marx, D.; Hutter, J. Ab Initio Molecular Dynamics: Theory and Implementation. *Mod. Methods Algorithms Quantum Chem.* **2000**, *1* (301–449), 141.

(24) Monticelli, L.; Tieleman, D. P. Force Fields for Classical Molecular Dynamics. In *Biomolecular Simulations: Methods and Protocols*; Monticelli, L., Salonen, E., Eds.; Humana Press: Totowa, NJ, 2013; pp 197–213. https://doi.org/10.1007/978-1-62703-017-5_8.

(25) Lubich, C. *From Quantum to Classical Molecular Dynamics: Reduced Models and Numerical Analysis*, 1st ed.; Zurich Lectures in Advanced Mathematics; EMS Press, 2008; Vol. 12. https://doi.org/10.4171/067.

(26) Foulkes, W. M. C.; Mitas, L.; Needs, R. J.; Rajagopal, G. Quantum Monte Carlo Simulations of Solids. *Rev. Mod. Phys.* **2001**, *73* (1), 33–83. https://doi.org/10.1103/RevModPhys.73.33.

(27) *Mathematical Approaches to Biomolecular Structure and Dynamics*; Mesirov, J. P., Schulten, K., Sumners, D. W., Eds.; Friedman, A., Gulliver, R., Series Eds.; The IMA Volumes in Mathematics and its Applications; Springer: New York, NY, 1996; Vol. 82. https://doi.org/10.1007/978-1-4612-4066-2.

(28) Hünenberger, P. H. Thermostat Algorithms for Molecular Dynamics Simulations. In *Advanced Computer Simulation: Approaches for Soft Matter Sciences I*; Dr. Holm, C., Prof. Dr. Kremer, K., Eds.; Springer: Berlin, Heidelberg, 2005; pp 105–149. https://doi.org/10.1007/b99427.

(29) Ke, Q.; Gong, X.; Liao, S.; Duan, C.; Li, L. Effects of Thermostats/Barostats on Physical Properties of Liquids by Molecular Dynamics Simulations. *J. Mol. Liq.* **2022**, *365*, 120116. https://doi.org/10.1016/j.molliq.2022.120116.

(30) Eslami, H.; Müller-Plathe, F. Molecular Dynamics Simulation in the Grand Canonical Ensemble. *J. Comput. Chem.* **2007**, *28* (10), 1763–1773. https://doi.org/10.1002/jcc.20689.

(31) Boltzmann, L. *Vorlesungen über Gastheorie: 2. Teil*; BoD – Books on Demand, 2017.

(32) Moore, C. C. Ergodic Theorem, Ergodic Theory, and Statistical Mechanics. *Proc. Natl. Acad. Sci.* **2015**, *112* (7), 1907–1911. https://doi.org/10.1073/pnas.1421798112.

(33) Tian, W.; Qi, L.; Chao, X.; Liang, J.; Fu, M. Periodic Boundary Condition and Its Numerical Implementation Algorithm for the Evaluation of Effective Mechanical Properties of the Composites with Complicated Micro-Structures. *Compos. Part B Eng.* **2019**, *162*, 1–10. https://doi.org/10.1016/j.compositesb.2018.10.053.

(34) Dabo, I.; Kozinsky, B.; Singh-Miller, N. E.; Marzari, N. Electrostatics in Periodic Boundary Conditions and Real-Space Corrections. *Phys. Rev. B* **2008**, *77* (11), 115139. https://doi.org/10.1103/PhysRevB.77.115139.

(35) Young, C. A.; Goodwin, A. L. Applications of Pair Distribution Function Methods to Contemporary Problems in Materials Chemistry. *J. Mater. Chem.* **2011**, *21* (18), 6464–6476. https://doi.org/10.1039/C0JM04415F.

(36) Svishchev, I. M.; Kusalik, P. G. Structure in Liquid Water: A Study of Spatial Distribution Functions. *J. Chem. Phys.* **1993**, *99* (4), 3049–3058. https://doi.org/10.1063/1.465158.

(37) Kirkwood, J. G.; Boggs, E. M. The Radial Distribution Function in Liquids. *J. Chem. Phys.* **1942**, *10* (6), 394–402. https://doi.org/10.1063/1.1723737.

(38) Pedersen, J. S. Analysis of Small-Angle Scattering Data from Colloids and Polymer Solutions: Modeling and Least-Squares Fitting. *Adv. Colloid Interface Sci.* **1997**, *70*, 171–210. https://doi.org/10.1016/S0001-8686(97)00312-6.

(39) Crocker, J. C.; Grier, D. G. Methods of Digital Video Microscopy for Colloidal Studies. *J. Colloid Interface Sci.* **1996**, *179* (1), 298–310. https://doi.org/10.1006/jcis.1996.0217.

(40) Newman, K. E. Kirkwood–Buff Solution Theory: Derivation and Applications. *Chem. Soc. Rev.* **1994**, *23* (1), 31–40. https://doi.org/10.1039/CS9942300031.

(41) Dawass, N.; Krüger, P.; Schnell, S. K.; Simon, J.-M.; Vlugt, T. J. H. Kirkwood-Buff Integrals from Molecular Simulation. *Fluid Phase Equilibria* **2019**, *486*, 21–36. https://doi.org/10.1016/j.fluid.2018.12.027.

(42) Wochner, P.; Gutt, C.; Autenrieth, T.; Demmer, T.; Bugaev, V.; Ortiz, A. D.; Duri, A.; Zontone, F.; Grübel, G.; Dosch, H. X-Ray Cross Correlation Analysis Uncovers Hidden Local Symmetries in Disordered Matter. *Proc. Natl. Acad. Sci. U. S. A.* **2009**, *106* (28), 11511–11514. https://doi.org/10.1073/pnas.0905337106.

(43) Tóth, C. D. Binary Space Partitions: Recent Developments. *Comb. Comput. Geom.* **2005**, *52*, 525–552.

(44) Dirichlet, G. L. Über die Reduction der positiven quadratischen Formen mit drei unbestimmten ganzen Zahlen. *J. Für Reine Angew. Math. Crelles J.* **1850**, *1850* (40), 209–227. https://doi.org/10.1515/crll.1850.40.209.

(45) Tanemura, M.; Ogawa, T.; Ogita, N. A New Algorithm for Three-Dimensional Voronoi Tessellation. *J. Comput. Phys.* **1983**, *51* (2), 191–207. https://doi.org/10.1016/0021-9991(83)90087-6.

(46) Du, Q.; Faber, V.; Gunzburger, M. Centroidal Voronoi Tessellations: Applications and Algorithms. *SIAM Rev.* **1999**, *41* (4), 637–676. https://doi.org/10.1137/S0036144599352836.

(47) Gong, H.-L.; Li, H.; Xiao, D.; Cheng, S. Reactor Field Reconstruction from Sparse and Movable Sensors Using Voronoi Tessellation-Assisted Convolutional Neural Networks. *Nucl. Sci. Tech.* **2024**, *35* (5), 43. https://doi.org/10.1007/s41365-024-01400-w.

(48) Fukami, K.; Maulik, R.; Ramachandra, N.; Fukagata, K.; Taira, K. Global Field Reconstruction from Sparse Sensors with Voronoi Tessellation-Assisted Deep Learning. *Nat. Mach. Intell.* **2021**, *3* (11), 945–951. https://doi.org/10.1038/s42256-021-00402-2.

(49) Delaunay, B. Sur La Sphère Vide. A La Mémoire de Georges Voronoï. *Известия Российской Академии Наук Серия Математическая* **1934**, No. 6, 793–800.

(50) Fortune, S. A Sweepline Algorithm for Voronoi Diagrams. *Algorithmica* **1987**, *2* (1), 153–174. https://doi.org/10.1007/BF01840357.

(51) Ruocco, G.; Sampoli, M.; Vallauri, R. Molecular Dynamics Simulations of Liquid Water: Voronoi Polyhedra and Network Topology. *J. Mol. Struct.* **1991**, *250* (2), 259–270. https://doi.org/10.1016/0022-2860(91)85033-Y.

(52) Housmans, J. A. J.; Wu, G.; Schymkowitz, J.; Rousseau, F. A Guide to Studying Protein Aggregation. *FEBS J.* **2023**, *290* (3), 554–583. https://doi.org/10.1111/febs.16312.

(53) Wang, W.; Nema, S.; Teagarden, D. Protein Aggregation - Pathways and Influencing Factors. *Int. J. Pharm.* **2010**, *390* (2), 89–99. https://doi.org/10.1016/j.ijpharm.2010.02.025.

(54) Zhang, L.; Cole, J. M. Dye Aggregation in Dye-Sensitized Solar Cells. *J. Mater. Chem. A* **2017**, *5* (37), 19541–19559. https://doi.org/10.1039/C7TA05632J.

(55) Eisfeld, A.; Briggs, J. S. The J- and H-Bands of Organic Dye Aggregates. *Chem. Phys.* **2006**, *324* (2), 376–384. https://doi.org/10.1016/j.chemphys.2005.11.015.

(56) Bramley, A. S.; Hounslow, M. J.; Ryall, R. L. Aggregation during Precipitation from Solution: A Method for Extracting Rates from Experimental Data. *J. Colloid Interface Sci.* **1996**, *183* (1), 155–165. https://doi.org/10.1006/jcis.1996.0530.

(57) Zhang, X.; Zeng, L.; Wang, Y.; Tian, J.; Wang, J.; Sun, W.; Han, H.; Yang, Y. Selective Separation of Metals from Wastewater Using Sulfide Precipitation: A Critical Review in

Agents, Operational Factors and Particle Aggregation. *J. Environ. Manage.* **2023**, *344*, 118462. https://doi.org/10.1016/j.jenvman.2023.118462.

(58) Scott, W.; Müller-Plathe ,F.; and Van Gunsteren, W. F. Molecular Dynamics Study of the Mixing and Demixing of a Binary Lennard-Jones Fluid. *Mol. Phys.* **1994**, *82* (5), 1049–1062. https://doi.org/10.1080/00268979400100744.

(59) Muzet, N.; Engler, E.; Wipff, G. Demixing of Binary Water−Chloroform Mixtures Containing Ionophoric Solutes and Ion Recognition at a Liquid−Liquid Interface: A Molecular Dynamics Study. *J. Phys. Chem. B* **1998**, *102* (52), 10772–10788. https://doi.org/10.1021/jp981869v.

(60) Jain, A. K.; Murty, M. N.; Flynn, P. J. Data Clustering: A Review. *ACM Comput. Surv.* **1999**, *31* (3), 264–323. https://doi.org/10.1145/331499.331504.

(61) Jain, A. K. Data Clustering: 50 Years beyond K-Means. *Pattern Recognit. Lett.* **2010**, *31* (8), 651–666. https://doi.org/10.1016/j.patrec.2009.09.011.

(62) Ester, M.; Kriegel, H.-P.; Sander, J.; Xu, X. A Density-Based Algorithm for Discovering Clusters in Large Spatial Databases with Noise. In *Proceedings of the Second International Conference on Knowledge Discovery and Data Mining*; KDD'96; AAAI Press: Portland, Oregon, 1996; pp 226–231.

(63) Campello, R. J. G. B.; Moulavi, D.; Sander, J. Density-Based Clustering Based on Hierarchical Density Estimates. In *Advances in Knowledge Discovery and Data Mining*; Springer, Berlin, Heidelberg, 2013; pp 160–172. https://doi.org/10.1007/978-3-642-37456-2_14.

(64) Ankerst, M.; Breunig, M. M.; Kriegel, H.-P.; Sander, J. OPTICS: Ordering Points to Identify the Clustering Structure. *SIGMOD Rec* **1999**, *28* (2), 49–60. https://doi.org/10.1145/304181.304187.

(65) Idrissi, A.; Vyalov, I.; Georgi, N.; Kiselev, M. On the Characterization of Inhomogeneity of the Density Distribution in Supercritical Fluids via Molecular Dynamics Simulation and Data Mining Analysis. *J. Phys. Chem. B* **2013**, *117* (40), 12184–12188. https://doi.org/10.1021/jp404873a.

(66) Moss, G. P. Basic terminology of stereochemistry (IUPAC Recommendations 1996). *Pure Appl. Chem.* **1996**, *68* (12), 2193–2222. https://doi.org/10.1351/pac199668122193.

(67) Chiu, S. W.; Clark, M.; Balaji, V.; Subramaniam, S.; Scott, H. L.; Jakobsson, E. Incorporation of Surface Tension into Molecular Dynamics Simulation of an Interface: A

Fluid Phase Lipid Bilayer Membrane. *Biophys. J.* **1995**, *69* (4), 1230–1245. https://doi.org/10.1016/S0006-3495(95)80005-6.

(68) Feller, S. E. Molecular Dynamics Simulations of Lipid Bilayers. *Interface Sci.* **2000**.

(69) Kalinichev, A. G.; Wang, J.; Kirkpatrick, R. J. Molecular Dynamics Modeling of the Structure, Dynamics and Energetics of Mineral–Water Interfaces: Application to Cement Materials. *Cem. Concr. Res.* **2007**, *37* (3), 337–347. https://doi.org/10.1016/j.cemconres.2006.07.004.

(70) Harvey, S. C.; Tan, R. K.-Z.; Cheatham III, T. E. The Flying Ice Cube: Velocity Rescaling in Molecular Dynamics Leads to Violation of Energy Equipartition. *J. Comput. Chem.* **1998**, *19* (7), 726–740. https://doi.org/10.1002/(SICI)1096-987X(199805)19:7<726::AID-JCC4>3.0.CO;2-S.

(71) Bai, L.; and Breen, D. Calculating Center of Mass in an Unbounded 2D Environment. *J. Graph. Tools* **2008**, *13* (4), 53–60. https://doi.org/10.1080/2151237X.2008.10129266.

(72) Adamson, A. W.; Gast, A. P. *Physical Chemistry of Surfaces*; Interscience publishers New York, 1967; Vol. 150.

(73) Aguilella, V. M.; Pellicer, J.; Aguilella-Arzo, M. Gibbs' Dividing Surface between a Fixed-Charge Membrane and an Electrolyte Solution. Application to Electrokinetic Phenomena in Charged Pores. *Langmuir* **1999**, *15* (19), 6156–6162. https://doi.org/10.1021/la980773p.

(74) Pártay, L. B.; Hantal, G.; Jedlovszky, P.; Vincze, Á.; Horvai, G. A New Method for Determining the Interfacial Molecules and Characterizing the Surface Roughness in Computer Simulations. Application to the Liquid–Vapor Interface of Water. *J. Comput. Chem.* **2008**, *29* (6), 945–956. https://doi.org/10.1002/jcc.20852.

(75) Sega, M.; Kantorovich, S. S.; Jedlovszky, P.; Jorge, M. The Generalized Identification of Truly Interfacial Molecules (ITIM) Algorithm for Nonplanar Interfaces. *J. Chem. Phys.* **2013**, *138* (4), 044110. https://doi.org/10.1063/1.4776196.

(76) Lee, B.; Richards, F. M. The Interpretation of Protein Structures: Estimation of Static Accessibility. *J. Mol. Biol.* **1971**, *55* (3), 379-IN4. https://doi.org/10.1016/0022-2836(71)90324-X.

(77) Sega, M.; Hantal, G.; Fábián, B.; Jedlovszky, P. Pytim: A Python Package for the Interfacial Analysis of Molecular Simulations. *J. Comput. Chem.* **2018**, *39* (25), 2118–2125. https://doi.org/10.1002/jcc.25384.

(78) Shuttleworth, R. The Surface Tension of Solids. *Proc. Phys. Soc. Sect. A* **1950**, *63* (5), 444. https://doi.org/10.1088/0370-1298/63/5/302.

(79) Tirrell, M. Measurement of Interfacial Energy at Solid Polymer Surfaces. *Langmuir* **1996**, *12* (19), 4548–4551. https://doi.org/10.1021/la950894e.

(80) Marshall, S. J.; Bayne, S. C.; Baier, R.; Tomsia, A. P.; Marshall, G. W. A Review of Adhesion Science. *Dent. Mater.* **2010**, *26* (2), e11–e16. https://doi.org/10.1016/j.dental.2009.11.157.

(81) Rusanov, A. I.; Shchekin, A. K.; Varshavskii, V. B. Three-Dimensional Aspect of the Surface Tension: An Approach Based on the Total Pressure Tensor. *Colloid J.* **2001**, *63* (3), 365–375. https://doi.org/10.1023/A:1016664715084.

(82) Broughton, J. Q.; Gilmer, G. H. Molecular Dynamics Investigation of the Crystal-Fluid Interface. VI. Excess Surface Free Energies of Crystal-Liquid Systems. *J. Chem. Phys.* **1986**, *84*, 5759–5768. https://doi.org/10.1063/1.449884.

(83) Hoyt, J. J.; Asta, M. Atomistic Computation of Liquid Diffusivity, Solid-Liquid Interfacial Free Energy, and Kinetic Coefficient in Au and Ag. *Phys. Rev. B* **2002**, *65* (21), 214106. https://doi.org/10.1103/PhysRevB.65.214106.

(84) Hannay, J. H.; Nye, J. F. Fibonacci Numerical Integration on a Sphere. *J. Phys. Math. Gen.* **2004**, *37* (48), 11591. https://doi.org/10.1088/0305-4470/37/48/005.

(85) Sit, P. H.-L.; Marzari, N. Static and Dynamical Properties of Heavy Water at Ambient Conditions from First-Principles Molecular Dynamics. *J. Chem. Phys.* **2005**, *122* (20), 204510. https://doi.org/10.1063/1.1908913.

(86) Holian, B. L.; Lomdahl, P. S. Plasticity Induced by Shock Waves in Nonequilibrium Molecular-Dynamics Simulations. *Science* **1998**, *280* (5372), 2085–2088. https://doi.org/10.1126/science.280.5372.2085.

(87) Deming, S. N.; Michotte, Y.; Massart, D. L.; Kaufman, L.; Vandeginste, B. G. M. *Chemometrics: A Textbook*; Elsevier, 1988.

(88) Alder, B. J.; Wainwright, T. E. Decay of the Velocity Autocorrelation Function. *Phys. Rev. A* **1970**, *1* (1), 18–21. https://doi.org/10.1103/PhysRevA.1.18.

(89) Culbertson, C. Diffusion Coefficient Measurements in Microfluidic Devices. *Talanta* **2002**, *56* (2), 365–373. https://doi.org/10.1016/S0039-9140(01)00602-6.

(90) Miller, C. C.; Walker, J. The Stokes-Einstein Law for Diffusion in Solution. *Proc. R. Soc. Lond. Ser. Contain. Pap. Math. Phys. Character* **1997**, *106* (740), 724–749. https://doi.org/10.1098/rspa.1924.0100.

(91) Michalet, X. Mean Square Displacement Analysis of Single-Particle Trajectories with Localization Error: Brownian Motion in an Isotropic Medium. *Phys. Rev. E* **2010**, *82* (4), 041914. https://doi.org/10.1103/PhysRevE.82.041914.

(92) Heiser, G. A.; Shukla, R. C.; Cowley, E. R. Average Square Atomic Displacement: A Comparison of the Lattice-Dynamics, Molecular-Dynamics, and Monte Carlo Results. *Phys. Rev. B* **1986**, *33* (4), 2158–2162. https://doi.org/10.1103/PhysRevB.33.2158.

CHAPTER 3
BULK CURCUMIN

In this chapter, we report the results of molecular dynamics simulations of different polymorphs of bulk CUR. First, we have analyzed four transferable force field models of CUR and estimated their ability to reproduce density, melting temperature and conformational distributions. After, the best performing model is adjusted with the help of quantum chemical (QC) calculations. Then the bulk structure of each polymorph is investigated using first moments (average, standard deviation) of the distributions of local properties, such as nearest neighbor radial distributions functions (NRDFs) and interaction energies (electrostatic – ES, Lennard-Jones – LJ).

3.1. Computational Methods

Molecular dynamics simulations were performed using the GROMACS 2024.4[1] program package. Simulations of isobaric conditions were performed with the use of Parinello-Bussi[2,3] thermostat and anisotropic Berendsen[4] barostat. Preliminary comparison between isotropic, semi-isotropic and non-accelerated patched anisotropic Parinello-Bussi[2,3] barostats vs the Berendsen ones showed that typical drawbacks of the Berendsen formulation do not impact properties investigated in this work to a significant degree. Simulation boxes contained 480 fully flexible curcumin molecules. Each starting point corresponds to the crystal of a specific polymorph, with data taken[5,6] from CCDC. Chosen configurations are summarized in Table 3.1. Molecular dynamics models were built via transferable force fields, such as OPLS-AA[7,8], GAFF[9,10], GROMOS[11,12] and CGENFF.[13] Minimization was performed with GROMACS using conjugate gradient (CG) method with a 0.001 nm step size and as many steps as needed until convergence. For Lennard-Jones, we have used a cut-off scheme with potential-shifting and r_c = 10.0 Å. For electrostatic interactions, a reaction-field potential with the same cutoff as Lennard-Jones was chosen instead of PME in order to keep electrostatic treatment consistent between bulk and interfacial simulations (see Ch. 4).

Table 3.1. Initial configurations of the three polymorphs of curcumin, POLY-I, POLY-II and POLY-III. Space groups, as well as absolute values of the corresponding cell axes are given along with the β angle. Angles α and γ are in all cases equal to 90°.

	Space Group	|a|, nm.	|b|, nm.	|c|, nm.	β, °
POLY-I	P2/n	10.0140	2.8292	7.5373	94.94
POLY-II	Pca2(1)	9.2657	3.2563	7.9416	90.0
POLY-III	Pbca	7.8085	3.2928	8.9850	90.0

Quantum chemical calculations were performed with ORCA 6.0.1 program[14] suit. Relaxation of molecular geometry and calculation of minimal basis iterative stockholder (MBIS) atomic charges was performed at M06-SX/cc-pVDZ level. Relaxed potential energy surface scans were done with r2SCAN-3c[15] and PBEh-3c[16] composite DFT-based methods. Most of the settings were left to the default values, except integration grid, which was tightened to "DEFGRID3" setting. **Resolution of Identity (RI)** approximation was used with automatically generated decontracted auxiliary basis.

For isobaric simulations, pressure was kept consistent at 1 atmosphere. The temperature was consistently varied from 300 K to 600 K with a step of 15 K. Equations of motion were integrated in time steps of 1 fs. After at least 10 ns long equilibration period, statistical data (such as temperatures, pressures, nearest neighbor distances, local densities, etc.) was collected using 3000 equilibrium sample configurations, separated from each other by 2 ps, from the 6 ns long production run at every temperature.

Nearest neighbor calculations were done up to the 30^{th} nearest neighbor to a reference molecule, using molecular COMs for all configurations along the generated equilibrium trajectories. Interaction energies were calculated for every frame.

Conformations are assigned based on comparison with unique structures extracted from crystalline data. Details of the chosen algorithm are described in Ch. 2. Angle distributions functions are calculated with TRAVIS[17] MD analysis program. Diffusion coefficients and velocity autocorrelation functions are computed with gmx-msd and gmx-velacc GROMACS tools respectively. All other MD trajectory analysis is performed via custom programs written in Julia programming language.

3.2. Force Field Development

3.2.1. Density Estimation

We have chosen to first investigate several available transferable force field models of CUR. In this particular case, it is imperative that the models are able to adequately describe both the melting point temperature, for all three polymorphs, and the conformational distribution.

CUR exists in three polymorphs – I, II, and III – in the solid state[6,18]. In each of these polymorphs, the conformation adopted by the CUR molecules in the unit cell are quite different. CUR is a good example of conformational polymorph based on flexible seven carbon linker between two terminal phenyl rings and also flexible hydroxyl and methoxy groups. The functional moieties that are present at the three faces of each polymorph are quite different and one has to consider the conformational changes along the three directions.

We started by investigating four classical force fields, namely, OPLS-AA, CGENFF, GAFF and GROMOS with respect to their ability to reproduce the experimental density, melting temperature and the conformations distribution in each of the three polymorphs of curcumin.

As an illustration, we show in Fig 3.1 (a), the dependence of the density on the temperature of POLY-I, under atmospheric pressure in the NPT MD simulation. While all the available models overestimate the melting point, OPLS-AA force field appears to be more suited to CUR compared to other force fields. Melting point temperatures, here estimated as midpoints of abrupt density changes, are 668 K, 683 K, 651 K and 532 K for GROMOS, GAFF, CGENFF and OPLS-AA, respectively. Additionally, room temperature density of curcumin POLY-I is estimated experimentally[6] to be around 1390 kg/m^3. In our simulations, the densities are 1353 kg/m^3, 1311 kg/m^3, 1264 kg/m^3 and 1270 kg/m^3 for GROMOS, GAFF, CGENFF and OPLS-AA, respectively.

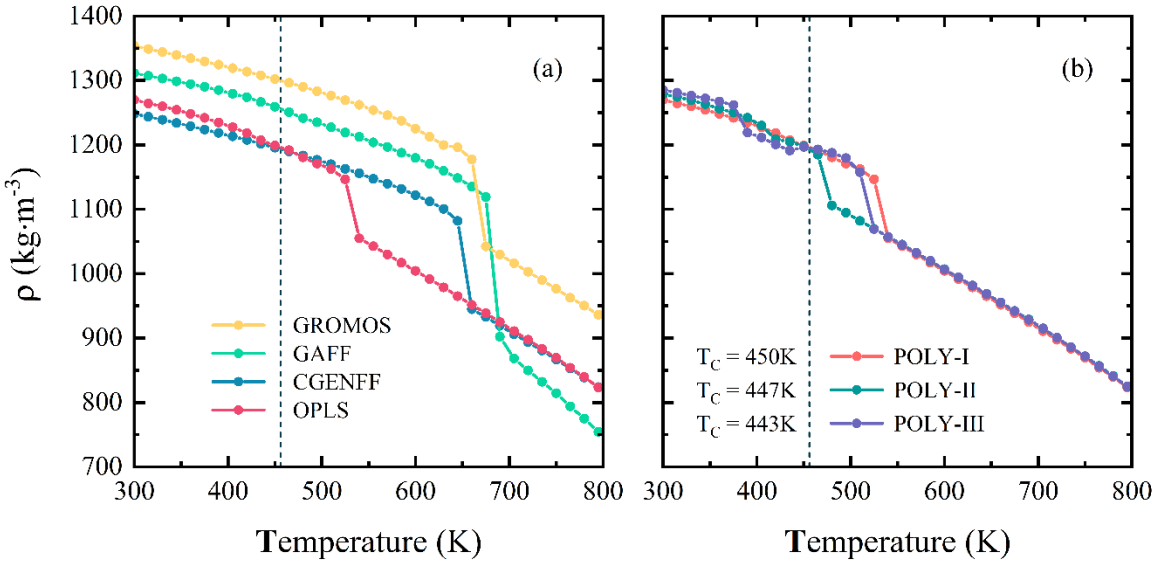

Figure 3.1. (a) The dependence of the density of the bulk-crystal of POLY-I of CUR on the temperature during melting, from 300 K to 800 K with a step of 15 K at an atmospheric pressure, for each considered force field. Vertical dashed line indicates experimental melting point. (b) The dependence of the density of the bulk-crystal of three considered polymorphic forms on the temperature during melting, from 300 K to 800 K with a step of 15 K at an atmospheric pressure, using the unmodified OPLS-AA model.

After identifying OPLS-AA as the most effective model, we evaluated its capability to replicate the experimental temperatures of CUR's three polymorphs. The temperature-dependent density variations are illustrated in Fig. 3.1 (b). At room temperature, the calculated densities for the three polymorphs are 1270 kg/m³, 1279 kg/m³, and 1285 kg/m³, respectively, aligning well with experimental data. The graph legend includes experimental (DSC) measurements of the melting points for each polymorph. However, the melting points, derived from the OPLS-AA model, determined by the midpoint of significant density changes, are 531 K, 471 K, and 516 K. Notably, POLY-II and POLY-III deviate from the experimental trend. Furthermore, POLY-III exhibits experimentally non-observed intermediate transformation beginning at approximately 375 K.

3.2.2. Conformational Distributions

We also checked the ability of this force field to reproduce the distribution of conformation of curcumin in each polymorph. In order to attribute a certain conformation to a molecule in the simulation, we have utilized the following algorithm: we first characterized the

conformation of curcumin molecules in each of its three polymorphs taken from crystallographic data. The values of a set of dihedral angles in each conformation of curcumin are taken as reference values that characterize the conformation. We found that the POLY-I (see Ch. 1) is characterized by curcumin molecules that have conformation 1 (CONF-1), the POLY-III is characterized by CONF-2 while POLY-II is characterized by 50% of CONF 2 and 50% CONF 3.

We applied Alg. 2.3 (see Ch.2) to sample the conformation of curcumin molecules during the increase of the temperature beyond the melting temperature to obtain fractions of every considered conformation for each polymorph. Temperature dependence of said fractions for POLY-I and POLY-II are given in Fig. 3.2 (a,b). Obtained results point out the shortcomings of the used force field when it comes to its ability to reproduce the conformation distribution in each polymorph. This is demonstrated by the absence of significant changes at the melting temperature (indicated by a dashed vertical line in Fig. 3.2) and, also, by the wrong conformation distribution in POLY-II at 300 K. In fact, instead of obtaining 50% of CONF-2 and 50% of CONF-3, applied force field predicts 100% of CONF-3.

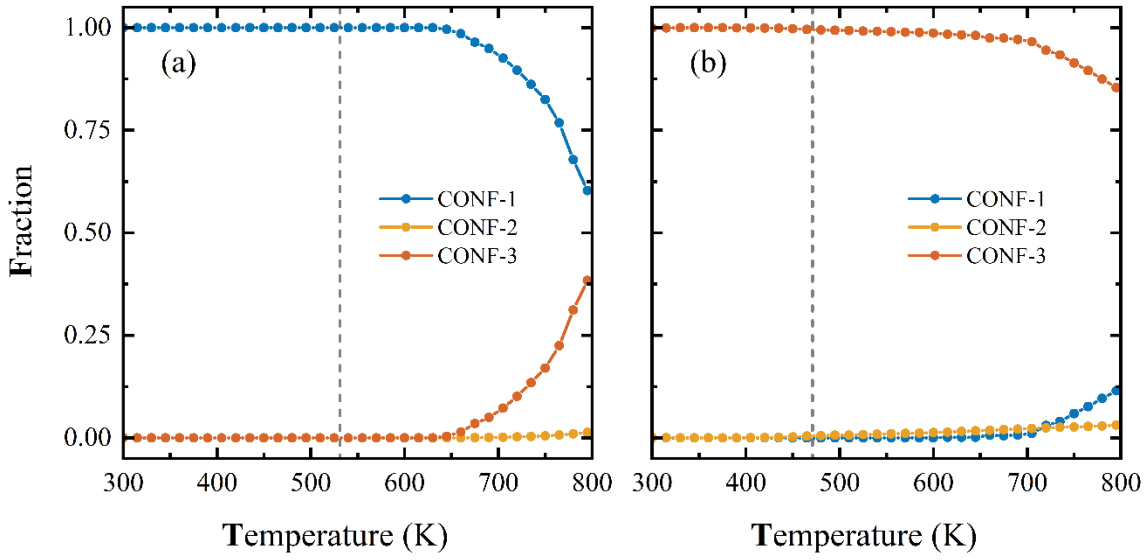

Figure 3.2. Dependence of the fraction of 3 studied conformations on the temperature during melting of (a) POLY-I and (b) POLY-II, from 300 K to 800 K with a step of 15 K at an atmospheric pressure, using the unmodified OPLS-AA model. Vertical line indicates model bulk melting point.

3.2.3. Optimization of Intramolecular Parameters

This underscores the significance of the intramolecular parameters of the force field in accurately describing the conformations of each polymorph, which has traditionally been a weakness of the relatively simple potential energy functions used in classical force fields. Our recent analysis revealed that the differences in intermolecular parameters among the three conformations are relatively small. Specifically, MBIS charges obtained at the M06-SX/cc-pVDZ level differ, on average, by an absolute value of 0.05 between CONF-1 and CONF-2. This finding allows us to concentrate on the intramolecular parameters, particularly the dihedral angles. Fig. 3.3 schematically illustrates the dihedral angles that drive conformational changes in curcumin.

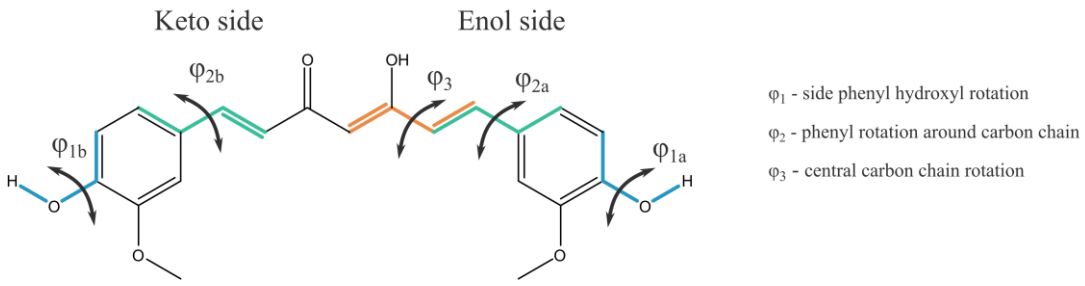

Figure 3.3. Schematic representation of curcumin molecule with highlights indicating dihedral angles that are different between conformations found in the experimental crystalline structures. Symmetry is not taken into account.

We began by examining the OPLS-AA intramolecular parameters that describe the dihedral angles. As shown in Fig. 3.4 (a), the OPLS-AA model significantly underestimates the rotational barrier of the phenol OH group. This is the key reason behind incorrect conformational distributions observed in Fig. 3.2 (b), as even at T = 300 K the 50%-50% ratio of CONF-2 and CONF-3 in the initial configuration turned into 100%-0% split after equilibration.

To refine the intramolecular parameters, we conducted relaxed potential energy surface scans – optimizations with one torsion constrained – for the three key dihedral angles at both the DFT/PBEh-3c (or DFT/r2SCAN-3c) and OPLS-AA levels. The results are presented in Fig. 3.4 (a–c). For the phenol-OH group rotation, which is the main difference between CONF-

2 and CONF-3, the initial OPLS-AA model reproduces the correct shape, with the global minimum corresponding to the intramolecular hydrogen-bonded orientation. However, the potential barrier between the global and local minima is only 6 kJ/mol, whereas the DFT-predicted value is approximately 16 kJ/mol – over twice as high. This explains why previous models predicted incorrect conformational distributions even at room temperature.

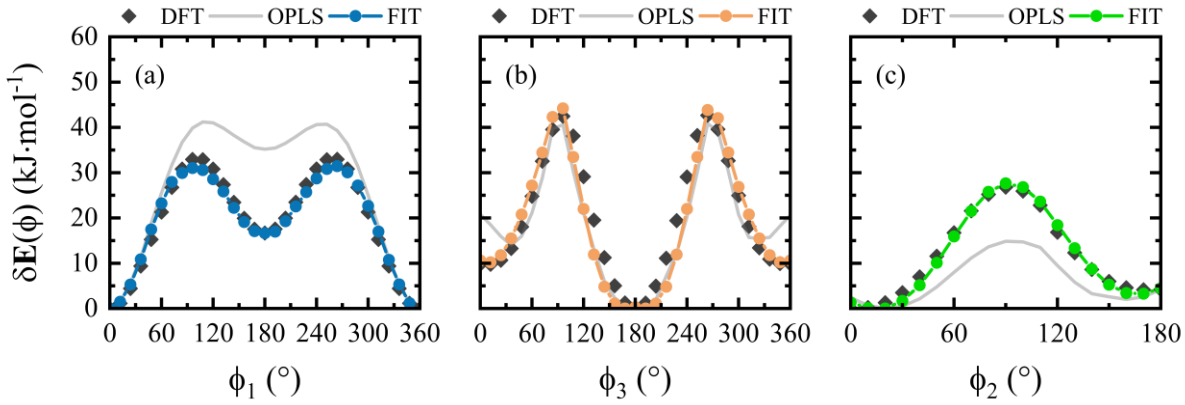

Figure 3.4. Comparison between potential energy surfaces for three dihedral angles optimized in this work. (a) phenol-OH dihedral angle with respect to r2SCAN-3c, (b) Central backbone with respect to r2SCAN-3c and (c) phenyl-backbone dihedral with respect to PBEh-3c. Black dots correspond to the QC DFT data. Gray lines represent potential energy surfaces of original OPLS-AA model. Colored lines represent potential energy surfaces of the re-parametrized model.

The rotation between the vinyl fragments and the central double-carboxyl unit has a relatively high potential energy barrier of 45 kJ/mol, compared to other dihedral angles. While the original OPLS-AA model produced a reasonable barrier value, it incorrectly predicted the energy difference between cis and trans conformations. Quantum chemical (QC) calculations estimate this difference to be around 10 kJ/mol – roughly half the value suggested by OPLS-AA. Furthermore, the actual minimum was located at 35°, rather than at 0° as predicted by the original model.

The rotation of the phenyl fragment relative to the backbone proved challenging to parametrize. The OPLS-AA model significantly underestimated the barrier – nearly by a factor of two (15 kJ/mol for OPLS-AA versus 28 kJ/mol from QC). However, after parametrizing with r2SCAN, the force field's ability to reproduce the melting point of POLY-I deteriorated noticeably. After benchmarking various QC methods, the relatively fast PBEh-3c method demonstrated better performance. Parametrization based on PBEh-3c yielded more accurate

practical results and was therefore selected for this particular dihedral angle. This may be due to the fact that the hybrid PBEh-3c method has reduced self-interaction error compared to non-hybrid meta-GGA methods when describing aromatic system conjugation breaking.

The somewhat arbitrary nature of the choice of reference potential (QC method) was a key reason why we decided to re-parametrize only the dihedral angles critical for reproducing conformational changes. Moreover, as illustrated in Fig. 3.5, fully re-parametrized force fields perform significantly worse in terms of thermodynamic properties (e.g., melting temperature, density). Unlike OPLS-AA – which, despite being a transferable force field, has been extensively validated against experimental data – QC calculations do not necessarily ensure accurate reproduction of experimental properties.

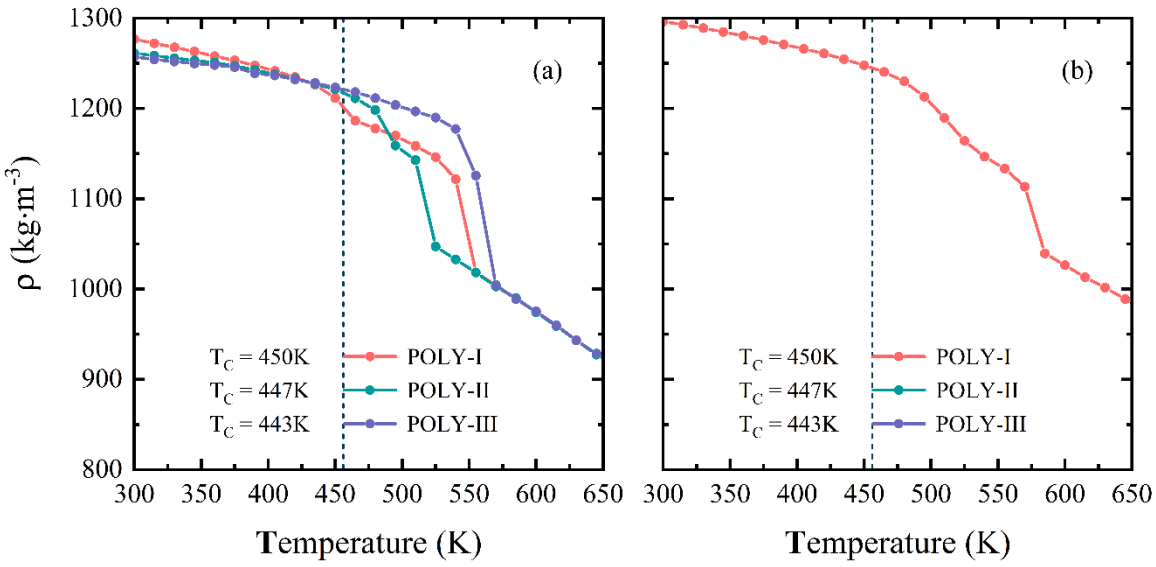

Figure 3.5. The dependence of the density of the bulk-crystal of three considered polymorphic forms on the temperature during melting, from 300 K to 650 K with a step of 15 K at an atmospheric pressure, using the (a) partially modified OPLS-AA model and (b) fully modified OPLS-AA model. Vertical dashed line indicates experimental melting point for POLY-I.

Although the intra- and intermolecular components of the force field are formally separated in the topology, they are not independent in practice. Changes in dihedral angles during MD simulations alter the spatial arrangement of atomic charges, thereby affecting the overall electrostatic field and, consequently, the dipole moment. This effect is illustrated in Fig. 3.6 (a–c), which shows the average dipole moments for POLY-I, POLY-II, and POLY-III in the

OPLS-AA model, our dihedral-angle-reparametrized model, and the fully r2SCAN-based parametrization. In the crystalline phase of POLY-I, the fully reparametrized model exhibits an average dipole moment approximately 0.5 a.u. higher than both the OPLS-AA and the partially reparametrized models.

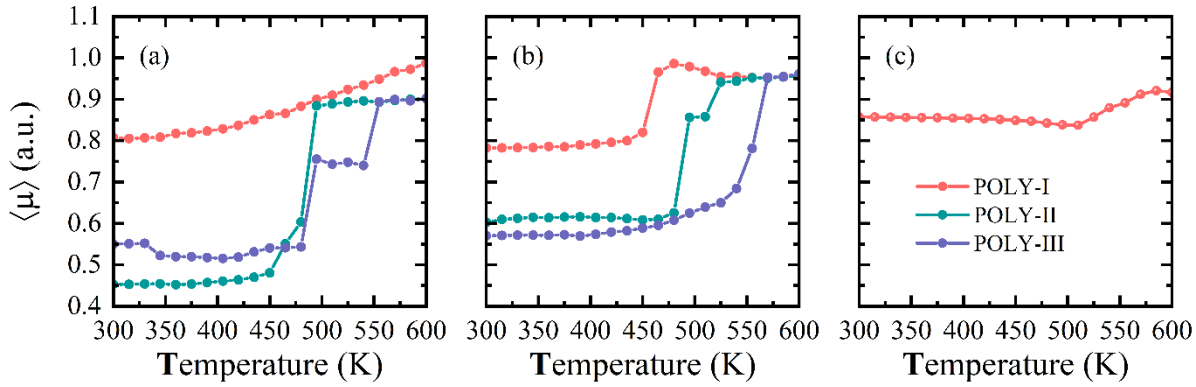

Figure 3.6. Dependence of the average values of dipole moments for POLY-I, POLY-II and POLY-III in the (a) OPLS-AA model, (b) our parametrization of dihedral angles and (c) our full r2SCAN based parametrization on temperature.

After careful adjustments of select dihedral angle parameters, new OPLS-AA model correctly predicts both the conformational distributions at the starting configuration and melting point changes. Fig. 3.7 (a,b,c) shows the dependence of the conformational distributions for POLY-I, POLY-II and POLY-III with the new OPLS-AA model.

As shown in the graph, at low temperatures, the conformational fractions of CONF-1, CONF-2, and CONF-3 align closely with those expected for POLY-I, POLY-II, and POLY-III of CUR. Notably, the new OPLS-AA force field accurately reproduces the observation that at low temperatures CONF-2 and CONF-3 are present in equal proportions of approximately 50% each.

After the melting point, the conformational fractions of CONF-1, CONF-2, and CONF-3 become similar regardless of the CUR polymorph. CONF-3 has the lowest energy among the three conformations, which explains why, after melting, around 65% of all curcumin molecules adopt the CONF-3 conformation. Approximately equal amounts of CONF-2 and CONF-1 are present in the melt, and these proportions remain relatively stable as the temperature increases.

The fact that experimental melt-recrystallization of curcumin typically produces POLY-I suggests that there is no simple relationship between conformational distribution in the bulk phase and polymorphic behavior.

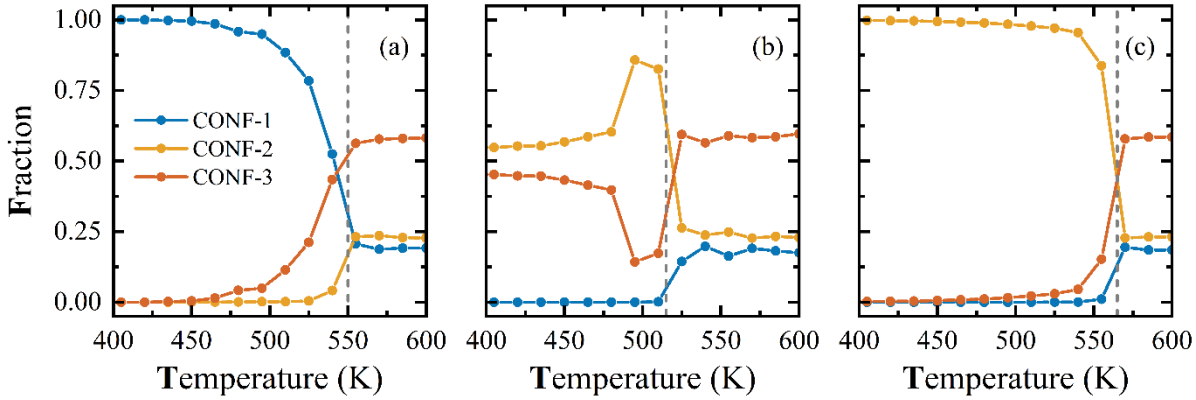

Figure 3.7. Dependence of the fraction of 3 studied conformations on the temperature during melting of (a) POLY-I, (b) POLY-II and (c) POLY-III, from 400 K to 600 K with a step of 15 K at an atmospheric pressure, using the modified OPLS-AA model. Vertical line indicates model bulk melting point.

Beyond melting, accurately simulating the full melt-recrystallization process should ideally capture the crystallization behavior when the system is cooled below the melting point. In molecular dynamics (MD) simulations, it is common to observe hysteresis in the melting-cooling density curves, even for substances that do not exhibit such behavior experimentally. This discrepancy arises primarily from the short time scales and rapid cooling rates typical of MD simulations, which prevent the system from adequately sampling all possible, yet statistically improbable, configurations.

More problematic, however, are cases where standard MD protocols fail to produce any crystalline structure upon cooling, instead yielding amorphous substances. Unfortunately, this is the case with CUR. The density plots for the cooling simulations, conducted at the same rate as the melting simulations, are shown in Fig. 3.8 (a). Although the melt states for all three different starting points (polymorphs) are identical, we present the results for all three simulations for completeness.

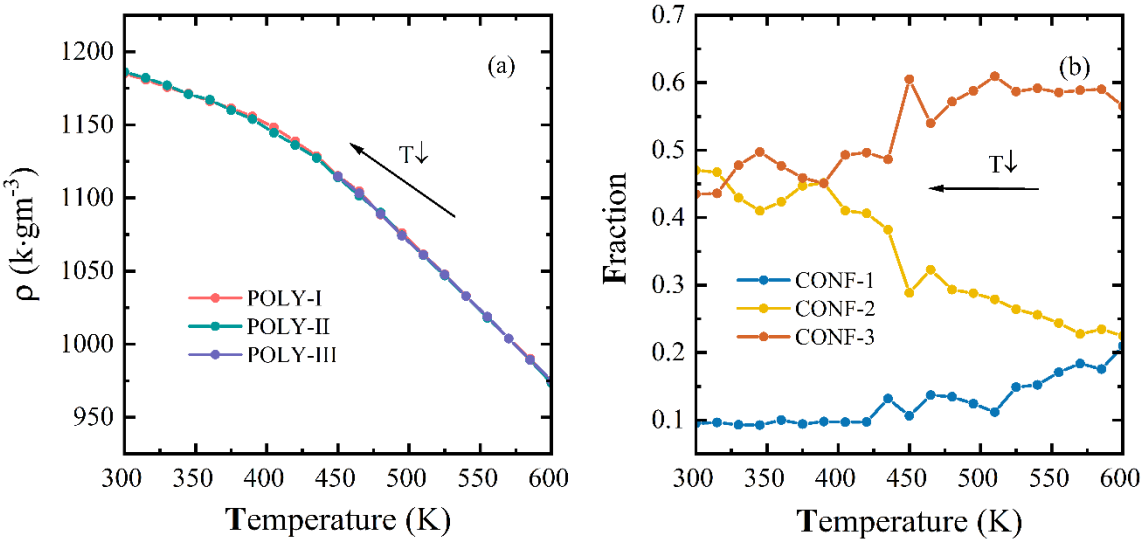

Figure 3.8. (a) Dependence of the bulk-density of CUR on the temperature for 3 systems under study. (b) Dependence of the fraction of every considered conformation of CUR in the cooling simulation on the temperature.

The absence of any sharp density changes suggests the formation of an amorphous phase. Analysis of local properties, such as conformational distribution (Fig. 3.8(b)), also shows only gradual changes. Interestingly, the amorphous state of CUR resembles the composition of POLY-II, despite the challenges[19] in experimentally obtaining the latter. Increased "noisiness" of the temperature dependence in Fig. 3.8 (b), which was not present in Fig. 3.7, further reflects incomplete sampling of all possible configurations.

Since CUR is a "conformational polymorph," the challenges in cooling simulations are twofold: efficient sampling of both conformational states and molecular positions and orientations needed to reproduce the crystalline structure. Without enhanced sampling techniques such as metadynamics, such simulations appear infeasible. Therefore, instead of relying solely on cooling simulations, we focus on analyzing a broad range of structural and dynamical properties during the heating simulations, often localized to a few neighboring molecules, and correlate them with conformational distributions. The assumption is that trends characteristic of different polymorphs upon melting will reflect similar trends that would be present in the crystallization simulation.

3.3. Structural Properties of Bulk Curcumin

3.3.1. Voronoi Tessellation

When a crystal melts, it undergoes substantial structural changes as it transitions from an ordered solid to a disordered liquid. In the solid state, atoms or molecules are arranged in a well-defined, repeating lattice structure, which provides mechanical rigidity. As the material absorbs heat and approaches the melting point, molecular motion intensifies, leading to increased disorder and eventual breakdown of the lattice structure.

To analyze the structural changes that occur as the temperature approaches the melting point, the distribution of local density is a key factor to consider. While several methods exist for sampling the molar density of different regions of a system, the Voronoi tessellation approach offers a straightforward and nearly parameter-free solution. The details of the method and its implementation are provided in Ch. 2.

An important decision when working with Voronoi Polyhedra (VP) is how to represent the entire molecule – either by a single point or multiple positions. In this study, we calculate density distributions (see Fig. 3.9 (a)) at each temperature using the center of mass (COM) of each CUR molecule.

The results are clear, especially for POLY-I: below the melting point, the density distributions have a symmetric, narrow Gaussian shape, centered around 0.002 $Å^{-3}$. Above the melting point, the distributions become slightly broader and more skewed toward higher density values, though they remain unimodal – which is not necessarily expected for molecules of CUR's size.

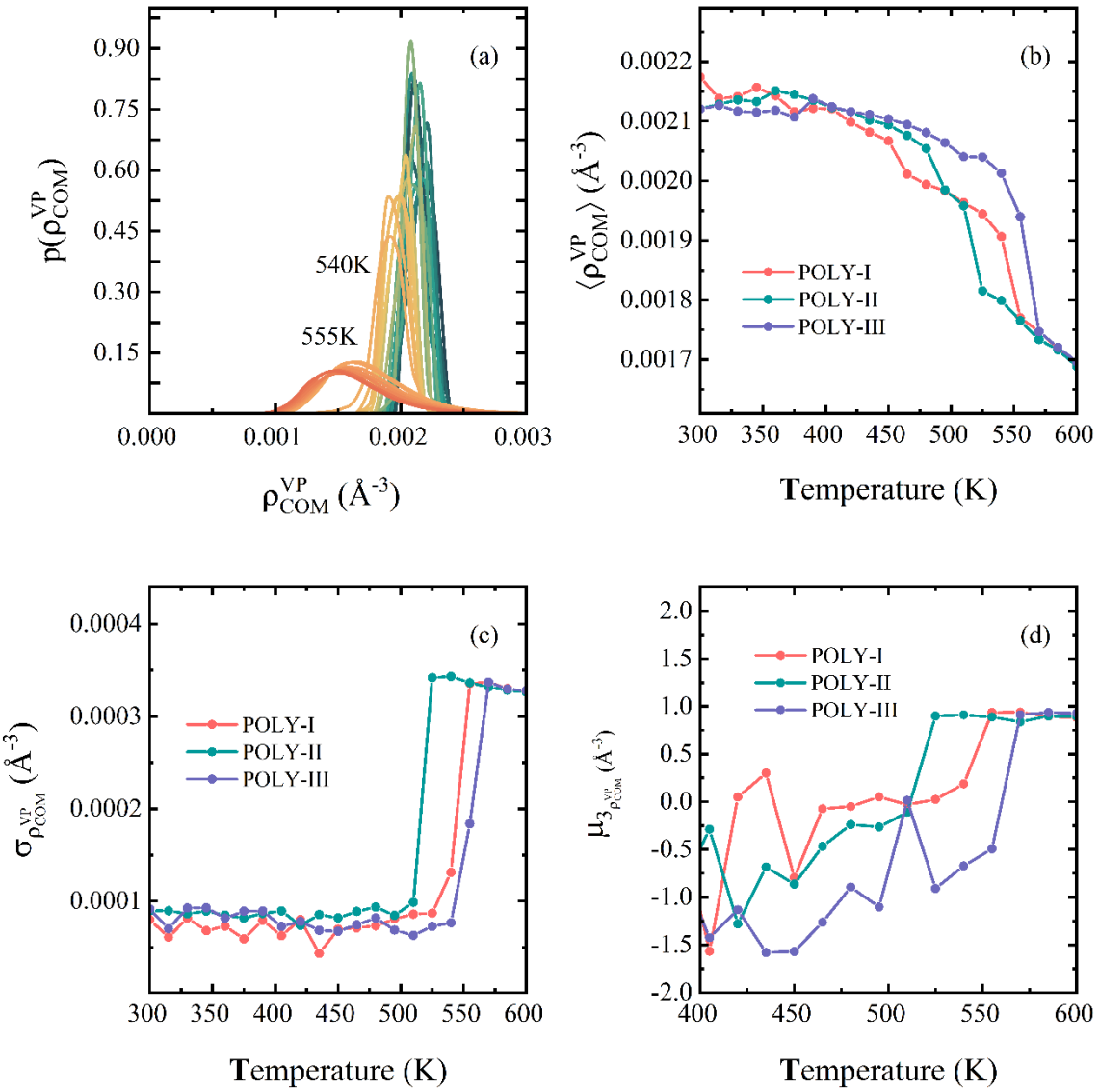

Figure 3.9. (a) Dependence of the probability density distributions of the VP density on the temperature for POLY-I. Other polymorphs give similar graphs, but at different temperatures. (b) Dependence of the average value of VP density on the temperature for all considered polymorphs of CUR. (c) Dependence of the fluctuation of VP density on the temperature for all considered polymorphs of CUR. (d) Dependence of the skewness of VP density on the temperature for all considered polymorphs of CUR.

Average values of CUR local density for every considered system are given in Fig. 3.9 (b). After about 400 K, slow decrease of the average local density mirrors that of the system density (see Fig. 3.5), with about the same ranking of CUR polymorphic forms from most to least dense, with POLY-III being the most tightly packed one, followed by POLY-II. Naturally, fluctuations (Fig. 3.9 (c)) of the local density sharply increase upon melting, but after that show a very small gradual decline, indicating that the largest inhomogeneity is achieved exactly at the T_m. The

skewness of the corresponding distributions, shown in Fig. 3.9 (d), also rises at T_m before settling at a value very close to 1. Below the melting point, however, most density distributions skew negatively – toward lower density values – indicating presence of a small amount of tightly packed CUR molecules. POLY-III displays the largest degree of such tendency, followed by POLY-II, indicating that one of the possible causes might be π-stacking of the phenyl rings of planar CONF-2 and CONF-3.

3.3.2. Nearest Neighbor Distribution

A bit more information about the structural organization (packing) of the CUR polymorphs can be obtained from the radial distribution functions (RDF). As we are interested in the general spatial arrangement, we utilize COM-COM RDFs. In Fig. 3.10 (a) we illustrate the RDF in POLY-I at 300 K along with its decomposition on the nearest-neighbor radial distribution functions (or NRDF for short) for the first 20 neighbors. The RDF has many distinct peaks, reflecting the crystalline nature of the system. First two peaks correspond to the first two direct neighbors – π-stacked structures. The third and largest peak marks the end of the first "solvation" shell and corresponds to the 4 molecules lying in the same plane as reference CUR – 2 near the phenolic -OH groups, and 2 are closer to the central keto-enol unit.

Use of the NRDFs allows us to get more succinct information by computing average distances between closest neighbors as expectation values of the corresponding NRDFs (provided appropriate normalization). In the Fig. 3.10 (c-d), we have illustrated temperature dependence of the average distance between neighbors in each polymorph respectively.

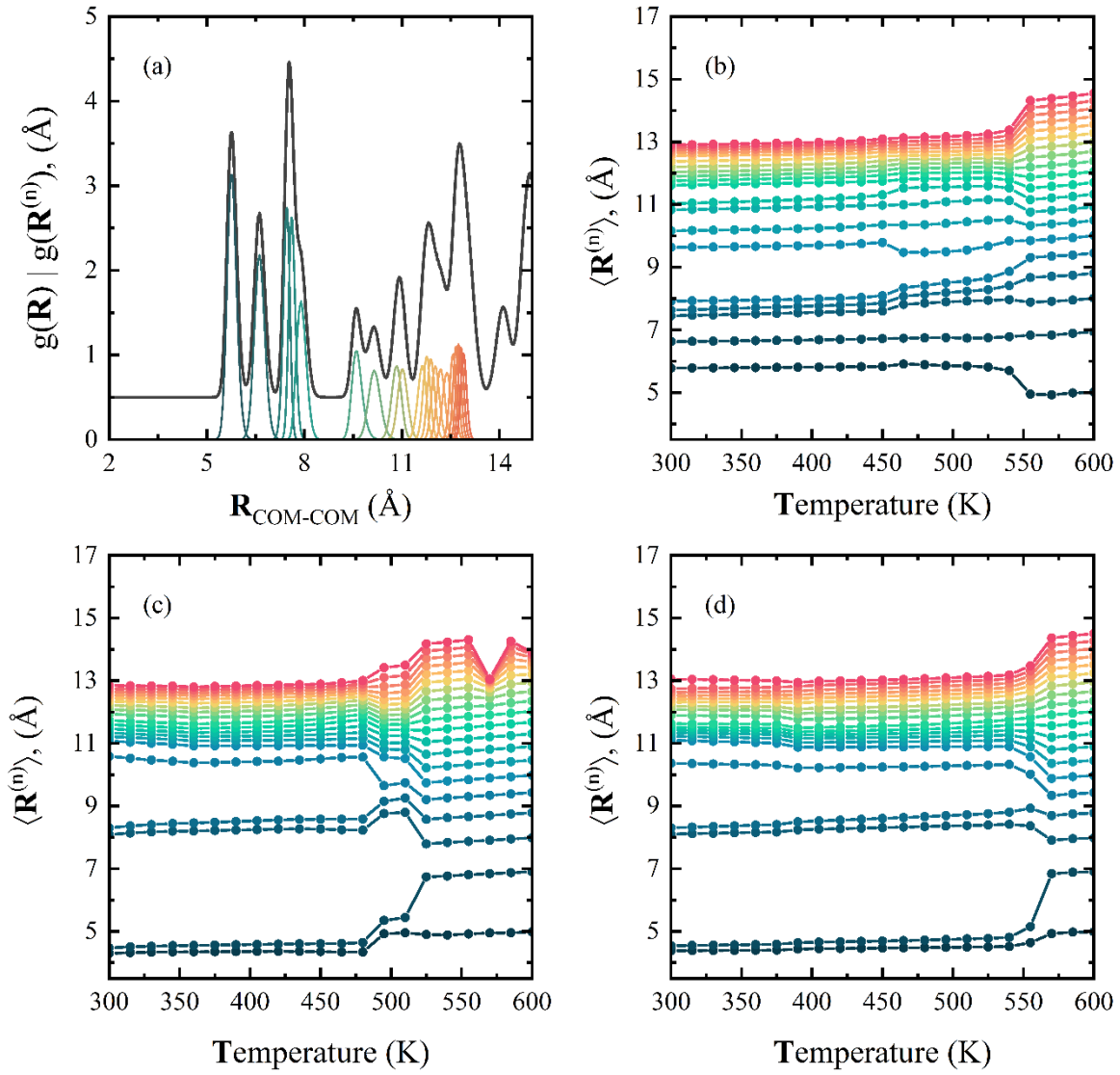

Figure 3.10. (a) Radial distribution functions (gray) and the first 20 nearest neighbor radial distribution functions (colored, redder color indicates further neighbor) for POLY-I at T = 300 K. (b-d) Dependence of the average nearest neighbor distance on the temperature during melting of (b) POLY-I, (c) POLY-II and (d) POLY-III, from 300 K to 600 K with a step of 15 K at an atmospheric pressure, using the modified OPLS-AA model. First 20 nearest neighbors are taken into account. Color indicates rank of the neighbor – from blue to red.

The behavior of $\langle R^{(n)} \rangle$ as a function of temperature clearly shows that near the melting temperature, the distance to the first neighbor decreases, while the distance to the second neighbor remains almost unchanged compared to its value in the crystalline state. At the same time, the average distances to the third through seventh neighbors increase, with the most pronounced increase occurring for the fifth neighbor. The average distances to the eighth

through eleventh neighbors appear to be largely unaffected by the melting transition. However, beyond the eleventh neighbor, the average distances increase sharply, indicating significant structural rearrangement in the longer-range order as the system transitions from a crystalline to a disordered state.

3.3.3. Angle Distribution Function

Besides RDF, spatial organization of molecules can be examined with angle distribution functions (ADF). They provide information about distributions of angle between two vectors. We analyze two angles, definitions of which are schematically represented in Fig. 3.11. The first angle – θ_1 – is between the vector perpendicular to the plane one of the phenyl rings and the vector connecting two centers of the phenyl rings of two different molecules. The second angle – θ_2 – is defined in terms of the two vectors, each on a different molecule, perpendicular to their molecule's respective phenyl rings. These two angles will allow us to capture important information about potential π-π stacking of those phenyl fragments.

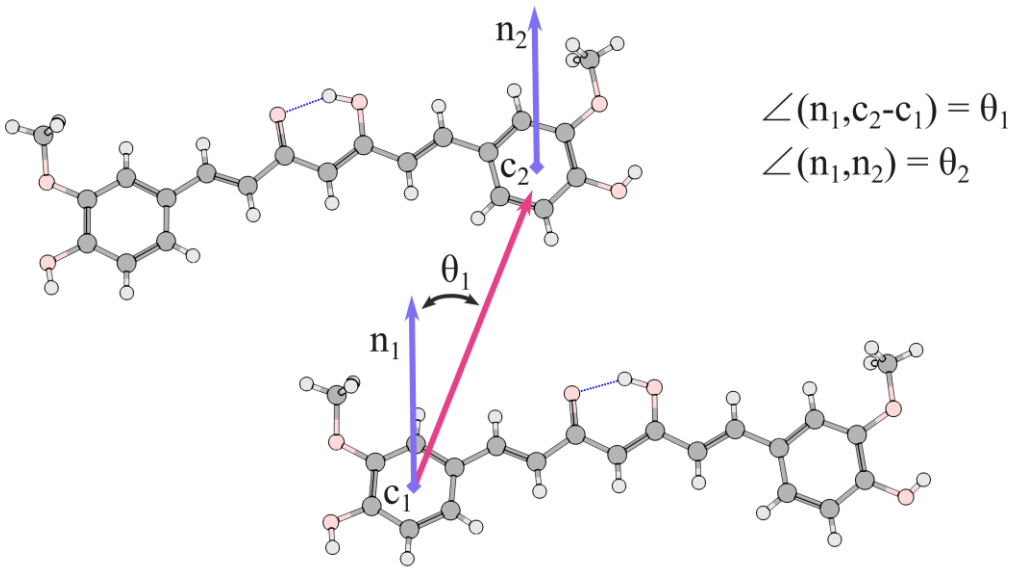

Figure 3.11. Schematic representation of angles between two curcumin molecules analyzed in this work.

Dependence of the distribution of $P(\theta_1)$ on the temperature is given in Fig 3.12 for each polymorph. Although it is tempting to summarize those distributions via their moments, or, more specifically, their circular moments, as they are multimodal, it is easier to analyze them directly.

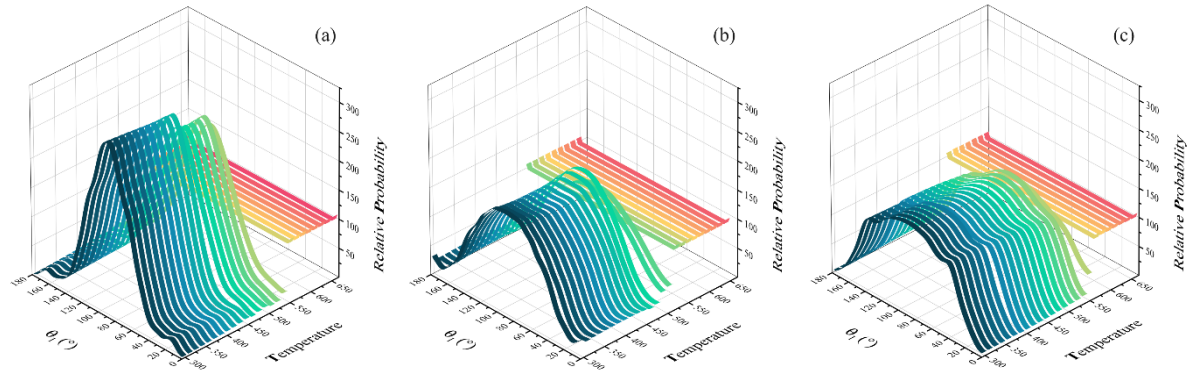

Figure 3.12. Dependence of the probability distribution of the angle between vector perpendicular to the phenol side ring and vector connecting the same phenol side rings of two different CUR molecules (see Fig. 3.11) on the temperature for (a) POLY-I, (b) POLY-II, (c) POLY-III.

The graphs in Fig. 3.12 represent relative, non-normalized probability. For temperature beyond the melting temperature, one common feature for all three polymorphs is the absence of angular preference, i.e., distributions are uniform. In the crystalline phase, POLY-II and POLY-III have significantly wider distributions than POLY-I. This is related to the packing nature in those polymorphs – specifically the cross-pattern of organization. At around 500 K, POLY-II shows even wider distribution, which is likely related to the conformational changes from CONF-2 to CONF-3, as the rotation of -OH group to establish intramolecular hydrogen bond allows greater mobility of the corresponding phenol moiety with respect to the first neighbors. In POLY-III, an interesting feature is the consistent appearance of small local maxima around 60 degrees.

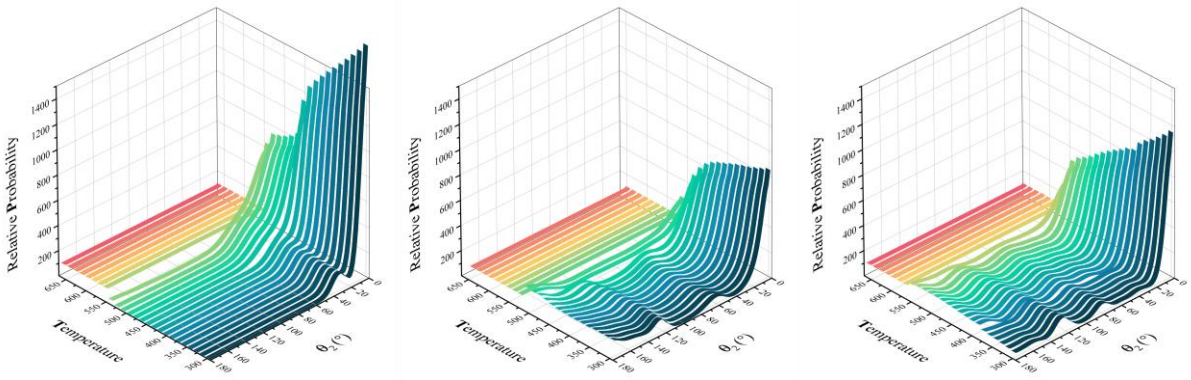

Figure 3.13. Dependence of the probability distribution of the angle between vector perpendicular to the phenol side ring and vector perpendicular to the phenol side ring of other CUR molecules (see Fig. 3.11) on the temperature for (a) POLY-I, (b) POLY-II, (c) POLY-III.

This feature can be further analyzed by looking at the distributions for $P(\theta_2)$. Fig. 3.13 shows that POLY-III has multiple local maxima around 0°, 80° and 135°. The maximum around 0°, indicating parallel orientation of the phenyl rings, i.e., stacking, is present and dominant in all polymorphs. Small maximum around 35° in POLY-I is again related to the non-planar nature of CONF-1, but the wave-like pattern in POLY-II and POLY-III is different. The 135° angles come from the cross-pattern of arrangement of CUR molecules in the crystals of POLY-II and POLY-III. In POLY-II, this maximum disappears around 500 K, before the melting point, as conformational changes in that crystal begin to occur. Angles around 80° are likely to come from additional bit of small rotation of phenyl rings around carbon chain backbone that is present in CONF-2 and CONF-3, but to a lesser extent than in CONF-1. Perhaps such rotations are possible due to the hydrogen-bonding network in CUR crystals.

3.4. Interactions in Bulk Curcumin

3.4.1. Hydrogen Bonding

An interesting feature of Fig. 3.7 (b) is the sudden change in the ratio of CONF-2 to CONF-3 around 500 K. The preference toward CONF-2 likely indicates an increase of probability to establish hydrogen-bonding, as CONF-2, when isolated, is higher in energy than CONF-3, but has one phenol hydroxyl group available for inter-molecular hydrogen bonding. In order to test this, we have computed the average number of hydrogen bonds with typical length and angle restrictions, namely 3.0 Å and 150°. The resulting dependence of the average number of hydrogen bonds on the temperature is illustrated in Fig. 3.14 (a).

POLY-II starts with low number of hydrogen bonds, but even before melting, thermal energy allows enough mobility to both cross the rotational barrier (Fig. 3.14 (e)) and reposition to form a strong hydrogen bond network. The former point is interesting, as probability density of finding phenol hydroxyl in trans-configuration (180°) is maximized around 480 K – 500 K, and even becomes preferred, indicating energetic favorability of inter-molecular hydrogen bond formation. Similarly, POLY-I has the same increase, modulated by largely the same factors, as seen from Fig. 3.14 (d). However, because CONF-1 has to overcome much larger barrier to change into CONF-2 or CONF-3, those are not seen in POLY-I simulations until a melt phase forms.

Average number of hydrogen bonds highly depends on the criteria used for their detection. As Fig. 3.14 (b-c) shows, angle deviation cut-off (from the strictly linear hydrogen bond) has much greater impact than the donor-acceptor distance cut-off. This is perhaps not surprising, as crystalline state limits the degree of maneuverability of phenyl rings of CUR, so the increase of the angle allows to encompass more hydrogen bonds. However, one could expect hydrogen bond energies to quickly fall off as the distance or the angle increases. Although the choice of 3.0 Å and 150° is arbitrary, it is quite often used in the literature and as a default set of parameters for MD analysis software, so we will stick with it in further chapters.

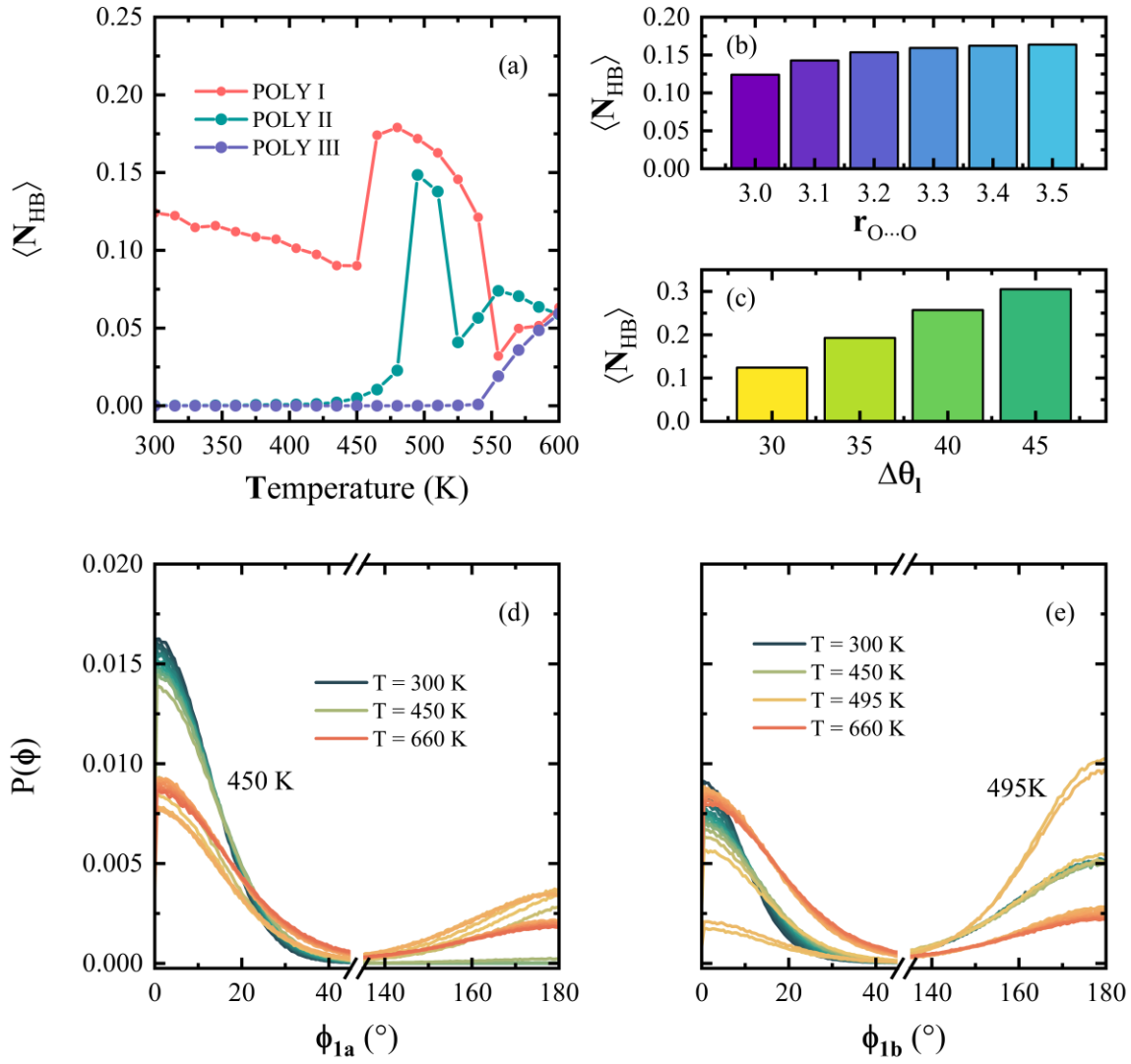

Figure 3.14. (a) Dependence of the average number of hydrogen bonds per molecule on the temperature for all three considered polymorphs. (b) Dependence of the average number of hydrogen bonds in POLY-I at 300 K on the O···O cutoff distance used in the algorithm. (c) Dependence of the average number of hydrogen bonds in POLY-I at 300 K on the O-H···O cutoff angle deviation (from 180°) used in the algorithm. (d) The probability density function for the enol side phenol hydroxyl dihedral angle in POLY-I. (e) The probability density function for the keto side phenol hydroxyl dihedral angle in POLY-II.

Interestingly, the average number of hydrogen bonds in POLY-III is always very low, only increasing in the melt. Because POLY-III is the only polymorph that has lower average number of hydrogen bonds in the crystalline state compared to a melt state, upon cooling, crystallization of the melt into POLY-III would be associated with energy penalty due to hydrogen bond

breaking. This could potentially lead to a POLY-III being kinetically limited, depending on the strength of the CUR-CUR hydrogen bonds.

Estimating such a barrier is rather difficult. Calculations of the hydrogen bond energy are quite sensitive toward which terms of the intermolecular (and, perhaps, intramolecular) potential are included. In this work, we include ES and LJ contributions from O···O and H···O interactions, as well as O-H intramolecular bond energy. This neglects any contributions from the X-O-H angular part, as well as other intermolecular interactions, but should include most of the main terms. The results suggest that the average hydrogen bond energy, in the melt, at 600 K, is about 28 kJ/mol. Those decently strong hydrogen bonds might significantly affect nucleation kinetics. This number, however, should be placed in the context of the total CUR-CUR interaction energies.

3.4.2. Pair Interaction Energies

Besides analyzing hydrogen bond energies, one can analyze full pair interaction energies between neighboring molecules. Importantly, although neighboring molecules are sorted by distance between their centers of mass, they are not necessarily in the same order as lowest interaction energy, since major interaction sites for curcumin – phenol methoxy and hydroxyl groups – are as far away from center of mass as possible. Nevertheless, analysis of pair interaction energies, as seen in Fig. 3.15 (a-d), confirms that, firstly, LJ contributions to the pair interaction energy are higher than the ES ones for close neighbors. Lower ES interaction energies with high-ranked far-away neighbors are the result of head-to-tail hydrogen bonding of the elongated curcumin molecule (COM-COM distance within the first shell is maximized for such head-to-tail configurations).

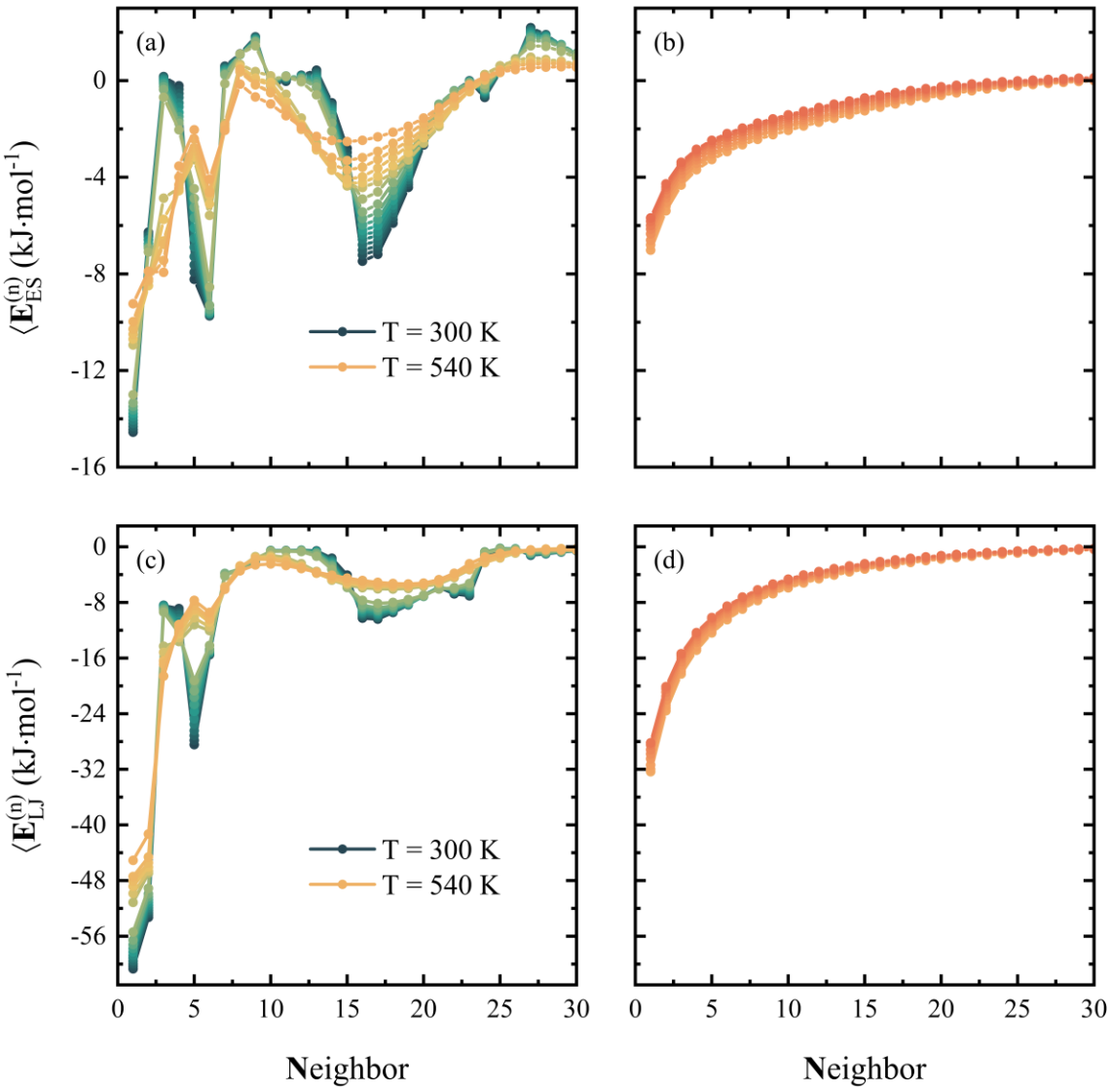

Figure 3.15. Dependence of the average value of electrostatic (a,b) and Lennard-Jones (c,d contribution to pair interaction energy of POLY-I in the crystalline state, from 300 K to 540 K with a step of 15 K at an atmospheric pressure, and melt state, from 555 K to 600 K, using the modified OPLS-AA model. First 30 nearest neighbors are taken into account. Color indicates temperature – red hues indicate higher values.

In order to investigate the temperature dependence of the ES and LJ contributions, we will compare their behavior at two temperature ranges, namely between T = 300 K and T = 500 K, where the polymorphs are in the crystal state and T=540 K and beyond the meting temperature of the polymorphs. Of note is that at melt state the distribution of conformation is the same independently of the polymorph type, and pair-interaction energies in the melt follow a

logarithmic pattern, with higher temperatures giving more convex curves. In the crystalline state (Fig 3.15 (a,c)), however, a few notable exceptions are present. For example, neighbors 5 and 6 have significantly lower ES and LJ contributions compared to neighbors 3 and 4. This is because the former neighbors are situated near the -OH groups, with strong ES interactions at the hydrogen bonds, while the latter are in the plane of CUR near the central keto-enol group, where not much interactions are possible, since phenyl rings prevent CUR molecules coming too close.

Even more interesting is crystalline state of POLY-II, with pair-interaction energies given in Fig. 3.16 (a,b). Again, neighbors 3 and 4 have actually repulsive ES interactions, given by hydrogen-hydrogen repulsion (mostly between aromatic hydrogens in the phenyl rings). Noticeably, pair-interaction energies change significantly before the actual melting point – in large part, due to the conformational changes associated with phenyl hydroxyl group rotation, as shown by the fact that ES changes are much more pronounced than the LJ ones. But even beyond that, temperatures between 480 K and 510 K give just enough mobility for CUR molecules to reorient themselves to engage in strong hydrogen bonding – nearly eight-time spike in the number of hydrogen bonds in Fig. 3. 14 (a) is accompanied virtually by the same increase in strength, as neighbors 8-14 all have, simultaneously, significantly more attractive ES interactions. This shows that although the packing of CUR is LJ dominated, transformations of conformations and polymorphs can still be electrostatically driven.

The crystalline state of POLY-III is, in some sense, very similar to that of POLY-II, and not only by their structure, but by their interactions, as seen in Fig. 3.16 (c,d). In particular, LJ contributions are similar for most of the temperatures, with the exception of the 500 K – 540 K range due to the conformational changes in POLY-II. The electrostatic interactions are also quite similar, but the dip near 15-20 neighbor rank is quite a bit deeper than that in the POLY-II. This is due to the fact that half of the CUR molecules in POLY-II start with CONF-3, with intramolecular hydrogen bond, while all CUR molecules in POLY-III are in CONF-2, leading to more possible interactions. One has to consider, however, that as Fig. 3.14 has revealed, those hydrogen bonds must be weaker in nature than those in POLY-I, as they are longer than 3.0 Å and 150°. Perhaps a significant part of the attraction comes from the methoxy groups – C-H···O interactions were not included in Fig. 3.14, but are, of course, part of the total pair-interaction energies.

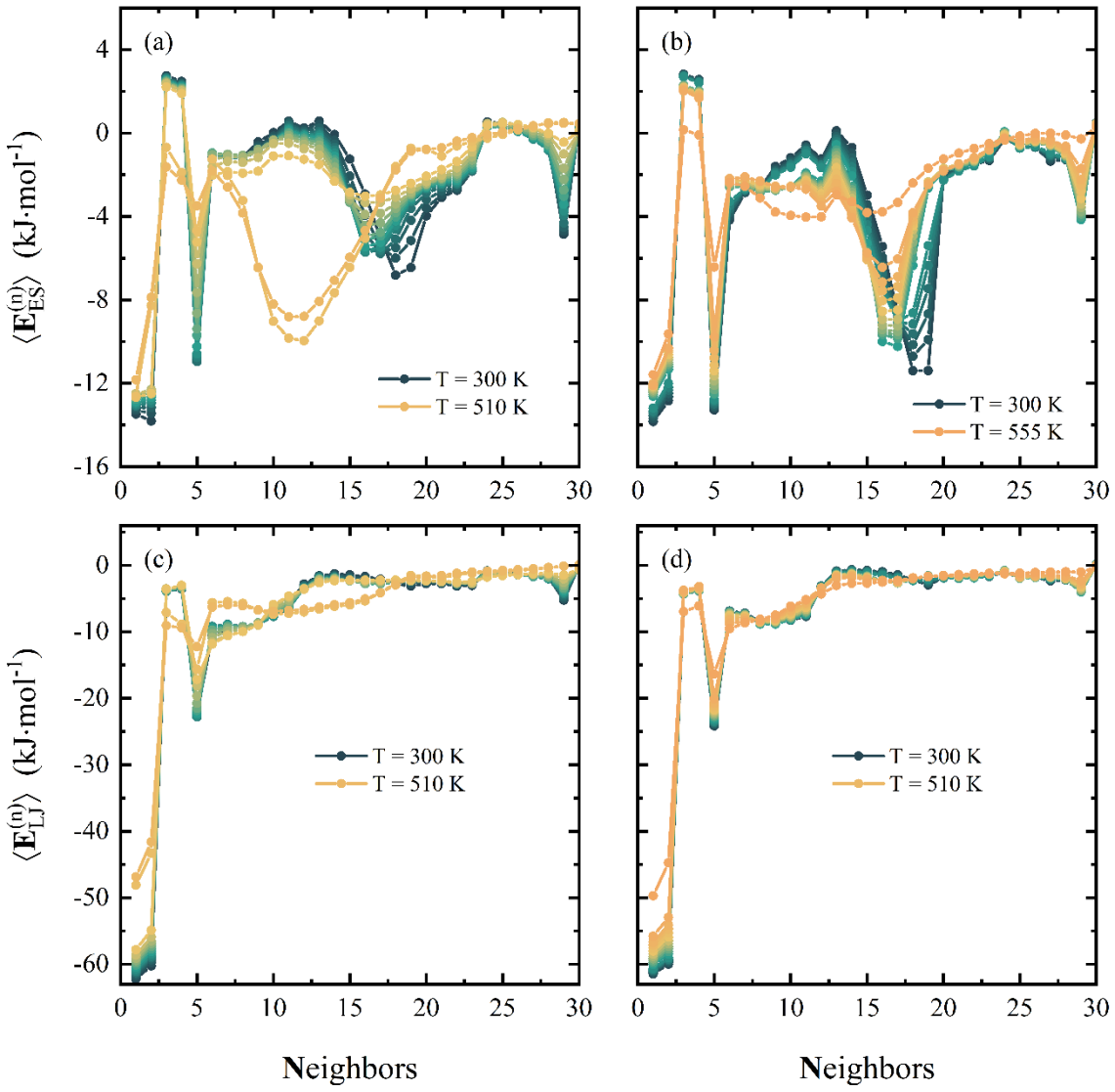

Figure 3.16. Dependence of the average value of electrostatic (a,b) and Lennard-Jones (c,d contribution to pair interaction energy of (a,c) POLY-II in the crystalline state, from 300 K to 510 K, and (b,d) POLY-III in the crystalline state, from 300 K to 555 K. First 30 nearest neighbors are taken into account. Color indicates temperature – red hues indicate higher values.

3.4.3. Cohesive Energy Density

Integration of the pair-interaction energies across all of the neighbors, with the addition of energies of internal degrees of freedom, would give total classical energy of the system. Although not an observable, and not strictly useful on its own, it can be used to calculate cohesive energy density[20] (CED). CED is given as enthalpy of evaporation/sublimation, minus RT and divided by molar volume. Equivalently, it is the given by Eq. 3.1:

$$CED = \frac{NE_{VAC} - E_{BULK}}{V} \tag{3.1}$$

This formula becomes slightly more complicated for a system of molecules that might possess different conformations. To see how much impact different conformations of CUR would have, we performed vacuum MD simulations for a single molecule, starting from 3 different conformations. The results of such calculations are given in Fig. 3.17 (a). Fortunately, energy of 3 different conformations seems to be quite similar. It is worth noting that conformational changes do occur at higher temperatures, but since energies are similar at low temperatures, neglect of the energy difference between conformations is unlikely to significantly affect final results.

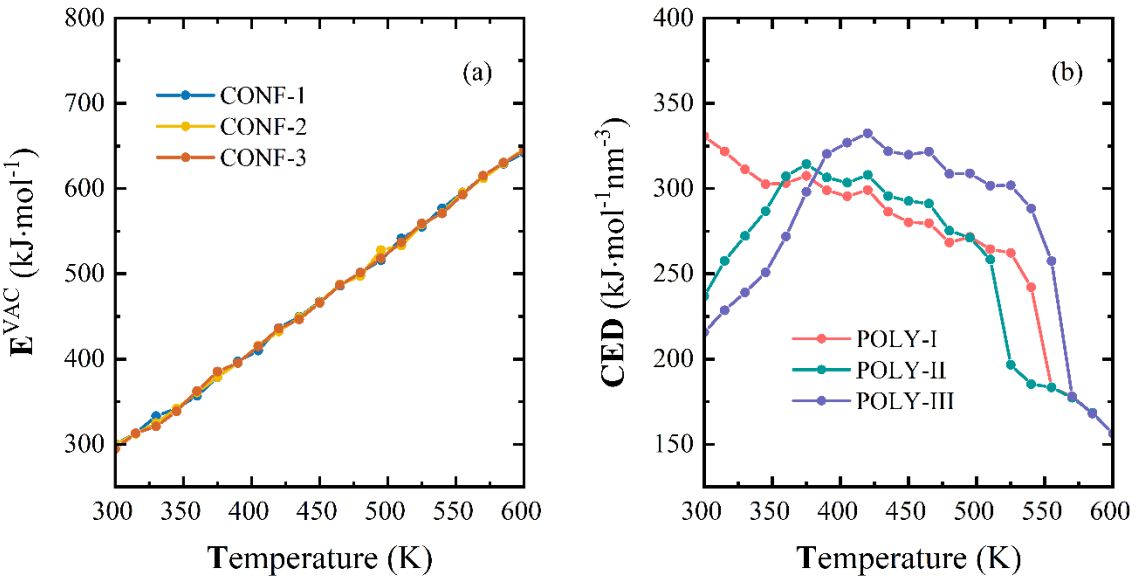

Figure 3.17. (a) Dependence of the energy of a single CUR molecule in vacuum on the temperature, starting from each of the considered conformations. (b) Dependence of the Cohesive Energy Density on the temperature, calculated according to Eq. 3.1.

The dependence of the CED on the temperature is given in Fig. 3.17 (b). Larger CED values indicate tighter binding, and, as consequence, higher stability. One can note that, at room temperature, before about 400 K, POLY-I is the most stable form, with highest CED. This is consistent with the general uniquity of that exact form. But even more interestingly, POLY-II, which is hardest to obtain, appears to be "hidden" – above 400 K and below the melting point, its CED is always strictly less than that of POLY-III. This might correlate with experimental observations suggesting preferential occurrence of POLY-III over POLY-II in various conditions.

3.5. Dynamics of Bulk Curcumin

3.5.1. Diffusivity

Beside structural and energetic information, MD simulations allow one to understand the short-time dynamics of the systems – dynamics that would be difficult to probe experimentally. First dynamics-related property that we discuss is the self-diffusion coefficient, whose temperature-dependent behavior is shown in Fig. 3.18. It is immediately obvious that below 500 K, all simulations are in crystalline state – the corresponding diffusion coefficients are vanishingly small. Diffusion picks up sharply near the melting point. The most gradual change is seen for POLY-II, most likely reflecting conformational changes, as the diffusion coefficient calculation in GROMACS is based on atomic, not molecular, movement. In the melt state, diffusion coefficient is about $0.8 \cdot 10^{-5}$ cm^2/s, some $2.5 \cdot 10^{-5}$ cm^2/s lower than that of water at room temperature. This means that the dynamics in the melt are restricted, but clearly allow enough mobility for spatial and orientational changes.

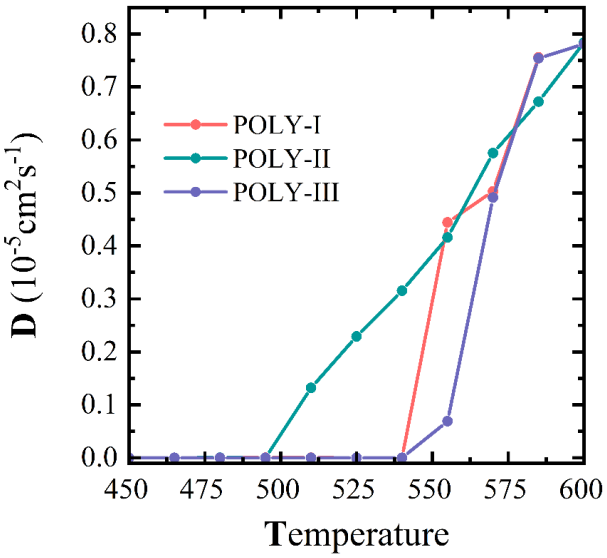

Figure 3.18. Dependence of the atomic self-diffusion coefficient on the temperature, starting from each of the CUR polymorphs considered in this work.

3.6. Conclusions

In this chapter, we have tested several CUR force field models on their ability to reproduce melting point and conformational properties. After slight modifications, using data from QC calculations, the model is well-correlated with experimental results. We have shown how the conformations of CUR molecules in each polymorph change as the temperature goes close to and beyond the melting one. We have also shown that CUR polymorphs significantly differ in their ability to form hydrogen bonds (with POLY-I having significantly more hydrogen bonds) and their stability (with POLY-II being less stable than the other two in the entire temperature range). Additionally, we demonstrate that the melt state of CUR allows enough molecular mobility to relax to equilibrium conformational, radial and orientational structures.

3.7. Bibliography

(1) Abraham, M. J.; Murtola, T.; Schulz, R.; Páll, S.; Smith, J. C.; Hess, B.; Lindahl, E. GROMACS: High Performance Molecular Simulations through Multi-Level Parallelism from Laptops to Supercomputers. *SoftwareX* **2015**, *1–2*, 19–25. https://doi.org/10.1016/j.softx.2015.06.001.

(2) Bussi, G.; Donadio, D.; Parrinello, M. Canonical Sampling through Velocity Rescaling. *J. Chem. Phys.* **2007**, *126* (1), 014101. https://doi.org/10.1063/1.2408420.

(3) Bussi, G.; Zykova-Timan, T.; Parrinello, M. Isothermal-Isobaric Molecular Dynamics Using Stochastic Velocity Rescaling. *J. Chem. Phys.* **2009**, *130* (7), 074101. https://doi.org/10.1063/1.3073889.

(4) Berendsen, H. J. C.; Postma, J. P. M.; van Gunsteren, W. F.; DiNola, A.; Haak, J. R. Molecular Dynamics with Coupling to an External Bath. *J. Chem. Phys.* **1984**, *81* (8), 3684–3690. https://doi.org/10.1063/1.448118.

(5) Groom, C. R.; Bruno, I. J.; Lightfoot, M. P.; Ward, S. C. The Cambridge Structural Database. *Acta Crystallogr. Sect. B Struct. Sci. Cryst. Eng. Mater.* **2016**, *72* (Pt 2), 171–179. https://doi.org/10.1107/S2052520616003954.

(6) Sanphui, P.; Goud, N. R.; Khandavilli, U. B. R.; Bhanoth, S.; Nangia, A. New Polymorphs of Curcumin. *Chem. Commun.* **2011**, *47* (17), 5013–5015. https://doi.org/10.1039/C1CC10204D.

(7) Jorgensen, W. L.; Tirado-Rives, J. Potential Energy Functions for Atomic-Level Simulations of Water and Organic and Biomolecular Systems. *Proc. Natl. Acad. Sci.* **2005**, *102* (19), 6665–6670. https://doi.org/10.1073/pnas.0408037102.

(8) Dodda, L. S.; Cabeza de Vaca, I.; Tirado-Rives, J.; Jorgensen, W. L. LigParGen Web Server: An Automatic OPLS-AA Parameter Generator for Organic Ligands. *Nucleic Acids Res.* **2017**, *45* (W1), W331–W336. https://doi.org/10.1093/nar/gkx312.

(9) Wang, J.; Wolf, R. M.; Caldwell, J. W.; Kollman, P. A.; Case, D. A. Development and Testing of a General Amber Force Field. *J. Comput. Chem.* **2004**, *25* (9), 1157–1174. https://doi.org/10.1002/jcc.20035.

(10) Sousa da Silva, A. W.; Vranken, W. F. ACPYPE - AnteChamber PYthon Parser interfacE. *BMC Res. Notes* **2012**, *5* (1), 367. https://doi.org/10.1186/1756-0500-5-367.

(11) Schmid, N.; Eichenberger, A. P.; Choutko, A.; Riniker, S.; Winger, M.; Mark, A. E.; van Gunsteren, W. F. Definition and Testing of the GROMOS Force-Field Versions 54A7 and 54B7. *Eur. Biophys. J. EBJ* **2011**, *40* (7), 843–856. https://doi.org/10.1007/s00249-011-0700-9.

(12) Malde, A. K.; Zuo, L.; Breeze, M.; Stroet, M.; Poger, D.; Nair, P. C.; Oostenbrink, C.; Mark, A. E. An Automated Force Field Topology Builder (ATB) and Repository: Version 1.0. *J. Chem. Theory Comput.* **2011**, *7* (12), 4026–4037. https://doi.org/10.1021/ct200196m.

(13) Vanommeslaeghe, K.; Hatcher, E.; Acharya, C.; Kundu, S.; Zhong, S.; Shim, J.; Darian, E.; Guvench, O.; Lopes, P.; Vorobyov, I.; MacKerell, A. D. CHARMM General Force Field (CGenFF): A Force Field for Drug-like Molecules Compatible with the CHARMM All-Atom Additive Biological Force Fields. *J. Comput. Chem.* **2010**, *31* (4), 671–690. https://doi.org/10.1002/jcc.21367.

(14) Neese, F.; Wennmohs, F.; Becker, U.; Riplinger, C. The ORCA Quantum Chemistry Program Package. *J. Chem. Phys.* **2020**, *152* (22), 224108. https://doi.org/10.1063/5.0004608.

(15) Grimme, S.; Hansen, A.; Ehlert, S.; Mewes, J.-M. r2SCAN-3c: A "Swiss Army Knife" Composite Electronic-Structure Method. *J. Chem. Phys.* **2021**, *154* (6), 064103. https://doi.org/10.1063/5.0040021.

(16) Grimme, S.; Brandenburg, J. G.; Bannwarth, C.; Hansen, A. Consistent Structures and Interactions by Density Functional Theory with Small Atomic Orbital Basis Sets. *J. Chem. Phys.* **2015**, *143* (5), 054107. https://doi.org/10.1063/1.4927476.

(17) Brehm, M.; Kirchner, B. TRAVIS - A Free Analyzer and Visualizer for Monte Carlo and Molecular Dynamics Trajectories. *J. Chem. Inf. Model.* **2011**, *51* (8), 2007–2023. https://doi.org/10.1021/ci200217w.

(18) Tønnesen, H. H.; Karlsen, J.; Mostad, A.; Samuelsson, B.; Enzell, C. R.; Berg, J.-E. Structural Studies of Curcuminoids. I. The Crystal Structure of Curcumin. *Acta Chem. Scand.* **1982**, *36b*, 475–479. https://doi.org/10.3891/acta.chem.scand.36b-0475.

(19) Pandey, K. U.; Dalvi, S. V. Understanding Stability Relationships among Three Curcumin Polymorphs. *Adv. Powder Technol.* **2019**, *30* (2), 266–276. https://doi.org/10.1016/j.apt.2018.11.002.

(20) Bristow, G. M.; Watson, W. F. Cohesive Energy Densities of Polymers. Part 1. Cohesive Energy Densities of Rubbers by Swelling Measurements. *Trans. Faraday Soc.* **1958**, *54* (0), 1731–1741. https://doi.org/10.1039/TF9585401731.

CHAPTER 4
VACUUM INTERFACE

In this chapter, we explore structural and dynamic behavior of curcumin (CUR) at vacuum interfaces for its three known polymorphs: POLY-I, POLY-II, and POLY-III. Special emphasis is placed on identifying interfacial molecules and analyzing their orientational and conformational properties relative to the interface normal. Through detailed molecular dynamics simulations, we compare how different crystallographic planes ([100], [010], and [001]) influence interfacial structure, packing, and thermal response.

Our analysis integrates multiple descriptors – local density, orientation distributions, conformational states, hydrogen bonding, surface tension, and mobility metrics – to build a comprehensive picture of how interfacial behavior diverges from the bulk.

4.1. Computational Methods

Molecular dynamics simulations were performed using the GROMACS 2024.4[1] program package. Simulations within the NVT ensemble were performed with the use of Parinello-Bussi[2,3] thermostat with relaxation time of 0.2 ps. Simulation boxes contained 480 fully flexible curcumin molecules. Each starting point corresponds to the crystal of a specific polymorph, with data[4,5] taken from CCDC. Chosen configurations are summarized in Table 3.1 in Ch. 3. The boxes were padded by 3 times the initial volume along one of the simulation box axes. Minimization was performed with GROMACS using conjugate gradient (CG) method with a 0.001 nm step size and as many steps as needed until convergence. For Lennard-Jones, we have used a cut-off scheme with potential-shifting and rc = 10.0 Å. For electrostatic interactions, a reaction-field potential with the same cutoff as Lennard-Jones was chosen instead of PME in order to minimize unwanted interactions in the interfacial slab simulations.

The temperature was consistently varied from 300 K to 600 K with a step of 15 K. Equations of motion were integrated in time steps of 1 fs. After at least 10 ns long equilibration period, statistical data (such as temperatures, pressures, nearest neighbor distances, local densities, etc.) was collected using 3000 equilibrium sample configurations, separated from each other by 2 ps long trajectories each, from the 6 ns. long production run at every temperature.

Nearest neighbor calculations were done up to the 30th nearest neighbor to a reference molecule, using all configurations along the generated equilibrium trajectories. Interaction energies were calculated for every frame.

To investigate the effect of increasing temperature on the structure and dynamic of molecules belonging to the vacuum interface of CUR, we use statistical observables that include mass density profile, orientation to the interface normal, nearest neighbor radial distribution functions and local density as determined from Voronoi polyhedra analysis. To quantify the change in the shape of these distributions as a function of temperature, we used quantities that are based on their moments (average values, fluctuation). The conformation distribution of interfacial CUR molecules is assigned based on comparison with unique structures extracted from crystalline data. Details of the chosen algorithm are described in Ch. 2. During the analysis of interfacial calculations, layer decomposition of the crystal was performed via the ITIM[6] method using the PYTIM[7] package (see Ch. 2 for details). Probe-sphere grid spacing was set to 0.4 Å and probe radius to 1.7 Å. Vapor-phase molecules, if present, were cut using the

DBSCAN algorithm (see Ch. 2). In our analysis we will refer to the crystalline and melt phase of CUR that are associated with low and high temperature, respectively. The temperature at which the transition between the two phases is defined by the large increase/decrease of the average values of the statistical observables defined previously.

4.2. Structure of the Interface

4.2.1. Density Profiles

In order to characterize the density distribution of CUR at the vacuum interface of each polymorph, first, one needs to determine which molecules lie at the interface. Although more traditional definitions, such as Gibbs dividing surface, have their merits, we chose to utilize ITIM method.[6] Fig. 4.1 (a) illustrates the ability of this algorithm to identify CUR molecules at the first three layers of POLY-I along the [100] at 350 K. We then calculated the mass-density profile at the interface and also the mass density profile associated with each layer. As an illustration we show them in Fig. 4.1 (b) at 600 K where CUR is in the melt state. It is readily noticeable that, although the mass density profiles for individual layers overlap, they have a well-defined Gaussian shape. However, their shape in the crystalline phase at lower temperature can become multimodal with contribution at two different distances. In those cases, we consider each peak separately and calculate the average values of the distribution with the largest distance value.

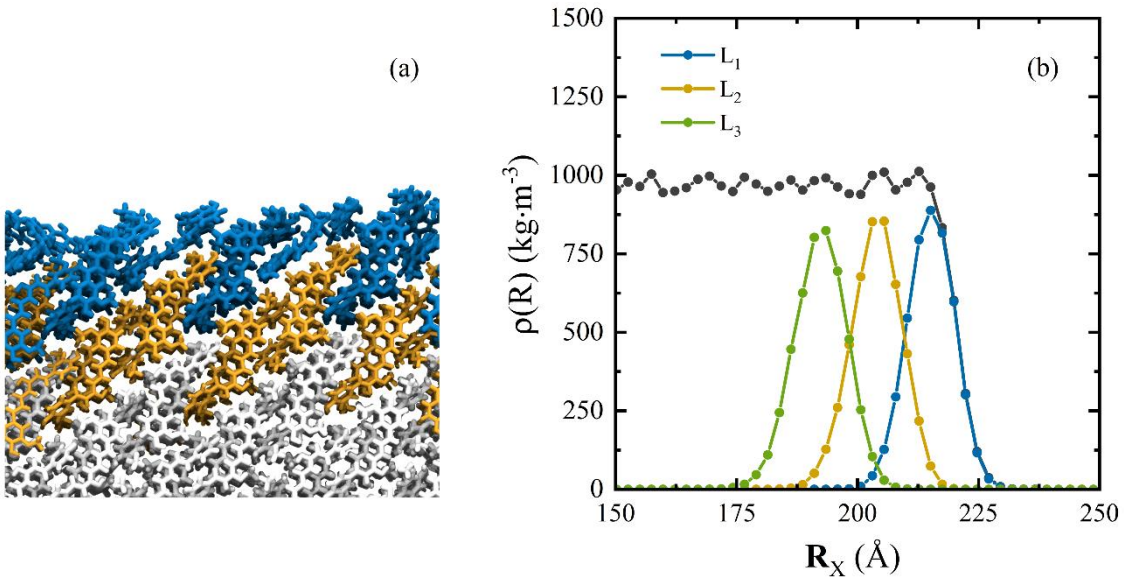

Figure 4.1. Visualization of the first (blue), second (yellow) and third (white) layers of curcumin in POLY-I discovered via ITIM method for T = 350 K. (b) Total mass-density profile along the [100] (black) along with mass-density profiles for each individual layer (colored) for T = 600 K for POLY-I. The center of mass of CUR molecules was used to calculate these distributions

The mass density profile was estimated using the coordinates of atoms belonging to the OH, methoxy, and phenyl ring moieties. This allowed us to investigate which parts of CUR prefer to lie at the interface. Because different functional groups have different masses, the values in Fig. 4.2 have been normalized to the [0,1] interval for easier comparison. In the crystalline state (Fig. 4.2 (a,b)), the mass-density profiles are quite difficult to analyze on account of their unsmooth nature. Indeed, at low temperatures, mobility, even in the interfacial layers, is not enough to sample all possible states. Nevertheless, the key takeaway idea is that in POLY-I, methoxy and hydroxyl groups of CONF-1 point away from the bulk of the crystal, toward vacuum. The same picture can be seen for other polymorphs, although their mass-density profiles are even more difficult to analyze. One particular feature, seen in Fig 4.2. (b), is that the second smaller peak of the hydroxyl and other groups corresponds to what can be called "layer 1.5" – a subset of CUR molecules in between the molecules of the main interfacial layer, but offset by slightly more than half molecular length – see Fig 4.1 (a). In contrast, in the melt state, the shape of all the mass density distributions, shown in Fig. 4.2 (c)., is mono-modal with hydroxyl moieties positioned directly at the interface. Of note is that the mass density distributions associated with the methoxy and phenyl moieties indicate that these groups are also present at the interface. The only part of the CUR molecule that is always closer to the bulk than to the interface is the central keto-enol unit. This suggests that in the melt, preferable orientation is actually almost "flat" – CUR molecular plane coinciding with the lateral plane of the interface – with only slight deviations for the -OH groups to orient themselves toward the vacuum. Reasons for this orientation are likely due to the hydrophobic nature of the CUR. This will be elaborated on in the subsequent section, specifically in the analysis of pair-interaction energies.

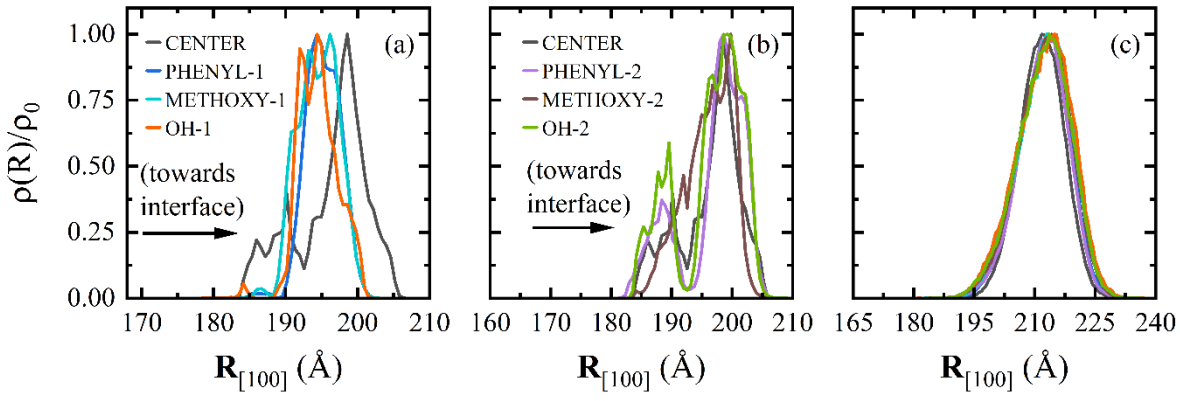

Figure 4.2. Normalized mass-density (probability) of a functional group on the (a) one side of the CUR molecule and (b) on the other side of the CUR molecule to be in a certain position along the normal to the [100] interface of POLY-I at 300 K. (c) Normalized mass-density (probability) of a functional group of the CUR molecule to be in a certain position along the normal to the [100] interface of POLY-I at 600 K.

To compare variations in the average positions of the layers across different systems and temperatures on a consistent scale, we define a thermal expansion parameter relative to the reference temperature of 300 K – the lowest temperature used in our simulations. For each crystallographic plane [lmn], we compute the difference: $\delta R_{[lmn]} = \langle R_{[lmn]}(T)\rangle - \langle R_{[lmn]}(T = 300\ K)\rangle$ This quantity captures the relative shift in the average position of each layer as a function of temperature and serves as a measure of thermal expansion along the [lmn] direction. The temperature dependence of $\delta R_{[lmn]}$ for all three polymorphs across the [100], [010], and [001] crystallographic planes is shown in Fig. 4.3 (a).

As expected, at low temperatures, thermal expansion of the interfacial layers is vanishingly small. At higher temperatures, in several cases, such as for POLY-I at the [100] and [001] planes, POLY-II at [100], and POLY-III at [001], we observe pronounced increase in $\delta R_{[lmn]}$, beginning at temperatures lower than the bulk melting temperatures identified in Ch. 3. In these cases, the onset of interfacial layer expansion precedes global breakdown of the long-distance crystalline order.

A particularly noteworthy trend is found in POLY-I at [100], where the 1st layer exhibits the highest thermal expansion. In other systems, like for POLY-II at [100], the 2nd layer has higher expansion. The difference is likely due to the orientation of CUR molecules at those distinct interfaces.

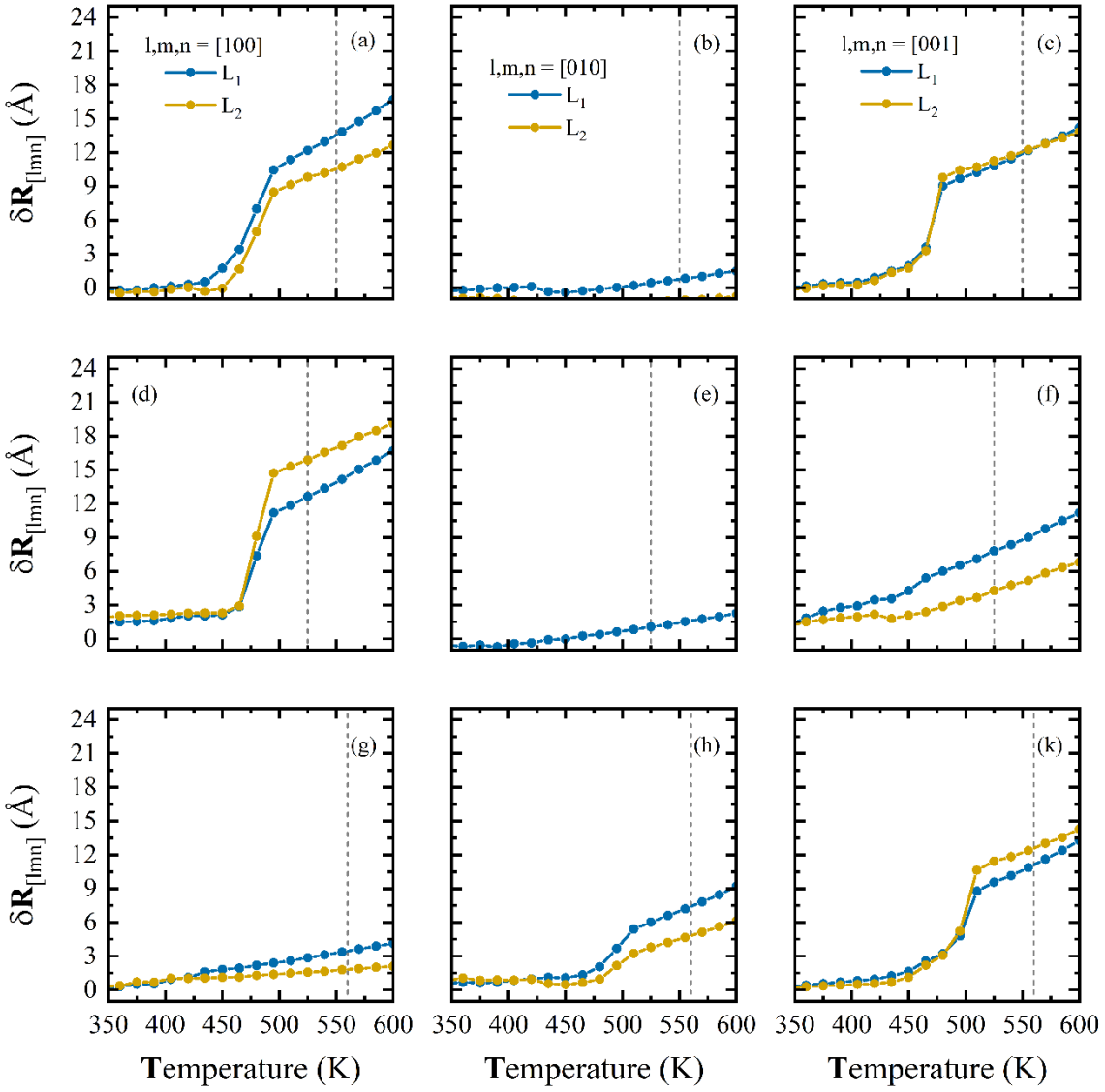

Figure 4.3. Temperature dependence of the change in the average distance value of the first two layers (difference between average of the mass-density profile at a specific temperature and that at 300 K) for (a) POLY-I [100], (b) POLY-I [010], (c) POLY-I [001], (d) POLY-II [100], (e) POLY-II [010], (f) POLY-II [001], (g) POLY-III [100], (h) POLY-III [010] and (k) POLY-III [001] interfaces.

We also calculated the fluctuation in the position of the layers. The values are depicted in Fig. 4.4.

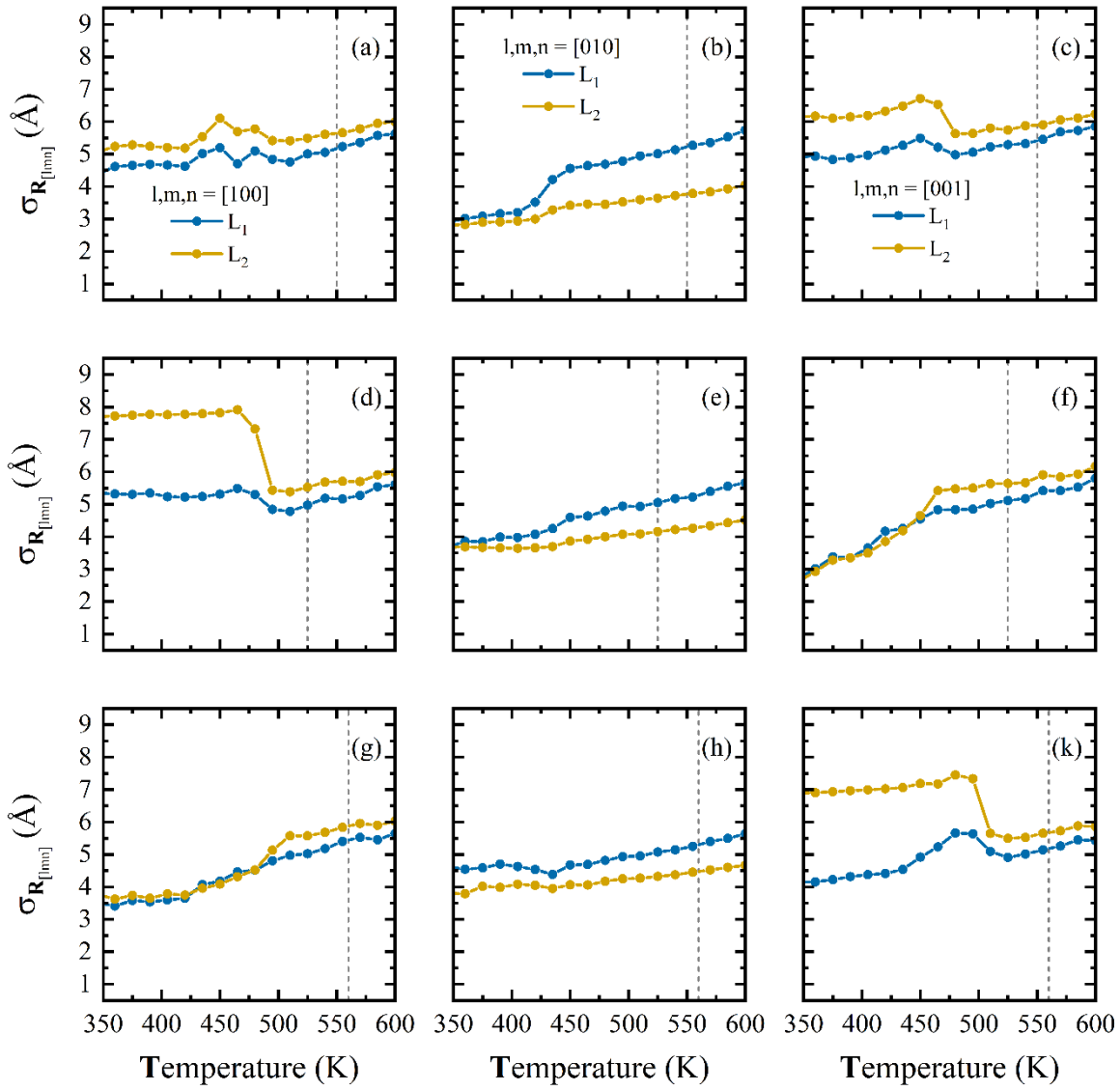

Figure 4.4. Temperature dependence of the fluctuation of the first two layers (difference between average of the mass-density profile at a specific temperature and that at 300 K) for (a) POLY-I [100], (b) POLY-I [010], (c) POLY-I [001], (d) POLY-II [100], (e) POLY-II [010], (f) POLY-II [001], (g) POLY-III [100], (h) POLY-III [010] and (k) POLY-III [001] interfaces.

The cases in which the fluctuations, $\sigma_{R_{[nlm]}}$, in the positions of the layers exhibit a pronounced maximum – varying in magnitude depending on the crystallographic plane and polymorph – coincide with sharp increases in the average interlayer distances. This behavior reflects a growing inhomogeneity in the spatial distribution of the layers. Conversely, when the changes in average layer positions occur more gradually – whether increasing or decreasing – the associated fluctuations also vary smoothly, indicating a more uniform structural response to temperature.

Furthermore, these fluctuations offer important insight into the local structural stability and can be directly linked to the curvature of the underlying free energy surface. Indeed, larger fluctuations, $\sigma_{R_{[nlm]}}$, correspond to shallower free energy minima, indicating increased flexibility and reduced structural order. Conversely, smaller fluctuations are associated with more rigid, energetically stable interfaces. By comparing the fluctuation values with the average layer displacements, $\delta R_{[lmn]}$, we observe that in layers exhibiting sharp increases in $\delta R_{[lmn]}$ with temperature, such as the first layer of POLY-I at the [100] plane or the third layer of POLY-III at [001], the corresponding $\sigma_{R_{[nlm]}}$values also go through a maximum. This suggests that these layers are experiencing a softening of the free energy landscape, i.e., the system becomes more thermally responsive and structurally labile prior to interfacial breakdown or melting.

In contrast, for polymorph-plane combinations where the $\delta R_{[lmn]}$ curve shows only gradual changes, the associated $\sigma_{R_{[nlm]}}$ also varies smoothly. This behavior reflects a more stable and stiff free energy well, consistent with strong cohesive interactions and limited molecular rearrangement.

This fluctuation-based analysis provides a thermodynamic rationale for the layer-resolved behavior seen across different planes and polymorphs. It also reinforces the notion that the onset of interfacial disorder is not always signaled by abrupt changes in average properties, but may be preceded by increasing positional fluctuations – a signature of the system approaching a critical structural transition.

4.2.2. Orientation

We want to address in this part the orientation of the interfacial CUR molecules. For this purpose, we choose, among all the possible options, the vector between centers of the two phenyl rings of CUR with respect to the vectors normal to the chosen interface. The orientation distributions are summarized in Fig. 4.5.

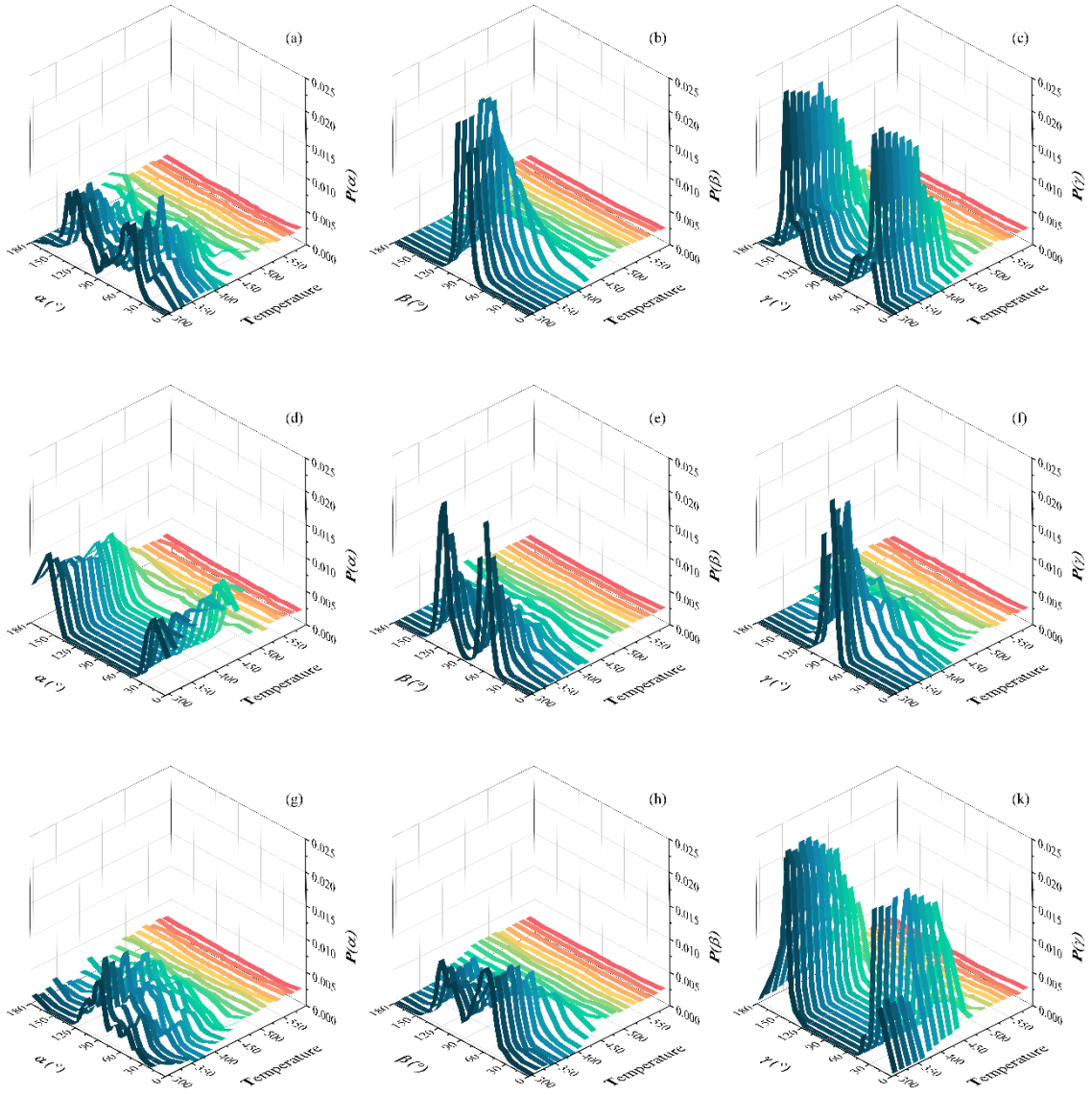

Figure 4.5. Dependence of the probability distributions of the angle of an interfacial CUR molecule with respect to the normal vector on the temperature for (a) POLY-I [100], (b) POLY-I [010], (c) POLY-I [001], (d) POLY-II [100], (e) POLY-II [010], (f) POLY-II [001], (g) POLY-III [100], (h) POLY-III [010], (k) POLY-III [001]. CUR vector is defined by the center of the two phenyl rings.

The results show that in POLY-I, POLY-II and POLY-III at [010], [001] and [100], respectively, the maximum occurs at 90°, indicating that the interfacial CUR molecules have, on average, a parallel orientation with respect to the surface. While in the other cases the CUR molecules have a tilted orientation, far from being parallel to the interface. The extent of this tilted orientation depends on the polymorph types and the crystallographic plane. Indeed, CUR orientation is markedly tilted in POLY-I [001], POLY-II [100], and POLY-III [001].

The observation that molecules have a tilted orientation (distorted parallel orientation) is correlated with an increased melting temperature that can be attributed to enhanced molecular stability and stronger intermolecular interactions associated with this orientation. Indeed, first, parallel orientation (to the surface normal) tends to promote more efficient packing and reduced molecular degrees of freedom. When molecules are closely packed and well-organized, the structural rigidity increases, which raises the energy barrier required to disrupt the crystalline order. This leads to an increase in the melting temperature. Second, parallel alignment enhances specific intermolecular interactions, such as van der Waals forces and π-π stacking between aromatic rings (in the case of CUR). These interactions are stronger and more numerous when molecules are closely packed, further stabilizing the crystalline phase and increasing resistance to thermal agitation.

Third, the "caging" effect also plays a significant role. In tightly packed structures, the movement of individual molecules is restricted by neighboring molecules, requiring a higher input of thermal energy to induce disorder. This confinement effect makes it more difficult for the system to transition from an ordered to a disordered state, thus raising the melting temperature. Additionally, reduced surface area per molecule contributes to this effect. When the surface area per molecule is small due to compact packing, melting becomes even more of a cooperative process, meaning that multiple intermolecular contacts need to break simultaneously for the phase transition to occur. This increases the overall energy requirement for melting. Finally, parallel alignment helps preserve both orientational and translational order over a larger structural range. Since the loss of both types of order is necessary for melting, the system becomes more resistant to disorder, further increasing the melting point. Direct calculation of the effective surface area will be provided in subsequent sections.

Interestingly, the melting point – defined as the temperature at which the distributions become nearly uniform – does not vary significantly within a given polymorph. However, the temperature at which distortions become apparent varies depending on the choice of the interface, with differences of up to 50 K.

4.2.3. Nearest Neighbor Distribution

Besides orientation with respect to the interface normal, a significant amount of information can, usually, be gained by examining radial packing of CUR neighbors.

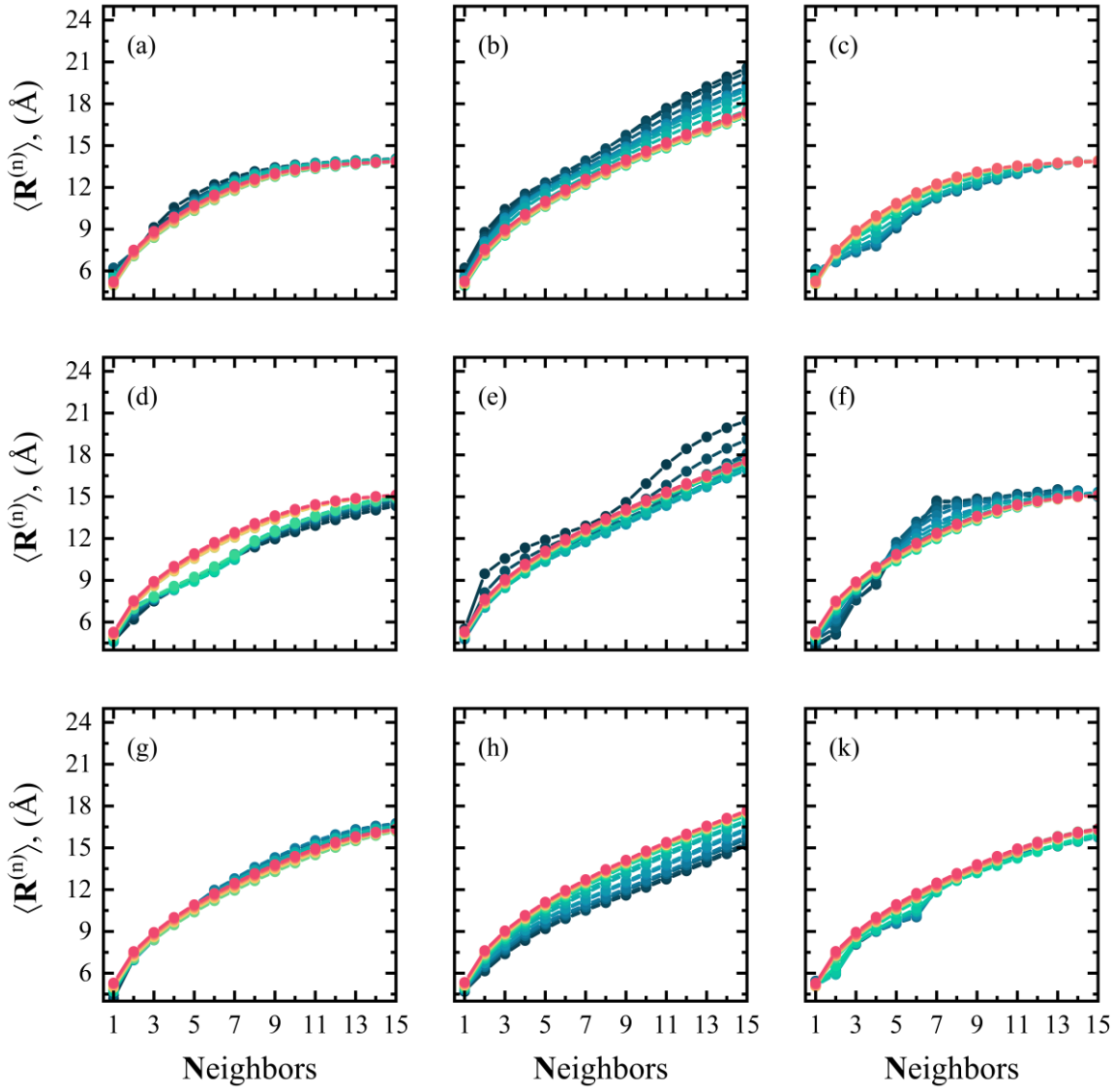

Figure 4.6. Average distance to the n^{th} nearest neighbor as a function of the rank of said neighbor for different temperatures for CUR molecules strictly within the 1^{st} layer of (a) POLY-I [100], (b) POLY-I [010], (c) POLY-I [001], (d) POLY-II [100], (e) POLY-II [010], (f) POLY-II [001], (g) POLY-III [100], (h) POLY-III [010] and (k) POLY-III [001] interfaces.

We calculated the nearest-neighbor distributions for interfacial CUR molecules across the three polymorphs and crystallographic planes. From these distributions, we derived the temperature-dependent average distances shown in Fig. 4.6.

As expected, the average distance between a reference CUR molecule and its successive neighbors increases nonlinearly with temperature. The extent and rate of this increase are strongly dependent on both the polymorph and the crystallographic orientation. Notably, the

largest increases are observed for the nearest neighbors – typically up to the fourth – while the rate of increase diminishes for more distant neighbors.

Among all systems, POLY-II at the [010] plane exhibits the most pronounced variation in average nearest-neighbor distances. Interestingly, for POLY-II at the [001] plane, temperature elevation leads to an increase in average distances for neighbors closer than the fourth, while distances to farther neighbors decrease – a non-trivial redistribution of local packing.

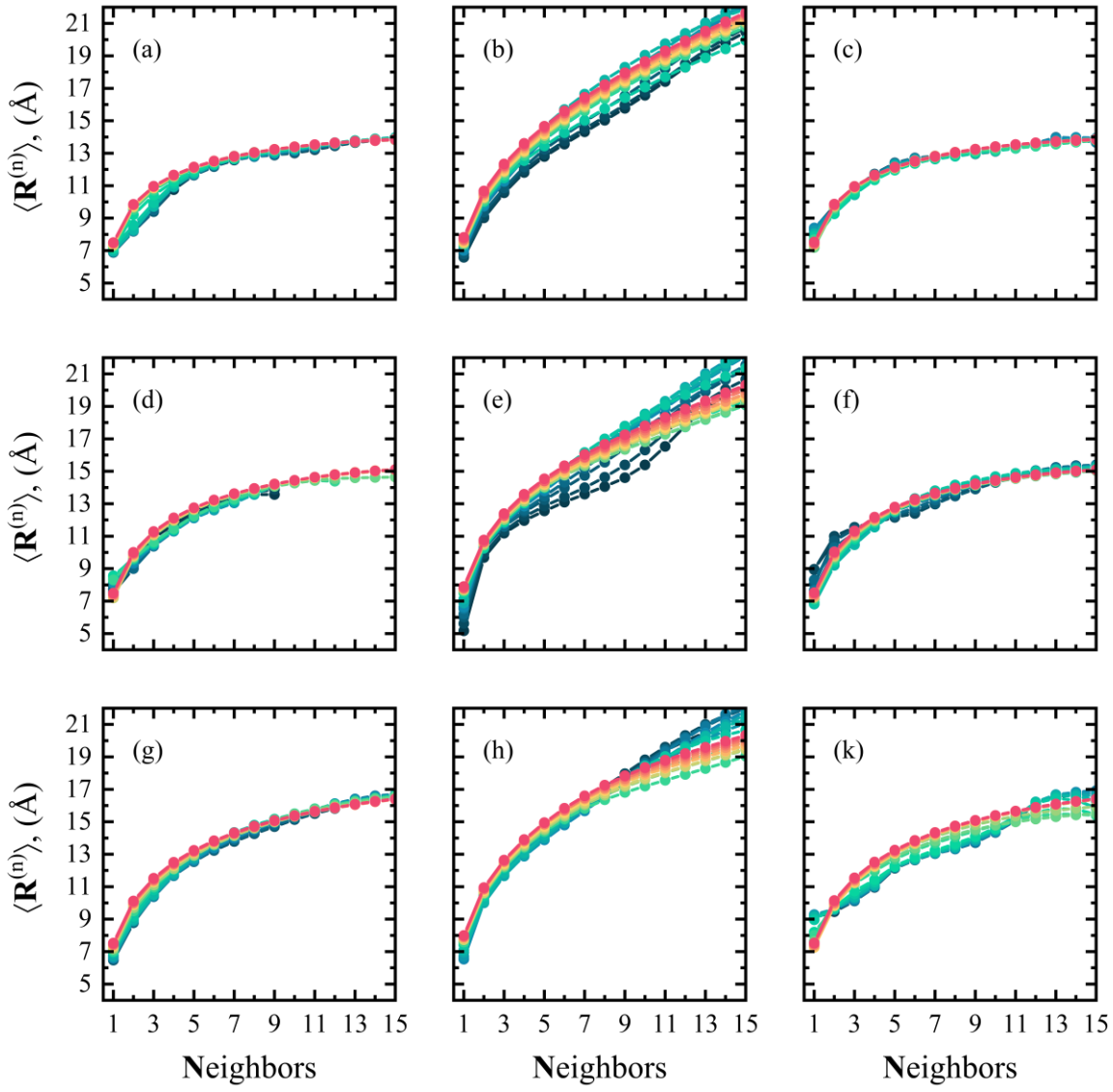

Figure 4.7. Average distance to the n^{th} nearest neighbor as a function of the rank of said neighbor for different temperatures for CUR molecules between 1^{st} and 2^{nd} layers of (a) POLY-I [100], (b) POLY-I [010], (c) POLY-I [001], (d) POLY-II [100], (e) POLY-II [010], (f) POLY-II [001], (g) POLY-III [100], (h) POLY-III [010] and (k) POLY-III [001] interfaces.

Similar behavior is observed when analyzing interlayer distances (see Fig. 4.7), specifically between a CUR molecule in the first layer and its neighbors in the second layer. For all three polymorphs at the [010] plane, we observe a decrease in average distances for neighbors between the second and fifth positions, and again for more distant neighbors beyond the tenth. In POLY-I and POLY-II along the [100] and [010] directions, temperature predominantly affects the spacing of nearest neighbors, suggesting that thermal disorder begins by disrupting local contacts before extending to longer-range packing.

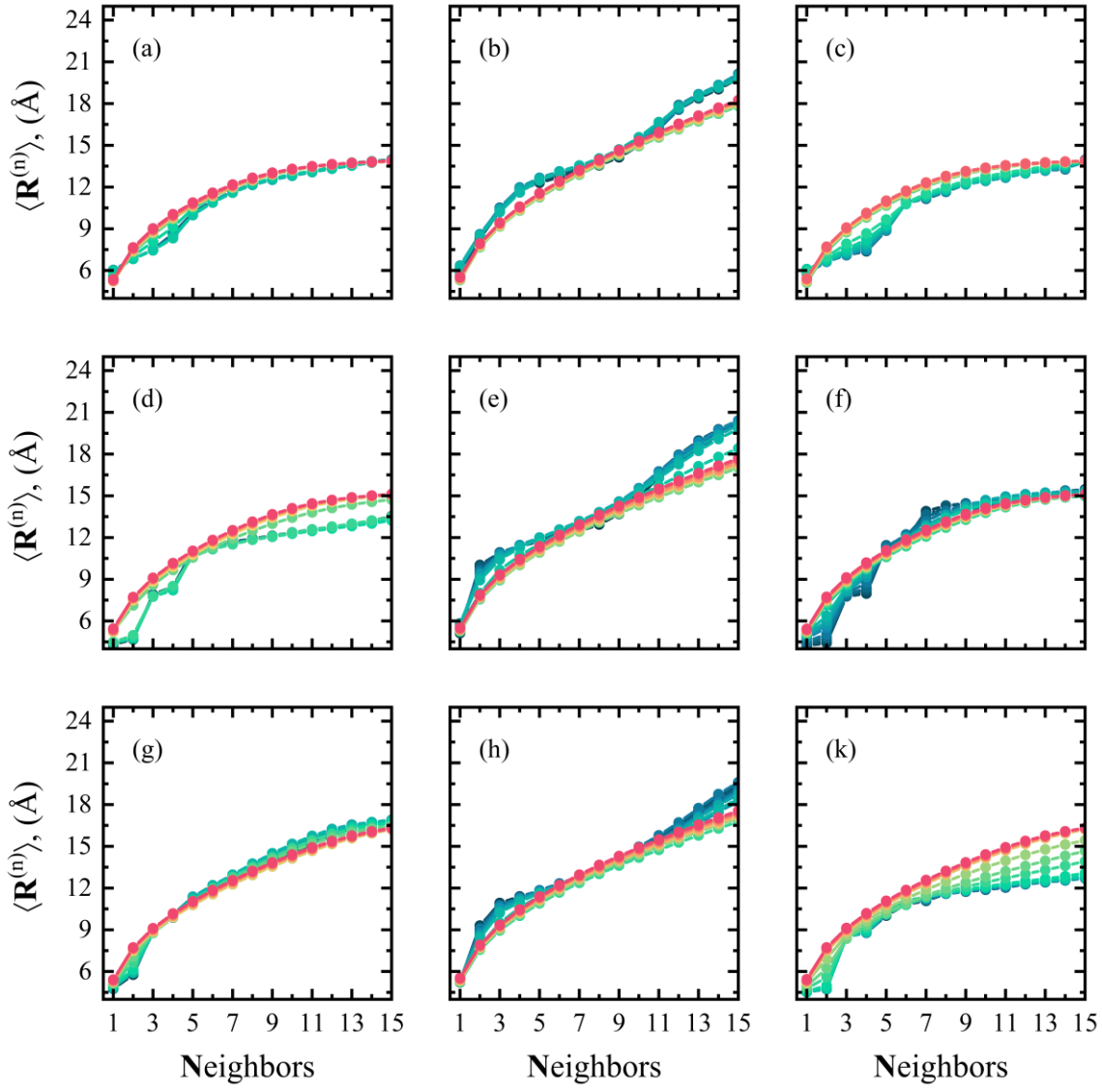

Figure 4.8. Average distance to the n^{th} nearest neighbor as a function of the rank of said neighbor for different temperatures for CUR molecules strictly within the 2^{nd} layer of (a) POLY-I [100], (b) POLY-I [010], (c) POLY-I [001], (d) POLY-II [100], (e) POLY-II [010], (f) POLY-II [001], (g) POLY-III [100], (h) POLY-III [010] and (k) POLY-III [001] interfaces.

Intralayer distances for the 2nd layer, shown in Fig. 4.8., generally follow similar trends to the interfacial distances (Fig. 4.6). Specifically, POLY-II [010] and POLY-II [001] have the same characteristic non-linear relationships. Other systems, best exemplified by POLY-III [001], show much more gradual increase of the average distance in the 2nd layers with the neighbor rank at low temperatures compared to the data for the 1st layer. This helps to highlight the extent of the shallowness of the energy landscape for interfacial layers of most of the systems considered in this study.

4.2.4. 2D Voronoi

To deepen our analysis of the local interfacial structure of CUR, we have employed the Voronoi tessellation approach, which allows us to examine the impact of temperature on the surface local surface density, $\langle \rho_{COM}^{VP} \rangle$, for CUR molecules at the vacuum interface. COM coordinates of interfacial CUR molecules identified via the ITIM algorithm were projected onto the three crystallographic planes ([100], [010], and [001]) for each polymorph. The analysis focused on the first two interfacial layers, and the results are presented in Fig. 4.9 (a-c). Our findings show that in POLY-I, the first-layer local surface density is highest along the [001] plane, while the [100] and [010] planes exhibit nearly identical values. In contrast, POLY-II displays isotropic behavior, with similar local densities across all three planes. POLY-III shows notable anisotropy, with the highest surface density along [001] and the lowest along [100].

The temperature dependence of the first-layer local density reveals that changes – either increases or decreases – tend to occur at lower temperatures, except in the case of POLY-I and POLY-III at the [100] and [001] planes, respectively, where temperature has a minimal effect. In POLY-I, POLY-II, and POLY-III, a gradual increase in surface density is observed with rising temperature at the [010], [001], and [100] planes, respectively, reaching a plateau at elevated temperatures. Conversely, a steady decrease is observed at the POLY-I [001], POLY-II [100], and POLY-III [010] planes.

When analyzing the second layer, the temperature has a more pronounced effect compared to the first layer, particularly at the [001], [100], and [001] planes in POLY-I, POLY-II, and POLY-III, respectively.

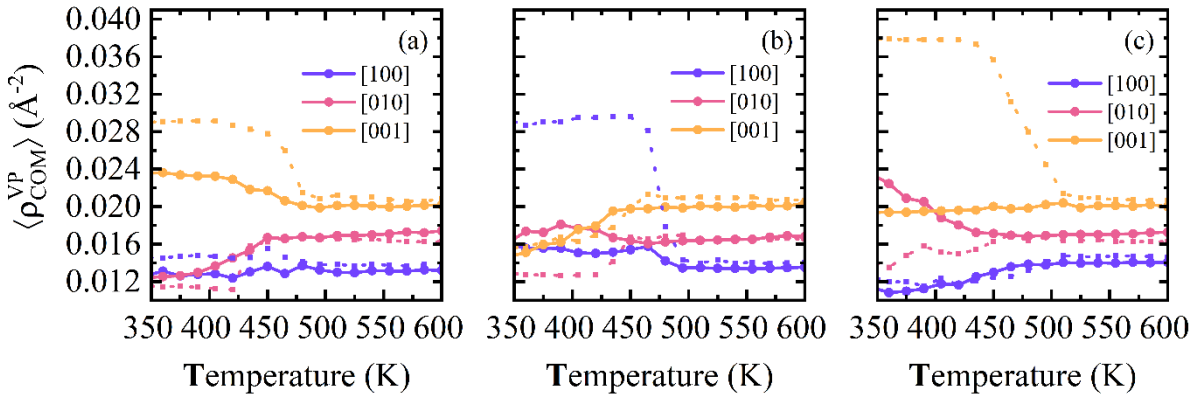

Figure 4.9. Voronoi Polygon (VP) density as a function of a temperature for 2 sequential layers (solid line - 1st, dashed line – 2nd), of (a) POLY-I, (b) POLY-II, (c) POLY-III for all crystallographic planes.

A closer examination of the crystallographic interfaces suggests that the anisotropy in local density observed for each polymorph may be linked to the specific molecular moieties exposed in each plane. Each interface presents a unique arrangement of functional groups – such as phenyl rings, methoxy groups, carbonyls, or hydroxyls – which influence how efficiently molecules can pack.

For instance, in POLY-III, the [010] plane, which exhibits the highest local density, exposes planar phenyl groups favorably aligned for π–π stacking, whereas the lower-density [100] plane may involve sterically hindered orientations or protruding methoxy groups that reduce packing efficiency. In POLY-I, the highest density along the [001] plane may be attributed to the exposure of hydrogen-bond-capable moieties that enhance cohesive interactions. POLY-II, which shows more uniform density across planes, may reflect a more balanced distribution of moieties or a less pronounced orientational anisotropy. These observations point to a strong interplay between molecular conformation, functional group orientation, and interface-specific packing behavior – all of which influence local structural stability and may play a role in direction-dependent melting or recrystallization behavior.

4.3. Conformational Distributions

We examine the conformational distributions at the interface and compare them with the bulk ones. Here, in Fig. 4.10., we highlight conformational distributions in the interfacial layers of each of the crystallographic planes of POLY-I, POLY-II and POLY-III.

It is immediately apparent that the conformational distributions of CUR molecules in the interfacial layers differ significantly from those in the bulk and are strongly dependent on the crystallographic plane of the polymorph. A systematic shift is observed in the temperature at which major changes in conformational fractions occur – consistently lower at the interface compared to the bulk. Additionally, these changes tend to occur at slightly higher temperatures in the second layer than in the first, indicating a gradual progression of structural reorganization from the surface into the bulk.

In the case of POLY-I, the temperature dependence of conformational fractions closely mirrors the bulk trend (see Fig. 3.7 (a)), but with a key distinction: the onset of conformational transitions occurs at lower temperatures in the interfacial layers. Interestingly, the behavior of conformational fractions is broadly consistent across the three crystallographic planes, with only minor differences in absolute values between the first and second layers. This pattern is particularly evident for CONF-1 in both POLY-II and POLY-III, where its fraction remains close to zero between 350 K and 450 K in both layers, followed by a gradual increase that peaks around 0.02 at higher temperatures. Notably, this increase begins at a slightly lower temperature in the first layer than in the second. At high temperatures, the fraction of CONF-1 becomes approximately equal to that of CONF-2 in both POLY-II and POLY-III.

The behavior of CONF-2 and CONF-3 in POLY-II and POLY-III diverges considerably from their bulk counterparts, revealing complex interfacial dynamics. In both polymorphs, the CONF-2 fraction exhibits a sharp decrease around $T \approx 450$ K, while the CONF-3 fraction increases significantly in parallel. These changes plateau at higher temperatures, suggesting a reorganization of conformational populations localized to a narrow temperature window. In POLY-III, the decrease in CONF-2 is more pronounced in the second layer than in the first, a trend that contradicts the bulk behavior where CONF-2 is the dominant conformation.

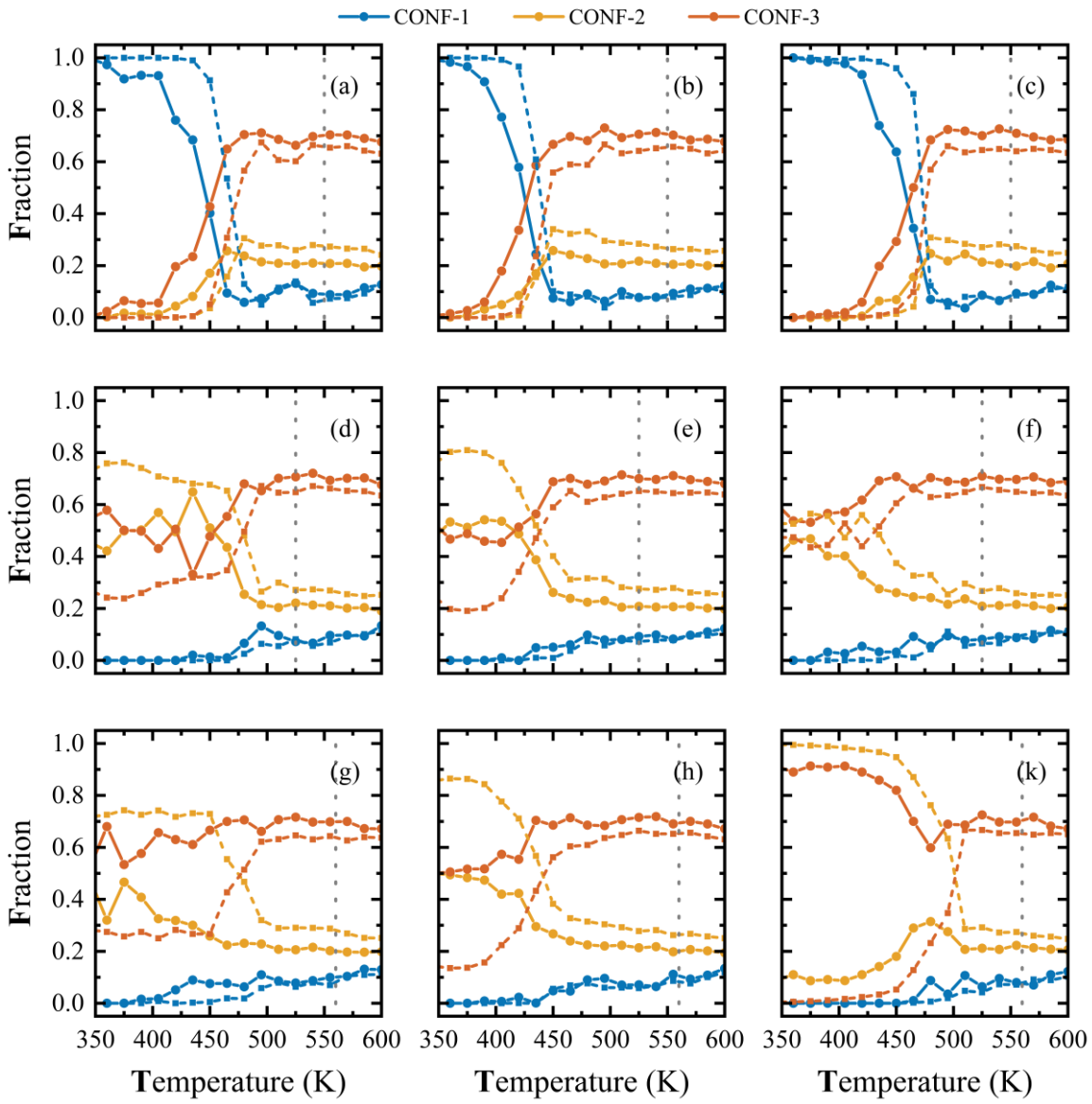

Figure 4.10. Dependence of the fraction of the first conformation of curcumin in the 1st (solid lines) and 2nd (dashed lines) layers on the temperature during melting of (a) POLY-I [100], (b) POLY-I [010], (c) POLY-I [001], (d) POLY-II [100], (e) POLY-II [010], (f) POLY-II [001], (g) POLY-III [100], (h) POLY-III [010] and (k) POLY-III [001] systems from 300 K to 600 K with a step of 15 K at an atmospheric pressure, using the modified OPLS-AA model. Vertical line indicates model bulk melting point.

The evolution of CONF-3 fraction further highlights the complex interfacial behavior. In POLY-II, the CONF-3 fraction in both layers shows only modest temperature dependence, remaining relatively stable. In contrast, POLY-III exhibits more nuanced behavior. In the [100] and [010] planes, CONF-3 fractions in the first layer remain largely unchanged with increasing temperature, while those in the second layer display a noticeable rise at T ≈ 450 K, followed by stabilization. A particularly striking case is observed in the [001] plane of POLY-III: here, the

CONF-3 fraction in the first layer is already high (~0.9) in the crystalline phase and decreases significantly at T ≈ 450 K. Meanwhile, the second layer begins with a CONF-3 fraction of zero, which rapidly increases to match the first layer's value around the same temperature. This inversion of conformational population between layers underscores the sensitivity of interfacial structure to both temperature and molecular orientation, and further illustrates how surface-driven disorder can propagate into subsurface regions during the melting process.

4.4. Interactions at the interface

4.4.1. Hydrogen Bonding

We can directly analyze the number of hydrogen bonds within and between each layer at different interfaces of different polymorphs. The algorithm and the hyper parameter values are exactly the ones used in similar analysis in Ch. 3. We summarize in Fig. 4.11 the temperature behavior of the hydrogen bond number between CUR molecules at the interface of the three polymorphs.

Fig. 4.11 (a,b) reveals that interfacial CUR molecules exhibit distinct hydrogen-bonding patterns compared to those in the bulk. This interfacial average $\langle N_{HB}^{L_{i=1,2}} \rangle$ is lower than that in the bulk.

The values of $\langle N_{HB} \rangle$ are small, indicating that the hydrogen bond interactions are in general weak between interfacial CUR molecules, with the exception of POLY-III at [001], where this number is relatively higher than at the other planes. At high temperature, the values of $\langle N_{HB} \rangle$ converge almost to the same value independently of the nature of the interface and the crystallographic planes. A maximum seen for some systems at low temperatures is shallower in the interface compared to bulk. In general, at low temperature, the values of $\langle N_{HB} \rangle$ are almost the same between CUR belonging to the same layer and that between the two first layers. Two exceptions to this behavior are observed in POLY-II and POLY-III at [100] plane, where these values are the lowest/highest, respectively

A large contrast in the temperature dependence (in particular at lower range) concerns the behavior of $\langle N_{HB} \rangle$ in POLY-II, within the layers and between the layers. It is the highest between the layer and the lowest with the first layer. In this case a large decrease in the values of $\langle N_{HB} \rangle$ is observed for CUR molecules within the second layer and for those between the two layers.

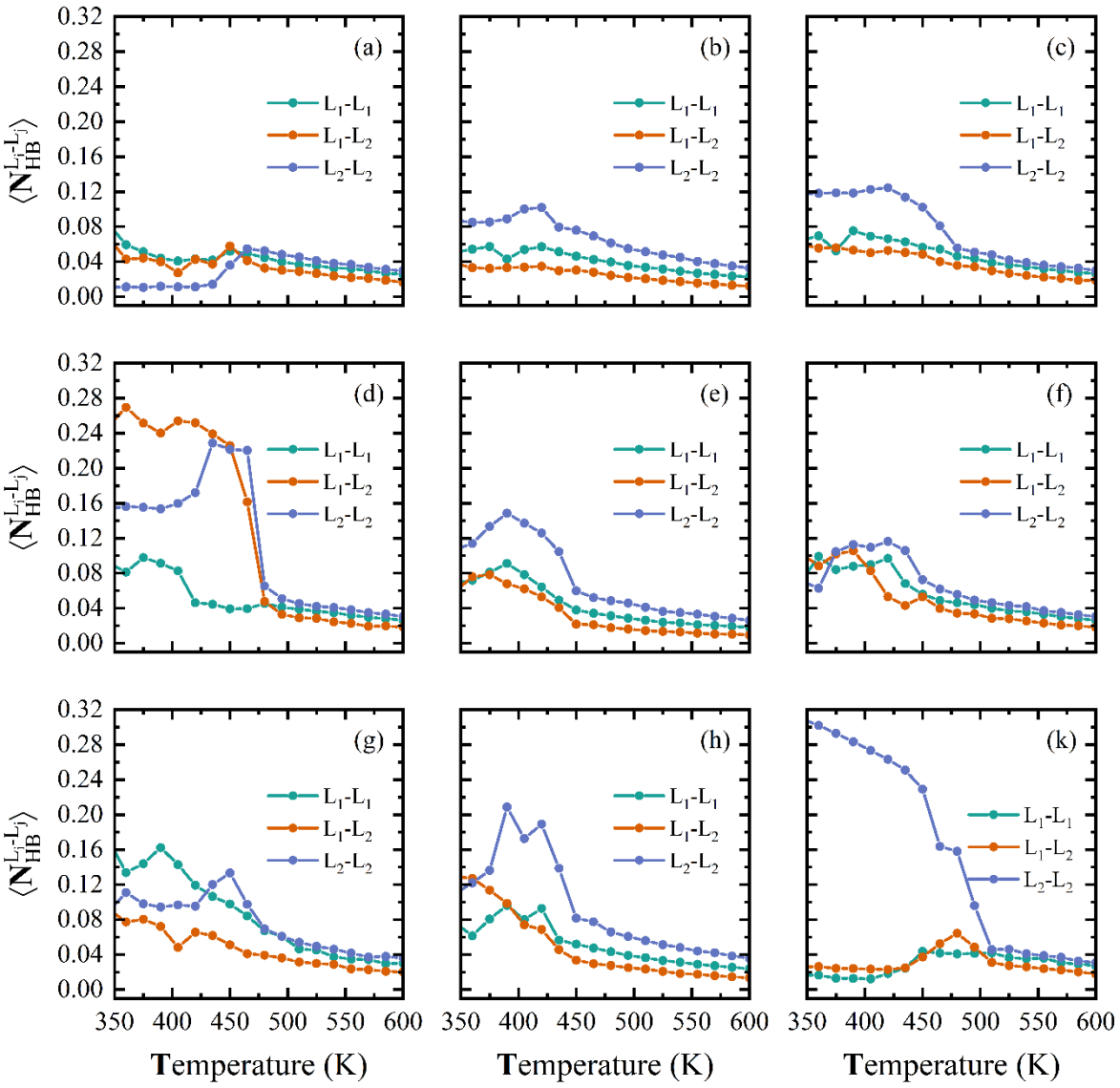

Figure 4.11. Temperature dependence of the average number of hydrogen bonds for CUR molecules in the specified layers of (a) POLY-I [100], (b) POLY-I [010], (c) POLY-I [001], (d) POLY-II [100], (e) POLY-II [010], (f) POLY-II [001], (g) POLY-III [100], (h) POLY-III [010] and (k) POLY-III [001] interfaces.

The values of $\langle N_{HB} \rangle$ in the second layer systematically go through a maximum in all the polymorphs and at all the crystallographic planes. This maximum is well defined in the case of POLY-II and POLY-III for [010] plane and it is the less defined in POLY-I for [100] plane.

4.4.2. Pair Interaction Energies

To better understand how the breakdown of interfacial layer occurs, we have examined the pair interaction energies between CUR molecules within the first two layers and compared them with the interaction energy between said layers. As such, Fig. 4.12 and Fig. 4.13 compare 1st nearest neighbor ES and LJ interaction energies within 1st and 2nd layers and also between them for the three CUR polymorphs at the three planes.

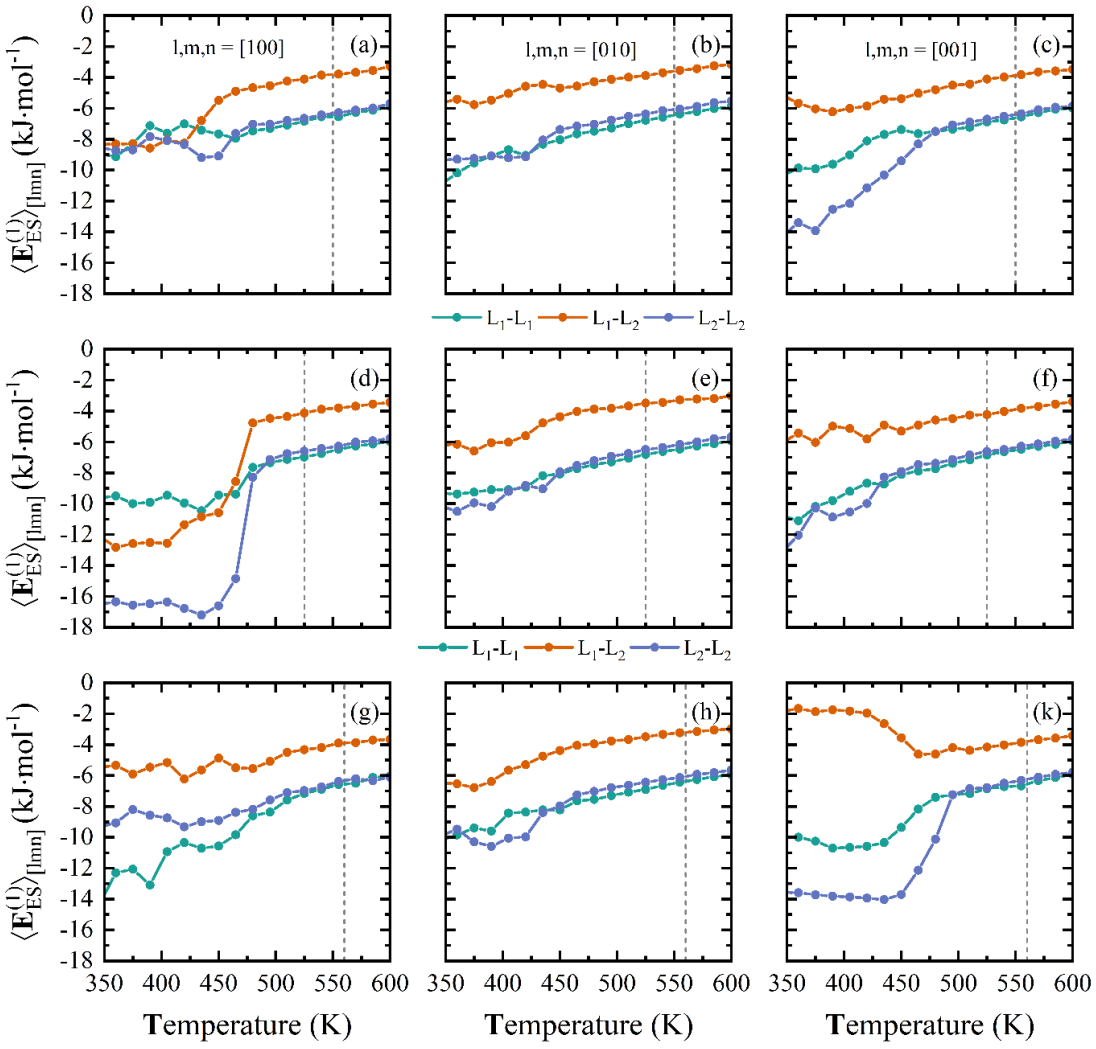

Figure 4.12. Temperature dependence of ES pair-interaction energies between a reference molecule and it first neighbor within and between the first two layers along the [100] face during melting of (a) POLY-I [100], (b) POLY-I [010], (c) POLY-I [001], (d) POLY-II [100], (e) POLY-II [010], (f) POLY-II [001], (g) POLY-III [100], (h) POLY-III [010] and (k) POLY-III [001], from 350 K to 600 K with a step of 15 K at an atmospheric pressure, using the new OPLS-AA model. Vertical dashed line indicates model bulk melting point.

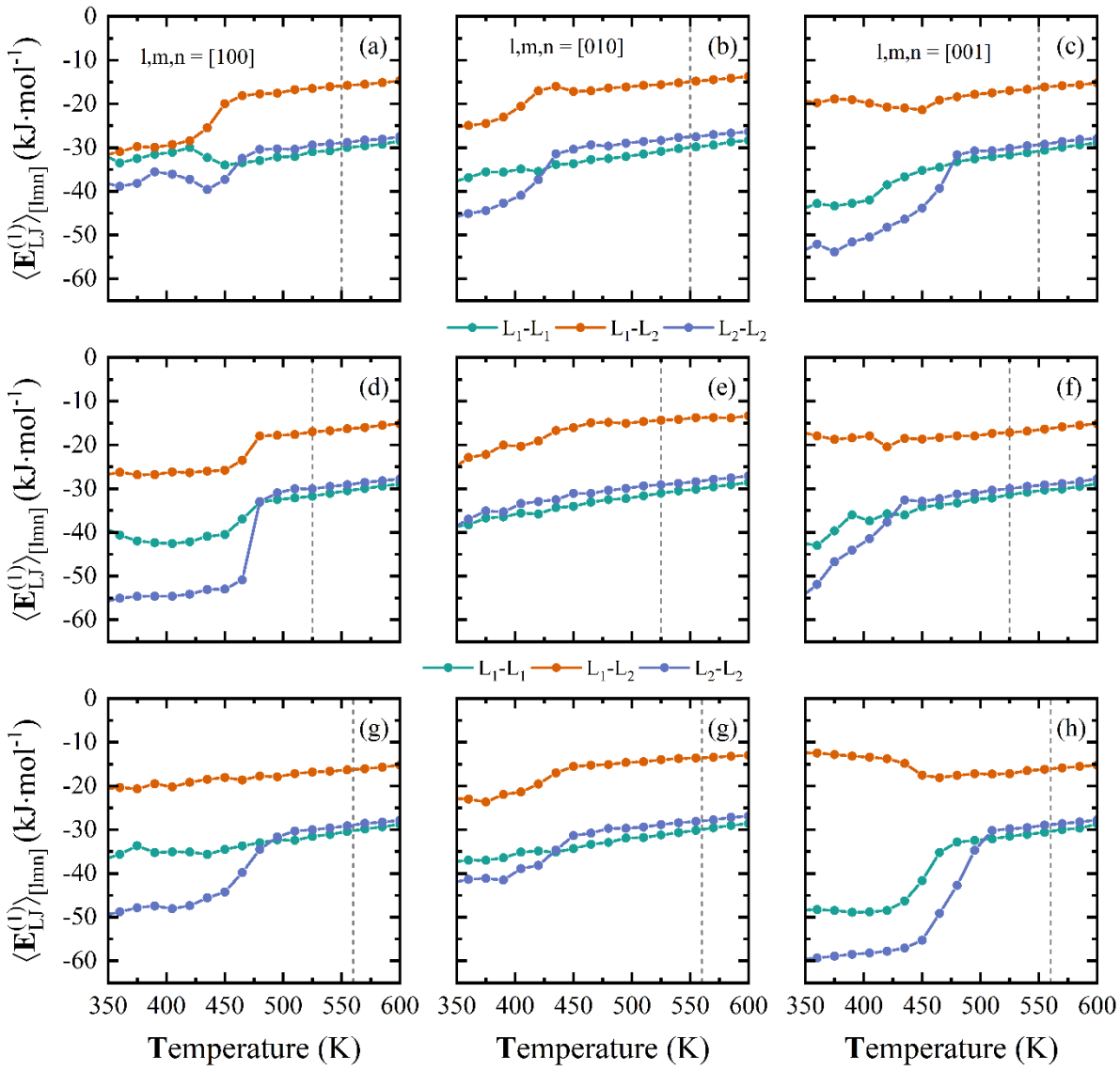

Figure 4.13. Temperature dependence of LJ pair-interaction contribution to the interaction energies between a reference molecule and it first neighbor within and between the first two layers along the [100] face during melting of (a) POLY-I [100], (b) POLY-I [010], (c) POLY-I [001], (d) POLY-II [100], (e) POLY-II [010], (f) POLY-II [001], (g) POLY-III [100], (h) POLY-III [010] and (k) POLY-III [001], from 350 K to 600 K with a step of 15 K at an atmospheric pressure, using the new OPLS-AA model. Vertical dashed line indicates model bulk melting point.

In the crystalline state of CUR, it is observed that, regardless of the polymorph or crystallographic interface, the Lennard-Jones (LJ) and electrostatic (ES) contributions to the interaction energies between a reference CUR molecule and its nearest neighbor within the layers, as well as between the two layers, are more attractive for the former than for the later

type of interactions. Furthermore, the onset of temperature at which a noticeable weakening of the LJ and ES interactions is lower than that observed in the bulk. The LJ and ES interactions for the first neighbors located within the second layer is noticeably stronger, suggesting that lateral cohesion is more pronounced just beneath the surface. This could be attributed to tighter packing or reduced surface relaxation effects in the subsurface region compared to the outermost layer.

As temperature increases, the LJ and ES interactions within the first layer exhibit only a modest and gradual decrease, indicating that the surface retains a relatively stable structure under moderate thermal excitation. However, both the LJ and ES interactions within the second layer and those bridging the first and second layers undergo a more significant drop around $T \approx 450$ K. This pronounced weakening points to the onset of structural rearrangement below the surface – possibly involving the loosening of lateral packing, partial decoupling of adjacent layers, or increased molecular mobility within the second layer. These changes may reflect the early stages of interfacial disordering, where the breakdown of cohesive interactions begins not at the very surface, but just beneath it. Beyond this transition temperature, the continued but slower decrease in these interactions suggests progressive softening of the structure, consistent with the approach to surface or partial melting. This layered response to thermal excitation underscores the cooperative nature of melting, where destabilization initiates within subsurface regions and gradually propagates toward the surface and bulk.

4.4.3. Surface Tension and Surface Area

Another key property to the surface structure is surface tension (common name for liquids) or interfacial energy (usually reserved for solids). Different ways of estimating surface tension have been discussed in Ch. 2. Results of the pressure-based surface tension calculations are given in Fig. 4.14.

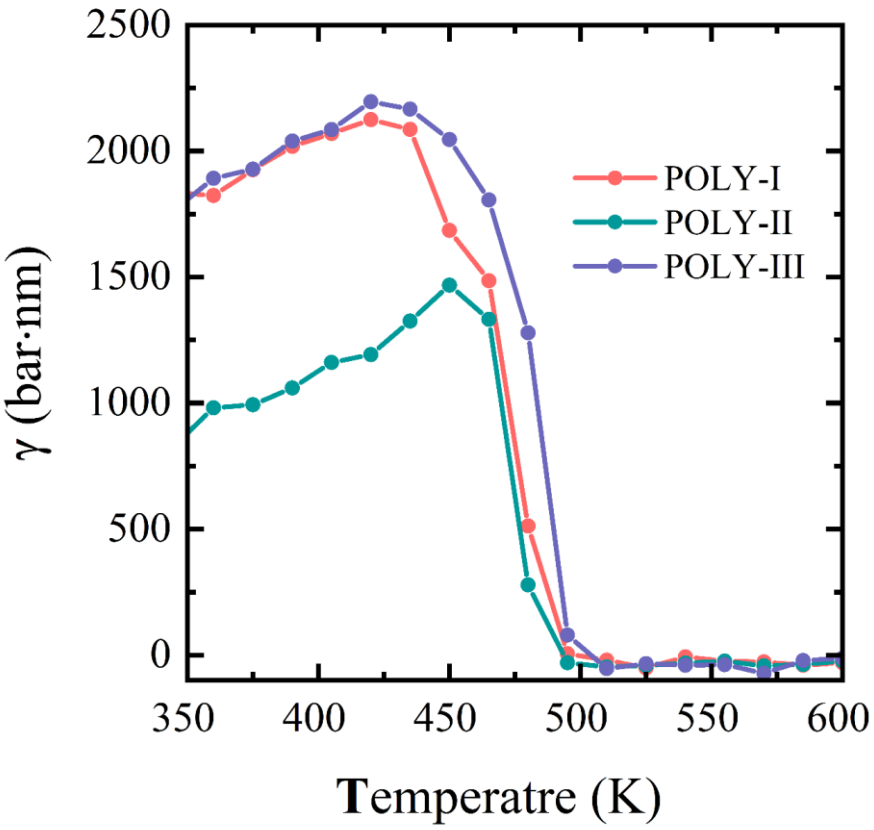

Figure 4.14. Temperature-dependent surface tension for [100] interfaces of different polymorphs of CUR.

It is immediately apparent that the surfaces tension in the crystalline phase is much higher than in the melt state, with the lowest value at 350 K being 526 bar·nm (POLY-II), while typical values in the melt are 4 bar·nm. The similarity between POLY-I and POLY-III is unsurprising, considering the similarity in the orientation of CUR molecules in those polymorphs (and despite the conformational differences). Interestingly, although [100] interface of POLY-II is less prone to thermal degradation, as seen in Fig. 4.4 (d), it displays lower surface tension values and higher slope of the linear part of the curve between 350 K and 450 K. This can be explained by actually higher surface density (as seen from the VP analysis of Fig. 4.7 (c)), or, equivalently, lower surface area.

As temperature increases in the crystalline phase, surface tension initially rises, reaching a maximum at an intermediate temperature. This initial increase likely reflects enhanced molecular mobility and surface reorganization, allowing the system to optimize intermolecular

interactions at the interface, thereby increasing cohesive forces (see Fig. 4.16 later). The maximum marks a point of balance between structural order and thermal agitation. As the temperature continues to rise, a sharp decrease in surface tension is observed and can be associated with the fact that, at this temperature, surface cohesion begins to break down due to the onset of surface disorder. Beyond the temperature at which the decrease occurs, the surface tension stabilizes at a lower value characteristic of the liquid–vacuum interface, where molecular mobility is high and the structure is isotropic. This plateau reflects the system's transition to a fully disordered, fluid-like surface regime.

To give molecular level explanation to the behavior of the surface tension, we calculated the effective surface area per molecule. It is essentially a measure of how much "space" each molecule has to interact with its neighbors at the interface. This quantity reflects both molecular packing density and freedom of motion, and can strongly influence structural organization and the onset of interfacial disorder. Indeed, smaller effective surface area per molecule implies a tighter packing at the interface that can be driven by strong intermolecular interactions while larger surface area suggests a loser packing which may correlates with large change in the conformation and increased susceptibility to thermal fluctuation.

In order to calculate effective surface area, we utilize ITIM algorithm with a double-pass over atomic spheres – a procedure proposed in Ch. 2. Averaging over the whole trajectory and dividing by the number of molecules at the interface, one obtains surface area per molecule, shown in Fig. 4.15 (a-c) for each polymorph at its three faces.

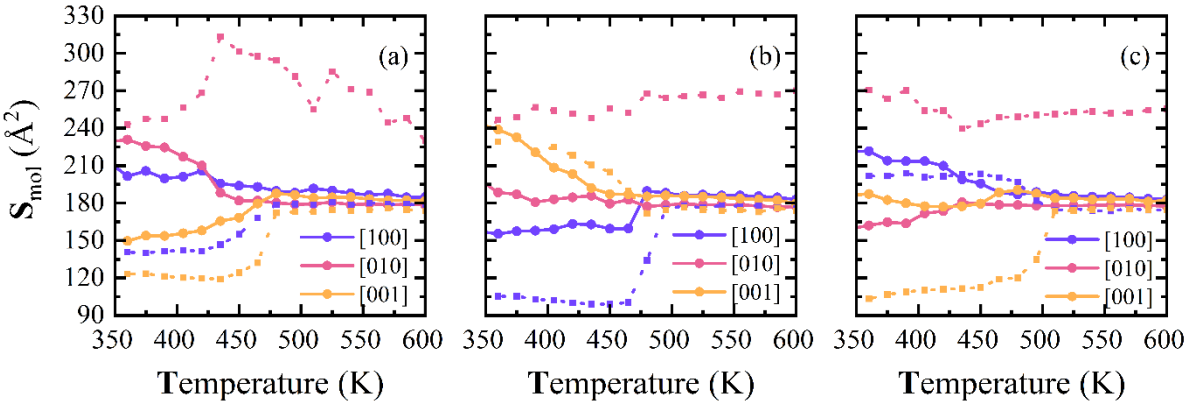

Figure 4.15. Dependence of the surface area per CUR particle on the temperature for the 1st (solid) and 2nd (dashed) layers of different interfaces of (a) POLY-I, (b) POLY-II and (c) POLY-III.

These figures show clearly that at high temperature, in the melt phase, the values of the effective surface area, S_{mol}, converge to the same value independently on the nature of the polymorph and on the considered crystallographic face. The difference in the values of S_{mol} in POLY-III in the three crystallographic faces is small compared to that in the other two polymorphs. This suggests a small difference in the packing in the three crystallographic faces. In POLY-I and POLY-II, the smallest S_{mol} values indicate that the surface packing of CUR molecules is tightest at [001] and [100] surfaces respectively. Surface area values increase with temperature, reducing the packing efficiency until it is equal in all the three crystallographic planes. In POLY-I, increasing the temperature induces a gradual decrease in the values of the S_{mol} in the [100] plane, while in the [010] plane a noticeable decrease in the values of S_{mol} is observed around 400 K, before stabilizing at higher temperatures. This indicates that the packing density of CUR molecules increases in this plane with temperature. In POLY-III, a sharp decrease of S_{mol} values is observed at temperature lower than 350 K, indicating that CUR molecules become more packed along this plane, while the extent of decrease of S_{mol} in the [001] plane is less than that in the [010]. This indicates that increase of the packing efficiency along this plane is slow compared to the previous one.

To investigate the correlation between the behavior of the S_{mol} values across crystallographic planes and the role of different interfaces in influencing the thermodynamic ranking of crystalline stability, we have computed the cohesive energy densities (CED) for each interface. The temperature dependence of CED for all three polymorphs is shown in Fig. 4.16 (a–c). Importantly, CED at the interface acts as a quantitative measure of local structural integrity, reflecting how efficiently molecules interact and pack within the surface layer. By comparing CED values across different planes and polymorphs, we can identify which interfaces are structurally robust and which are more susceptible to early thermal disorder or surface melting.

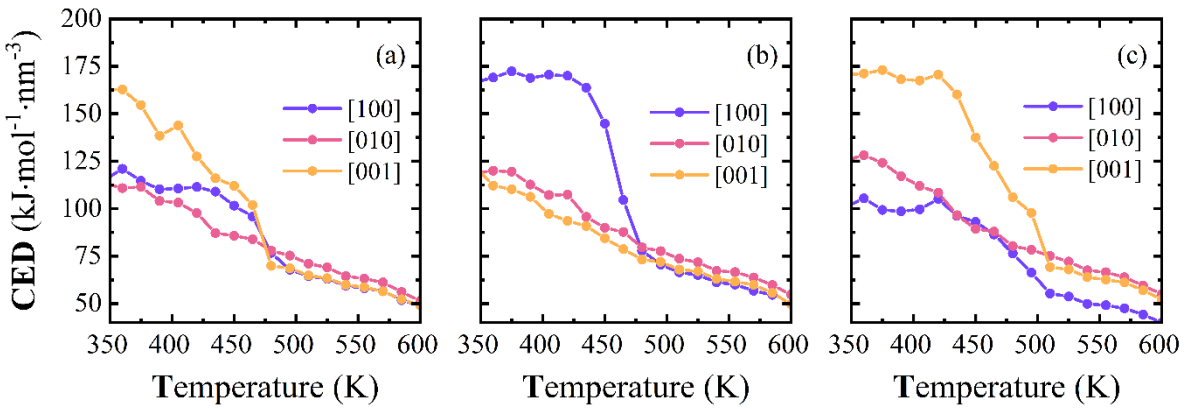

Figure 4.16. Temperature behavior of the cohesive energy density for different interfaces of (a) POLY-I, (b) POLY-II and (c) POLY-III.

Our results indicate that the highest CED values – approximately 175 kJ·mol^{-1}·nm^{-3} – are found in the [001] plane of POLY-I, the [100] plane of POLY-II, and again the [001] plane of POLY-III, suggesting that these surfaces are particularly tightly packed. This value represents the upper bound across all investigated planes, suggesting a particularly robust interfacial structure in these crystallographic planes. These high-CED planes exhibit a similar temperature-dependent profile, marked by a noticeable drop around T ≈ 450 K, consistent with the onset of interfacial destabilization.

In POLY-I, the CED values for the [010] and [001] planes are nearly equivalent, indicating comparable interfacial cohesion. A similar trend is observed in POLY-II for the [010] and [001] planes. In contrast, in POLY-III, the CED is notably lower in the [100] plane compared to the [010] plane, pointing to weaker surface cohesion and potentially earlier surface disordering in that orientation.

4.5. Dynamics at the Interface

Understanding the dynamics at crystal interfaces is critical for interpreting and predicting structural transformation, interfacial stability, and thermodynamic behavior. These dynamic properties provide insight beyond what static structures can offer, revealing how molecular mobility, anisotropy, and conformational freedom shape the response of different crystal faces to temperature increase.

4.5.1. Time of Residence

Measuring the residence time of CUR molecules at crystal interfaces provides dynamic insight into the stability and reactivity of the surface. It reflects the strength of interfacial interactions, reveals the onset of disorder, and connects directly to thermally activated processes such as melting, dissolution, and polymorphic transformation. Tracking residence times across crystallographic planes allows for a more complete understanding of how structural and dynamic anisotropy influence interfacial behavior. Simple algorithms of computing mean time of residence, τ_{OR}, are available in the literature[8] and implemented by us in Julia (specifically algorithm 2).

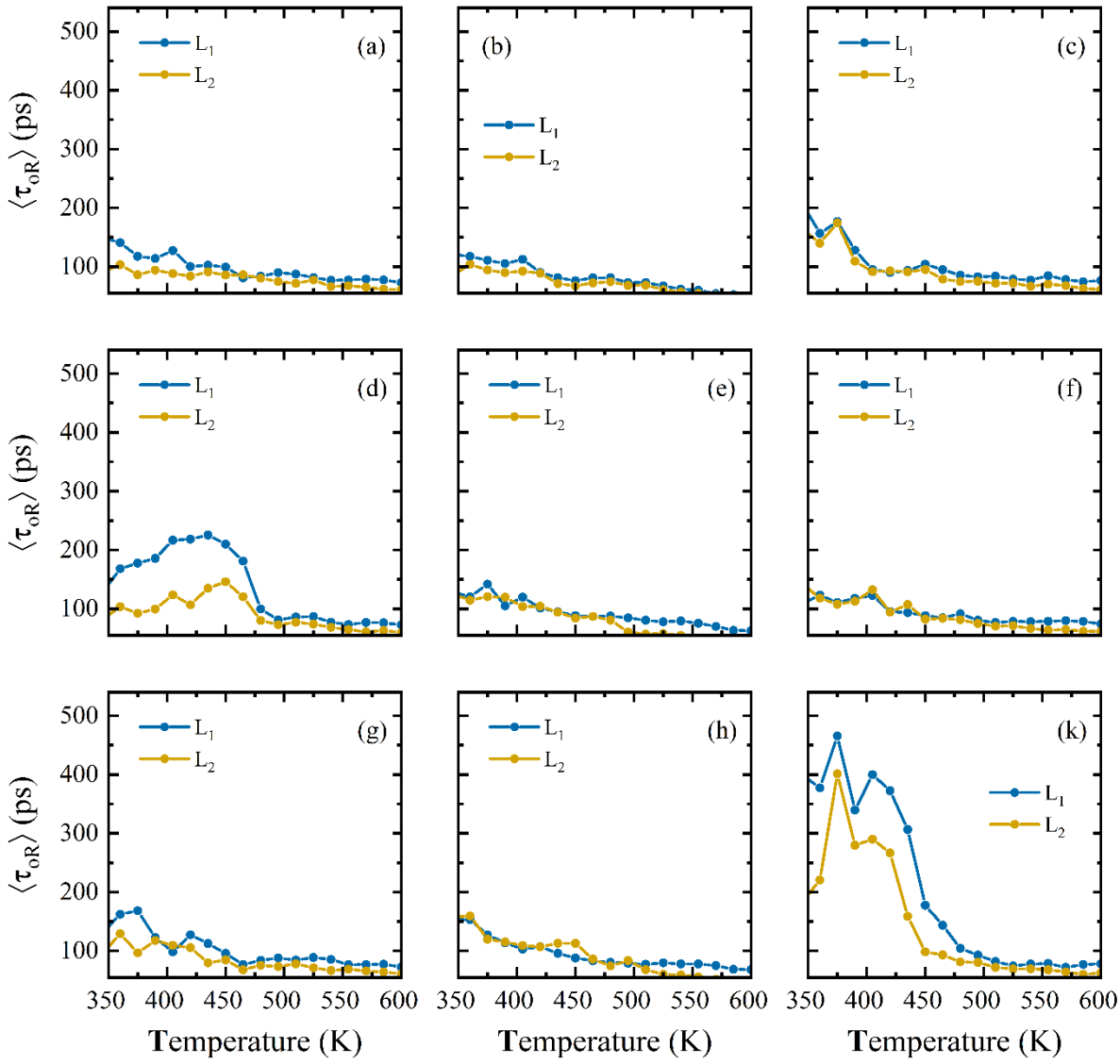

Figure 4.17. Temperature dependence of the average residence time of the fast-moving (less than 50% of time spent in the designated layer) CUR molecules in each layer of (a) POLY-I [100], (b) POLY-I [010], (c) POLY-I [001], (d) POLY-II [100], (e) POLY-II [010], (f) POLY-II [001], (g) POLY-III [100], (h) POLY-III [010] and (k) POLY-III [001].

We have calculated τ_{oR} for the three polymorphs of CUR belonging to the three first layers. The temperature dependence of τ_{oR} at the three crystallographic planes is displayed in Fig 4.17. In general, our results indicate a gradual decrease of the residence time of interfacial CUR molecules. In the melt phase, at high temperature, the τ_{oR} values are similar for the first two layers. Of note is that the temperature dependence of τ_{oR} is quite different in POLY-II and POLY-III at [100] and [001] planes, respectively. Indeed, the values of τ_{oR} go through a maximum before sharply decreasing at T ≈ 450 K.

4.5.2. Diffusion Coefficient

Evaluating the lateral $D_{\parallel}$ and perpendicular $D_{\perp}$ diffusion coefficients of CUR molecules within interfacial layers provides detailed insight into the directional mobility and structural integrity of the surface. Lateral diffusion reflects the degree of in-plane molecular freedom and packing efficiency, while perpendicular diffusion reveals interlayer coupling and the onset of structural destabilization. Together with residence time and cohesive energy density, these directional diffusion metrics offer a dynamic, layer-resolved view of the interfacial behavior critical for understanding melting, polymorph transitions, and surface-driven phenomena. The results of the calculations are shown in Fig. 4.18. for POLY-I.

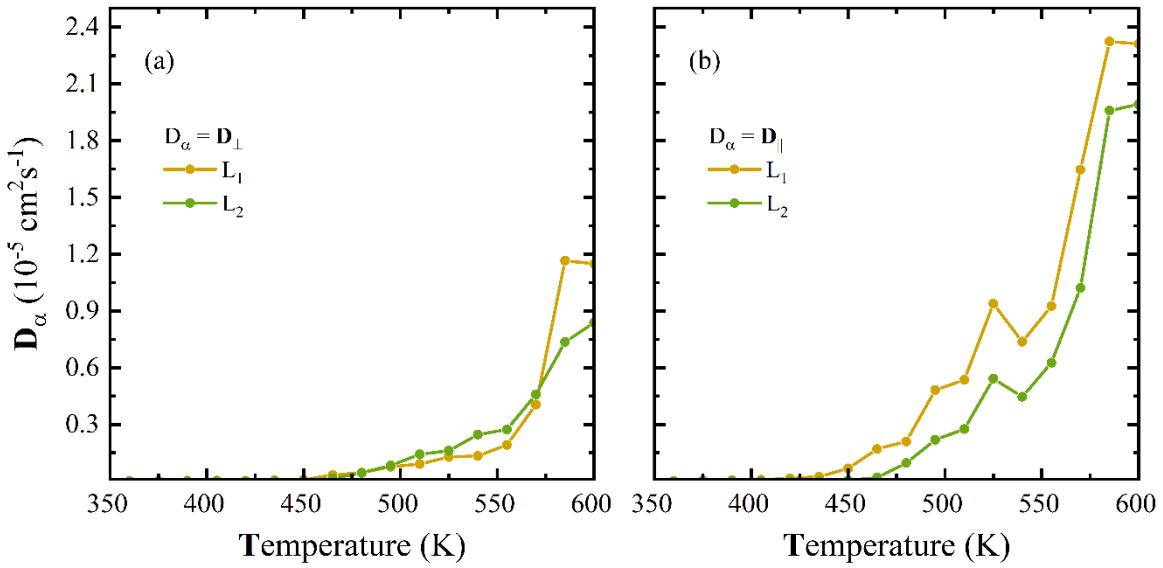

Figure 4.18. (a) Perpendicular and (b) lateral diffusion coefficients for different layers of [100] interface of POLY-I.

Our results indicate that the perpendicular diffusion coefficients, $D_{\perp}$, of CUR molecules in the first and second layers are quite similar. As expected, in the crystalline phase, CUR molecules exhibit negligible perpendicular diffusion, reflecting their confinement within well-ordered layers. However, $D_{\perp}$ increases significantly once the temperature exceeds approximately $T \approx 450$ K, coinciding with the onset of surface disordering or partial melting.

The temperature dependence of the lateral diffusion coefficient $D_{||}$ mirrors that of $D_{\perp}$ showing a similar rise beyond the transition temperature. Interestingly, in this case, CUR

molecules in the first interfacial layer exhibit slightly higher lateral mobility than those in the second layer. This suggests that while vertical exchange between layers is limited, in-plane motion at the surface becomes increasingly active with temperature, likely due to weaker lateral packing or increased conformational freedom at the outermost interface.

This interpretation is supported by conformational data (Fig. 4.10), which shows that conformational transitions at the interface begin at lower temperatures than in the bulk. The first layer undergoes conformational rearrangements earlier, which likely enhances lateral mobility due to reduced steric hindrance and loss of molecular planarity. Additionally, the surface tension data (Fig. 4.14) show a decline in cohesive surface forces around the same temperature range, further supporting the picture of increasing molecular freedom at the interface. Altogether, these observations reveal a coupled structural-dynamic transition: as CUR molecules at the surface adopt more flexible conformations, their ability to diffuse laterally increases, while perpendicular motion remains constrained until later stages of interfacial disordering.

4.5.3. Voronoi Correlation Time

The Voronoi polyhedra-based density correlation function provides a sensitive and spatially-resolved measure of local structural relaxation at the interface. Unlike global diffusion metrics, it captures how quickly the molecular environment changes, revealing the dynamic stability of the surface layers. By comparing correlation decay across layers and temperatures, this function helps identify the onset of surface disorder, conformational flexibility, and pre-melting behavior, offering a nuanced view of interfacial dynamics.

The Voronoi polyhedra (VP) density autocorrelation functions were fitted using a bi-exponential decay model, yielding two characteristic relaxation times: a fast component τ_1^{VR} and a slow component τ_2^{VR}. Slow component, τ_2^{VR}, appears to be completely independent of the system under consideration. This behavior indicates the presence of long-lived, temperature-independent structural correlations, likely intrinsic to the CUR molecular arrangement.

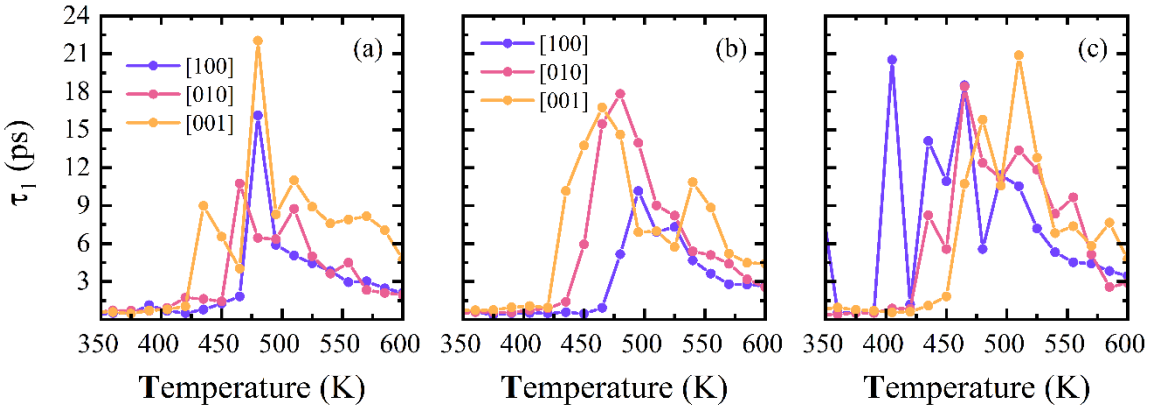

Figure 4.19. Fast relaxation time components of the bi-exponentially fitted VP 2D density autocorrelation functions for every temperature for every interface of (a) POLY-I, (b) POLY-II and (c) POLY-III.

The temperature dependence of the fast component, τ_1^{VR}, is shown in Fig. 4.19. In the crystalline phase, for all three crystallographic planes of both POLY-I and POLY-II, τ_1^{VR} remains nearly constant at ~2 ps. A sharp peak appears near T ≈ 450 K, marking a regime of maximum local density fluctuation likely associated with the onset of interfacial melting. Beyond this point, τ_1^{VR} gradually decreases with further heating. Interestingly, this peak occurs at a lower temperature for the [001] plane, suggesting an earlier onset of structural destabilization at this interface compared to [100] and [010]. POLY-III shows excessively higher correlation times at lower temperatures, around 430 K, even compared to POLY-I with very similar interfacial orientation. The reason most likely lies in the interface-dependent breakdown of the hydrogen bonding pattern, as similar low temperature spike is seen for POLY-I [001]. Another reason might lie in the difficulty of computing autocorrelation function right near the phase transition, as uncertainty in several key factors, including determination of interfacial molecules, rapidly increases.

4.6. Conclusions

This chapter has presented an in-depth molecular dynamics study of the vacuum-facing interfaces of curcumin polymorphs. By combining orientation and radial distribution functions, we revealed distinctive patterns of molecular packing and motion across crystallographic planes, identifying strong directional dependence in interfacial properties.

Our findings highlight several key insights:

- Conformational transitions occur earlier at the interface than in the bulk, especially for CONF-2 and CONF-3 in POLY-II and POLY-III, indicating enhanced flexibility and reduced energy barriers at the surface.
- Orientation plays a decisive role: molecules aligned parallel to the interface normal exhibit higher thermal stability, supported by greater packing efficiency, stronger π–π stacking, and reduced conformational freedom.

Hydrogen bonding remains a key driver of local structure, but its impact is modulated by competition with Van der Waals and π–π interactions, varying with polymorph and interface.

Voronoi-based local density correlation functions were introduced as sensitive probes of structural relaxation and used to identify breakdown temperatures and onset of interfacial melting. These proved especially effective in capturing subtle differences between planes and polymorphs.

Surface tension and effective surface area measurements confirmed that tightly packed surfaces correlate with increased thermal resilience, while more loosely packed planes (e.g., [010] in POLY-I) show earlier signs of disorder.

Dynamically, layer-resolved diffusion and residence time analysis confirmed the presence of elevated molecular mobility at the interface, with mobility gradients across layers reinforcing the idea of melting as a layer-propagating process.

Altogether, these results underscore the anisotropic nature of CUR polymorphs, where surface orientation, molecular conformation, and interfacial energy are tightly coupled. This chapter also established analytical tools – particularly VP-based structural and dynamic metrics – that will be applied in the next chapter to study CUR interfaces with supercritical CO_2.

4.7. Bibliography

(1) Abraham, M. J.; Murtola, T.; Schulz, R.; Páll, S.; Smith, J. C.; Hess, B.; Lindahl, E. GROMACS: High Performance Molecular Simulations through Multi-Level Parallelism from Laptops to Supercomputers. *SoftwareX* **2015**, *1–2*, 19–25. https://doi.org/10.1016/j.softx.2015.06.001.

(2) Bussi, G.; Donadio, D.; Parrinello, M. Canonical Sampling through Velocity Rescaling. *J. Chem. Phys.* **2007**, *126* (1), 014101. https://doi.org/10.1063/1.2408420.

(3) Bussi, G.; Zykova-Timan, T.; Parrinello, M. Isothermal-Isobaric Molecular Dynamics Using Stochastic Velocity Rescaling. *J. Chem. Phys.* **2009**, *130* (7), 074101. https://doi.org/10.1063/1.3073889.

(4) Groom, C. R.; Bruno, I. J.; Lightfoot, M. P.; Ward, S. C. The Cambridge Structural Database. *Acta Crystallogr. Sect. B Struct. Sci. Cryst. Eng. Mater.* **2016**, *72* (Pt 2), 171–179. https://doi.org/10.1107/S2052520616003954.

(5) Sanphui, P.; Goud, N. R.; Khandavilli, U. B. R.; Bhanoth, S.; Nangia, A. New Polymorphs of Curcumin. *Chem. Commun.* **2011**, *47* (17), 5013–5015. https://doi.org/10.1039/C1CC10204D.

(6) Pártay, L. B.; Hantal, G.; Jedlovszky, P.; Vincze, Á.; Horvai, G. A New Method for Determining the Interfacial Molecules and Characterizing the Surface Roughness in Computer Simulations. Application to the Liquid–Vapor Interface of Water. *J. Comput. Chem.* **2008**, *29* (6), 945–956. https://doi.org/10.1002/jcc.20852.

(7) Sega, M.; Hantal, G.; Fábián, B.; Jedlovszky, P. Pytim: A Python Package for the Interfacial Analysis of Molecular Simulations. *J. Comput. Chem.* **2018**, *39* (25), 2118–2125. https://doi.org/10.1002/jcc.25384.

(8) Sánchez, H. R. Residence Times from Molecular Dynamics Simulations. *J. Phys. Chem. B* **2022**, *126* (43), 8804–8812. https://doi.org/10.1021/acs.jpcb.2c03756.

CHAPTER 5
SUPERCRITICAL FLUIDS

In this chapter, we characterize the dependence of the microscopic structure of CO_2 on temperature along various isobars near the critical point. To achieve this goal, we test the ability of available CO_2 force fields to reproduce critical point parameters. We then quantify the density fluctuations along seven isobars using the CRM model. We then address how the difference in the spatial extent of attractive contributions from electrostatic (ES) and Lennard-Jones (LJ) potentials, modulated by the change in the thermodynamic conditions, drives these structural changes and density fluctuations.

5.1. Computational Methods

Molecular dynamics simulations were performed using the GROMACS 2024.1[1] program package. Among the tested CO_2 models[2] were those parametrized via transferable force fields, such as OPLS-AA[3,4], GAFF[5,6] and CGENFF.[7] Model due to Cygan et al.,[8] hereafter referred to as CRM, was also analyzed. Functional forms of such force fields are described by the following equations:

$$E_{ES} = \sum_{i=1}^{N} \sum_{j<i}^{N} \frac{q_i q_j}{4\pi\varepsilon_0 r_{ij}} \tag{5.1}$$

$$E_{LJ} = \sum_{i=1}^{N} \sum_{j<i}^{N} 4\varepsilon_{ij} \left(\left(\frac{\sigma_{ij}}{r_{ij}} \right)^{12} - \left(\frac{\sigma_{ij}}{r_{ij}} \right)^{6} \right) \tag{5.2}$$

$$E_b = \sum_{i=1}^{N_b} \frac{k_i^r}{2} (r_i - r_i^0)^2 \tag{5.3}$$

$$E_a = \sum_{i=1}^{N_a} \frac{k_i^\theta}{2} (\theta_i - \theta_i^0)^2 \tag{5.4}$$

$$E_a = \sum_{i=1}^{N_a} \left[\frac{k_i^\theta}{2} (\theta_i - \theta_i^0)^2 + \frac{k_i^{UB}}{2} (r_i - r_i^0)^2 \right] \tag{5.5}$$

The electrostatic (ES, Eq. 5.1) and Lennard-Jones (LJ, Eq. 5.2) potentials describe the intermolecular part of the potential. Intramolecular part is comprised of bond (Eq. 5.3) and angle (Eq. 5.4) terms for OPLS, GAFF and CRM potential. CGENFF, however, uses Urey-Bradley terms (Eq. 5.5) for the angle part of the potential instead of a simple harmonic form.

Model parameters for all four considered potentials are available in Table 5.1. First, vapor-liquid coexistence curve simulations were done in the NVT ensemble. After, phase-space mapping was performed with the NPT ensemble. Simulations of isobaric conditions utilized Parinello-Bussi[9,10] thermostat and barostat. Simulation boxes contained 2048 flexible CO_2 molecules. Vapor-liquid coexistence curve simulations were done in the NVT ensemble with the same thermostat. Initial configurations were prepared by placing 2048 CO_2 molecules, arranged in two phases, in a 5x5x15 nm orthorhombic box. For isobaric simulations, pressure

was varied from 70 bar to 100 bar with a step of 5 bar. Preliminary work also included isobaric simulations from 70 bar to 100 bar with a step of 10 bar and from 100 bar to 750 bar with a step of 50 bar. These values were chosen to sample a couple of isobars close to the critical pressure and with larger step away from it. The temperature was consistently varied from 250 K to 450 K with a step of 10 K. Equations of motion were integrated in time steps of 1 fs. Additional test simulations with 0.5 fs step and/or special, non-harmonic, linear angle potentials did not reveal any inconsistencies. After at least 12.5 ns long equilibration period, statistical data (such as temperatures, pressures, nearest neighbor distances, local densities, etc.) was collected using 7500 equilibrium sample configurations, separated from each other by 1 ps, from the 7.5 ns long production run at every temperature-pressure pair. Nearest neighbor calculations were done up the 50^{th} nearest neighbor to a reference CO_2 molecule, using all configurations along the generated equilibrium trajectories. As the force file is flexible, we decided to use the center-of-mass of the CO_2 molecule to calculate the radial distribution functions (RDFs). Interaction energies were calculated in frames separated by 100 timesteps each to save computational time. Voronoi calculations were done as described in Ch. 2. Similarly, DBSCAN[11,12] also utilized the minimal possible distance between molecules. Finally, the DBSCAN parameters, namely the radius and minimal number of neighbors, were chosen based on the nearest neighbor RDF calculations at the same thermodynamic state, except for special cases when it is stated otherwise.

Additional MD simulations of scH_2O and $scNH_3$ utilized same general parameters as those of $scCO_2$. Utilized force field models are summarized in Table 5.2 and Table 5.3, respectively.

MC simulations of coexistence curves of $scCO_2$ were performed with[13] the MCCCS Towhee 8.2.2. Simulation boxes were prepared with PACKMOL program suite[14] and contained 1024 CO_2 molecules. Equilibration and production runs were done for 10000 cycles each, where cycle is defined as sum of the moves for all molecules in the box. Simulations were performed with two boxes, initial populations of 700 and 300 molecules in the NVT ensemble. Unlike MD simulations, MC simulations utilized analytical tail corrections instead of potential/force-shifting for the LJ potential. Electrostatic potential was modeled with PME functional with 11 Å cutoff.

Table 5.1. Intermolecular and intramolecular parameters for four considered CO_2 force field models. Charge values, q, are given in units of e. Lennard-Jones parameters, σ and ε, are given in nm and kJ·mol^{-1}, respectively. Bond distance and force constant, r and k_b, are given in nm and kJ·mol^{-1}·nm^{-2}. Equilibrium angle is always 180°.
Angle force constant, k_θ, is in kJ·mol^{-1}·rad^{-2}. Functional forms are consistent with GROMACS 2024.4.

	q		σ		ε		C-O		O-C-O
	C	O	C	O	C	O	r	k_b	k_θ
GAFF	0.8790	-0.4395	0.34790	0.30481	0.66777	0.61212	0.1175	587230	775.55
OPLS	0.5904	-0.2952	0.33000	0.29600	0.27614	0.87864	0.1171	585760	1338.88
CGENFF	0.6860	-0.3430	0.27850	0.30148	0.24267	0.69036	0.1170	825084	376.56
CRM	0.6512	-0.3256	0.28000	0.30280	0.23400	0.66830	0.1162	844300	451.90

Table 5.2. Intermolecular and intramolecular parameters for the considered H_2O force field model. Charge values, q, are given in units of e. Lennard-Jones parameters, σ and ε, are given in nm and kJ·mol^{-1}, respectively. Bond distance and force constant, r and k_b, are given in nm and kJ·mol^{-1}·nm^{-2}. Angle force constant, k_θ, is in kJ·mol^{-1}·rad^{-2}. Functional forms are consistent with GROMACS 2024.4. M represents a virtual site. All parameters not given in the table are assumed to be zero.

	q		σ	ε	O-M		O-H		H-O-H	
	M	H	O	O	R	k_b	R	k_b	θ	k_θ
TIP4P/2005	-1.1128	0.5564	0.3159	0.7749	0.01546	∞	0.09572	∞	140.52	∞

Table 5.3. Intermolecular and intramolecular parameters for the considered NH_3 force field model. Charge values, q, are given in units of e. Lennard-Jones parameters, σ and ε, are given in nm and kJ·mol^{-1}, respectively. Bond distance and force constant, r and kb, are given in nm and kJ·mol^{-1}·nm^{-2}. Angle force constant, k_θ, is in kJ·mol^{-1}·rad^{-2}. Functional forms are consistent with GROMACS 2024.4. All parameters not given in the table are assumed to be zero.

	q		σ	ε	N-H		H-N-H	
	N	H	N	N	R	k_b	θ	k_θ
KRI3 (MOD.)	-1.035	0.345	0.3390	1.4142	0.10124	403402	106.7	366.723

5.2. Force Field Selection

There exists a significant amount of research on parametrization of CO_2 MD models. Among them, only a handful are able to describe critical point properties with sufficient accuracy while not utilizing fixed bonds/angles. To select the most appropriate model for the description of the structure of CO_2 in the critical regime, we compared coexistence curves of several transferable force fields, as well as model of Cygan et al.[8] – CRM. The critical temperature and density were obtained from liquid-vapor NVT simulations. Mass-density profiles (Fig. 5.1) along the interface (2:1 ratio of vapor to liquid phase volumes) were fit with modified version of the commonly used hyperbolic tangent profiles (Eq. 5.6). Critical temperature is obtained from the following equations:

$$\rho = 0.5(\rho_l + \rho_v) - 0.5(\rho_l - \rho_v)tanh(2d(|x - x_0| - x_1)) \tag{5.6}$$

$$\rho_l - \rho_v = \Delta\rho_0 \sum_{i=1}^{n} \left(1 - \frac{T}{T_c}\right)^{\beta+0.5(i-1)} \tag{5.7}$$

$$0.5(\rho_l + \rho_v) = \rho_c + A(T_c - T) \tag{5.8}$$

$$P = P_c e^{\frac{T_c}{T}} \tag{5.9}$$

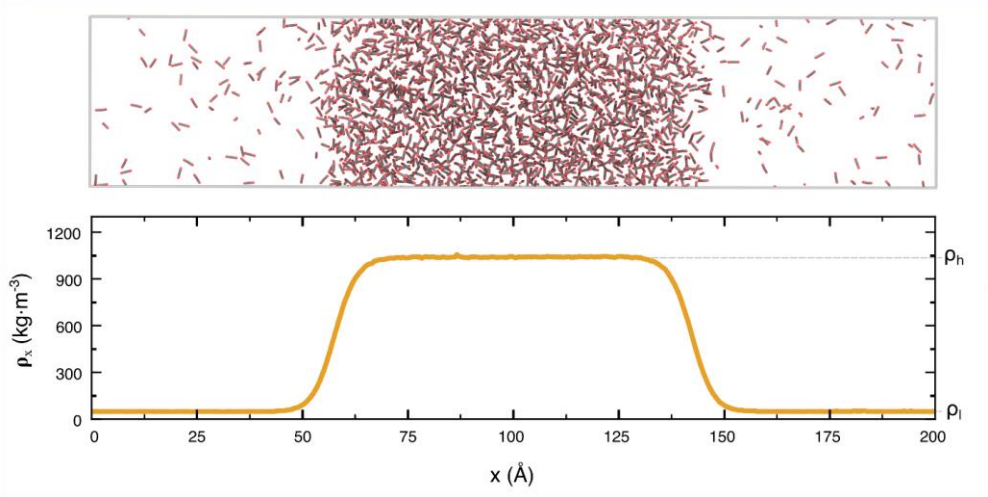

Figure 5.1. Mass-density profile (bottom) along with a visualization of the simulation box (top) for vapor-liquid coexistence curve simulation at T = 250 K.

Calculated high/low densities, denoted ρ_h and ρ_l, respectively and corresponding to liquid and vapor phase densities, along with fits according to Eqs. (5.6-5.8), are shown in Fig. 5.2 (a). Overall, transferable force fields (OPLS-AA and GAFF), although advantageous for their ubiquity, offer poor reproducibility of the critical temperature, while CHARMM model (CGENFF) gives a reasonably good critical point temperature $T_c = 308 \pm 0.2$ K, but significantly overestimates critical point pressure at $P_c = 201 \pm 45$ bar (error estimates are based on the non-linear-least-squares estimates and given as standard deviations). On the other hand, CRM gives equally good $T_c = 298 \pm 0.3$ K, but much better $P_c = 68 \pm 15$ bar, in agreement with the corresponding experimental values $T_c = 304$ K, $P_c = 73.8$ bar and $\rho_c = 467.6$ kg/m^3. The behavior of the CRM model with respect to (T,P) is shown in Fig. 5.2 (b).

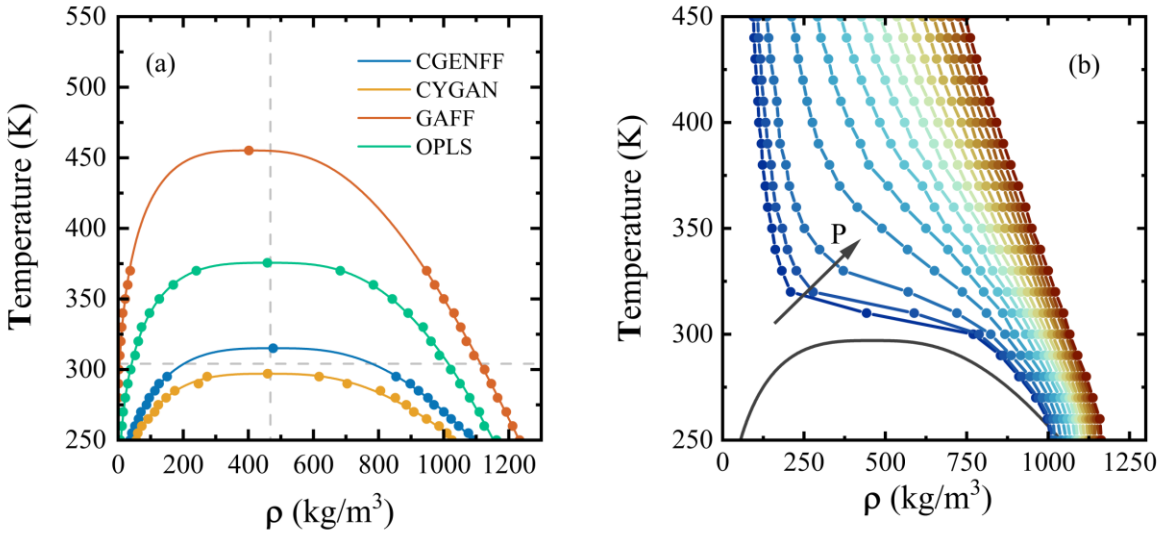

Figure 5.2. (a) Coexisting liquid and vapor phase densities of the systems simulated, for the four investigated CO_2 force filed models at various temperatures (full circles), along with their fits according to Eqs. 5.6-5.9 (solid curves). The dashed lines indicate the experimental critical density and temperature. (b) Calculated (CRM model[8]) CO_2 isobars (full circles) with the corresponding coexistence curve. The arrow indicates increasing pressure (from 70 bar (blue circles) to 100 bar (cyan circles) with a step of 10 bar and from 100 bar to 750 bar (brown circles), in steps of 50 bar).

Critical point thermodynamics properties are, perhaps, the most sensitive properties with respect to the approximate treatment of ES and LJ potentials. Truncation can have tremendous impact on the results. In order to double-check the MD data, we have performed MC simulations of coexistence curves within the NVT-Gibbs ensemble. Comparison between

various MC and MD simulations in shown in Fig. 5.3. As can be seen, MC simulations predict very similar critical densities, but slightly higher T_c = 310 K. Overall, the difference most likely comes from the difference in the treatment of LJ part, as Towhee does not implement force shifting, while MD interfacial simulations break spherical symmetry that is ideal for application of analytical tail corrections.

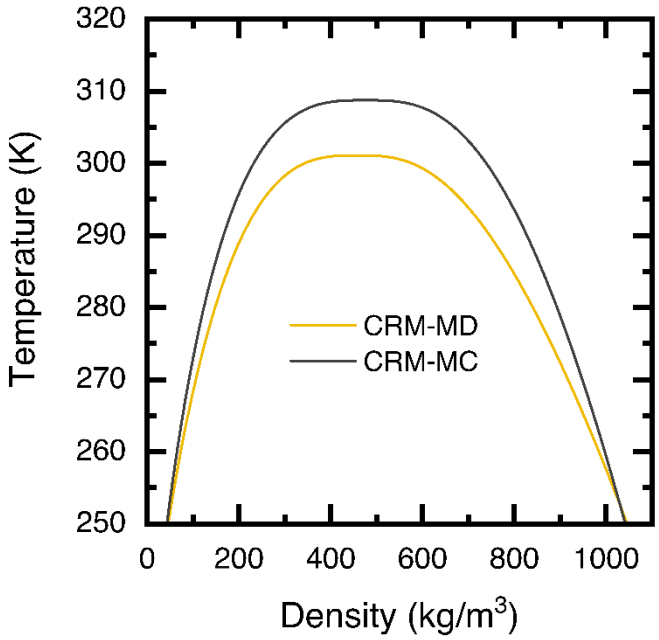

Figure 5.3. Comparison between MD and MC coexisting liquid and vapor phase densities of the systems simulated with CRM model, fit according to Eqs. 5.6-5.9 (solid curves).

5.3. Density Fluctuations

Density fluctuations result from notable changes in the structure, influencing molecular arrangements, orientations, and interaction energies. To capture these fine structural variations and correlate them with density fluctuations, we employ a variety of local statistical observables. These observables include nearest neighbor radial[15], orientation and interaction energy distributions, properties of the Voronoi polyhedra,[16] and those of density domains identified using the DBSCAN algorithm.[17]

Firstly, we have performed space partitioning by means of the Voronoi tessellation. Thus, we determined the Voronoi polyhedron around each CO_2 molecule, represented by its center-of-mass (COM). By calculating the reciprocal volume of these polyhedra, we can estimate the local density, ρ_{COM}^{VP}, around each CO_2 molecule. Probability distributions of the local density, $p(\rho_{COM}^{VP})$, are shown in Fig. 5.4 (a). The shape of these distributions evolves from being almost symmetric to high-density skewed, while shifting from the median value of ~0.014 $Å^{-3}$ to 0.005 $Å^{-3}$. The transition occurs right upon crossing the critical temperature at around 300 K to 310 K. The temperature dependence of the average value of the local density, $\langle\rho_{COM}^{VP}\rangle$, calculated from the corresponding distributions, is shown in Fig. 5.4 (b). At low temperatures, independently from the pressure, the rate of decrease of $\langle\rho_{COM}^{VP}\rangle$, is similar. The $\langle\rho_{COM}^{VP}\rangle$, values near the critical point decrease with a large magnitude, and this rate of decrease is reduced upon further increase of the temperature beyond the critical point. This behavior is similar to previously reported results for supercritical water[18], albeit with different local density / clustering method. The dependence of the standard deviation of this local density, $\sigma_{\rho_{COM}^{VP}}$, on the temperature is shown Fig. 5.4 (c).

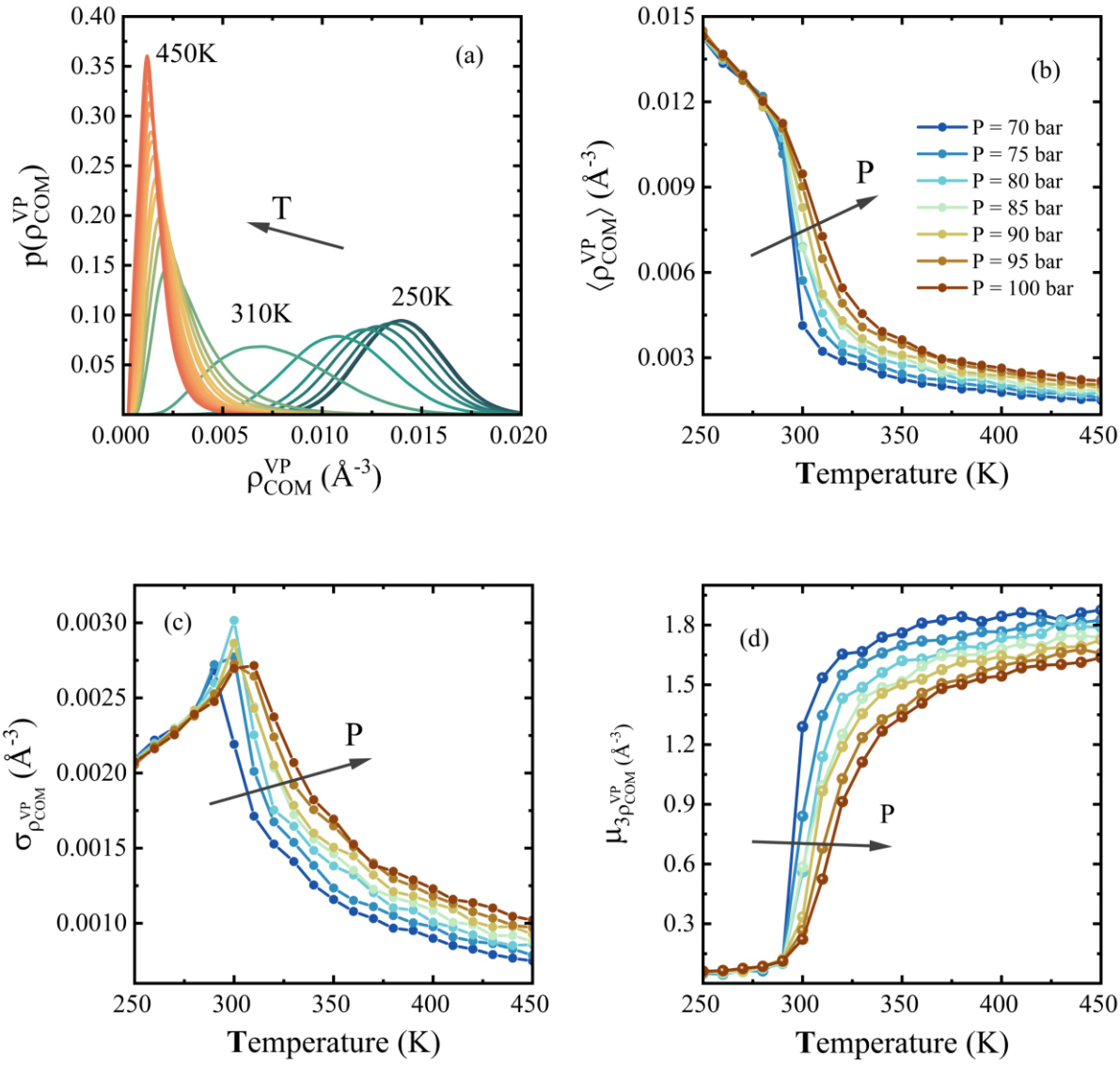

Figure 5.4. (a) Distribution of the local density, as obtained by the Voronoi polyhedral analysis, for different temperature values in the 250-450 K range (from green to orange in the steps of 5 degrees). MD simulations were performed in the NPT ensemble following the P = 70 bar isobar. (b) The dependence of the average value of local density (reciprocal VP volume) on temperature for every studied isobar. (c) The dependence of local density standard deviation on temperature for every studied isobar. (d) The dependence of local density skewness on temperature for every studied isobar.

This curve has a lambda symbol shape in the entire considered temperature range. A well-defined maximum is observed along each isobar when the temperature is equal to the critical one, indicating an inhomogeneous distribution of the local density of CO_2 molecules near the

phase transition. This behavior seems to be a general characteristic of supercritical fluids, as it was observed for supercritical ammonia,[19] water,[17] and Ar.[11] Notably, for temperatures below the critical point, the skewness parameter values, $\mu_{3\,\rho_{COM}^{VP}}$, displayed in Fig. 5.4 (d), are small, suggesting, again, that the density distribution of CO_2 molecules is nearly homogeneous. However, as the temperature approaches and exceeds the critical point, the $\mu_{3\,\rho_{COM}^{VP}}$ values increase at a faster rate, reflecting that, concomitantly to the main density associated with the main peak, many other higher density domains begin to form. For temperatures above the critical point, the skewness parameter stabilizes, reaching a plateau. This suggests that, in this temperature range, the ratio of high-density domains relative to the main peak becomes T/P-independent. When an isobar is farther from the critical one, the above-mentioned behavior is still present, but to a lesser extent.

The VP analysis allows to quantify the radii of the spherical voids, r_{COM}^{VP}, between the COMs of CO_2 molecules. The r_{COM}^{VP} distributions for P = 70 bar, as well as their corresponding average value, fluctuation and skewness are presented in Fig. 5.5. Void radii show opposite trend to the local densities with respect to the temperature, but similar one with respect to pressure. At low temperature, the amount of free space is low, and the molecules pack tightly. As temperature approaches the critical one, large changes happen both in the average values and in fluctuations. Notably, the skewness values go through a maximum at $T = T_c$, indicating that in those conditions, the inhomogeneity of the packing (i.e., close packing between some of the molecules, large empty spaces between others) is maximized. Both local density and void radius behave similarly as pressure moves away from the critical point.

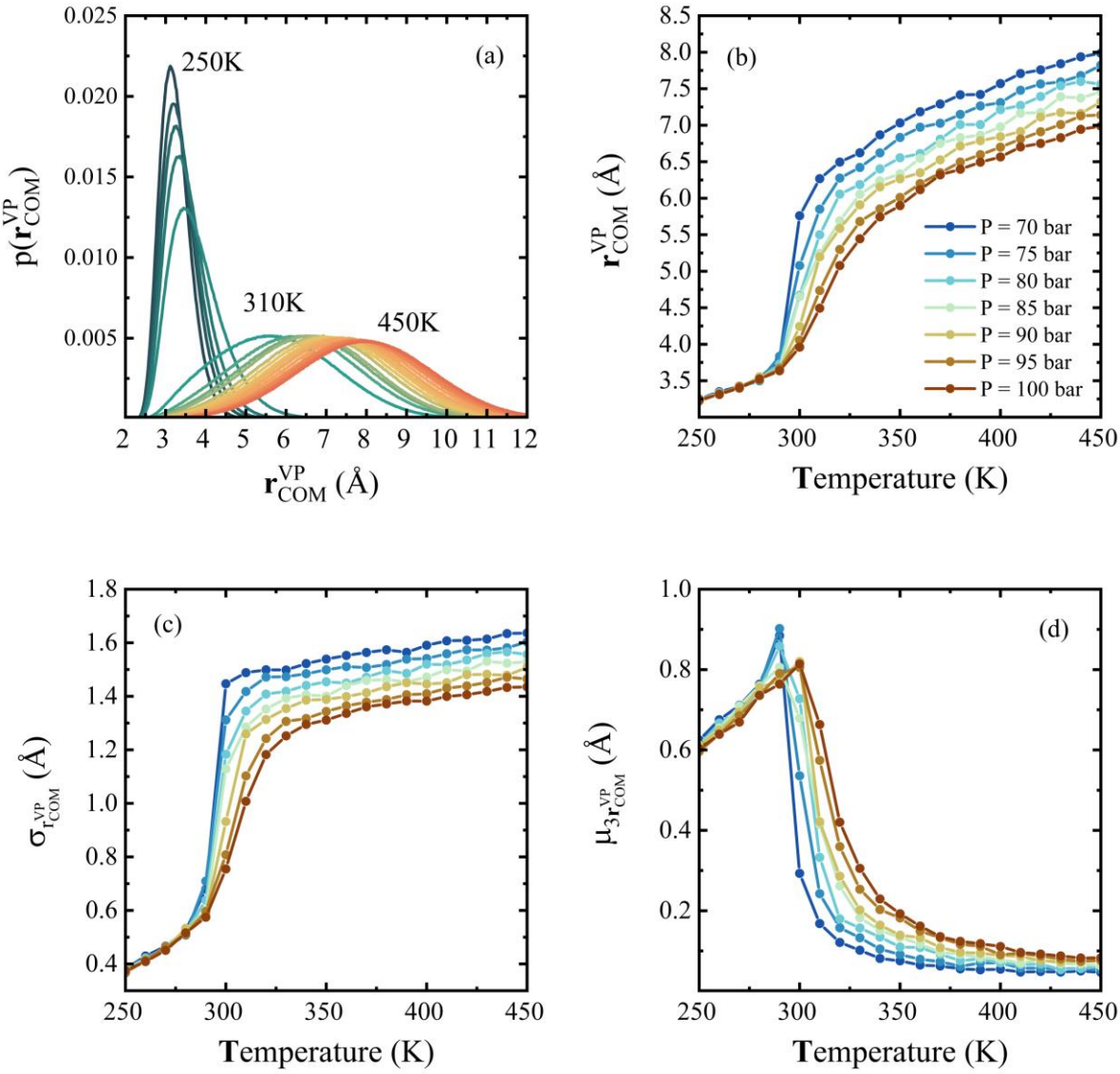

Figure 5.5. (a) The distribution of Voronoi polyhedral void radii, r_{COM}^{VP}, for different temperature values in the 250-450 K range (from green to red). MD simulation were performed in the NPT ensemble following the P = 70 bar isobar. (b) The dependence of the average value of void radii on temperature for every studied isobar. (c) The dependence of void radii standard deviation on temperature for every studied isobar. (d) The dependence of void radii skewness on temperature for every studied isobar. Lighter colors indicate higher pressure.

In order to quantify the time persistence of the local density fluctuations as obtained from the VP analysis, we calculated the Voronoi density correlation functions, $\langle \rho_{COM}^{VP}(t) \cdot \rho_{COM}^{VP}(0) \rangle$. Their time behavior is illustrated in Fig. 5.6 (a). We have fit decay curves at each T,P by a single exponential function and determined the corresponding correlation times, which are

displayed in Fig. 5.6 (b). These results show that the correlation time goes through a maximum at the critical temperature, indicating that here these density fluctuations are quite persistent, with a maximum time duration of ~15 ps.

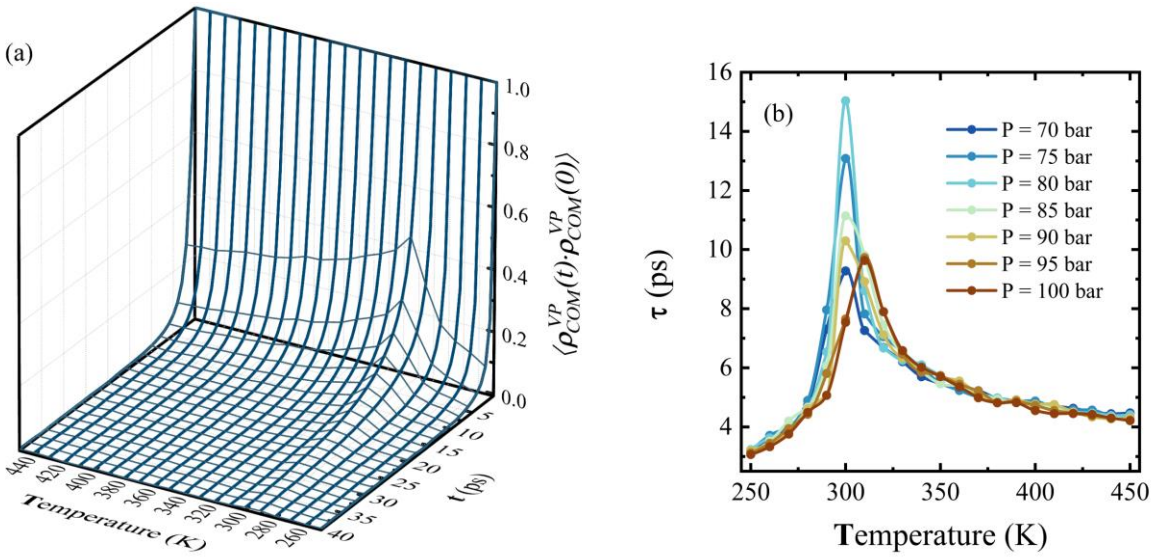

Figure 5.6. (a) Voronoi polyhedra density autocorrelation function for all temperatures along the P = 70 bar isobar. (b) Temperature dependence of the correlation time along every isobar considered. The arrow indicates increasing pressure from 70 bar (blue circles) to 100 bar (brown circles), in steps of 5 bar.

Next, to quantify the behavior of the density domains of $scCO_2$, we have applied the DBSCAN algorithm[17] to molecular positions obtained from molecular dynamics simulations. Previous works have shown[20] the importance of clustering and networking in supercritical fluids. We have shown in our previous work that the optimal values of DBSCAN parameters – ε and N – can be estimated from the position of extrema of the radial distribution function.[11] RDF analysis is discussed in a subsequent section. DBSCAN parameter *N* can be selected as the rank of the neighbor, *n*, for which $\sigma_{r^{(n)}_{COM-COM}}$ is maximized, while ε is the corresponding $\langle r^{(N)}_{COM-COM} \rangle$, see Fig. 5.10 (b,c). Applying such protocol for every thermodynamic state point to select DBSCAN parameters and using the coordinates of the COM of the CO_2 molecules at a given temperature along various isobars, we computed the distributions $p(N^{CORE}_{COM})$ and $p(N^{BORDER}_{COM})$, representing the number of core CO_2 molecules forming the core and the border region of the largest density domain, as identified by the DBSCAN algorithm.

An illustration of the discovered density domains is given in Fig. 5.7. In the low temperature regime, almost the majority of CO_2 molecules experience the same density. Here the core molecules are indicated by a given dark color while the border ones are indicated by the corresponding light color. As the temperature approaches T_c, larger amount of different density domains becomes identifiable. The size of each domain is decreasing with respect to the largest density domain at low temperature. This substantiates that near the T_C, the distribution of the density domain is inhomogeneous. At higher temperatures, the overall system is separated into many small density domains, thus indicating more homogeneous distribution of CO_2 molecules.

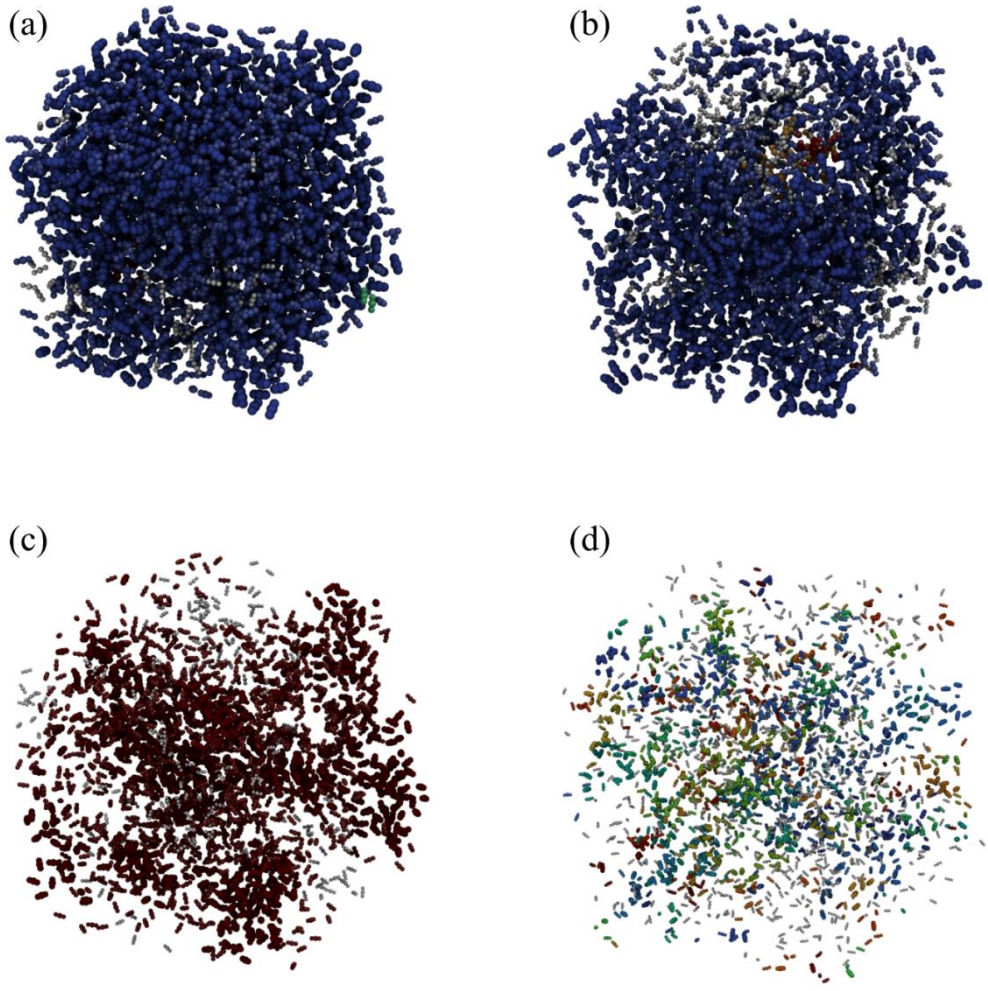

Figure 5.7. Color-coded images of different density domains as determined by the DBSCAN algorithm considering the center of mass of the CO_2 molecules at (a) liquids state T = 250 K; (b) at T = 290 K (c) near the critical temperature T = 300 K; (d) T = 450 K along the isobar P = 70 bar. A given color defines a density domain where the dark and light color identify its core and border CO_2 molecules. Gray color is reserved for noise-like molecules.

Below the critical temperature, distributions of density domain sizes are centered at just less than half the total amount of molecules with a standard deviation of 100 molecules. This indicates that largest density domain includes most of the molecules. However, at the critical point, the distributions become very wide, but still remain monomodal. This allows us to easily calculate and analyze moments of corresponding distributions and their dependence on the thermodynamical parameters. DBSCAN algorithm provides information not only about the distribution of core molecules of the density domains, but also that of the border molecules. The corresponding distributions are shown in Fig. 5.8 for P = 70 bar. As it is shown in this figure, temperature dependence of core and border distributions are quite similar. In this particular case, further analysis of border regions is redundant.

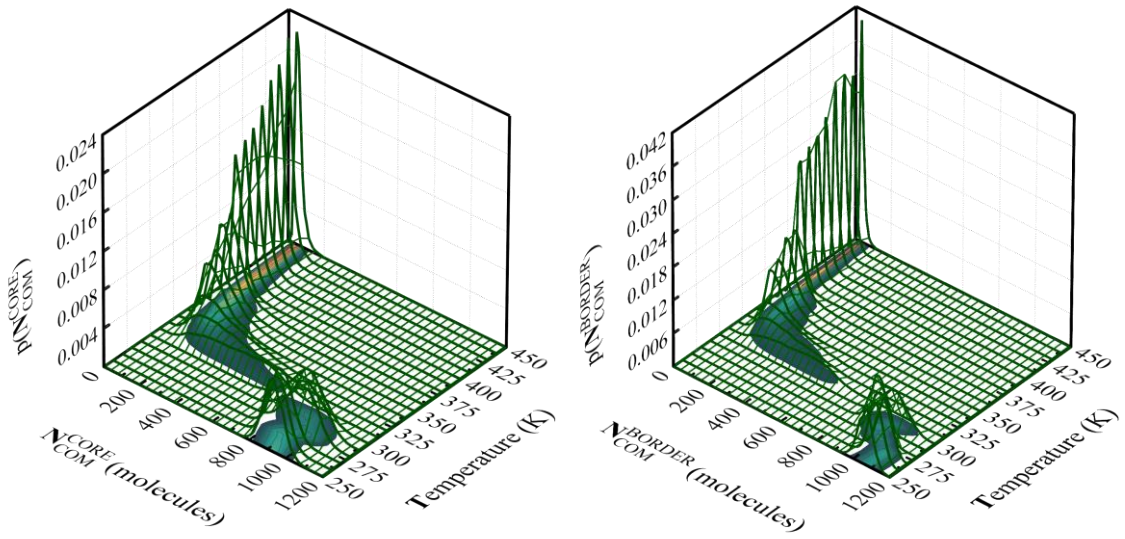

Figure 5.8. (a) Temperature dependence of the probability distribution of the number of CO_2 molecules in the core region of the largest DBSCAN density domain for P = 70 bar isobar. (b) The dependence of the probability distribution of the number of the border CO_2 molecules of the largest DBSCAN density domain for P = 70 bar isobar.

To quantify the changes in the shape of these distributions determined by the DBSCAN algorithm, along the various isobars, we have calculated first moments of these distributions, specifically the average values $\langle N_{COM}^{CORE} \rangle$ and the fluctuations, $\sigma_{N_{COM}^{CORE}}$. The behavior of these two metrics is shown in Fig. 5.9, highlighting the structural changes associated with temperature variations. At low temperatures, below the critical one, the average values $\langle N_{COM}^{CORE} \rangle$, shown in

Fig. 5.9 (a), seem not to be sensitive to the value of the pressure – at least in the 70 bar to 100 bar range, where about 50% of the molecules are part of the same density domain. This is consistent with the small compressibility of liquid CO_2. Near the critical temperature, the $\langle N_{COM}^{CORE} \rangle$ values decrease drastically, with a rate that is maximum near the critical pressure. That rate of change, however, is still much more modest than the corresponding rate of change for VP density or void radius. This indicates that maximally localized parameters, i.e., single molecule neighborhood density, are far more sensitive to changes in thermodynamic conditions than the more "global" functionals, like the DBSCAN density. Predictably, this rate of change decreases when the considered isobar is farther from the critical pressure. More interestingly, the $\sigma_{N_{COM}^{CORE}}$ values, shown in Fig. 5.9 (b), associated with the largest density domains, go through a maximum, indicating an increase in the fluctuation of the number of CO_2 molecules forming the corresponding density domains. This once again correlates with the increase of the inhomogeneity of the density near the critical point.

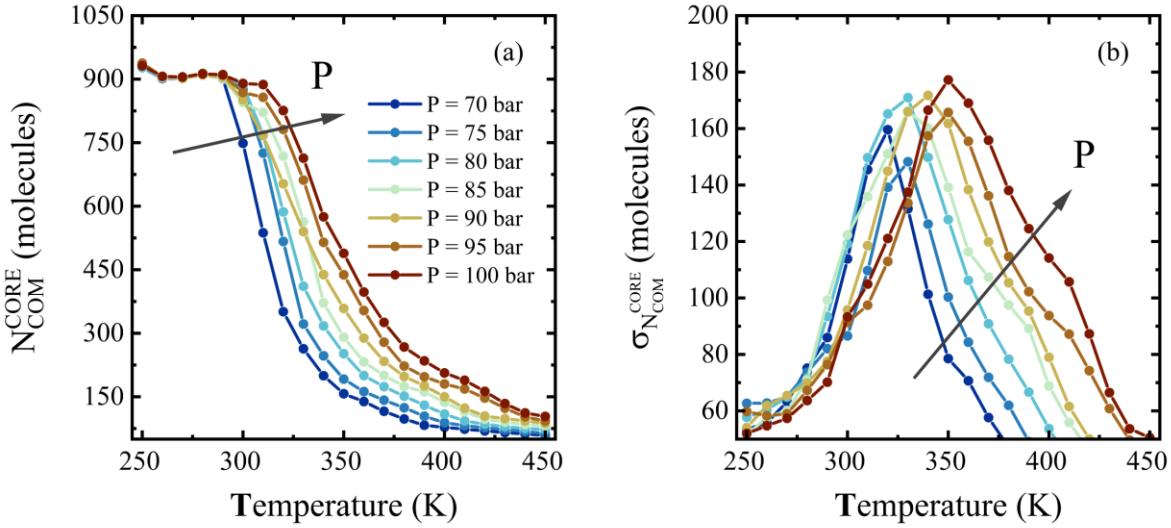

Figure 5.9. The dependence of the distribution average value (a) and standard deviation (b) of the number of CO_2 molecules in the core region of the largest DBSCAN density domain for some studied isobars. The arrow indicates increasing pressure from 70 bar (blue circles) to 100 bar (brown circles), in steps of 5 bar.

5.4. Local Structure

In order to gain better insight into the spatial arrangement of CO_2 molecules within density domains, we have calculated RDFs and NRDFs taking the center-of-mass (COM) of the CO_2 molecule as representative of its position. The RDF – g(r) – for the isobar P = 70 bar at T = 259 K is illustrated in Fig. 5.10 (a). At low temperatures, the positions of the well resolved minima at 6 Å and 9 Å define the first and second solvation shells, respectively. As the temperature crosses the critical value, the second minimum fades away completely while the first one undergoes the same change for temperatures higher than 350 K. In a second step, we calculated the nearest neighbor radial distributions[21,22] along each isobar. Based on these distributions, we calculate the average value of the nth nearest neighbor from the central one, $\langle r_{COM-COM}^{(n)} \rangle$ and the corresponding fluctuation, $\sigma_{r_{COM-COM}^{(n)}}$.

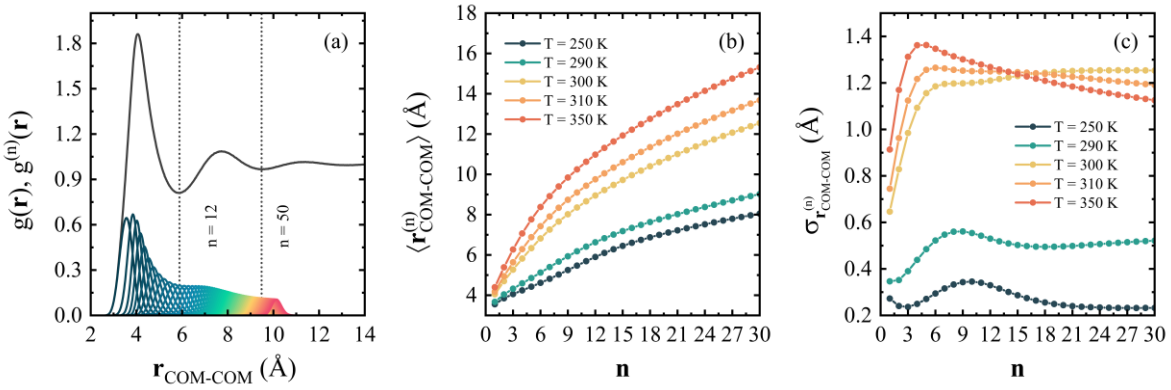

Figure 5.10. (a) Radial distribution function, (g(r)), and nearest neighbor radial distribution functions, ($g^n(r)$), for the first n = 50 neighbors indicated with color (more reddish colors correspond to more distant topological neighbors) along the isobar of P = 70 bar; (b) average distance to the center of mass of the nth neighbor from that of a reference CO_2 molecule in the liquid and supercritical states; (c) standard deviation of this distance.

Fig. 5.10 (a) shows that the minima in the RDFs correspond to the average values of certain nearest neighbor RDFs, for example, n = 12 and n = 50 for T = 250 K. Fig. 5.10 (b) shows that the $\langle r_{COM-COM}^{(n)} \rangle$ data increase nonlinearly with the temperature. In fact, this increase is the largest when the temperature is close to the critical value. As it was shown in our previous papers, the maximum in $\sigma_{r_{COM-COM}^{(n)}}$, shown in Fig. 5.10 (c), defines the spatial extent of the first

solvation shell[19,22]. It is smeared out when the temperature is close to the critical one and, more interestingly, we observe a noticeable jump in the value of $\sigma_{r^{(n)}_{COM-COM}}$. For values of *n* larger than 5, these standard deviations are almost equal, indicating that the fluctuation in the average distance reaches the order of the simulation box size. This behavior mimics the process of opalescence observed in SCF when crossing the critical temperature.

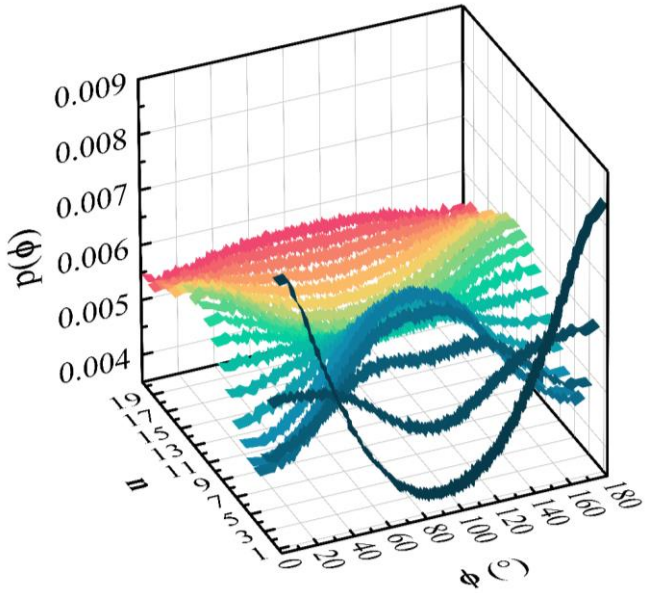

Figure 5.11. Dependence of probability density of the mutual angle between different nearest neighbor CO_2 molecules (indicated with color, red – higher neighbors) on the rank of the neighbor for T = 250 K and P = 70 bar.

Orientational behavior of $scCO_2$ is quite a bit more interesting than that of other fluids. CO_2 molecules, due to their symmetry, lack a permanent dipole moment. Instead, the charge distribution within the molecule is governed by its quadrupole moment, with a charge of -0.35 e localized on the oxygen atoms. The orientation between two CO_2 molecules is described by the angle – φ – between their O–O axes. As it is shown in Fig. 5.11, the most stable configuration is a parallel orientation with an offset, where the carbon atom of one molecule aligns closely with the oxygen atom of the other. For more distant neighbors, typically the third and beyond, a strong tendency toward a perpendicular orientation emerges. Our results, presented in subsequent sections, indicate that these preferences are primarily driven by attractive ES interactions between oxygen and carbon atoms. Beyond these proximities, the mutual orientations of CO_2 molecules eventually become random and uniformly distributed.

5.5. Pair-Interaction Energies

The behavior of local density fluctuations is driven by the specific behavior of the attractive and repulsive interactions, which are modulated by variations of the temperature and pressure. To investigate this point, we calculated the interaction energy distributions between a reference CO_2 molecule and its n nearest neighbors along the 70 bar and 100 bar isobars in the temperature range of 250 K to 450 K. As can be seen from Fig. 5.12, the distributions of the total interaction energy (TOT), electrostatic (ES) and Lennard-Jones (LJ) contributions for different neighbors have, generally, skew-Gaussian shape. Total interaction energy distributions and that associated with the LJ contribution skew towards lower values i.e., more attractive interactions. While those of the ES interaction energy, on the other hand, seem to be symmetric around zero, even for the first nearest neighbor. Due to the dominance of the LJ contribution, TOT plots are quite similar to the LJ ones.

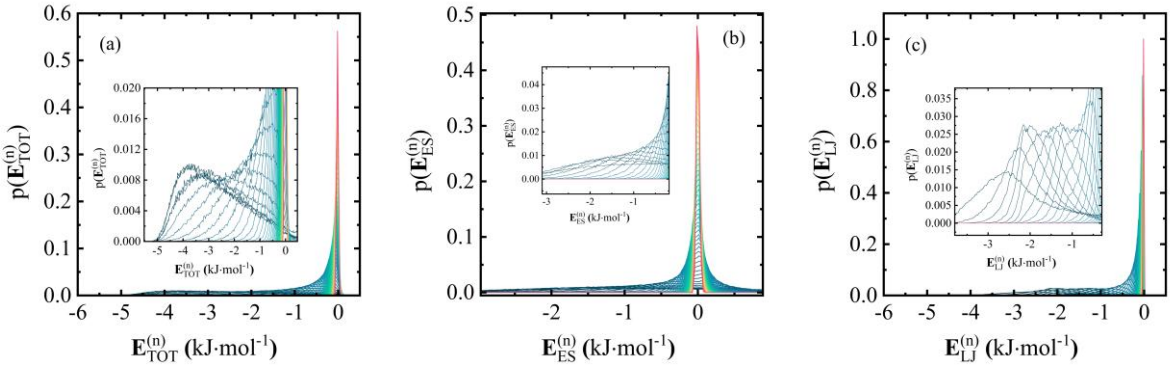

Figure 5.12. Distributions of (a) total interaction energy, (b) electrostatic and (c) LJ contributions between a reference CO_2 molecule and its neighbors (n = 1 – 50) as determined by the nearest neighbor radial distribution function for T = 250 K and P = 70 bar. Higher neighbors are indicated with redder colors.

The average values, $\langle E^{(n)}_{TOT} \rangle$, $\langle E^{(n)}_{LJ} \rangle$ and $\langle E^{(n)}_{ES} \rangle$, corresponding to the total interaction energy, the contributions from LJ potential and ES potential, were extracted for each neighbor *n* and are presented in Fig. 5.13. These averages demonstrate that interactions between CO_2 molecules are predominantly attractive. At lower temperatures (liquid state of CO_2), the attractive interactions $\langle E^{(n)}_{TOT} \rangle$, $\langle E^{(n)}_{LJ} \rangle$ show significant spatial extent even beyond the first solvation shell and remain still attractive even for neighbors located in the second solvation

shell, although the corresponding values are smaller. At higher temperatures, on the other hand, their spatial extent is strongly reduced below that of the first solvation shell. It is particularly striking that a gap arises in the rate of decrease of the three average interaction energies when crossing the critical temperature along an isobar near the critical point. However, this gap narrows as the isobar shifts further away from the critical region.

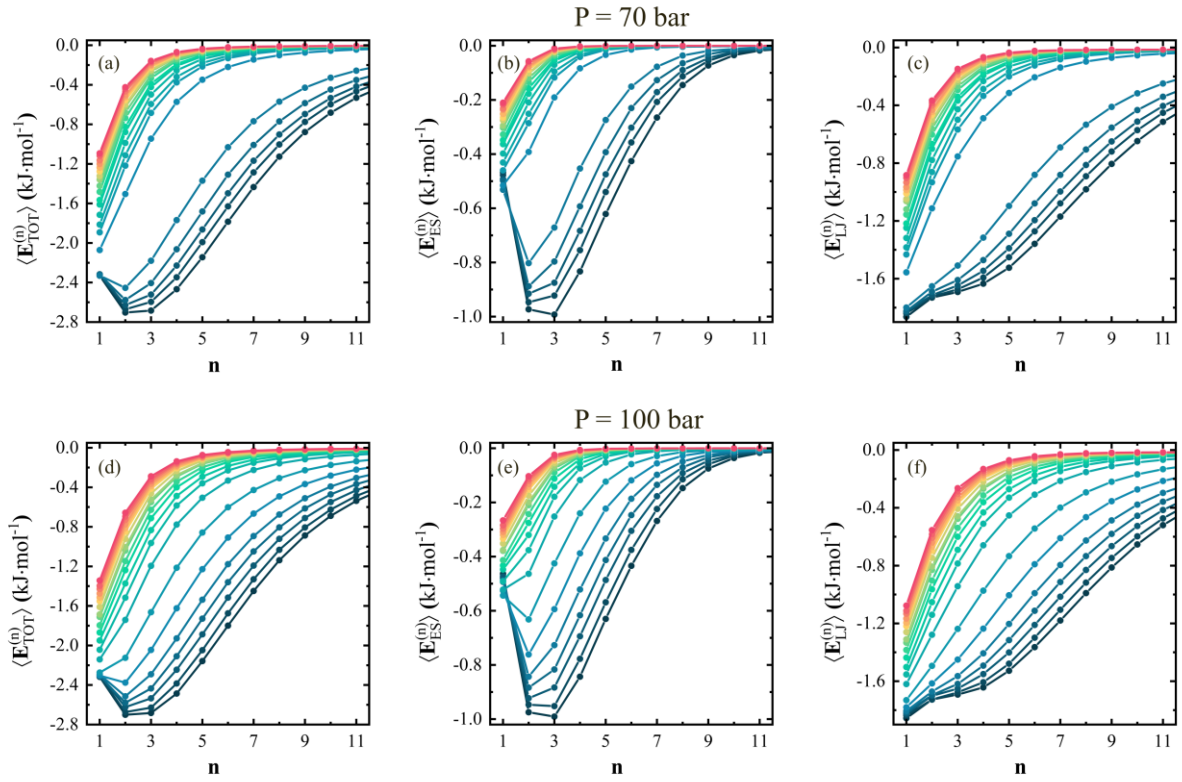

Figure 5.13. Dependence of the average value of the total interaction energy (a,d), electrostatic (b,e) and Lennard-Jones (c,f) between different neighbors in the temperature range of 250 K to 450 K along two isobars: P = 70 bar (a,b,c) and P = 100 bar (d,e,f). Higher temperature data are shown by more reddish shades. The inset of these figures highlights the behavior of the interaction energies involving close nearest neighbors.

The spatial range and magnitude of $\langle E_{ES}^{(n)} \rangle$ are lower than those of $\langle E_{LJ}^{(n)} \rangle$. The attractive effect of the electrostatic contribution is, on average, reduced for neighbors beyond the first solvation shell. This finding is rather counterintuitive, given the much slower decrease of the Coulomb potential than that of the Lennard-Jones potential. One possible explanation lies in the fact that, for the CO_2 molecule, dipole moment is negligible (even when the angle in the

simulation is not exactly 180°) and quadrupole interactions decay quite quickly with range, leading to a strong cancellation at large distances. Interestingly, an inflection point and a maximum are observed in the $\langle E_{ES}^{(n)} \rangle$ and $\langle E_{LJ}^{(n)} \rangle$ values, respectively, between a reference CO_2 molecule and its third-nearest neighbor.

To investigate the effect of temperature on the relative contributions of ES and LJ potentials to the total energy as a function of the neighbor rank, *n*, the ratio of their average values to the total sum of their average values was computed. This analysis was performed along the two extreme isobars studied – 70 bar and 100 bar. Results are summarized in Fig. 5.14. Independently on the temperature and pressure values, LJ contribution ratios are higher than those of the ES. It is noteworthy that for temperatures below the critical point, some neighboring particles (e.g., neighbor n = 12 and n = 21 for T = 250 K, P = 70 bar) exhibit ES ratio values close to zero and LJ ratio values close to 1. These extrema mark the boundary of the first and second solvation shells. Within each shell, the ES ratio reaches a maximum value for neighbors around n ~ 2–3 and around n ~ 21, while the LJ ratio exhibits a minimum value for the same neighbors (though it remains higher than the ES ratio). Of note is that the neighbors at which these extrema occur are characterized by distances that are located within the RDF's first and second maxima, respectively, as was shown in Fig. 5.10 (a).

When the temperature increases, the extremum, occurring for the two ratios at the level of the second solvation shell (n ~ 21), shifts to lower *n* values and vanishes when the temperature is higher than the critical one, while the extremum occurring at the level of the first solvation shell (n ~ 2–3) shifts to occur for *n* = 1. For isobars located beyond the critical one, the ES ratio progressively decreases with each neighbor *n*, eventually reaching zero at the fifth neighbor (*n* = 5). In contrast, the LJ ratio steadily increases with each *n* and approaches a value of 1 for the same neighbor. It is noteworthy that when examining isobars farther from the critical one, such as P = 100 bar, the interplay between the ES and LJ attractive ratios in CO_2 still resembles that observed near the critical isobar. The key distinction, however, lies in the pattern of weakening for these attractive interactions: rather than exhibiting a gap, a gradual reduction in the strength of the ES attractive interactions and a gradual increase in the strength of the LJ attractive contributions is observed.

The balance between the LJ and ES contributions is in favor of the former one. As a consequence, LJ potential determines the packing of CO_2 molecules while the ES one promotes their orientation. This interplay between the spatial extent of the ratios of LJ and ES contributions then defines the radial and orientation behavior of CO_2 molecules in the first and

second solvation shells. For instance, as the result of the minimal attractive contribution of the ES (with respect to the LJ attractive contribution) to the first neighbor, it typically adopts a non-minimum energy parallel orientation with substantial positional fluctuations, while the second and third neighbor exhibit a perpendicular orientation (T-shape) distribution with minimal distance fluctuations (see Fig. 5.11).[22] This is driven by a concomitant maximal and minimal contribution of the ES and LJ contributions ratios, respectively, to these neighbors (although the relative contribution of dispersion is always higher than that of electrostatic interaction).

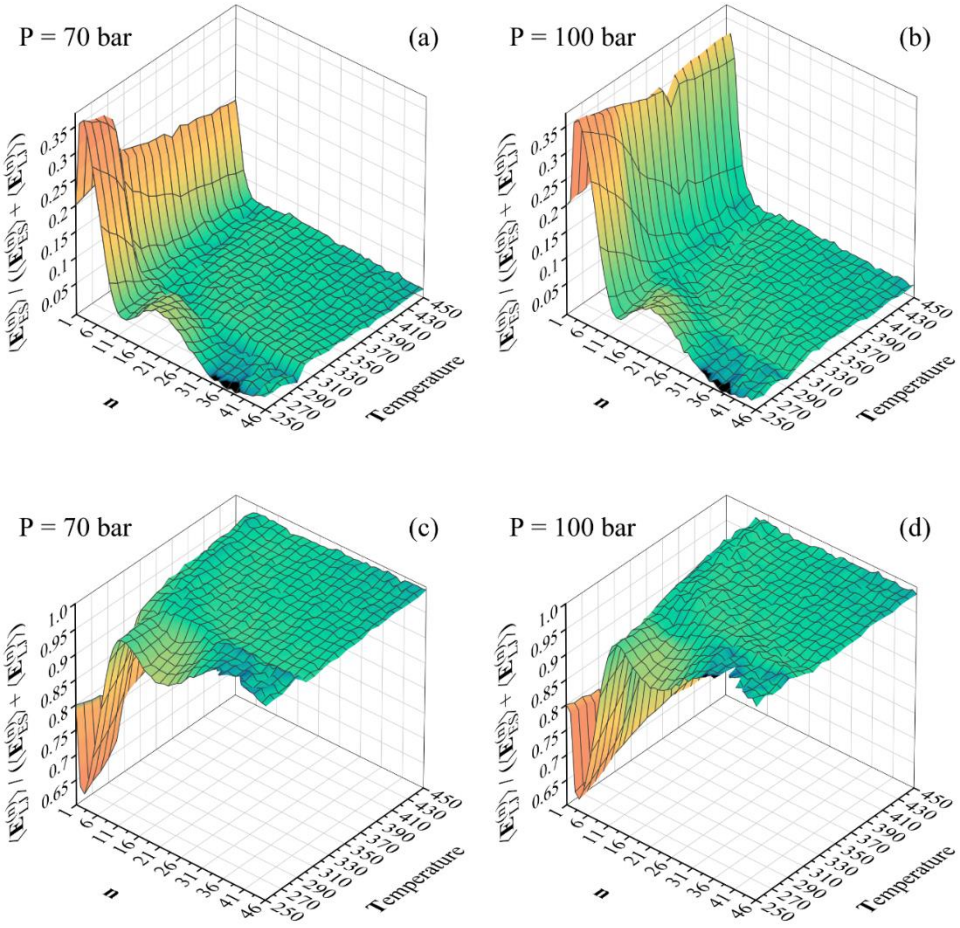

Figure 5.14. Dependence of the ratio of the average values of ES (a,b) and LJ (c,d) contributions to the total interaction energy for the different topological neighbors, as obtained in the temperature range between 250 K and 450 K along two isobars: P = 70 bar (a,c) and P = 100 bar (b,d).

The behavior of the local density as a function of the temperature as obtained from the Voronoi analysis and the DBSCAN algorithm is compatible with the above described weakening of the spatial extent of the ES and LJ attractive contributions to the total interaction

energy. Indeed, as the spatial extent of attractive interactions decreases, CO_2 molecules can only interact with their immediate neighbors. This causes the creation of high-density zones in which CO_2 molecules are more strongly bonded together. Low-density domains arise when CO_2 molecules are far apart and have weaker or negligible interactions. The weakening of attractive interactions makes the local structure more susceptible to changes caused by an increase in thermal energy, resulting in density fluctuations.

However, $scCO_2$ results are not exactly universal to supercritical fluids in general. To back up this conclusion, we performed molecular dynamics simulations on supercritical water and ammonia. Same analysis, particularly pair-interaction energy analysis, was carried out for these two molecular systems along various isobars. The average values, $\langle E_{TOT}^{(n)} \rangle$, $\langle E_{LJ}^{(n)} \rangle$ and $\langle E_{ES}^{(n)} \rangle$ were extracted for each neighbor *n* and are presented in the Fig 5.15 and Fig. 5.16 for scH_2O and $scNH_3$, respectively.

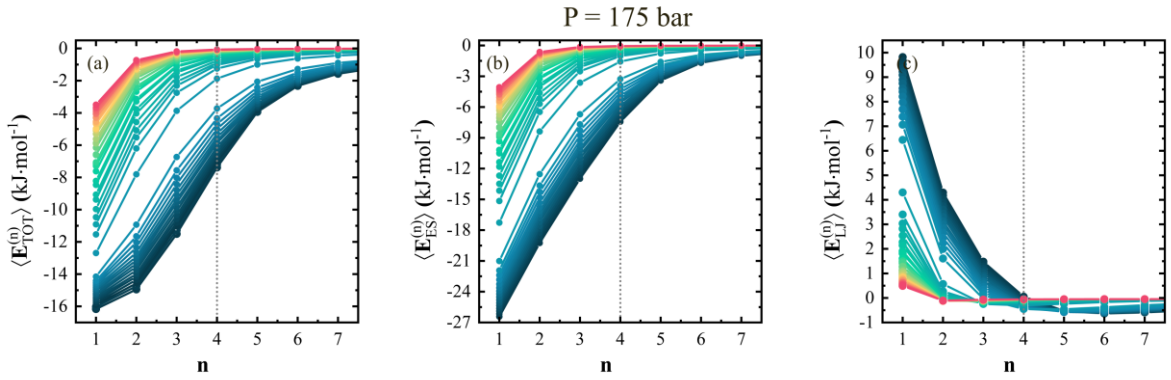

Figure 5.15 Dependence of the average value of the ES, LJ and TOT contributions to pair interaction energies between a reference water molecule and its neighbors in the temperature range of 500 K to 1000 K along the isobar P = 175 bar. Higher temperature data are shown by more reddish shades. The vertical dashed line indicates the coordination number determined by the position of the first minimum in the radial distribution function.

The results show that similarly to what we found in CO_2, the $\langle E_{TOT}^{(n)} \rangle$, $\langle E_{LJ}^{(n)} \rangle$ and $\langle E_{ES}^{(n)} \rangle$, values undergo a noticeable change when crossing the critical temperature. However, in both water and ammonia, in contrast to CO_2, ES interactions overwhelmingly dominate over LJ interactions, leading to a distinct local organization. Furthermore, at room temperature, in both water and ammonia, the apparent effective distance of the ES potential is higher than that of the LJ one. Indeed, in water, the former interactions approach zero for the $n \sim$ 6-7 neighbor while

the later do so for $n \sim 4$-5. Unlike CO_2, where molecules typically have ~12 nearest neighbors in the first solvation shell (position of the first minimum in the radial distribution function), water's strong electrostatic interactions result in a tetrahedral arrangement with only 4-5 nearest neighbors. Upon a temperature increase along the isobar at 175 bars in water, or along the 110 bar isobar in ammonia, similarly to what we observed in CO_2, the spatial extent of the ES and LJ contributions is reduced.

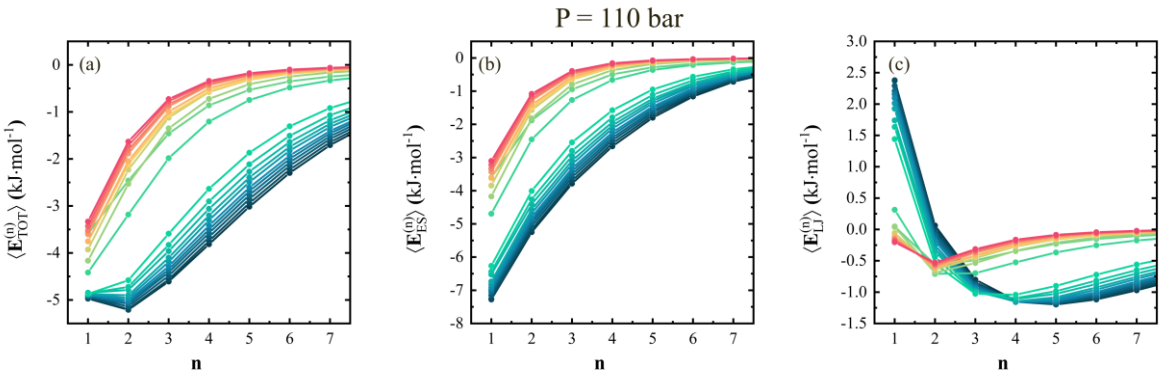

Figure 5.16. Dependence of the average value of the ES, LJ and TOT contributions to pair interaction energies between a reference ammonia molecule and its neighbors in the temperature range of 350 K to 450 K along the isobar P = 110 bar. Higher temperature data are shown by more reddish shades. The vertical dashed line indicates the coordination number determined by the position of the first minimum in the radial distribution function.

These comparison shows clearly that the analysis of the interplay between the electrostatic and non-electrostatic interactions is pertinent to analyze the change in the local structure. Regardless of the fluid involved, MD simulations are able to capture the discontinuity in the thermodynamic properties near the critical point and, even more importantly, are able to demonstrate same discontinuity in structural properties as well. Coupled with general advantages of $scCO_2$, underlined in Ch. 1, this underlines our decision to study CUR-$scCO_2$ interfaces in subsequent chapters.

5.6. Conclusions

In summary of this chapter, the analysis of the local statistical observables has allowed us to determine the thermodynamic conditions where the density fluctuations are occurring. Various functionals, such as the nearest neighbor radial distribution functions and corresponding interaction energies, Voronoi polyhedra properties and DBSCAN-identified density domains, all point to the maximization of density fluctuations directly at the critical point. They also underline how quickly those fluctuations become less prominent at temperatures and pressures higher than the critical ones.

A key contributor to such dependence is the interplay between the attractive electrostatic and non-electrostatic interactions. We have shown how this interplay affects structuring (radial and orientation) of the first and second solvation shells of CO_2 and other fluids. The ranks of the neighbors at which attractive ES and LJ interactions display, respectively, maximal and minimal contributions define the extent of n^{th} solvation shell. Upon increasing the temperature beyond the critical one, the spatial extent of the ES and LJ interactions is drastically reduced, which results in less pronounced structuration within the solvation shells.

5.7. Bibliography

(1) Abraham, M. J.; Murtola, T.; Schulz, R.; Páll, S.; Smith, J. C.; Hess, B.; Lindahl, E. GROMACS: High Performance Molecular Simulations through Multi-Level Parallelism from Laptops to Supercomputers. *SoftwareX* **2015**, *1–2*, 19–25. https://doi.org/10.1016/j.softx.2015.06.001.

(2) Zhu, A.; Zhang, X.; Liu, Q.; Zhang, Q. A Fully Flexible Potential Model for Carbon Dioxide. *Chin. J. Chem. Eng.* **2009**, *17* (2), 268–272. https://doi.org/10.1016/S1004-9541(08)60204-9.

(3) Jorgensen, W. L.; Tirado-Rives, J. Potential Energy Functions for Atomic-Level Simulations of Water and Organic and Biomolecular Systems. *Proc. Natl. Acad. Sci.* **2005**, *102* (19), 6665–6670. https://doi.org/10.1073/pnas.0408037102.

(4) Dodda, L. S.; Cabeza de Vaca, I.; Tirado-Rives, J.; Jorgensen, W. L. LigParGen Web Server: An Automatic OPLS-AA Parameter Generator for Organic Ligands. *Nucleic Acids Res.* **2017**, *45* (W1), W331–W336. https://doi.org/10.1093/nar/gkx312.

(5) Wang, J.; Wolf, R. M.; Caldwell, J. W.; Kollman, P. A.; Case, D. A. Development and Testing of a General Amber Force Field. *J. Comput. Chem.* **2004**, *25* (9), 1157–1174. https://doi.org/10.1002/jcc.20035.

(6) Sousa da Silva, A. W.; Vranken, W. F. ACPYPE - AnteChamber PYthon Parser interfacE. *BMC Res. Notes* **2012**, *5* (1), 367. https://doi.org/10.1186/1756-0500-5-367.

(7) Vanommeslaeghe, K.; Hatcher, E.; Acharya, C.; Kundu, S.; Zhong, S.; Shim, J.; Darian, E.; Guvench, O.; Lopes, P.; Vorobyov, I.; MacKerell, A. D. CHARMM General Force Field (CGenFF): A Force Field for Drug-like Molecules Compatible with the CHARMM All-Atom Additive Biological Force Fields. *J. Comput. Chem.* **2010**, *31* (4), 671–690. https://doi.org/10.1002/jcc.21367.

(8) Cygan, R. T.; Romanov, V. N.; Myshakin, E. M. Molecular Simulation of Carbon Dioxide Capture by Montmorillonite Using an Accurate and Flexible Force Field. *J. Phys. Chem. C* **2012**, *116* (24), 13079–13091. https://doi.org/10.1021/jp3007574.

(9) Bussi, G.; Donadio, D.; Parrinello, M. Canonical Sampling through Velocity Rescaling. *J. Chem. Phys.* **2007**, *126* (1), 014101. https://doi.org/10.1063/1.2408420.

(10) Bussi, G.; Zykova-Timan, T.; Parrinello, M. Isothermal-Isobaric Molecular Dynamics Using Stochastic Velocity Rescaling. *J. Chem. Phys.* **2009**, *130* (7), 074101. https://doi.org/10.1063/1.3073889.

(11) Idrissi, A.; Vyalov, I.; Georgi, N.; Kiselev, M. On the Characterization of Inhomogeneity of the Density Distribution in Supercritical Fluids via Molecular Dynamics Simulation and Data Mining Analysis. *J. Phys. Chem. B* **2013**, *117* (40), 12184–12188. https://doi.org/10.1021/jp404873a.

(12) Ester, M.; Kriegel, H.-P.; Sander, J.; Xu, X. A Density-Based Algorithm for Discovering Clusters in Large Spatial Databases with Noise. In *Proceedings of the Second International Conference on Knowledge Discovery and Data Mining*; KDD'96; AAAI Press: Portland, Oregon, 1996; pp 226–231.

(13) Martin, M. G. MCCCS Towhee: A Tool for Monte Carlo Molecular Simulation. *Mol. Simul.* **2013**, *39* (14–15), 1212–1222. https://doi.org/10.1080/08927022.2013.828208.

(14) Martínez, L.; Andrade, R.; Birgin, E. G.; Martínez, J. M. PACKMOL: A Package for Building Initial Configurations for Molecular Dynamics Simulations. *J. Comput. Chem.* **2009**, *30* (13), 2157–2164. https://doi.org/10.1002/jcc.21224.

(15) Idrissi, A.; Vyalov, I.; Damay, P.; Frolov, A.; Oparin, R.; Kiselev, M. Assessment of the Spatial Distribution in Sub- and Supercritical CO_2 Using the Nearest Neighbor Approach: A Molecular Dynamics Analysis. *J. Phys. Chem. B* **2009**, *113* (48), 15820–15830. https://doi.org/10.1021/jp9042107.

(16) Okabe, A.; Boots, B. N.; Sugihara, K. *Spatial Tessellations: Concepts and Applications of Voronoi Diagrams*; Wiley & Sons, 1992.

(17) Shagurin, A.; Miannay, F. A.; Kiselev, M. G.; Jedlovszky, P.; Affouard, F.; Idrissi, A. Widom Line in Supercritical Water in Terms of Changes in Local Structure: Theoretical Perspective. *J. Phys. Chem. Lett.* **2024**, *15* (22), 5831–5837. https://doi.org/10.1021/acs.jpclett.4c01142.

(18) Simeski, F.; Ihme, M. Supercritical Fluids Behave as Complex Networks. *Nat. Commun.* **2023**, *14* (1), 1996. https://doi.org/10.1038/s41467-023-37645-z.

(19) Idrissi, A.; Vyalov, I.; Kiselev, M.; Fedorov, M. V.; Jedlovszky, P. Heterogeneity of the Local Structure in Sub- and Supercritical Ammonia: A Voronoi Polyhedra Analysis. *J. Phys. Chem. B* **2011**, *115* (31), 9646–9652. https://doi.org/10.1021/jp204078u.

(20) Choudhary, A.; Kundu, A.; Singh, C.; Sharma, A.; Pant, K. K.; Chandra, A. Supercritical Water: Density-Independent Angular Jumps. *J. Phys. Chem. B* **2025**, *129* (1), 329–337. https://doi.org/10.1021/acs.jpcb.4c05676.

(21) Keyes, T. Neighborship Structure and Dynamics in Supercooled Liquids. *J. Chem. Phys.* **1999**, *110* (2), 1097–1105. https://doi.org/10.1063/1.478153.

(22) Idrissi, A.; Damay, P.; Kiselev, M. Nearest Neighbor Assessments of Spatial Distribution in CO2: A Molecular Dynamics Analysis. *Chem. Phys.* **2007**, *332* (1), 139–143. https://doi.org/10.1016/j.chemphys.2006.11.037.

CHAPTER 6
$scCO_2$ INTERFACE

In the first part of this chapter, we investigate both how the local structure and dynamics of the supercritical CO_2 are affected once $1.1 \cdot \rho_c$ of CO_2 is brought in contact with [100] interface of POLY-I as the temperature increases between 250 K and 350 K. In the second part, we investigate the structure and dynamics of the CUR-supercritical CO_2 interface at the [100] crystallographic plane of the three CUR polymorphs. We use the same descriptor of the structure and dynamics as in Ch. 4.

6.1. Computational Methods

Molecular dynamics simulations were performed using the GROMACS 2024.4[1] program package. Simulations within the NVT ensemble were performed with the use of Parinello-Bussi[2,3] thermostat. Simulation boxes contained 480 fully flexible curcumin molecules. Each starting point corresponds to the crystal of a specific polymorph, with data[4,5] taken from CCDC. Chosen configurations are summarized in Table 3.1 in Ch. 3. The boxes were padded by 3 times the initial volume along the "a" crystallographic axis. Empty volume was filled with flexible CO_2 molecules to the desired density. Exact number of used CO_2 molecules is summarized in Table 6.1. Further discussion is centered on the $1.1 \cdot \rho_c$ calculations.

Table 6.1. Exact amount of CO_2 molecules used in each simulation in this chapter. Densities are given as a proportion of the critical point density of the CRM model of CO_2.

	$0.9 \cdot \rho_c$	$1.0 \cdot \rho_c$	$1.1 \cdot \rho_c$
POLY-I	2406	2673	2940
POLY-II	2364	2627	2890
POLY-III	2525	2805	3086

Minimization was performed with GROMACS using conjugate gradient (CG) method with a 0.001 nm step size and as many steps as needed until convergence. For Lennard-Jones, we have used a cut-off scheme with potential-shifting and r_c = 10.0 Å. For electrostatic interactions, a reaction-field potential with the same cutoff as Lennard-Jones was chosen instead of PME in order to minimize unwanted interactions in the interfacial slab simulations.

Equations of motion were integrated in time steps of 1 fs. After an at least 10 ns long equilibration period, statistical data (such as temperatures, pressures, nearest neighbor distances, local densities, etc.) was collected using 3000 equilibrium sample configurations, separated from each other by 2 ps long trajectories each, from the 6 ns long production run at every temperature.

During the analysis of interfacial calculations, identification of the molecules (either CUR or CO_2) was performed via the ITIM[6] method using the PYTIM[7] package (see Ch. 2 for details). Probe-sphere grid spacing was set to 0.4 Å and probe radius to 1.7 Å.

6.2. Structure and Dynamics of CO_2 at the Interface

In the range of temperature between 250 K and 350 K, CUR remains in the crystalline phase. It was interesting to investigate the effect of the presence of this solid interface with CO_2 on the local properties and compare them with the ones determined in the bulk CO_2 (as it is discussed in Ch. 5). We have then performed additional simulation at [100] CUR interface of POLY-I in contact with CO_2 at $1.1 \cdot \rho_C$ density of $scCO_2$ between 250 K and 350 K with a step of 10 K.

6.2.1. Density Profiles

The first key question concerns the organization of the CO_2 molecules at the crystal CUR interface. In order to investigate this, we have calculated mass-density profiles of CO_2 along the axis of the interface. Fig. 6.1 (a) provides a visual snapshot of multiple layers of CUR and CO_2 molecules situated at said interface. Fig. 6.1 (b) shows the total mass density profiles of CO_2 for different temperatures.

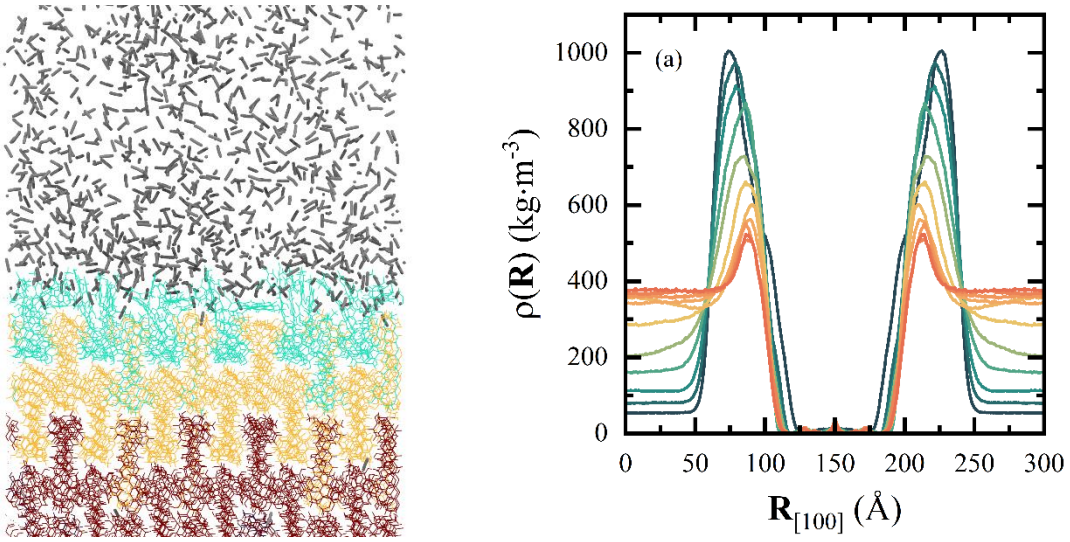

Figure 6.1. (a) Snapshot of the CO_2 molecules and CUR layers at their interface. (b) Mass-density profiles of CO_2 along the normal to the [100] interface of POLY-I. Temperature varies from 250 K to 350 K. Redder shades indicate higher temperature.

As expected, CO_2 mass density distributions have two contributions: one corresponding to the liquid density near the CUR and vapor density at the edges of the simulation box. The extent of the difference between the two densities decreases with temperature, but never becomes zero. This suggests a favorable energetic interaction between CO_2 and CUR, leading to adsorption at the interface.

6.2.2. Residence Time and Adsorption

To quantify how strong is the adsorption of CO_2 on the CUR interface, we have compared residence times at different interfacial layers of CO_2. As is the case in Ch. 4, distributions of the residence times are highly bi-modal, even for CO_2, so we have split the analysis for "slow" and "fast" times of residence of CO_2 molecules at the interface. Average values of the fast residence times are given in Fig. 6.2.

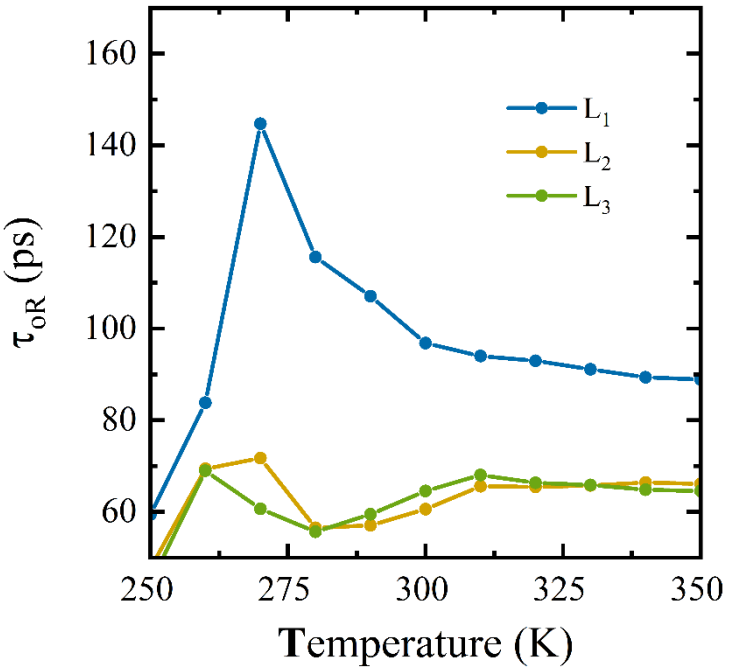

Figure 6.2. Temperature-dependent average time of residence at the designated layer for fast-moving CO_2 molecules (less than 50% of the time spent in the designated layer) at the [100] interface of POLY-I.

This figure shows that the time of residence of CO_2 molecules belonging to the first interfacial layer is significantly higher than that of the molecules belonging to the second one. This is consistent with the presence of a contribution, near CUR interface in the total mass

density distributions. Interfacial ToR also has a maximum around 275 K, which is not as prominent for the subsequent layers. This maximum indicates that the adsorption strength is maximized for the liquids CO_2, since the residence time is lower at T_c = 300 K. This is likely due to the confounding factors of higher mobility of interfacial CUR molecules leading to more favorable interactions and increased diffusivity of the supercritical CO_2 as compared to the liquid one.

6.2.3. Local Density

We used Voronoi polyhedra approach to analyze the local structure of the interfacial CO_2 molecules. The average values of the local density and standard deviations of the VP density are given in Fig. 6.3 (a,b) respectively, as well as those calculated in the bulk CO_2. Of note is that in the bulk CO_2, the local density is sampling the liquid and vapor phases that are present at the CUR interface and at the edges of the simulation box, respectively, while when applied to CO_2 molecules at the interface of CUR, the VP approach samples only the liquid density.

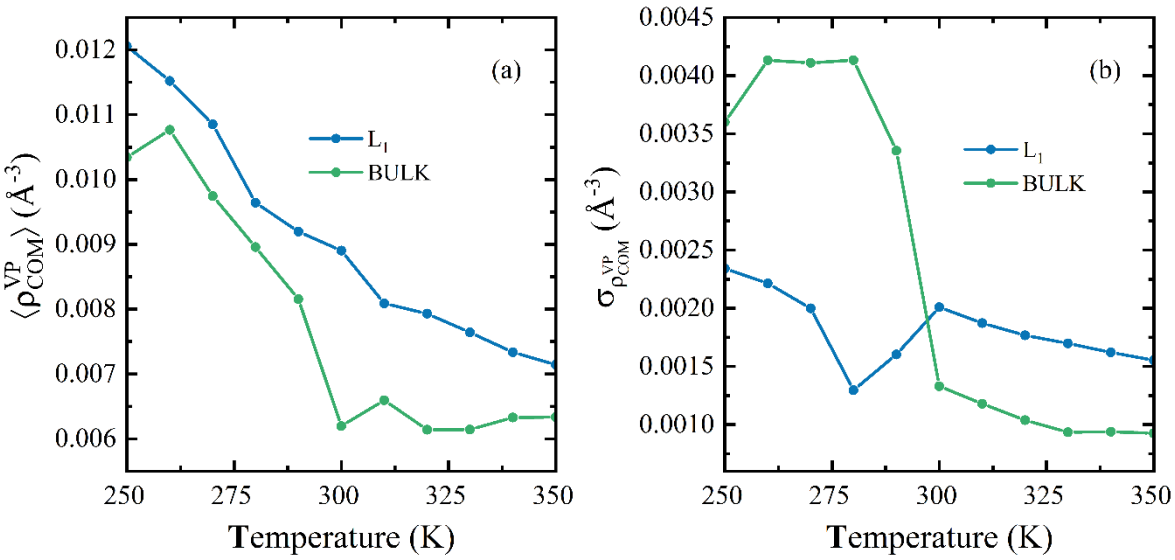

Figure 6.3. Comparison of the temperature dependence of the (a) average value and (b) standard deviation of the VP density of interfacial and bulk molecules in the simulation of [100] interface of POLY-I in contact with scCO₂.

The local density changes around 300 K, seen in Ch. 5, are significantly smoothed out by the presence of the CUR interface. The rate of decrease of the local density is high for temperatures below 300 K and it plateaus for further increase of the temperature. The local density of the interfacial CO_2 molecules decreases steadily with temperature without any noticeable large change in the rate of decrease near T = 300 K. Fluctuation values are higher in the bulk and max out at lower temperatures in the interfacial simulation. The 1st layer seems to be totally different, with fluctuation values having a minimum in the liquid state. Both graphs in Fig. 6.3 have about the same numerical scale as those of the pure $scCO_2$ simulation, though the densities are noticeably lower, while the fluctuations are noticeably higher. This is, most likely, because of the strong interactions between the interfacial CO_2 molecules and the CUR molecules.

6.2.4. Nearest Neighbor Distributions

One of the unique properties of $scCO_2$, compared to other SCFs, is the fluctuation in the position of the first nearest neighbor. Said fluctuation is, in the liquid state, higher than that of the 2nd neighbor. As we have seen in the previous chapter, the reason for such behavior lies in the interplay between ES and LJ contributions to the total pair interaction energy within the first solvation shell. Notably, this small peak in the fluctuation-neighbor graph disappears upon crossing the critical point. To test the state of the CO_2 in the CUR interfacial simulations, we have summarized average distance between neighbors and their fluctuation in Fig. 6.4 (a,b).

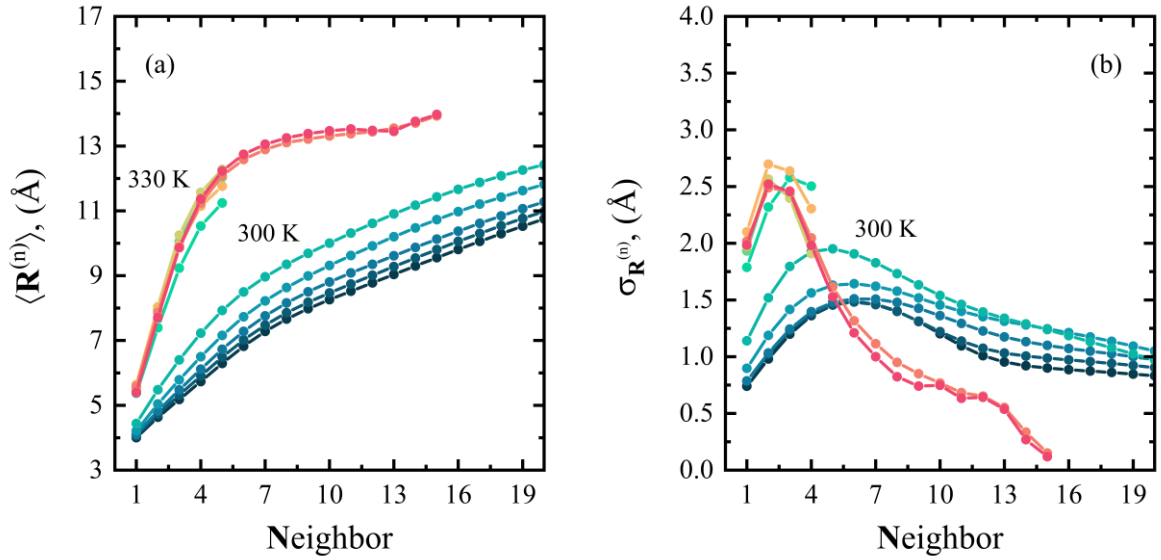

Figure 6.4. Temperature dependence of the (a) average position and (b) standard deviation of said position of the n^{th} nearest neighbor of CO_2 within the 1^{st} layer of [100] interface of POLY-I.

Immediately, one can notice that smooth increase of the average distances between neighbors, seen Fig. 5.10 (b), and present here at temperatures below the critical one, gives way to an under-sampled stretch between 300 K and 330 K, where only a few close neighbors can be determined. This happens due to unusually large fluctuations near the critical point, which result in such wide distributions, that the size of the box, dictated by the lowest dimension of CUR, does not allow sufficient sampling. It is reasonable then to assume that in bigger simulation, curves between 300 K and 330 K would follow those of 340 K and above, leaving big gap between 290 K and 300 K, similar to Fig. 5.10 (b).

Aside from technical challenges, it is worth noting that the average distance between given neighbors grows faster than in the bulk $scCO_2$. This is likely due to energetically favorable adsorption, and not just because of the CUR taking up significant amount of space at the interface, as average distances in the 2^{nd} and 3^{rd} layers also grow faster than those in Ch. 5.

Even more interestingly, as fluctuations in Fig. 6.4 (b) show, 1^{st} neighbor is no longer less stable than the second one. This is again the case for subsequent layers as well. The neighbor of maximal fluctuation, which defines the size of the first solvation shell, is much lower, around $n = 5\text{-}6$, compared to $n = 9\text{-}12$ for bulk liquid CO_2. Those numbers are, in fact, quite similar to bulk $scCO_2$, where fluctuation in the neighbor distances is maximized for $n = 3\text{-}4$. This is also the effect of attractive CUR interactions. Nevertheless, upon reaching 300 K, CO_2 molecules at

the interface experience large jump in the fluctuation of the position of the closest neighbors, but lowering in the fluctuation of the further ones, the cut-off being around $n = 3$. This is perhaps not surprising, since Fig. 6.4 (b) shows statistics of the intra-layer NRDFs, and CO_2 forms quite thin layers on the surface of CUR. Those thin layers also make it difficult to analyze the numerical scale of the fluctuations, but the presence of the large, almost 100% gap between 1st nearest neighbor values at 290 K and 300 K indicates phase transition to the SCF.

Analysis of NRDFs between a reference CO_2 molecule in the 1st layer and an observational CO_2 molecule in any part of the system, 1st layer or otherwise, seen in Fig. 6.5, also indicates lower size of the first solvation shell, although the cut-off lies at more reasonable $n = 4\text{-}6$ for the 1st layer and $n = 5\text{-}7$ for the 2nd layer in the liquid state. Moreover, in the 2nd layer, the instability in the position of the first neighbor is clearly defined up until the melting point, similar to the behavior of the $scCO_2$ bulk.

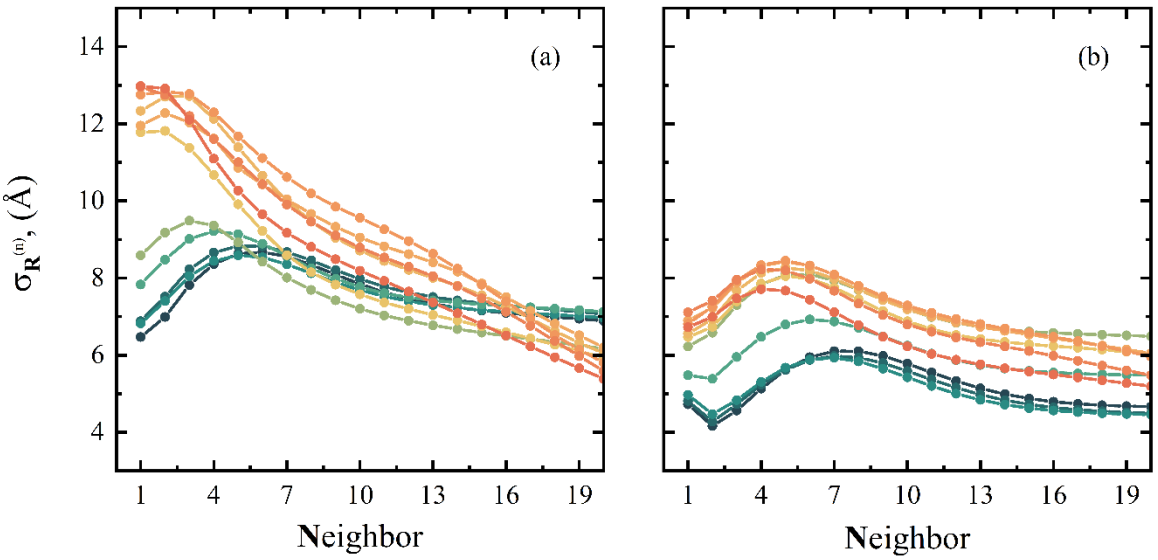

Figure 6.5. Temperature dependence of the standard deviation of the position of the nth nearest neighbor of CO_2 with the reference molecule being part of the (a) 1st and (b) 2nd layer of the [100] interface of POLY-I.

To get idea exactly how CO_2 forms the interfacial layers, we have obtained pair interaction energies for different neighbors within the $scCO_2$ layers. Separate ES and LJ contributions are given in Fig. 6.6 (a,b), respectively. Compared to the bulk values, both ES and LJ interactions are less attractive for the first few neighbors, likely as a consequence of the proximity of CUR molecules. The system is still LJ dominated, although the difference is not as significant. As

morphology of the CUR interface dictates the spatial organization of the adsorbed CO_2 molecules, the distances between those molecules end up being longer, which has larger impact on the LJ potential compared to the ES one.

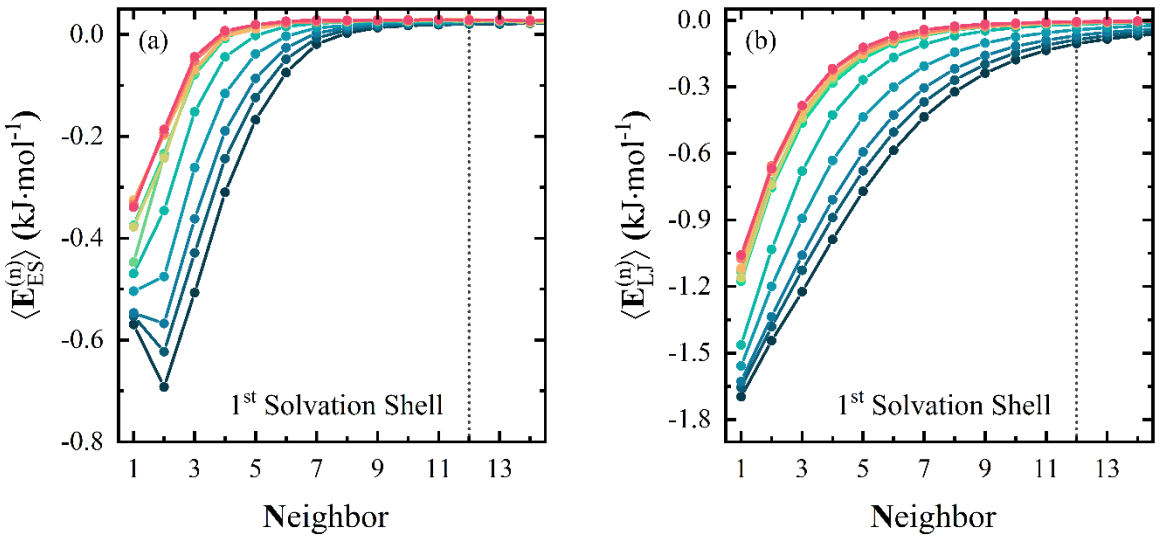

Figure 6.6. Dependence of the (a) ES and (b) LJ contribution to the total pair-interaction energy between CO_2 neighbors, with the reference molecule being at the [100] interface of POLY-I, on the rank of the neighbor for temperatures in the range between 250 K and 350 K. The 1st solvation shell cut-off is set according to the values for bulk $scCO_2$ in Ch. 5

Interestingly, the gaps between the curves for 290 K and 300 K, characteristic of the phase transition between liquid and supercritical states, are not as big as those of the neat $scCO_2$. This implies that the difference between forces in the liquid and supercritical phases is lower in the presence of the CUR interface. This is, perhaps, related to the hydrogen bonding ability of CUR, but that data will be discussed in the subsequent sections.

Although not given here, pair-interaction energies for the reference molecules of the 2nd layer, as well as subsequent layers, match up rather well with the data of Ch. 5, leaving no doubt about both the special properties of the interfacial layer of CO_2 and the fact that the conditions and the setup of the interfacial MD simulation fatefully reproduce the behavior of supercritical CO_2.

6.3. Structure of Curcumin at the Interface

In order to investigate the structure and dynamics of CUR molecules at the interface with supercritical CO_2, we considered the isochoric conditions where the density is equal 1.1 times the critical density ($1.1 \cdot \rho_C$) in the range of temperature between 350 K and 600 K. Of note is that at 350 K the CO_2 is in a supercritical state. This range of temperatures includes the macroscopic melting temperature of CUR as determined by the force field used in this simulation.

The investigation of the structure and dynamics of the interfacial molecules includes various descriptors that were used to analyze the CUR-Vacuum interface presented in Ch. 4. Only the [100] crystallographic plane is considered for the three polymorphs.

6.3.1. Mass Density Profiles

We have computed the mass density profiles of CUR molecules belonging to the first two interfacial layers along the [100] crystallographic plane of POLY-I. From these profiles, we have extracted both the average positions of the layers and their thermal fluctuations. To compare how these layers evolve with temperature, we define the parameter: $\delta R(T)$ using $\delta R(T) = \langle R(T) \rangle - \langle R(T = 300\ K) \rangle$ where, $\langle R(T) \rangle$ is the average position of a given layer at temperature T. This parameter, $\delta R(T)$, is the measure of the expansion of the interface as a function of temperature along the $1.1 \cdot \rho_C$ isochore. The results are summarized in Fig. 6.7.

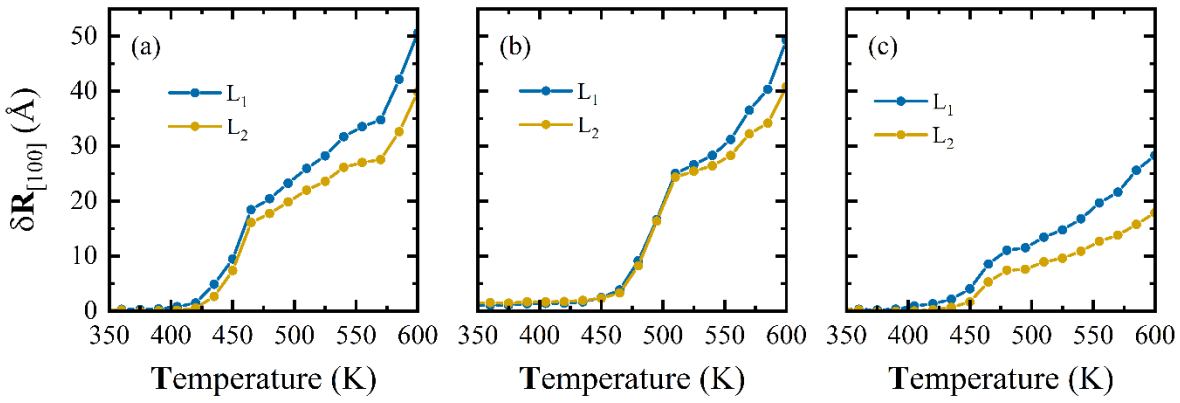

Figure 6.7. Temperature dependence of the thermal extension of CUR in different layers of [100] interface of (a) POLY-I, (b) POLY-II and (c) POLY-III.

The data in Fig. 6.7 (a) clearly indicates that interfacial expansion of POLY-I along the [100] direction begins at approximately 420 K, which is significantly below the bulk melting temperature ($T_m \approx 550$ K) and also lower than the corresponding onset observed in the CUR–vacuum interface (≈ 450 K). This suggests that interfacial melting is promoted by the presence of $scCO_2$, likely due to its ability to penetrate or disrupt surface interactions. Although changes for POLY-II and POLY-III happen at slightly higher temperatures, they are, nonetheless, much lower than the bulk ones, quite comparable to the values for the vacuum interface.

Furthermore, the extent of expansion decreases progressively from the first to the second layer, as both temperature (350 K to 600 K) and pressure exerted by $scCO_2$ (70 bar to 700 bar) increase. This trend indicates that thermal and pressure-driven reorganization proceeds from the surface into the subsurface layers, reflecting a gradual loss of crystalline order at the interface under supercritical conditions.

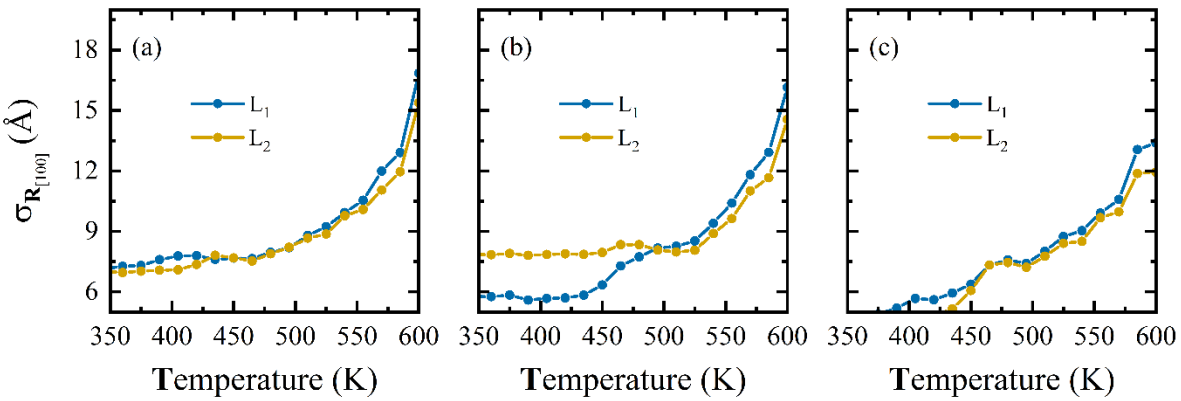

Figure 6.8. Temperature dependence of the fluctuation of mass-density profiles of CUR in different layers of [100] interface of (a) POLY-I, (b) POLY-II and (c) POLY-III.

The fluctuation in the position of the three first layers is given in Fig. 6.8. The values increase non-linearly with temperature. In POLY-I, the onset of temperature at which the rate of increases of the fluctuation increases is T ~ 450 K. In additions, this rate of increase is similar in all considered layers. In POLY-III, the onset of changes in the fluctuations is located at T = 380 K, at lower temperature than the bulk melting temperature. In POLY-II, the values of the fluctuations go through a shallow maximum at T ~ 470 K and increase for further increase of the temperature.

6.3.2. Nearest Neighbor Distribution

More information about the impact of increasing the temperature along the 1.1·ρ_C isochore on the structural organization of the CUR molecules at the first layer interface with $scCO_2$ can be obtained from the temperature dependence of the average distance, $\langle R^{(n)} \rangle$, between a reference CUR molecule and its subsequent neighbors belonging to the same layer. The results are displayed in Fig. 6.9.

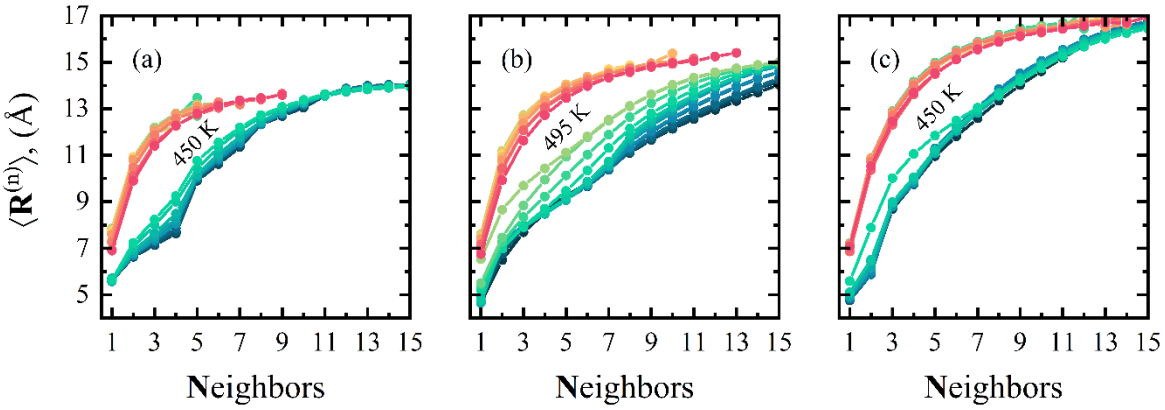

Figure 6.9. Temperature dependence of the average distance between nearest neighbors in the 1st layers of [100] interface of (a) POLY-I, (b) POLY-II and (c) POLY-III.

Contrary to the gradual behavior seen in Fig. 4.5 for vacuum interface, average intralayer neighbor distances have large changes around the melting point, even for the first neighbor. Additionally, instead of getting closer and organizing in pairs, CUR molecules seem to distance from each other. The transition at T ~ 450 K from the crystalline to the melt phase of CUR is accompanied by a jump in the average distance value. Of note is that at high temperature, in the melt phase of CUR, for neighbors *n = 5-7*, the distances become too big to accurately compute the relevant RDFs. Similar trends are observed for both POLY-II and POLY-III.

6.3.3. Voronoi

We have computed 2D VP densities distributions of CUR molecules in the three polymorphs of CUR belong to the first layer of the interface along the [100] plane with $scCO_2$ along the 1.1·ρ_C isochore. Based on these distributions, we have calculated Voronoi local surface density, $\langle \rho_{COM}^{VP} \rangle$, and its temperature dependence is illustrated in Fig. 6.10. This figure shows that there is almost no difference in the rate of increase of the surface local density

between the first and second layers, except in POLY-II, in the crystalline phase, where the surface local density values in the second layer are higher than those in the first one. They further undergo a large decrease to equal those of the first layer in the melt phase.

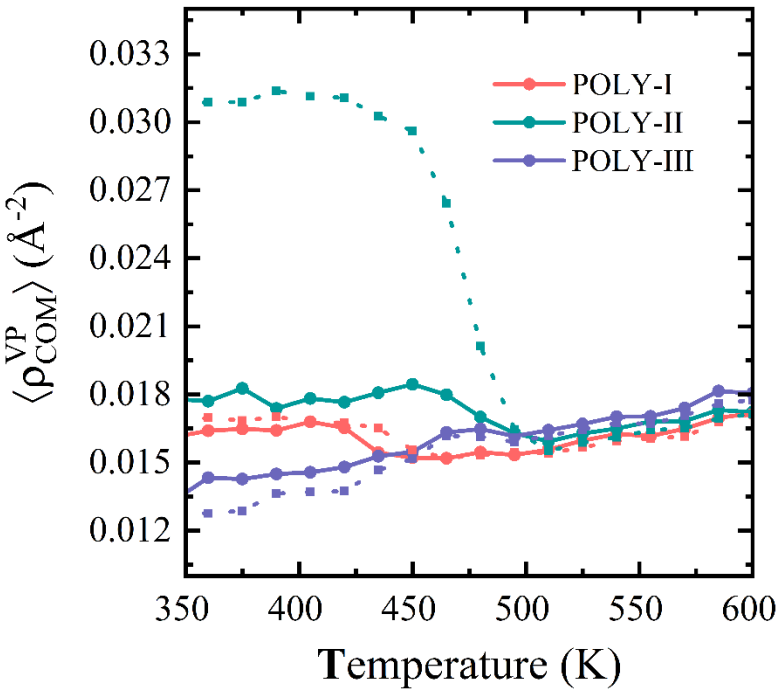

Figure 6.10. 2D VP density as a function of temperature for 1st (solid lines) and 2nd (dashed lines) layers of [100] interfaces of different polymorphs of CUR.

6.4. Conformational Transitions at the CO_2 Interface

We analyzed the temperature-dependent conformational distributions of CUR molecules within the first and second interfacial layers at the [100] surface of all three CUR polymorphs in the presence of supercritical CO_2. The results, displayed in Fig. 6.11, highlight the influence of CO_2 on conformational dynamics in comparison to the vacuum interface.

In POLY-I, the evolution of CONF-1, CONF-2, and CONF-3 fractions, in both interfacial layers, follows the same qualitative trend as observed under vacuum. However, a key distinction is that the onset temperature for conformational changes – i.e., the point where the fractions begin to rise or fall – is lower in the presence of CO_2, suggesting that the interface with CO_2 facilitates earlier conformational rearrangements.

The temperature dependence of CONF-1 fractions in POLY-II and POLY-III is also similar to that observed in vacuum, both in terms of general trend and relative magnitude, though the transitions still occur slightly earlier with CO_2. In contrast, the behavior of CONF-2 and CONF-3 is more complex and more sensitive to the presence of CO_2 – especially in POLY-II and POLY-III:

- For POLY-II, under vacuum, CONF-2 and CONF-3 are present in nearly equal amounts in the crystalline phase. However, with CO_2 at the interface, the fraction of CONF-2 becomes notably higher than that of CONF-3 at low temperatures.
- The temperature at which CONF-2 starts to decrease and CONF-3 begins to rise is lower with CO_2 than in vacuum, and the rate of change is steeper, indicating a stronger thermodynamic driving force or reduced energetic barrier for the transition.

In POLY-III, CONF-2 and CONF-3 also begin with similar fractions in the crystalline regime. However, the onset of their divergence (CONF-2 decreasing, CONF-3 increasing) occurs at lower temperature at the CO_2 interface than at the vacuum one. Interestingly, in the vacuum case, conformational distributions remain relatively stable, indicating that CO_2 plays a significant role in activating molecular rearrangement.

A particularly distinct behavior is observed in POLY-III's second layer: while the first layer displays the expected rise in CONF-3 at the expense of CONF-2, the second layer retains a dominant population of CONF-2 for longer, with the transition occurring at a higher temperature. This layer-resolved disparity suggests that conformational transitions initiate at the surface and propagate inward with a thermal lag. Eventually, in the melt phase, the conformational distributions of CONF-2 and CONF-3 converge in both layers.

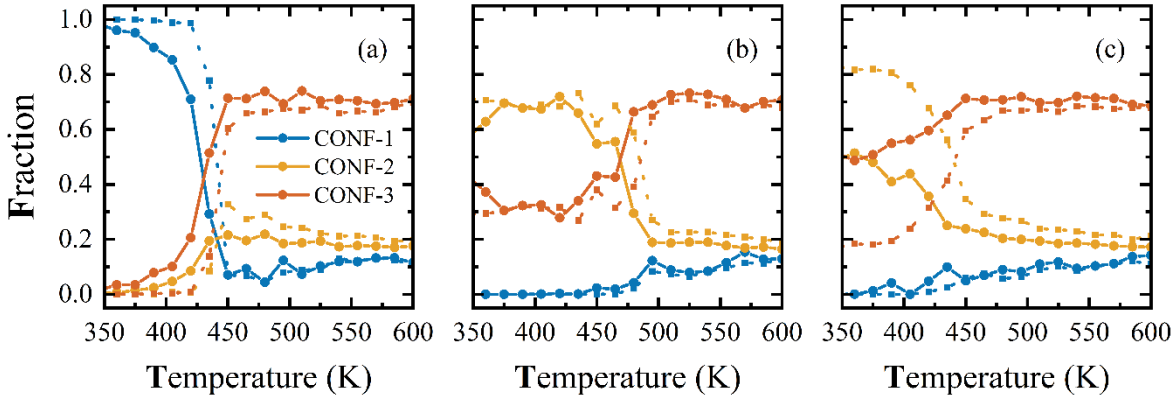

Figure 6.11. Temperature dependence of conformational distributions in the simulation of 1st (solid lines) and 2nd (dashed lines) layers of [100] interface of (a) POLY-I, (b) POLY-II and (c) POLY-III.

6.5. Interactions of Curcumin at the Interface

6.5.1. Hydrogen Bonding

To further investigate the structural implications of conformational changes, we have computed the average number of hydrogen bonds, $\langle N_{HB} \rangle$, between CUR molecules within the first two layers and between them at the [100] interface for each polymorph. The results, summarized in Fig. 6.12, show that the fraction of CUR molecules engaged in hydrogen bonding is relatively low across all systems, suggesting the dominance of Van der Waals and π–π stacking interactions in CUR stabilization. In POLY-I, during the crystalline phase, the $\langle N_{HB} \rangle$ values are similar within the first layer and between the first and second layers, and both are higher than those in the second layer. These values remain almost temperature-independent until melting occurs, indicating robust structural cohesion at the surface. Upon entering the melt regime $\langle N_{HB} \rangle$ decreases gradually both within and between layers, while in the second layer a small increase is first observed (possibly due to enhanced mobility or reorientation), before it too decreases and converges with the others. In POLY-III, $\langle N_{HB} \rangle$ is highest in the first layer and lower (but similar) in the second and between layers of the crystalline phase. With increasing temperature, all values gradually decline and converge in the melt, suggesting the loss of interlayer structural differentiation and the onset of interfacial disorder. POLY-II displays the most anisotropic hydrogen bonding behavior. Initially, $\langle N_{HB} \rangle$ is highest between layers, lowest within the first layer, and intermediate in the second layer. This points to strong interlayer coupling and a less ordered surface. Notably, the $\langle N_{HB} \rangle$ within the first layer decreases steadily with temperature, while the second layer exhibits a non-monotonic trend: values remain constant up to ~420 K, peak at 450 K, and then drop sharply – suggesting a delayed structural response and sudden loss of H-bond connectivity. Furthermore, the onset of HB loss between layers occurs earlier than in the vacuum interface, reinforcing the idea that CO_2 accelerates structural breakdown.

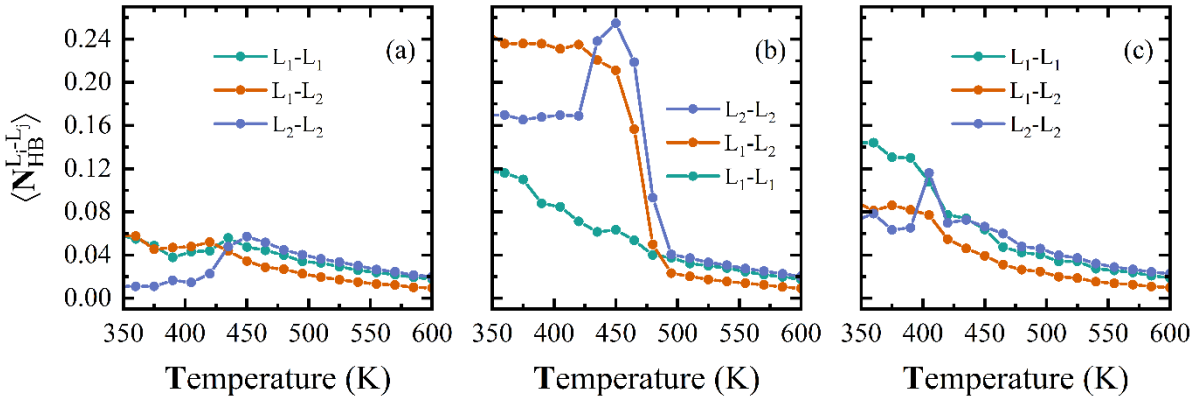

Figure 6.12. Average number of hydrogen bonds between two CUR molecules in the designated layers of [100] interface of (a) POLY-I, (b) POLY-II and (c) POLY-III as a function of temperature.

6.5.2. Pair Interaction Energies

The local structure of CUR molecules at the CO_2 interface is largely governed by the intermolecular interaction energies. To assess this behavior, we have investigated the pairwise interaction energies between a reference CUR molecule and its nearest neighbor, decomposing the total energy into ES and LJ contributions. The temperature dependence of these interactions is displayed in Fig. 6.13 and Fig. 6.14.

Overall, both LJ and ES interactions are attractive across all systems, with LJ contributions being consistently stronger in magnitude. In all systems, the LJ interactions within the same layer are strong and nearly equal, while those between layers are weaker, though still attractive. ES interactions in the first and second layers are generally comparable, with the exception of the POLY-II, where 2nd layer ES contribution is much more negative than that of the 1st layer. As temperature increases, ES interactions within the first layer weaken gradually, with only POLY-II displaying noticeable sharp changes at around T = 450 K. ES interactions in the second layer, as well as between the layers, also decrease gradually, again with the exception of POLY-II. These significant changes are emblematic of the hydrogen bonding behavior seen in Fig. 6.12 (b).

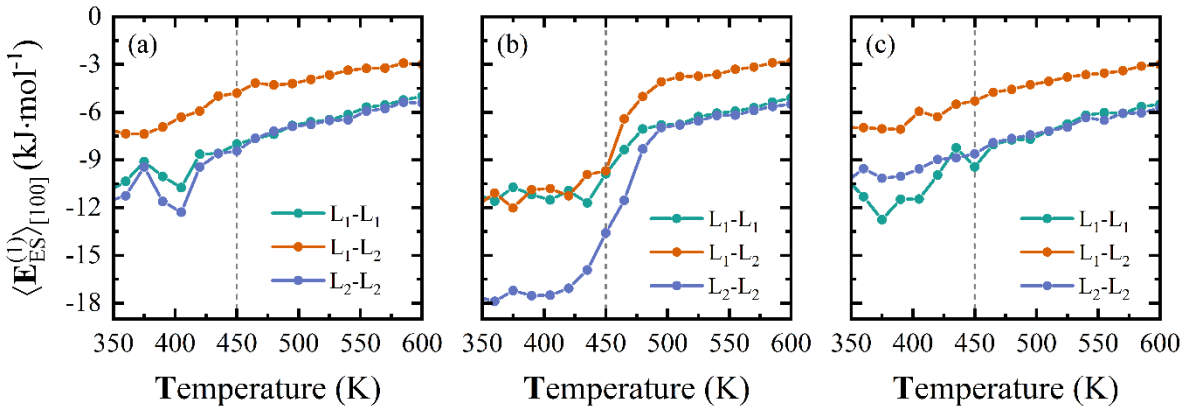

Figure 6.13. Temperature dependence of the ES pairwise interaction energies between a reference CUR molecule and its nearest CUR neighbor within the first layer, second layer, and across the first and second layers for the [100] crystallographic interface of (a) POLY-I, (b) POLY-II, and (c) POLY-III.

Interestingly, both interactions are strongly attractive within layers, and notably weaker between layers not only for the crystalline phase, but also for the melt phase. This interlayer to intralayer disparity happens in spite of conformational changes and long-range order breakdown.

Despite the presence of clearly competing forces, them being π-π stacking and hydrogen bonding, ES and LJ orderings and trends are quite similar between polymorphs and layers. The key distinction is seen for POLY-III, where second layer is much more LJ-bound than the first layer, while the ES contributions are similar. This provides an interesting correlation with the conformational differences between first and second layers of POLY-III seen in Fig. 6.11. Despite the main differences between CONF-2 and CONF-3 consisting of intramolecular hydrogen bond formation, conformational distribution changes appear to be LJ, not ES, driven.

These results have important implications for understanding interfacial structure and dynamics. The gradual decrease in interaction energies near T ≈ 450 K across all polymorphs, much more gradual than in vacuum, suggest that scCO₂ plays a major role in solvating even sub-interfacial layers. The initial strengthening of interlayer ES interactions, particularly in POLY-I and POLY-III, may reflect a transient structural reorganization, where molecules realign to maintain cohesion before the interface begins to disorder. This behavior supports the view that interfacial melting is not a sudden event but involves layer-specific and direction-dependent destabilization processes.

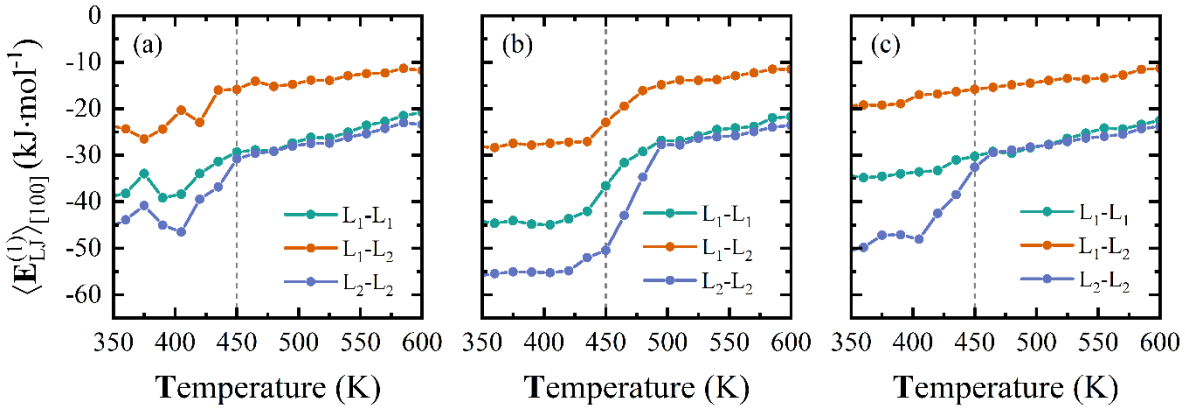

Figure 6.14. Temperature dependence of the LJ pairwise interaction energies between a reference CUR molecule and its nearest CUR neighbor within the first layer, second layer, and across the first and second layers for the [100] crystallographic interface of (a) POLY-I, (b) POLY-II, and (c) POLY-III.

6.5.3. Surface Tension and Surface Area

To deepen our understanding of interfacial behavior, we have computed surface tension for the [100] crystallographic plane of the three CUR polymorphs in contact with supercritical CO_2. The results are presented in Fig. 6.15 (a). For POLY-I and POLY-III, the surface tension exhibits a similar temperature-dependent trend: it remains nearly constant throughout the crystalline phase, followed by a sharp decline just below T ≈ 450 K, eventually approaching zero in the melt phase. This behavior reflects a sudden loss of interfacial cohesion and the onset of structural disorder at this critical temperature.

In contrast, POLY-II displays a distinct profile. The surface tension increases noticeably around T ≈ 450 K, likely indicating a transient enhancement of interfacial cohesion, before decreasing with further heating and finally reaching zero at a higher temperature than those observed for POLY-I and POLY-III. This suggests a delayed or more gradual interfacial destabilization process in POLY-II, possibly linked to its unique conformational behavior and hydrogen-bonding network.

Complementary insights are provided by the effective surface area per CUR molecule, shown in Fig. 6.15 (b). In both POLY-I and POLY-III, the interfacial surface area values are lower in the presence of $scCO_2$ compared to the vacuum interface, indicating tighter molecular packing at the interface due to CO_2-mediated compression.

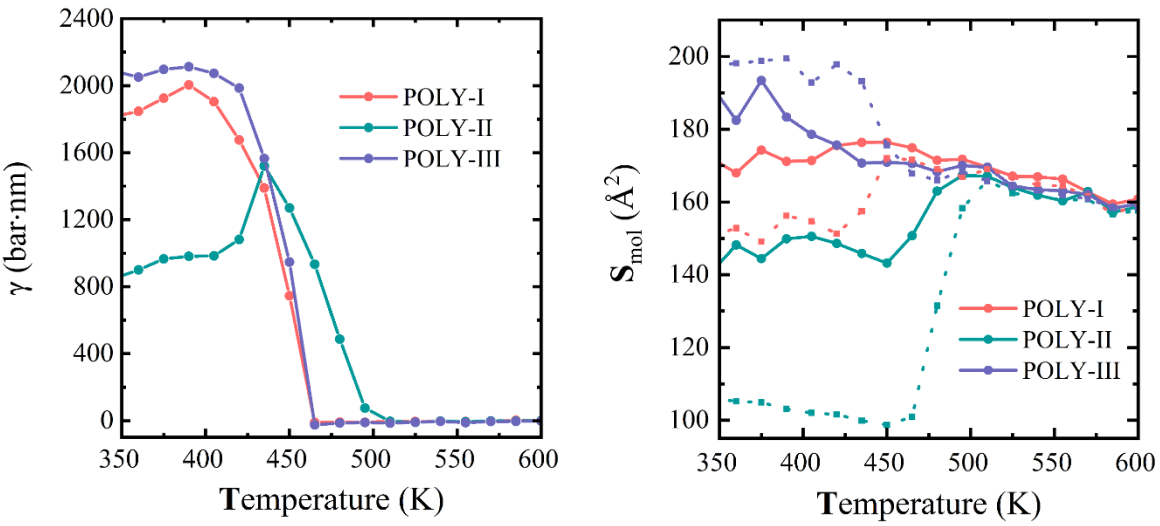

Figure 6.15. (a) Dependence of the surface tension of the [100] interfaces of different CUR polymorphs. (b) Surface Area per CUR molecule as a function of temperature for the 1st (solid lines) and 2nd (dashed lines) layers of [100] interfaces of different CUR polymorphs.

This suggests that $scCO_2$ promotes a more compact and possibly more stable interfacial arrangement. In contrast, for POLY-II, the surface area values remain comparable to those in vacuum, implying that CO_2 has minimal effect on the surface packing of this polymorph – possibly due to a less responsive or more structurally constrained interface.

Analysis of the CED values further confirms the equalizing effect of the $scCO_2$, as Fig. 6.16 clearly shows similarity in the behavior of different polymorphs. Comparison with the vacuum values of Ch. 4 shows same room temperature CED at around 150 kJ/mol/nm^3.

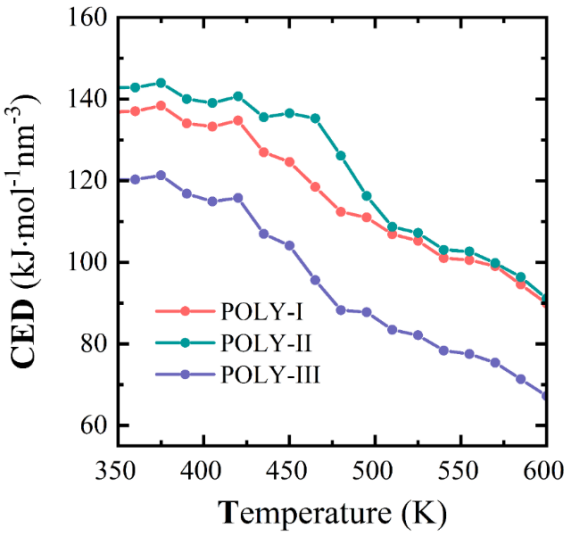

Figure 6.16. Temperature dependence of the cohesive energy density for all polymorphs in contact with $scCO_2$ at their respective [100] interfaces. Includes CO_2 interaction contributions.

6.6. Dynamics of Curcumin at the Interface

An important part of SCFs is their dynamical properties, such as diffusion coefficients and viscosities, which lie between those of gas and liquid. It is worth examining then how unique dynamics of SCFs impact the dynamics of solid and melt CUR in general, and their interfaces in particular.

6.6.1. Voronoi Correlation Time

The time correlation of the local density as calculated by 2D Voronoi are depicted in Fig 6.17. In the crystalline phase, below T = 450 K, the values of these parameters are almost equal for CUR molecules in the three polymorphs. The values show gradual decrease in the crystalline phase, for all of the considered layers, indicating slow increase in lateral molecular mobility. These values go through a more or less defined maximum at around T = 450 K, indicating the transition between from crystalline to the melt phase. This maximum also marks the transition from definitively bi-exponential decay to melt autocorrelation curves, curves that could be described with mono-exponential model to varying degrees of success.

Differences between VP density correlation times of different polymorphs of CUR are quite reminiscent of those at the vacuum interface. A tentative exception of POLY-III, which has fast relaxation times between 450 K and 500 K, is hard to analyze due to the noisiness of the data. CUR in $scCO_2$ generally shows faster dynamics, with slowest τ_1 with $scCO_2$ of 7.5 ps, compared to 18 ps in vacuum simulations. The biggest difference is seen at low temperatures, particularly at T = 300 K. This is most likely due to the inhomogeneity of $scCO_2$, as T = 300 K is very close to the critical point of CO_2.

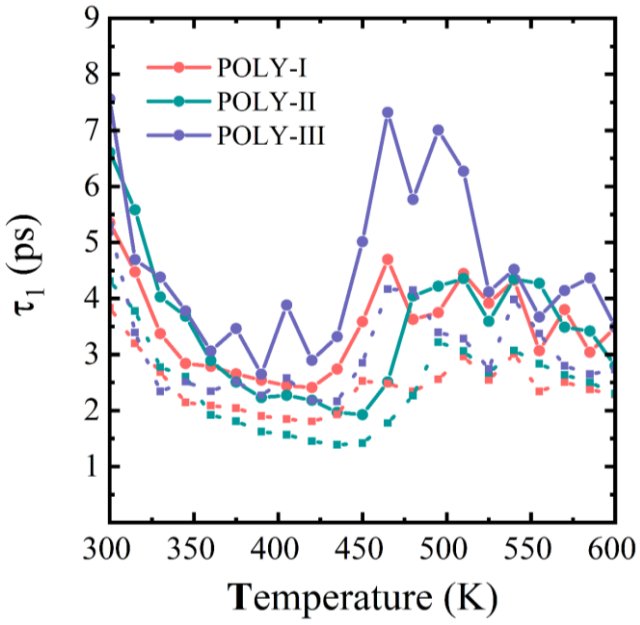

Figure 6.17. Dependence of the fast time component of the 2D VP autocorrelation function of the 1st (solid lines) and 2nd (dashed lines) layers on the temperature in the simulation of [100] interface of different polymorphs.

6.6.2. Time of Residence

To assess the impact of $scCO_2$ on interfacial dynamics, we have computed the time of residence (ToR) of CUR molecules in the first two layers of the [100] interface for all three polymorphs (Fig. 6.18). In POLY-I, ToR values for the first and second layers remain nearly constant over the full temperature range, indicating that $scCO_2$ stabilizes molecular positions and limits interlayer exchange. In POLY-II, $scCO_2$ increases the ToR of molecules in the second layer, effectively equalizing dynamics across the interface. A pronounced drop at ~450 K coincides with the melting transition, followed by a smooth decline in ToR in the melt. For POLY-III, ToR gradually decreases with temperature, with no sharp melting signature – suggesting more progressive surface disordering. Overall, the presence of CO_2 dampens the thermal sensitivity of ToR and promotes more uniform interfacial dynamics, particularly in POLY-I and POLY-II.

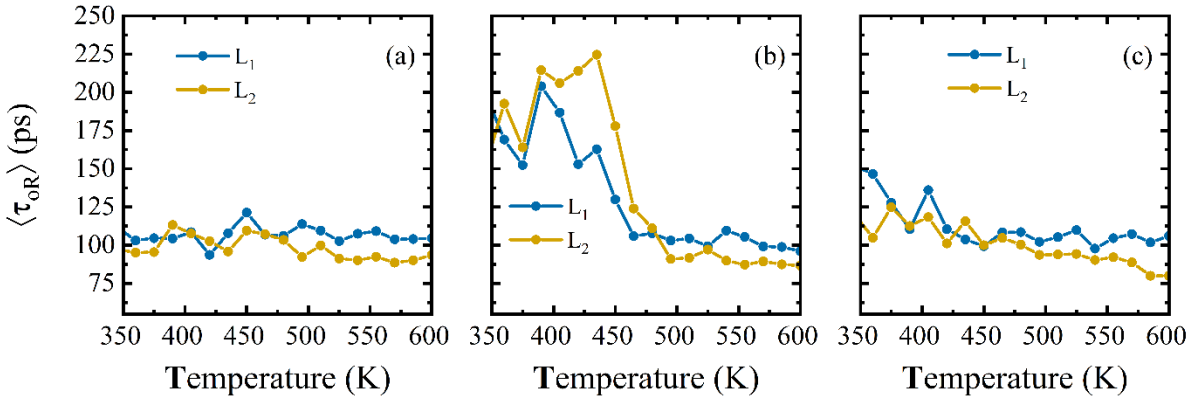

Figure 6.18. Dependence of the average time of residence of CUR in the designated layer of the [100] interface of (a) POLY-I, (b) POLY-II and (c) POLY-III on the temperature.

6.6.3. Diffusion

To deepen our understanding of the interfacial dynamics, we computed the lateral ($D_{=}$) and perpendicular ($D_{\perp}$) diffusion coefficients of CUR molecules for the three polymorphs at the [100] crystallographic plane in the presence of supercritical CO_2. The results are presented in Fig. 6.19.

Across the entire temperature range considered in our molecular dynamics simulations, two clear trends emerge:

- Lateral diffusion ($D_{=}$) consistently exceeds perpendicular diffusion ($D_{\perp}$) for all three polymorphs. This anisotropy reflects restricted movement across the interface normal, likely due to stronger confinement in the direction perpendicular to the surface.
- Both $D_{=}$ and $D_{\perp}$ are significantly higher than those observed at the vacuum interface, indicating that the presence of CO_2 enhances molecular mobility, possibly by reducing surface tension or disrupting cohesive interactions.

Another key observation is that the diffusion coefficients are nearly identical in the first and second interfacial layers, suggesting similar dynamic environments in these two layers and a lack of strong layering in terms of mobility constraints.

Finally, among the three polymorphs, POLY-III exhibits the highest onset temperature for perpendicular diffusion, indicating that its interfacial structure resists out-of-plane molecular motion more effectively than POLY-I and POLY-II. This delayed activation of perpendicular diffusion may be linked to stronger cohesive interactions or more rigid conformational states in the crystalline regime of POLY-III.

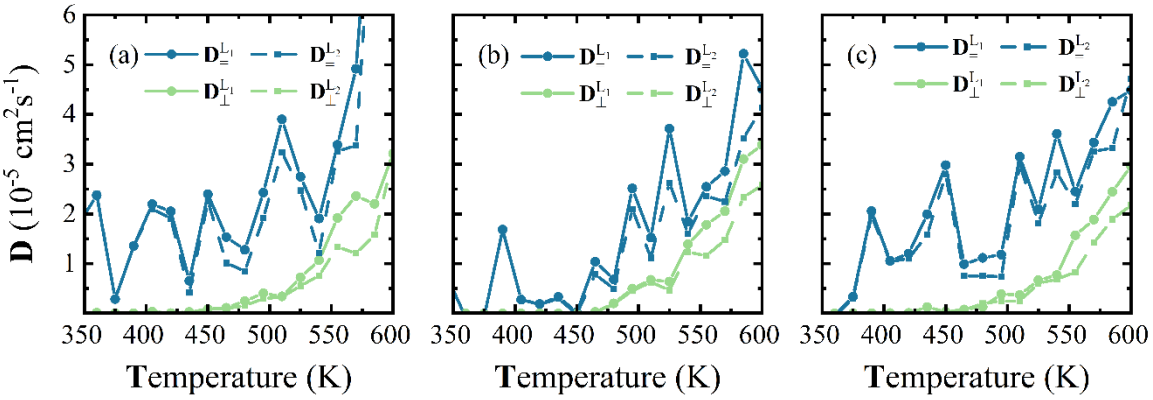

Figure 6.19. Temperature dependence of the lateral (blue lines) and perpendicular (green lines) diffusion coefficients of CUR molecules within the 1st (solid lines) and 2nd (dashed lines) layers of [100] interfaces of (a) POLY-I, (b) POLY-II and (c) POLY-III.

6.7. Conclusions

The presence of supercritical CO_2 at the interface of CUR polymorphs induces profound and polymorph-specific changes in both structural organization and molecular dynamics across the temperature range from 350 K to 600 K. Compared to the vacuum interface, $scCO_2$ acts as a plasticizing agent, facilitating molecular mobility, modulating conformational preferences, and reshaping interfacial cohesion.

The conformational fractions (CONF-1, CONF-2, and CONF-3) respond differently to $scCO_2$ across polymorphs:

- In POLY-I, the presence of $scCO_2$ lowers the onset temperature for conformational transitions (especially for CONF-1), without altering the overall sequence of transitions compared to vacuum.
- In POLY-II and POLY-III, $scCO_2$ promotes an earlier and more pronounced transition from CONF-2 to CONF-3, suggesting that $scCO_2$ stabilizes CONF-3 and destabilizes CONF-2. This is particularly evident in the first interfacial layer, with a thermal lag observed in the second layer.
- In all polymorphs, the fraction of CONF-1 becomes systematically higher in the melt when $scCO_2$ is present, indicating enhanced conformational freedom or stabilization of more flexible conformers.
- The average number of hydrogen bonds is slightly lower in the presence of $scCO_2$ in the crystalline regime but follows a more gradual decline upon melting.
- In POLY-II, the interlayer hydrogen bonding is enhanced at low temperatures.
- The shift in conformational distributions is strongly correlated with changes in hydrogen bonding networks – particularly the loss of CONF-2, which typically supports more H-bonding interactions.
- The average distance to nearest neighbors increases progressively with temperature, with a more pronounced expansion in the second and third layers compared to the first. This is indicative of onset of disorder beneath the interface.
- The fluctuations of these distances are also enhanced under $scCO_2$, especially in POLY-II and POLY-III, reflecting the increased local dynamics introduced by the fluid medium.
- In $scCO_2$, the weakening of ES interactions in the melt phase occurs more gradually.

- In POLY-II, $scCO_2$ seems to destabilize interlayer interactions at lower temperatures but strengthens within-layer LJ interactions, suggesting a restructuring of interfacial packing.
- The surface tension of POLY-I and POLY-III drops sharply around 450 K in the presence of $scCO_2$, mirroring the behavior in vacuum, but at slightly lower values, implying a softening of the interface.
- For POLY-II, the surface tension displays a temporary increase near 450 K, suggesting interfacial reorganization prior to collapse.
- The effective surface area per molecule is generally smaller in $scCO_2$ than in vacuum for POLY-I and POLY-III, indicating tighter molecular packing at the interface, while POLY-II shows minimal difference, implying a more disordered or looser interface under both conditions.
- ToR values are more stable across temperature in the presence of $scCO_2$, in contrast to the gradual decline observed in vacuum, especially in POLY-I.
- In POLY-II, the presence of $scCO_2$ equalizes ToR across the first couple of layers, suggesting enhanced dynamic uniformity and possibly more homogeneous interfacial structure.
- POLY-III still exhibits a gradual ToR decrease, but without sharp transitions, suggesting a progressive interfacial softening under CO_2.
- Both lateral ($D_{=}$) and perpendicular ($D_{\perp}$) diffusion coefficients are higher in $scCO_2$ than in vacuum, confirming that CO_2 enhances mobility.
- $D_{=} > D_{\perp}$ in all cases, indicating preferential in-plane motion, but the onset temperature for $D_{\perp} >> 0$ is highest in POLY-III, highlighting its more rigid interfacial structure.
- The similarity in diffusion between the first and second layers indicates that $scCO_2$ reduces dynamic stratification at the interface.

Supercritical CO_2 acts then as a modulator of interfacial properties, reducing the barriers to conformational transitions, weakening long-range hydrogen bonding, and facilitating enhanced local mobility. These effects are polymorph- and orientation-specific, with POLY-II showing the strongest $scCO_2$-induced reorganization and POLY-III maintaining relative rigidity. Understanding these behaviors provides critical insight into polymorph stability, interfacial crystallization, and transformation pathways, especially under process conditions relevant for pharmaceutical formulation or CO_2-assisted crystallization technologies.

6.8. Bibliography

(1) Abraham, M. J.; Murtola, T.; Schulz, R.; Páll, S.; Smith, J. C.; Hess, B.; Lindahl, E. GROMACS: High Performance Molecular Simulations through Multi-Level Parallelism from Laptops to Supercomputers. *SoftwareX* **2015**, *1–2*, 19–25. https://doi.org/10.1016/j.softx.2015.06.001.

(2) Bussi, G.; Donadio, D.; Parrinello, M. Canonical Sampling through Velocity Rescaling. *J. Chem. Phys.* **2007**, *126* (1), 014101. https://doi.org/10.1063/1.2408420.

(3) Bussi, G.; Zykova-Timan, T.; Parrinello, M. Isothermal-Isobaric Molecular Dynamics Using Stochastic Velocity Rescaling. *J. Chem. Phys.* **2009**, *130* (7), 074101. https://doi.org/10.1063/1.3073889.

(4) Groom, C. R.; Bruno, I. J.; Lightfoot, M. P.; Ward, S. C. The Cambridge Structural Database. *Acta Crystallogr. Sect. B Struct. Sci. Cryst. Eng. Mater.* **2016**, *72* (Pt 2), 171–179. https://doi.org/10.1107/S2052520616003954.

(5) Sanphui, P.; Goud, N. R.; Khandavilli, U. B. R.; Bhanoth, S.; Nangia, A. New Polymorphs of Curcumin. *Chem. Commun.* **2011**, *47* (17), 5013–5015. https://doi.org/10.1039/C1CC10204D.

(6) Pártay, L. B.; Hantal, G.; Jedlovszky, P.; Vincze, Á.; Horvai, G. A New Method for Determining the Interfacial Molecules and Characterizing the Surface Roughness in Computer Simulations. Application to the Liquid–Vapor Interface of Water. *J. Comput. Chem.* **2008**, *29* (6), 945–956. https://doi.org/10.1002/jcc.20852.

(7) Sega, M.; Hantal, G.; Fábián, B.; Jedlovszky, P. Pytim: A Python Package for the Interfacial Analysis of Molecular Simulations. *J. Comput. Chem.* **2018**, *39* (25), 2118–2125. https://doi.org/10.1002/jcc.25384.

CHAPTER 7
CONCLUSIONS

In this chapter, we summarize the results of the thesis, how they related to the stated objectives and goals, as well as give a brief overview of the perspectives and possible continuations of this research.

7.1. Conclusions

The present thesis was part of the project aimed at investigating the role of the surface properties of APIs, and, more broadly, all aspects of polymorphic transformations of said APIs. Each chapter contains conclusions specific to that stage of research. Overall, we have:

- Developed several new algorithms, including conformational assignment, effective surface area computation and more.
- Implemented many of the existing MD analysis algorithms, such as nearest neighbor distances and pair interaction energies.
- Parametrized and tested a force field model of CUR that can describe thermodynamic and conformational transformations, as well as tested CO_2, H_2O and NH_3 models on their ability to reproduce critical point properties.
- Shown that there are stark molecular level differences between 3 polymorphs of CUR, their organization and their structural properties. We have shown the impact of the interplay between hydrogen bonding and π-π stacking.
- By investigating vacuum interfaces of CUR polymorphs, we have demonstrated the importance of both the 1^{st} and 2^{nd} layers, as well as differences between them. We have also shown the difference between various interfacial planes and concluded that interfacial structure can matter as much as conformational distribution.
- Finally, we have shown that SCFs can increase the solubility of CUR, and decrease its melting point by 25 K – 50 K. It turned out that SCFs negate some of the difference in the structuration of different interfaces allowing clearer examination of the role of conformational changes on the overall polymorphic transformations.

7.2. Perspectives

In the course of this research, a few questions still remained unanswered and even more were raised. Below we summarize few possible continuations of the CUR-$scCO_2$ interface research that could help answer them:

- Analysis of CUR interface with different SCFs in order to check if the impact of different fluids would be bigger, especially considering that $scCO_2$ is one of only few LJ-dominated ones.
- Simulation of CUR interface with a mixture of multiple fluids. By picking fluids with different critical temperatures and pressures one should be able to find a mixture that would have its critical point right around the melting point of the CUR interface. This would maximize the impact of the density inhomogeneity of the SCFs.
- *Ab Initio* MD simulation of CUR in order to better understand the π-stacking behavior and its impact on the conformational transformations below the melting point.
- *Ab Initio* MD in order to simulate keto-enol transition of CUR and establish how much role it could potentially play.
- Conformational analysis with more complex algorithms and bigger number of conformations. Development of some kind of algorithm of selecting the most important conformations on the fly.
- Simulation of more fluid interfaces of different API that are structurally similar to CUR in order to establish more generalized trends.
- Simulation of CUR crystallization with the use of metadynamical methods.